

Site U1409¹

R.D. Norris, P.A. Wilson, P. Blum, A. Fehr, C. Agnini, A. Bornemann, S. Boulila, P.R. Bown, C. Cournede, O. Friedrich, A.K. Ghosh, C.J. Hollis, P.M. Hull, K. Jo, C.K. Junium, M. Kaneko, D. Liebrand, P.C. Lippert, Z. Liu, H. Matsui, K. Moriya, H. Nishi, B.N. Opdyke, D. Penman, B. Romans, H.D. Scher, P. Sexton, H. Takagi, S.K. Turner, J.H. Whiteside, T. Yamaguchi, and Y. Yamamoto²

Chapter contents

Background and objectives	1
Operations	2
Lithostratigraphy	4
Biostratigraphy	9
Paleomagnetism	12
Age-depth model and mass accumulation rates	15
Geochemistry	15
Physical properties	17
Stratigraphic correlation	19
References	20
Figures	22
Tables	70

Background and objectives

Integrated Ocean Drilling Program (IODP) Site U1409 (proposed Site SENR-22A; 41°17.75'N, 49°14.00'W; ~3500 m water depth) is a mid-depth site (~3050 meters below sea level [mbsl] paleodepth at 50 Ma) (Tucholke and Vogt, 1979) in the upper mid-depth end of the Expedition 342 Paleogene Newfoundland sediment drifts depth transect (Fig. F1). The site was positioned to capture a record of sedimentation ~1.5 km shallower than the largely sub-carbonate compensation depth (CCD) record drilled at Site U1403 (Figs. F2, F3). The location, well above the average late Paleogene CCD, should be sensitive to both increases and decreases in carbonate burial, whether these reflect variations in dissolution related to changes in the CCD, changes in carbonate production, or variations in background noncarbonate sedimentation. Our primary scientific objectives for drilling Site U1409 were

- To determine the age of the presumed lower to middle Eocene sediment drift to understand drift sedimentation;
- To obtain records of the Eocene in carbonate-rich sediment that hosts abundant foraminifers suitable to the construction of geochemical climate records;
- To evaluate the history of deep water and the CCD on sediment chemistry, grain size, and provenance; and
- To obtain a record of lower Eocene, Paleogene, and upper Cretaceous sediment in an expanded section with few major chert horizons.

Secondary objectives included the possible recovery of specific Paleogene hyperthermals such as the Eocene Thermal Maximum 2 (ETM2), Paleocene/Eocene Thermal Maximum (PETM), Danian-Selandian events, and a complete Cretaceous/Paleogene (K/Pg) boundary sequence for comparison with the record of these events elsewhere, particularly Site U1403 at the deep end of the Expedition 342 depth transect.

Site U1409 is a companion site to Site U1410 where we employed an offset drilling strategy to obtain advanced piston corer (APC) records through a thicker section of the same sediment drift. Drilling a similar pair of sites (U1407 and U1408) showed that the more expanded Site U1408 record is essentially a record similar to that at Site U1407 but with much more clay and a somewhat younger uppermost sediment record. We found largely the same geometry in the J-Anomaly Ridge sites, where the center of the drift has a massively expanded record of the same geological in-

¹Norris, R.D., Wilson, P.A., Blum, P., Fehr, A., Agnini, C., Bornemann, A., Boulila, S., Bown, P.R., Cournede, C., Friedrich, O., Ghosh, A.K., Hollis, C.J., Hull, P.M., Jo, K., Junium, C.K., Kaneko, M., Liebrand, D., Lippert, P.C., Liu, Z., Matsui, H., Moriya, K., Nishi, H., Opdyke, B.N., Penman, D., Romans, B., Scher, H.D., Sexton, P., Takagi, H., Turner, S.K., Whiteside, J.H., Yamaguchi, T., and Yamamoto, Y., 2014. Site U1409. In Norris, R.D., Wilson, P.A., Blum, P., and the Expedition 342 Scientists, *Proc. IODP*, 342: College Station, TX (Integrated Ocean Drilling Program). doi:10.2204/iodp.proc.342.110.2014

²Expedition 342 Scientists' addresses.



ervals that are present in relatively condensed sections at the ends of the drift. Hence, we expected that coring at Site U1410 would recover a sequence with more clay but with otherwise similar gross stratigraphy to the more condensed companion Site U1409.

The primarily calcareous sequence expected at Site U1409 recorded changes in ocean alkalinity and carbonate production. Sites U1403–U1405 were mainly positioned to capture large-amplitude CCD deepening events, such as the carbonate budget “overshoots” that are thought to be associated with the most extreme climate perturbations of the Cenozoic such as those involved with the K/Pg boundary, the PETM, and the Eocene–Oligocene transition (EOT) (see the “[Site U1403](#),” “[Site U1404](#),” and “[Site U1405](#)” chapters [Norris et al., 2014b, 2014c, 2014d]). These events are recorded at deepwater sites as stratigraphically thin intervals of calcareous sediment in otherwise noncalcareous sediment. In contrast, transient shoaling of the CCD in generally carbonate rich sequences are recorded at Site U1409 by decreasing carbonate preservation and decreasing carbonate content relative to clay or biosiliceous sediment, as we already observed at Sites U1406–U1408. As an upper mid-depth site on the Newfoundland depth transect at ~3500 mbsl, Site U1409 was positioned to allow us to reconstruct small changes in carbonate content between the records of Sites U1406 (3850 mbsl) and U1407 (3080 mbsl) and should have a few intervals in which the sediment is 100% carbonate but also intervals where carbonate abundance falls in the record. Carbonate content was expected to be generally higher at sites in shallower water depth, such as the majority of the sites located on Southeast Newfoundland Ridge, including Sites U1409 and U1410.

The high carbonate contents anticipated in sediment at Site U1409 will permit the construction of detailed stable isotope records and calcareous microfossil biostratigraphy that can be tied by physical property records and magnetostratigraphy to Sites U1403–U1406 further downslope. Ties between sites on Southeast Newfoundland Ridge and those on J-Anomaly Ridge will allow the isotope stratigraphy and biochronology developed for Sites U1406–U1408 to be exported to the lower ends of the depth transect. Site U1409 assumes greater importance in the depth transect because the early Paleogene and Cretaceous sedimentary sequence was expected to be better preserved and have more complete recovery than at any other Expedition 342 site.

Ultimately, the goal was to use the combination of the lower and middle Eocene record at Sites U1407–U1410 and the younger Paleogene record at Site

U1406 to produce composite stable isotope and carbonate content records that can be tied to the more intermittent geochemical records at Sites U1403–U1405. Our aim was to match carbonate-rich intervals across all of the J-Anomaly sites with the sites on Southeast Newfoundland Ridge to create an orbital-resolution record of fluctuations in ocean chemistry and deep water origins.

Site U1409 was proposed to test the hypothesis that there are several acoustically transparent drift packages on the Southeast Newfoundland Ridge that correlate to similar but more persistently developed reflector units on the toe of J-Anomaly Ridge (cored at Site U1403). Drilling on J-Anomaly Ridge showed that the uppermost acoustically transparent unit is of middle Eocene to early Miocene age and is separated from a thin, lower acoustically transparent interval by a set of very well developed reflectors of early Eocene to Cretaceous age. In turn, drilling at Site U1407 showed that the lower acoustically transparent interval overlies shallow-marine carbonates of Albian and older ages. At Site U1409, the putative early Paleogene and Cretaceous sequence is represented by a series of discontinuous reflectors, suggesting that the sequence may be more continuous and less plagued by chert formation than at other drill sites.

We inferred that Site U1409 would provide an expanded record of primarily calcareous ooze and chalk of rough age-equivalence to sites in deeper water on J-Anomaly Ridge. In particular, Site U1409 should provide our highest deposition rate record of the early Eocene to Late Cretaceous as a counterpart to the largely sub-CCD record at Site U1403 and thereby improve age and water depth control on the behavior of the CCD in the North Atlantic during this key interval. Coring at Site U1409 was also expected to recover the most complete and best preserved records of hyperthermal events.

Operations

All times are local ship time (UTC – 2.5 h). See Table [T1](#) for coring summary.

Hole U1409A summary

Latitude: 41°17.7501'N

Longitude: 49°13.9996'W

Water depth below sea level (m): 3503.2

Date started: 1010 h, 16 July 2012

Date finished: 0550 h, 18 July 2012

Time on hole (days): 1.8

Seafloor depth (m drilling depth below rig floor [DRF]): 3514.9

Seafloor depth estimation method: mudline core



Rig floor to sea level (m): 11.70
Penetration depth (m drilling depth below seafloor [DSF]): 200.1
Cored interval (m): 200.1
Recovered length (m): 183.33
Recovery (%): 92
Total cores (number): 26
APC cores (number): 16
Extended core barrel (XCB) cores (number): 10
Drilling system: 11 $\frac{7}{16}$ inch APC/XCB bit with 136.00 m BHA
Objective: core from seafloor to ~250 m DSF or until science objectives are met
Result: drilling terminated at 200 m penetration because of poor recovery in cherts; objectives met

Hole U1409B summary

Latitude: 41°17.7493'N
Longitude: 49°13.9852'W
Water depth below sea level (m): 3501.0
Date started: 0550 h, 18 July 2012
Date finished: 0340 h, 19 July 2012
Time on hole (days): 0.9
Seafloor depth (m DRF): 3512.7
Seafloor depth estimation method: mudline core
Rig floor to sea level (m): 11.70
Penetration depth (m DSF): 170.5
Cored interval (m): 170.5
Recovered length (m): 167.09
Recovery (%): 98
Total cores (number): 19
APC cores (number): 14
XCB cores (number): 5
Drilling system: 11 $\frac{7}{16}$ inch APC/XCB bit with 136.00 m BHA
Objective: core from seafloor to ~250 m DSF or until science objectives are met
Result: target shallower than planned; objectives met

Hole U1409C summary

Latitude: 41°17.7392'N
Longitude: 49°13.9853'W
Water depth below sea level (m): 3500.5
Date started: 0340 h, 19 July 2012
Date finished: 1515 h, 20 July 2012
Time on hole (days): 1.5
Seafloor depth (m DRF): 3512.2
Seafloor depth estimation method: mudline core
Rig floor to sea level (m): 11.75
Penetration depth (m DSF): 160.8
Cored interval (m): 160.8
Recovered length (m): 160.98
Recovery (%): 100

Total cores (number): 21
APC cores (number): 14
XCB cores (number): 7
Drilling system: 11 $\frac{7}{16}$ inch APC/XCB bit with 136.00 m BHA
Objective: repeat cored sequence from Hole U1409B
Result: target reached; objectives met

Description

The vessel arrived at Site U1409 at 1010 h on 16 July 2012 after a 26.3 nmi transit from Site U1408 that took 3.0 h at 8.8 kt. The plan for Site U1409 called for three holes to a depth of ~250 m DSF. In addition, the vibration-isolated television (VIT) camera system was to be deployed and tested for the repairs done after the damage sustained at Site U1403. The test was aborted because of the risks to the camera system from strong ocean currents. Holes U1409A, U1409B, and U1409C were successfully cored to 200.1, 170.5, and 160.8 m DSF, respectively. Overall recovery for Site U1409 was 96.2%. The total time spent at Site U1409 was 101.0 h (4.2 days).

Hole U1409A coring

The pipe trip to the seafloor was interrupted at 2863.3 m DRF to install the VIT with subsea camera system. The plan was to deploy the camera near the seafloor and record the shooting of the APC. After installing the VIT, it was determined that the surface currents posed a serious risk to the equipment, and the VIT frame was pulled back on board. After completing the pipe trip, a 1.07 m long mudline core defined the seafloor depth at 3514.9 m DRF (3503.2 mbsl). Hole U1409A was spudded at 2200 h on 16 July and Cores 342-U1409A-1H through 16H were recovered to 127.0 m DSF using nonmagnetic core barrels and the FlexIT core orientation tool. Core 15H experienced the first partial stroke and the APC was advanced by recovery to Core 16H. The XCB was deployed for Cores 17X through 26X to 200.1 m DSF. The seafloor was cleared at 0550 h on 18 July, ending Hole U1409A. Overall core recovery for Hole U1409A was 183.33 m for the 200.1 m interval cored (91.6% recovery). The total time spent on Hole U1409A was 43.5 h.

Hole U1409B coring

The vessel was offset 20 m east. The mudline recovery was 8.36 m and established the seafloor depth at 3512.7 m DRF (3501.0 mbsl). Hole U1409B was spudded at 0800 h on 18 July and Cores 342-U1409B-1H through 14H were retrieved to 122.5 m DSF using nonmagnetic core barrels and the FlexIT core orientation tool. The XCB was deployed for

Cores 15X through 19X to 170.5 m DSF. The seafloor was cleared at 0340 h on 19 July, ending Hole U1409B. The recovery for Hole U1409B was 167.09 m over the 170.5 m cored (98.0% recovery). The total time spent on Hole U1409B was 22.00 h.

Hole U1409C coring

The vessel was offset 20 m south, and Hole U1409C was spudded at 0800 h on 19 July. After the mudline core, which established the seafloor at 3512.2 m DRF (3500.5 mbsl), the wireline blow-out preventer (BOP) was observed to be leaking around one of the bonnets. The top drive had to be set back, and an attempt was made to tighten the leaking connection. The top drive was then reinstalled, and a core barrel was run to bottom to take Core 342-U1409C-2H. The wireline BOP was still leaking, and the top drive had to be set back again. This time the entire BOP bonnet assembly was changed out. The top drive was again reinstalled, and APC coring resumed to Core 14H (124.2 m DSF). Nonmagnetic core barrels were used for all APC cores. Core orientation was not performed on cores from Hole U1409C. XCB coring continued from Core 15X through 21X to the final depth of 160.8 m DSF. The seafloor was cleared at 1315 h on 20 July. The recovery for Hole U1409C was 160.98 m over the 160.8 m cored (100.1% recovery).

The drill string was pulled to ~3200 m DRF and the rig prepared for a transit in dynamic positioning mode to Site U1410. Although the beacon was tracked during its ascent after being released from the seafloor, it was never sighted at the surface because of poor weather conditions and strong surface currents. The drill floor was secured for transit, and the beacon recovery operations concluded at 1515 h on 20 July, ending Hole U1409C. The total time spent on Hole U1409C was 35.50 h.

Lithostratigraphy

At Site U1409, we recovered a sedimentary succession of deep-sea pelagic sediment of Pleistocene to early Paleocene age. Coring in Hole U1409A recovered the full sequence (200.47 m), whereas Holes U1409B and U1409C were terminated just below the Paleocene/Eocene boundary (Cores 342-U1409B-19X [170.57 mbsf] and 342-U1409C-21X [160.47 mbsf]).

The sediment of Site U1409 comprises four lithostratigraphic units (Figs. F4, F5, F6, F7, F8, F9, F10; Table T2). Unit I contains an ~18 m thick sequence of alternating brown to reddish brown Pleistocene to late Pliocene silty clay and nannofossil ooze with varying abundances of foraminifers and diatoms

(Figs. F6A, F8, F9, F10) and occasional layers of muddy sand with foraminifers (Figs. F5A, F5B, F11). Unit II comprises light yellowish brown to light brownish gray silty clay to nannofossil clay of Oligocene age (Fig. F6B). The ~17 m thick Unit II sediment contains manganese nodules, patches of disseminated sulfides, and rare concentrations of faint red oxide horizons (Fig. F5C). Unit III is an ~65 m thick sedimentary sequence of middle Eocene to early Oligocene age. The sediment of Unit III typically alternates on 50–100 cm scales between light greenish gray nannofossil clay and carbonate-rich white nannofossil ooze (Figs. F5D, F6C, F6D, F12, F13). The alternating light greenish gray and white sediment of Unit III exhibits longer (~13–18 m) wavelength variability in the color contrast observed between adjacent layers, with some intervals characterized by alternating light greenish gray and slightly lighter greenish gray (rather than white) sediment. Near the top of the ~15 m wide intervals of damped gray-white color variation in Unit III, we observed decimeter- to centimeter-scale red oxide horizons (Fig. F14). Unit IV is the thickest sedimentary unit (~100 m) and contains lithologies ranging from pinkish white nannofossil ooze with varying abundances of radiolarians and foraminifers to dark brown claystone, siliceous limestone, and chert (Figs. F5E, F5F, F5G, F7B, F7C, F8, F9, F10, F15). The lower Eocene to lower Paleocene sediment of Unit IV is divided into three subunits. Subunit IVa is composed primarily of pinkish white nannofossil ooze with radiolarians (Figs. F5E, F7B, F8, F9, F10). Subunit IVb is a chert-rich interval of highly varied lithologies including pink to dark brown or gray nannofossil ooze to chalk with interbedded chert, siliceous nannofossil limestone, and nannofossil claystone (Figs. F5, F7C, F8, F9, F10, F15). Subunit IVc contains pink to pale gray or pale brown nannofossil chalk (with and without radiolarians) with darker pink to pink-brown color banding, pink oxidative blebs, and mottling (Figs. F5G, F7D, F8, F9, F10).

Lithostratigraphic units and boundaries are defined by changes in lithology (as identified by visual core description and smear slide observations), physical properties, color reflectance (L^* , a^* , and b^*), and biogenic content (calcium carbonate and silica) (Fig. F4). The lithologic differences observed between units are primarily attributable to varying abundances of nannofossils, diatoms, radiolarians, and foraminifers (Figs. F7C, F8, F9, F10). Lithologic descriptions are based on sediment recovered from Hole U1409A and refined with observations from Holes U1409B and U1409C.

The Unit I/II boundary sits at the sharp contact between the banded and mottled brown to gray Pleis-



tocene- to late Pliocene-age sediment and the underlying, heavily bioturbated, light yellowish brown Oligocene-age silty clay. A sharp contact likewise delineates the boundary between the light yellowish brown Oligocene-age nannofossil clay of Unit II and the interbedded light greenish gray nannofossil clay and white nannofossil ooze of Unit III. The Unit III/IV boundary is defined by the transition from alternating nannofossil clay and ooze to pinkish white, carbonate-rich nannofossil ooze with foraminifers. Subunit IVb is divided from the overlying and underlying Subunits IVa and IVc by the first occurrence of chert and the last occurrence of siliceous facies. Lithologically, the sedimentary sequence recovered at Site U1409 strongly resembles that of Site U1408, with the exception of Unit IV. Unit IV at Site U1409 is expanded and lithologically diverse in comparison to similarly age sediment at Site U1408.

Unit I

Intervals: 342-U1409A-1H-1, 0 cm, to 3H-5, 101 cm; 342-U1409B-1H-1, 0 cm, to 3H-1, 72 cm; 342-U1409C-1H-1, 0 cm, to 3H-1, 19 cm

Depths: Hole U1409A = 0–17.61 mbsf; Hole U1409B = 0–18.52 mbsf; Hole U1409C = 0–15.99 mbsf

Age: Pleistocene to late Pliocene

Lithology: nannofossil ooze to nannofossil foraminiferal ooze, diatomaceous nannofossil ooze, silty clay with nannofossils or foraminifers, and muddy sand with foraminifers

Unit I is an ~18 m thick succession of Pleistocene to late Pliocene sediment with decimeter-scale interbedded deep reddish brown (2.5Y 4/1) clay, gray (5Y 6/1) silty clay, lighter gray nannofossil ooze with foraminifers, and dark greenish gray (10Y 4/1) diatomaceous nannofossil ooze (Figs. F5A, F5B, F6A, F8, F9, F10). The colors, lithologies, and minor sedimentary components of Unit I are variegated in comparison to the underlying sedimentary succession. For example, Core 342-U1409A-3H (10.60–20.64 mbsf) contains three intervals of muddy sand with foraminifers interbedded among gray nannofossil ooze with foraminifers and silty clay. The three muddy sand intervals are composed of crude to distinct intercalated beds of grayer, relatively foraminifer rich and greener, relatively silt rich sand, occasionally with normal grading (Fig. F11). Corresponding muddy sand beds are found in Core 2H in Holes U1409B and U1409C. The upper ~8 m of Unit I contains discrete layers of small pebbles of ice-rafted debris, whereas the lowermost ~1 m contains rare manganese nodules <1 cm in diameter. Sediment is moderately to completely bioturbated throughout

with the exception of the muddy sand layers, which are slightly bioturbated.

The Unit I/II boundary is defined by a sharp contact between the brown-, red-, and gray-banded Pleistocene sediment and the underlying yellowish brown Oligocene-age silty clay in Holes U1409A and U1409B. In Hole U1409C, a large 10 cm long manganese nodule obscures the sharp contact used to define the Unit I/II boundary. We place the Unit I/II boundary in Hole U1409C at the top of this manganese nodule given the scarcity of such nodules in Unit I in Holes U1409A and U1409B. In addition to lithology, the sediment of Units I and II is differentiated by physical properties such as magnetic susceptibility and increased yellow reflectance b^* and natural gamma radiation (NGR) in Unit II (Fig. F4; see “Physical properties”). Unit I sediment is characterized by the highest, most variable magnetic susceptibilities of the entire sedimentary succession. Magnetic susceptibility values decrease at the Unit I/II boundary. Sediment in the uppermost interval of Unit I (e.g., Cores 342-U1409A-1H through 2H; 0–10.67 mbsf) contain radiolarians and diatoms of varying abundances (Fig. F6A). These siliceous groups are only found in Unit I and Subunits IVa and IVc and serve to further distinguish Unit I sediment from that of the underlying Unit II (Figs. F8, F9, F10).

Unit II

Intervals: 342-U1409A-3H-5, 101 cm, to 5H-3, 59 cm; 342-U1409B-3H-1, 72 cm, to 4H-CC, 30 cm; 342-U1409C-3H-1, 19 cm, to 5H-5, 34 cm

Depths: Hole U1409A = 17.61–33.19 mbsf; Hole U1409B = 18.52–37.32 mbsf; Hole U1409C = 15.99–37.14 mbsf

Age: barren interval to early Oligocene

Lithology: silty clay to nannofossil clay

Unit II contains ~17 m of light yellowish brown (2.5Y 6/3) to light brownish gray (5Y 6/2) nannofossil clay with abundant centimeter- to decimeter-scale manganese nodules, disseminated black sulfide flecks, and faint red oxide horizons (Figs. F5C, F6B, F8, F9, F10). The uppermost ~3–5 m of Unit II sediment is barren of planktonic foraminifers and nannofossils (see “Biostratigraphy”) and is of uncertain age. At Site U1409, the presence of abundant manganese nodules is unique to Unit II sediment. The Oligocene-age sediment of Unit II is likewise distinctly characterized by a combination of physical properties and exhibits higher b^* color reflectance values and gamma ray attenuation (GRA) density values than sediment in other units. In Hole U1409A, Unit II mean values are approximately three and two



times higher than those observed in all other units for b* and NGR, respectively. Sharp, erosive contacts define the upper and lower stratigraphic boundaries of Unit II in all holes and coincide with abrupt changes in color, lithology, and the aforementioned physical properties between adjacent units (i.e., the Unit I/II and Unit II/III boundaries).

Unit III

Intervals: 342-U1409A-5H-3, 59 cm, to 12H-4, 49 cm; 342-U1409B-4H-CC, 30 cm, to 11H-CC, 20 cm; 342-U1409C-5H-5, 34 cm, to 12H-3, 27 cm

Depths: Hole U1409A = 33.19–101.09 mbsf; Hole U1409B = 37.32–102.69 mbsf; Hole U1409C = 37.14–100.57 mbsf

Age: middle Eocene

Lithology: nannofossil clay interbedded with nannofossil ooze

Unit III is an ~65 m thick sedimentary sequence composed primarily of interbedded light greenish gray nannofossil clay and carbonate-rich white nannofossil ooze (Fig. F5D, F6C, F6D, F8, F9, F10, F11, F12, F13). The light greenish gray (10Y 7/1 to 5GY 6/1) layers of Unit III are typically one-third thicker than the interbedded white (N 8) nannofossil ooze layers (Fig. F12). Carbonate content varies from ~30 wt% in the greenish layers to ~85 wt% in the white layers. The white nannofossil ooze and light greenish gray clay are further differentiated by physical properties, including color reflectance (L*), magnetic susceptibility, and NGR (Fig. F13).

The sharpness of the relative contrast in color between the interbedded light greenish gray and white layers also changes (Fig. F16). Some intervals contain sharply contrasting beds of light grayish green and white (e.g., Sections 342-U1409A-5H-5 through 6H-5 [35.6–46.6 mbsf] and 8H-2 through 9H-2 [59.6–70.61 mbsf]). Other intervals contain subtly contrasting beds of light grayish green and lighter grayish green (e.g., Sections 7H-1 through 7H-6 [48.6–57.62 mbsf] and 9H-3 through 10H-4 [70.61–83.1 mbsf]). Bioturbation is moderate throughout Unit III, with *Zoophycos*, *Planolites*, and *Chondrites* burrows mottling both the light greenish gray and white sediment. Rare green horizons hosting elevated concentrations of glauconite and chlorite occur throughout the light greenish gray beds of Unit III, but these are conspicuously absent from the white nannofossil ooze. The concentration of green horizons appears to be higher in the uppermost portion of the light greenish gray nannofossil clay intervals immediately underlying the white/green contacts and within the ~15 m thick intervals of reduced color contrast (see expanded dis-

cussion in “**Cyclicity in middle Eocene sediment**”).

Layered light greenish gray nannofossil clay and white nannofossil ooze of middle Eocene age were also recovered at Southeast Newfoundland Ridge Sites U1407 and U1408 (Unit III in both). Similar but less visually distinct alternations were recovered in Oligocene–Miocene sediment at J-Anomaly Ridge sites, most notably at Site U1405. The cyclical sediment of Unit III at Site U1409 contrasts with that of the previous Southeast Newfoundland Ridge sites (U1407 and U1408) by containing two intervals with decimeter- to centimeter-scale graded red-brown oxide horizons (see red-brown oxides in uppermost portions of Unit III in Sections 342-U1408A-4H-4 through 4H-5 in Fig. F17). The most notable red-brown oxide horizon extends over 50 cm of core (Fig. F14; see also Sections 342-U1409B-6H-4, 70 cm, through 6H-5, 90 cm [51.5–53.2 mbsf], and 342-U1409C-6H-7, 8 cm, through 7H-1, 50 cm [49.38–50.3 cm]) and grades upward from a sharp lower contact overlain by red-brown sediment to a diffuse light reddish brown sediment over ~50 cm. This occurrence of red-brown oxide is found near the top of an interval of reduced color cyclicity, as is a second interval of red-brown oxide in interval 342-U1409A-9H-3, 34–142 cm (70.95–72.03 mbsf and corresponding sections in Holes U1409B and U1409C).

A slump in the middle Eocene is indicated by convoluted bedding with centimeter- to decimeter-scale clasts, completely homogenized green nannofossil clay, and contorted bedding in Holes U1409A and U1409C (83.05–86.96 and 84.39–88.09 mbsf, respectively) (Fig. F18). Evidence for slumping is seen at comparable depths in Hole U1409B (e.g., Core 342-U1409B-9H and 10H). However, a fracture in interval 342-U1409B-9H-7, 3–12 cm (83.83–83.92 mbsf), underlain by ~1 m of homogenized green sediment suggests that the majority of slump sediment in Hole U1409B could lie between Cores 9H and 10H. Alternatively, lateral variability in the slump deposit may exist at the scale of tens of meters (e.g., the distance between holes). A second, smaller slump (or unconformity) may also account for the unusually sharp contact between adjacent light greenish gray and white layers in Sections 342-U1409A-12H-2, 342-U1409B-11H-6, and 342-U1409C-12H-2 just above the Unit III/IV boundary.

The Unit III/IV boundary is defined by the transition from interbedded gray and white nannofossil clay and ooze to pinkish white, carbonate-rich nannofossil ooze with foraminifers. The Unit III/IV boundary is observed as a contact in Holes U1409A and U1409C and is underlain by a series of closely spaced

pink horizons. In Hole U1409B, the Unit III–IV transition likely falls between Cores 342-U1409B-11H and 12H. The Unit III/IV boundary coincides with an abrupt downhole decrease in NGR values from a Unit I–III average of 22 cps to a Unit IV average of ~6 cps. Magnetic susceptibility values also decrease downhole from an average of ~32 SI in Unit III to ~26 SI in Unit IV (Fig. F4; see “Physical properties”). The carbonate content of sediment increases downhole at the Unit III/IV boundary from an average of 38 wt% in Units I–III to an average of 82 wt% in Unit IV.

Unit IV

Intervals: 342-U1409A-12H-4, 49 cm, to 26X-CC, 49 cm; 342-U1409B-12H-1, 0 cm, to 19X-CC, 24 cm; 342-U1409C-12H-3, 27 cm, to 21X-CC, 40 cm

Depths: Hole U1409A = 101.09–200.47 mbsf; Hole U1409B = 103.30–170.57 mbsf; Hole U1409C = 100.57–160.47 mbsf

Age: early Eocene to early Paleocene

Lithology: nannofossil ooze to chalk with foraminifers and/or radiolarians, radiolarian or clayey nannofossil ooze with foraminifers or radiolarians, chert, nannofossil claystone, and siliceous nannofossil limestone

Unit IV is an ~100 m thick sequence of lower Eocene to lower Paleocene sediment and is divided into three subunits. Subunits IVa and IVc are compositionally quite similar; both are composed of nannofossil ooze (or chalk) with or without radiolarians and/or foraminifers. The ooze–chalk transition spans the lowermost 10 m of Subunit IVa through IVb and provides the primary lithologic distinction between these subunits. Subunit IVb, in contrast, has numerous interbedded cherts and other silicified sediment, which clearly differentiate this subunit from Subunit IVa above and Subunit IVc below.

Subunit IVa

Intervals: 342-U1409A-12H-4, 49 cm, to 15H-CC, 14 cm; 342-U1409B-12H-1, 0 cm, to 14H-CC, 20 cm; 342-U1409C-12H-3, 27 cm, to 14H-CC, 21 cm

Depth: Hole U1409A = 101.09–126.13 mbsf; Hole U1409B = 103.30–122.50 mbsf; Hole U1409C = 100.57–124.23 mbsf

Age: early Eocene

Lithology: nannofossil ooze with foraminifers and/or radiolarians, radiolarian nannofossil ooze with foraminifers, and nannofossil ooze

Subunit IVa comprises ~25 m of pinkish white (N 8) to very pale brown (10YR 8/3) nannofossil ooze with

varying abundances of radiolarians and foraminifers (Figs. F5E, F6A, F8, F9, F10). Decimeter-scale banding between pinkish white (5YR 8/2 to 5YR 8/3), nearly white (N 8 with pink undertones), and light pinkish brown (10YR 8/3) occur throughout most of Subunit IVa. Sediment becomes darker downhole in Subunit IVb, progressing from a light pinkish white (N 8) to a very pale brown in Core 342-U1409A-15H. Heavy bioturbation, evidenced by faint mottling, occurs throughout. Bright pink (2.5YR 8/4) blebs and nodules of montmorillonite are common in a few sections near the top of the subunit (see montmorillonite in Sections 342-U1409A-13H-1, 0 cm, and 13H-2, 35 cm, in Fig. F19). The transition from the lower Eocene pink ooze of Subunit IVa to the underlying Subunit IVb is marked by the first downhole occurrence of chert.

Unit IVb

Intervals: 342-U1409A-16H-1, 0 cm, to 20X-3, 122 cm; 342-U1409B-15X-1, 0 cm, to 18X-6, 31 cm; 342-U1409C-15X-1, 0 cm, to 21X-CC, 40 cm

Depths: Hole U1409A = 126.10–155.02 mbsf; Hole U1409B = 122.50–158.73 mbsf; Hole U1409C = 124.20–160.47 mbsf (Note that the top depths of Subunit IVb in Holes U1409A and U1409C overlap with the bottom depths of Subunit IVa because the unit boundaries fall between cores and the core depths at CSF-A scale [mbsf] overlap because of core expansion.)

Age: early Eocene to late Paleocene

Lithology: clayey nannofossil ooze, nannofossil ooze with foraminifers or radiolarians, chert, nannofossil claystone, siliceous nannofossil limestone, and nannofossil chalk

Subunit IVb consists of light pinkish brown (10YR 7/3 to 10YR 8/2) nannofossil chalk with frequent centimeter- to decimeter-scale beds of light brown (10YR 4/3) chert and dark brown (10YR 4/1) silicified sediment (Figs. F5F, F15). Common chert layers slowed drilling, impeded core recovery, and likely contributed to the difference in the thickness of Subunit IVb among holes (~29 m in Hole U1409A, ~36 m in Hole U1409B, and ~36 m in Hole U1409C). Subunit IVb extends from lower Eocene nannofossil Zone NP12 just across the PETM into the latest Paleocene (nannofossil Subzone NP9a).

The thickest siliceous sequence in Subunit IVb is found near the base of the subunit and consists of ~45 cm of chert, siliceous nannofossil limestone, siliceous nannofossil claystone, and claystone (Fig. F15). The occurrence of nannofossil excursion taxa (nannofossil Subzone NP9b) within this ~45 cm thick siliceous sequence indicates that it coincides with at least a portion of the PETM. An unconfor-



mity coincident with dark brown (10YR 4/1) chert at the top of the silicified PETM sequence separates the overlying, heavily bioturbated, very pale brown (10YR 8/3) nannofossil chalk from the underlying dark brown (10YR 4/1) siliceous nannofossil claystone (see “[Biostratigraphy](#)”). The duration of the unconformity at the top of the PETM chert differs between Holes U1409A and U1409B, whereas the contact appears conformable in Hole U1409C (see “[Biostratigraphy](#)”). X-ray diffraction (XRD) samples from the lithified PETM interval show evidence of incipient silicification, denoted by a double peak in the diffractogram indicating the presence of tridynamite (20.5° and $21.6^\circ 2\theta$) and possibly also cristobalite ($21.9^\circ 2\theta$) (Fig. [F20](#)). In contrast, samples from the nannofossil chalk above and the claystone in the center of the PETM interval show a mineralogical background composition with mainly calcite, quartz, and clay minerals (e.g., illite). Upper Paleocene nannofossils are present in mottled light brownish (10YR 6/2) nannofossil claystone immediately below the siliceous nannofossil limestone in the lower portion of the silicified PETM interval (Fig. [F15](#)).

The lithologic boundary between Subunits IVb and IVc is defined by the last downhole occurrence of silicified sediment in Unit IV. The Subunit IVb/IVc boundary lies ~45 cm below the base of the PETM siliceous nannofossil limestone and is a 2 cm thick chert in Section 342-U1409A-20X-3, 122 cm, and a pair of ~5–10 cm thick siliceous limestones in Section 342-U1409B-18X-6. Drilling was terminated in Subunit IVb in Hole U1409C. Subunit IVb is additionally differentiated from the overlying and underlying sediment of Subunits IVa and IVc by the near-complete absence of radiolarians and diatoms (Figs. [F8](#), [F9](#), [F10](#)).

Subunit IVc

Intervals: 342-U1409A-20X-3, 122 cm, to 26X-CC, 49 cm; 342-U1409B-18X-6, 31 cm, to 19X-CC, 24 cm

Depths: Hole U1409A = 155.02–200.47 mbsf; Hole U1409B = 158.73–170.57 mbsf

Age: Paleocene

Lithology: nannofossil chalk with radiolarians and nannofossil chalk

Subunit IVc, a lower to upper Paleocene sedimentary succession, was recovered primarily in Hole U1409A. In Holes U1409B and U1409C, drilling was terminated just below the Paleocene/Eocene boundary. Subunits IVa and IVc are lithologically quite similar, despite spanning the ooze–chalk transition. Sediment in the uppermost portion of Subunit IVc is light brownish gray (10YR 6/2) and contains com-

mon to abundant radiolarians, rare diatoms, and centimeter-scale pink diagenetic blebs. The down-hole sedimentary succession includes a transition from nannofossil chalk with radiolarians to nannofossil chalk and several color transitions from light brownish gray (10YR 6/2) to very pale brown (10YR 7/3) to pink (5YR 8/3) to light bluish gray (10Y 8/1). Diagenetic crosscutting pink blebs characterize the brownish gray to light brownish gray sediment, along with faint traces of mottling. Lowermost pink and bluish gray sediment of Subunit IVc is relatively homogeneous. Drilling was terminated in Hole U1409A when relatively silicified sediment slowed drilling and resulted in poor core recovery.

Lithostratigraphic unit summary

Four lithostratigraphic units were identified in the ~200 m thick sedimentary succession of deep-sea sediment recovered at Site U1409. Unit I contains alternating brown to reddish brown Pleistocene silty clay and nannofossil ooze with varying abundances of foraminifers and diatoms and occasional layers of muddy sand with foraminifers. The Unit I/ II and II/ III boundaries are erosive contacts. Unit II is heavily bioturbated, light yellowish brown Oligocene-age silty clay to nannofossil clay containing manganese nodules, patches of disseminated sulfides, and rare concentrations of faint red oxide horizons. Unit III contains alternating beds of light greenish gray nannofossil clay and white nannofossil ooze, with some intervals containing oxide horizons and reduced color contrast between adjacent beds. Unit IV contains lithologies ranging from pinkish white nannofossil ooze with varying abundances of radiolarians and foraminifers to dark brown claystone, siliceous limestone, and chert. The middle Eocene to lower Paleocene sediment of Unit IV is divided into three subunits. Subunits IVa–IVc contain

- Pinkish white nannofossil ooze with radiolarians;
- Frequent cherts and highly varied lithologies including pink to dark brown or gray nannofossil ooze to chalk with interbedded chert, siliceous nannofossil limestone, and nannofossil claystone; and
- Pink to pale gray or pale brown nannofossil chalk.

The lithostratigraphy of Site U1409 strongly resembles that of Site U1408 in terms of appearance, lithology, and sedimentary succession for Units I–III and, to a lesser degree, Unit IV. We observed four lithostratigraphic commonalities among all sites drilled to date on the Southeast Newfoundland Ridge (Sites U1407–U1409). They include



1. Cyclic alternations of light greenish gray nannofossil clay and white (or lighter greenish gray) nannofossil ooze in middle Eocene sediment;
2. Cherts and other silicified sediment in the lower Eocene;
3. Red, red-brown, yellow, pink, and pink-brown Cenozoic sediment capping the greenish gray middle Eocene sequence; and
4. A step change in the carbonate content in sediment in nannofossil Zone NP14 around the lower to middle Eocene boundary with higher carbonate content in the older Eocene sediment.

The observed cyclicity in middle Eocene sediment is discussed in greater detail below.

Cyclicity in middle Eocene sediment

The middle Eocene sediment at Site U1409 exhibits strong cyclicity defined by alternating white nannofossil ooze with foraminifers and greenish gray nannofossil clay from the top of Unit II (Core 342-U1409A-5H) to Core 9H and from Core 11H to Section 342-U1409A-12H-4. The frequency of the cycles is consistent with astronomical forcing. One hypothesis is that clay dilution with astronomical periodicity is the main factor driving these cycles (Fig. F11). Green glauconite/chlorite bands are commonly seen 10–30 cm beneath the white ooze layers. These glauconite bands overprint the burrowing in the green clay-rich layers (Fig. F13), but can be cut by burrows that transport white ooze from above. This observation suggests that the glauconite layers are early diagenetic features that are roughly coeval with the deposition of the white ooze layers. We speculate that the distinct green glauconite bands represent times of relatively slow deposition caused by relatively low dilution by clay (see the “[Site U1408](#)” chapter [Norris et al., 2014e] for further discussion on the origin of the green layers), consistent with the clay-dilution hypothesis for the observed green–white cyclicity.

Biostratigraphy

Coring at Site U1409 recovered a 200 m thick sequence of Pleistocene to lower Paleocene nannofossil ooze and nannofossil clay, with foraminifers and radiolarians. Nannofossils, planktonic foraminifers, and benthic foraminifers are present through most of the succession, although all microfossil groups are absent through a short interval between the Pleistocene and Oligocene. Radiolarians are only present in the uppermost Pleistocene and the lower middle Eocene through the upper Paleocene. Thin Pleistocene and Oligocene intervals overlie a middle Eocene through lower Paleocene succession with significant hiatuses between the lower Pleistocene and upper

Oligocene (22 m.y. duration) and lower Oligocene and middle Eocene (8.3 m.y. duration). A short hiatus or condensed interval is also identified at the Paleocene/Eocene boundary. The Oligocene is highly condensed and may contain significant hiatuses. Sedimentation rates are 0.68–1.31 cm/k.y. through the middle Eocene, 0.51–1.44 cm/k.y. through the lower Eocene, and ~0.47–1.80 cm/k.y. through the Paleocene.

Benthic foraminifers are generally rare (the “present” category) throughout the recovered succession, with the exception of parts of the lower Oligocene and Sample 342-U1409A-22X-CC (179.32 mbsf), where they are dominant. Benthic foraminifer preservation is good to very good through most of the recovered Eocene sequence. Moderate to poor preservation occurs in the Oligocene and Paleocene.

An integrated calcareous and siliceous microfossil biozonation is shown in Figure F21. Datum and zonal determinations from nannofossils, planktonic foraminifers, and radiolarians are in close agreement. An age-depth plot including biostratigraphic and paleomagnetic datums is shown in Figure F30. A summary of calcareous and siliceous microfossil abundances and preservation is given in Figure F22.

Calcareous nannofossils

Calcareous nannofossil biostratigraphy is based on analysis of core catcher samples from Hole U1409A and additional working section half samples from Holes U1409A–U1409C. Depth positions and age estimates of biostratigraphic marker events are shown in Table T3. Calcareous nannofossil occurrence data are shown in Table T4. Note that the distribution charts are based on shipboard study only and are, therefore, biased toward age-diagnostic species.

At Site U1409, the preservation of calcareous nannofossils is generally good to exceptional in the middle Eocene and moderate to good in the Oligocene, lower Eocene, and upper Paleocene. The uppermost sediment from Hole U1409A contain abundant nannofossils indicative of Pleistocene Zones NN20/21–NN16 marked by the top of *Pseudoemiliania lacunosa* in Sample 342-U1409A-2H-CC (10.64 mbsf) and the top of *Discoaster pentaradiatus* in Sample 3H-4, 75 cm (15.85 mbsf). Samples 3H-4, 75 cm (15.85 mbsf), through 3H-CC (20.60 mbsf) are noncalcareous and do not contain nannofossils. The short interval from Sample 4H-CC to 5H-2, 75 cm (30.08–31.85 mbsf), is assigned to Oligocene Zones NP23–NP21 based on the top of *Reticulofenestra umbilicus* (Sample 342-U1409A-5H-2, 75 cm; 30.08 mbsf) and *Coccolithus formosus* (Sample 342-U1409B-4H-7, 27 cm; 36.57 mbsf). The identification of Zone NP21 in Sample 342-U1409B-4H-CC, 6.5 cm (37.08 mbsf), and Zone



NP17 in Sample 4H-CC, 15 cm (37.17 mbsf), indicates the presence of a hiatus of ~6 m.y., representing the upper Eocene to lowermost Oligocene.

Samples 342-U1409A-5H-4, 75 cm, through 26X-CC (34.85–200.03 mbsf) are assigned to middle Eocene to lower Paleocene nannofossil Zones NP17–NP4. The majority of primary zonal marker species are present and listed in Table T3.

The identification of Subzone NP14a in Sample 342-U1409A-14H-3, 110 cm (199.22 mbsf), and Zone NP12 in Sample 14H-5, 110 cm (122.20 mbsf), indicates the presence of a short hiatus (~1.5 m.y.). In addition, the samples taken in the lowermost part of the green clay-rich drift sediment contain nannofossils indicative of Zone NP14 alongside reworked nannofossils from lower in the Eocene (Zone NP12 equivalent). The same nannofossils, *Chiphragmolithus* spp., were also seen at comparable levels (i.e., at the onset of drift sedimentation, approximately Zone NP14) at Sites U1408 and U1406.

The Paleocene–Eocene transition is identified by the presence of Zone NP10 in Sample 342-U1409A-20X-3, 48 cm (154.28 mbsf); Subzone NP9b in Sample 20X-3, 56 cm (154.36 mbsf); and Subzone NP9a in Sample 20X-3, 77 cm (154.57 mbsf). The very short Subzone NP9b interval (<0.29 m) suggests condensed sedimentation and likely a short hiatus, but the presence of the nannofossil excursion taxon *Discoaster araneus* indicates that PETM-equivalent time is represented around Sample 20X-3, 56 cm (154.36 mbsf).

The sequence from Sample 342-U1409A-20X-3, 77 cm, to 26X-CC (154.57–200.03 mbsf) is assigned to Subzone NP9a–Zone NP4 based on the base of *Discoaster multiradiatus* (Sample 20X-5, 114 cm; 157.95 mbsf), the base of *Discoaster mohleri* (Sample 22X-4, 78 cm; 175.28 mbsf), and the base of *Heliolithus kleinpelli* (Sample 24X-2, 80 cm; 191.50 mbsf). The lowermost three cores, 342-U1409A-24X through 26X, contain poorly preserved nannofossil assemblages, but the absence of *Fasciculithus* and presence of *Toweius pertusus* suggests correlation with Zone NP4.

Radiolarians

Radiolarian biostratigraphy is based on analysis of all core catcher samples from Hole U1409A. No samples from Hole U1409B or U1409C were examined. Radiolarians are present in the uppermost part of Hole U1409A (Cores 342-U1409A-1H and 2H) but are either absent or rare in the underlying Pleistocene–middle Eocene interval downhole to Core 11H (96.4 mbsf). Below this level, radiolarians are very abundant in the uppermost lower Eocene, rare but well preserved in the underlying lower Eocene, and gen-

erally abundant and well preserved in the Paleocene. Depth positions and age estimates of biostratigraphic marker events are shown in Table T5, and the radiolarian distribution is shown in Tables T6 and T7. Note that the distribution charts are based on shipboard study only and are, therefore, biased toward age-diagnostic species.

Cores 1H through 2H (1.02–10.64 mbsf) contain a Pleistocene–Holocene radiolarian assemblage assigned to Zone RN17 based on the absence of *Stylactractus universus*.

Samples 342-U1409A-3H-CC through 11H-CC (20.6–96.4 mbsf) are either barren of radiolarians or contain only poorly preserved spumellarians that cannot be assigned to species.

In contrast, radiolarians are very abundant and well preserved in the core catcher samples from Cores 12H and 13H. Sample 12H-CC (105.96 mbsf) is assigned to Zone RP11 based on the presence of the primary index species *Dictyomitra mongolfieri* and the absence of *Eusyringium lagena*, the primary index species for Zone RP12. Sample 13H-CC (115.96 mbsf) is assigned to Zone RP9 based on the presence of the primary index species *Theocorys plesioanaclasta* and the absence of a key index species for Zone RP10, *Lithochytris vespertilio*. Zone RP10 was not identified but may be present within Core 13H because the zone has a duration of only 0.59 m.y.

Samples 14H-CC through 17X-CC (124.91–131.33 mbsf) contain common radiolarians of moderate preservation. This interval is assigned to Zone RP8 based on the presence of the primary index species *Buryella clinata* and the absence of *T. plesioanaclasta* and *Theocorys anaclasta*, both of which have bases in Zone RP9.

Samples 18X-CC through 19X-CC (138.99–141.21 mbsf) contain only rare and poorly preserved radiolarians.

Samples 20X-CC through 21X-CC (160.59–162.71 mbsf) contain abundant well-preserved radiolarians. Sample 20X-CC (160.59 mbsf) is assigned to Zone RP7 based on the common occurrence of the primary index species *Bekoma bidartensis*. As at Sites U1406–U1408, Zone RP7 in Hole U1409A includes earliest Eocene indicator species *Podocyrtis papalis*, *Theocorys? physylla*, and *Theocorys? aff. physylla* (sensu Sanfilippo and Blome, 2001). However, nannofossils indicate that this interval is of Paleocene age. Sample 21X-CC (162.71 mbsf) is assigned to Subzone RP6c based on the co-occurrence of the primary index species for Zone RP6, *Bekoma campechenensis*, and *Buryella pentadica*, which has its base in Subzone RP6c.



Planktonic foraminifers

Core catchers and additional samples from Hole U1409A working section halves were examined. The samples contain diverse and well-preserved assemblages of planktonic foraminifers from Pleistocene through Paleocene age. Depth positions and age estimates of identified biostratigraphic marker events are shown in Table T8. The stratigraphic distribution of planktonic foraminifers is shown in Table T9.

The uppermost Samples 342-U1409A-1H-CC to 2H-CC (0.97–10.61 mbsf) contain *Globorotalia truncatulinoides* and *Globorotalia inflata*, indicative of Pleistocene age. Sample 3H-CC (20.56 mbsf) contains a well-preserved but low-diversity assemblage of *G. inflata*, *Neogloboquadrina dutertrei*, and *Neogloboquadrina pachyderma*, suggesting an age of late Pliocene–Pleistocene. A poorly preserved Oligocene assemblage (mainly comprising *Catapsydrax unicavus*, *Dentoglobigerina tapuriensis*, *Globorotaloides suteri*, *Subbotina angiporoidea*, and *Subbotina corpulenta*) was recovered from Samples 4H-2, 110–112 cm, through 4H-CC (22.7–30.03 mbsf). Poorly preserved planktonic foraminifers of middle Eocene age are found in Samples 5H-3, 25–27 cm, through 5H-3, 65–67 cm (32.85–33.25 mbsf). The presence of the marker species *Acarinina bullbrookii*, *Globigerinathelka index*, and *Globigerinathelka mexicana* suggests that these poorly preserved assemblages are from middle Eocene Zones E11–E14.

Well-preserved and taxonomically diverse planktonic foraminifers of middle Eocene age are found in Samples 5H-3, 110–112 cm, through 13H-CC (33.7–115.41 mbsf). The uppermost portion of this middle Eocene sequence is assigned to Zone E10 based on the co-occurrence of the marker species *Guembelitroides nuttalli*, *Morozovelloides lehneri*, and *G. index*. The top of the morphologically distinctive *Morozovella aragonensis* marks the base of Zone E10 in Sample 7H-CC (58.5 mbsf).

The base of *Globigerinathelka kugleri* occurs in Sample 8H-5, 119–121 cm (65.29 mbsf), and is indicative of the base of Zone E9. The base of *G. nuttalli* in Sample 12H-CC (105.91 mbsf) indicates the base of Zone E8, whereas the base of *Turborotalia frontosa* in Sample 13H-CC (115.41 mbsf) indicates the base of Subzone E7b.

Samples 14H-2, 110–112 cm, through 14H-6, 110–112 cm (117.7–123.7 mbsf), contain planktonic foraminifers ranging from Subzone E7a to Zone E3. The base of *Acarinina cuneicamerata* in Sample 14H-6, 110–112 cm (123.7 mbsf), indicates the base of Subzone E7a, whereas the top of *Morozovella subbotinae* in Sample 14H-CC (124.86 mbsf) marks the base of the comparatively short Zone E6. The base of *M. ara-*

gonensis in Sample 18H-3, 87–89 cm (135.47 mbsf), indicates the base of Zone E5, and the coincident bases of *Morozovella formosa* and *Morozovella lensiformis* in Sample 19H-CC (141.2 mbsf) mark the base of Zone E4.

Zone E3 extends from Sample 20X-1, 55–56 cm (151.35 mbsf), to 20X-3, 36–38 cm (154.16 mbsf). Directly beneath this interval lies a silicified interval representing the PETM interval. In Sample 20X-3, 100–101 cm (154.8 mbsf), we find the PETM “excursion taxon” *Acarinina africana*. Below this level, the uppermost Paleocene Zone P5 contains moderate to poorly preserved foraminifers downhole to Sample 20X-4, 29–30 cm (155.59 mbsf). In contrast, Subzone P4c contains well-preserved foraminifers and spans Samples 20X-5, 114–115 cm, through 21X-1, 133–134 cm (157.94–161.73 mbsf), as defined by the top of *Globanomalina pseudomenardii* and the base of *Acarinina soldadoensis*, respectively. We recognize Subzone P4b in Samples 21X-CC through 22X-2, 100–102 cm (162.68–172.5 mbsf), based on the presence of a well-preserved assemblage including *Morozovella velascoensis*, *Morozovella occlusa*, *Morozovella pasionensis*, *Morozovella apanthesma*, *G. pseudomenardii*, *Acarinina subsphaerica*, and *Acarinina mckannai*. The base of Subzone P4a is identified in Sample 22X-4, 100–102 cm (175.5 mbsf), by the base of *G. pseudomenardii*. Zone P3 spans from Sample 22X-CC to 25X-CC (179.32–197.75 mbsf), with its base marked by the base of *Morozovella angulata*.

Benthic foraminifers

Benthic foraminifers were examined semiquantitatively in core catcher samples from Hole U1409A. Additional working section-half samples taken from Cores 342-U1409A-4H through 24X were examined for preservation and relative abundance of benthic foraminifers. Benthic foraminifers at this site are predominantly rare (the “present” category) relative to total sediment particles >150 µm in the Eocene and Paleocene and more abundant in the Oligocene (Fig. F22; Tables T10, T11).

Preservation of benthic foraminifer tests is generally good to very good in the Eocene to upper Paleocene, but the Oligocene and lower Paleocene successions contain poorly to moderately preserved benthic foraminifers (Fig. F22).

The well-preserved Pleistocene fauna of Samples 342-U1409A-1H-CC (0.97 mbsf) and 2H-CC (10.61 mbsf) is dominated by *Pullenia bulloides*, *Pyrgo* sp., *Uvigerina peregrina*, and *Uvigerina senticosa*. Sample 3H-CC (20.56 mbsf) is barren.

The lower Oligocene benthic foraminifer assemblage (Sample 4H-CC; 30.03 mbsf) is characterized by



high-productivity fauna, with *Cassidulina subglobosa* and *Stilostomella subspinosa* being the dominant species.

Samples 5H-CC through 19X-CC (38.66–141.20 mbsf) show typical lower to middle Eocene fauna dominated by calcareous taxa. Abundant calcareous taxa include *Alabamina dissonata*, *Bulimina* sp., *Chrysalonium* sp., *Cibicidoides subspiratus*, *Dentalina* sp., *Nuttallides truempyi*, *Oridorsalis umbonatus*, *Pleurostomella acuta*, and stiliostomellids (*Stilostomella gracillima*, *Stilostomella lepidula*, and *S. subspinosa*). *C. subglobosa* is abundant in the middle Eocene part of the succession only (Samples 5H-CC through 10H-CC; 38.66–86.86 mbsf). Overall, the Eocene assemblages described above suggest a normal deepwater environment. An exception is Sample 16H-CC (126.91 mbsf), which contains a benthic foraminiferal assemblage dominated by the infaunal taxa *Bigenerina* sp. and *Stilostomella* sp. and abundant *N. truempyi* but lacks other epifaunal species (Fig. F23).

Samples 20X-CC through 26X-CC (160.56–200.00 mbsf) are represented by Paleocene taxa characterized by *Bulimina* sp., *Dentalina* sp., *Gavelinella beccariiformis*, *Lenticulina whitei*, *Pullenia coryelli*, and *S. subspinosa*. Agglutinated taxa are mainly represented by *Dorothia trochoides*, *Gaudryina pyramidata*, and *Spiroplectammina spectabilis*. In general, preservation and abundance of Paleocene benthic foraminifers decreases downhole. Sample 24X-CC (196.97 mbsf) is barren of benthic foraminifers.

Paleomagnetism

We completed a paleomagnetism study of APC and XCB cores from Holes U1409A–U1409C with the primary objective of establishing a magnetostratigraphic age model for the site. The natural remanent magnetization (NRM) of each archive half section was measured at 2.5 cm intervals before and after demagnetization treatment in a peak alternating field (AF) of 20 mT for all cores from Hole U1409A. For all other cores, we only measured NRM after 20 mT demagnetization. Archive half section measurement data were processed by removing measurements made within 7.5 cm of section ends and from disturbed intervals described in the Laboratory Information Management System database. Cores 342-U1409A-1H through 16H and 342-U1409B-1H through 14H were azimuthally oriented using the FlexIT orientation tool (Table T12). All other cores were not oriented.

We also collected 125 discrete samples from working half sections to verify the archive half section measurement data and to measure anisotropy of mag-

netic susceptibility (AMS) and bulk susceptibility of Site U1409 sediment. Discrete samples were collected and stored in 7 cm³ plastic cubes and typically taken from the least disturbed region closest to the center of each section from Hole U1409A. Selected samples were subjected to measurements of AMS, including bulk susceptibility, and NRM measurements after 20 mT AF demagnetization. Twenty-one samples were selected for stepwise demagnetization at 0, 10, 20, 30, 40, and 60 mT. All discrete sample data are volume corrected to 7 cm³.

Results

Downhole paleomagnetism data after 20 mT demagnetization are presented for Holes U1409A, U1409B, and U1409C in Figures F24, F25, and F26, respectively. Similar to paleomagnetism results from previous Expedition 342 sites, section half measurement data from XCB-recovered cores are difficult to interpret because of biscuiting and substantial core disturbance. We chose to interpret only results obtained from APC cores.

We report the following principal features in the paleomagnetism data at Site U1409. First, we observed intensity zonation that correlates with lithostratigraphy except for three distinctive horizons at ~50, 70, and 90 mbsf. Second, inclination values cluster at ~60° and 0° to –45°, a trend that is associated with clustering of declination values at ~0° and 180°, respectively.

Magnetic intensity zonation

Downhole magnetic intensity values generally vary with lithostratigraphic units. Lithostratigraphic Units I and II (~0–30 mbsf), composed of Pleistocene nannofossil to foraminifer oozes and muddy sand and Oligocene silty clay and nannofossil clay (see “[Lithostratigraphy](#)”), are magnetically characterized by high intensity values (~10⁻² A/m). The ~70 m thick Unit III, composed of middle Eocene light green–gray nannofossil clay with interbedded nannofossil ooze, has background magnetic intensity values on the order of 10⁻⁵ A/m. However, three distinctive horizons within Unit III (~50, 70, and 90 mbsf) have exceptionally high (~10⁻² A/m) magnetic intensity values. These intervals of magnetic intensity are also distinguished by peaks in magnetic susceptibility and b* color reflectance data (see “[Physical properties](#)”). Core composite images (Cores 342-U1409A-6H, 9H, and 11H) clearly reveal the change from green and gray nannofossil clay to orange-red horizons at these intervals. We conclude that these intervals contain concentrations of oxidized magnetic minerals that are high above the



background levels. Finally, the ~100 m of lower Eocene to lower Paleocene nannofossil oozes and nannofossil chalk of Unit IV (Subunits IVa–IVc) have typical intensity values on the order of 10^{-3} A/m, with an order of magnitude variability over a wavelength of several meters.

Inclination and declination clustering

Inclination values following 20 mT AF demagnetization often cluster around 60° and -45° . Inclination clustering is usually associated with declination clustering at $\sim 0^\circ$ and 180° , respectively. The -45° inclination is shallow with respect to the reversed polarity value expected at the $\sim 40^\circ\text{N}$ latitude of Site U1409. This shallow bias is readily attributed to a small normal polarity drilling overprint that remains after 20 mT AF demagnetization. AF demagnetization at 20 mT is most effective at removing the drilling overprint in APC-recovered intervals, mainly from lithostratigraphic Unit III; it is less effective for other intervals but sufficient to reveal reversed polarity magnetozones. We can utilize the positive and negative polarity clustering behavior to readily identify magnetozones in Site U1409 sediment.

Comparison between pass-through and discrete sample data

AF demagnetization results for 73 discrete samples are summarized in Table T13. Of the 21 samples treated with a 60 mT peak AF demagnetization field, 5 reveal reasonably stable components of magnetization (e.g., Fig. F27A, F27B). These samples have remanent magnetizations that are strong enough to be measured by the onboard JR-6A spinner magnetometer. The remaining samples typically display NRM intensities that decrease by an order of magnitude following 20 mT field AF demagnetization. This behavior indicates that a drilling overprint probably obscures the primary magnetic signal. An example of such an overprint can be seen in Figure F27C. Nevertheless, these results are useful for verifying the 20 mT pass-through paleomagnetism data from the archive half sections.

In general, paleomagnetism data from archive half sections and discrete samples from oriented APC core intervals agree well. In contrast, discrete samples from XCB cores do not always show results that are consistent with the archive half section measurement data (Fig. F24). This discrepancy suggests that archive half section measurement data from XCB core intervals should be interpreted with care, similar to our conclusions regarding paleomagnetism data from previous Expedition 342 sites.

Magnetostratigraphy

The shipboard downhole results reveal a series of normal and reversed magnetozones between Cores 342-U1409A-1H and 13H (~ 0 –115 mbsf), between Cores 342-U1409B-1H and 13H (~ 0 –120 mbsf), and between Cores 342-U1409C-1H and 13H (~ 0 –115 mbsf). These magnetostratigraphies can be easily correlated among all three holes.

By utilizing radiolarian, foraminifer, and nannofossil biostratigraphic datums from Hole U1409A (see “[Biostratigraphy](#)”), we can correlate magnetozones to the geomagnetic polarity timescale (GPTS). The shipboard magnetostratigraphic age model is based on Hole U1409A, for which we have the most biostratigraphic datums. Extension of this age model to the magnetozonation observed in Holes U1409B and U1409C is contingent on the accuracy of the stratigraphic correlation between holes, which is corroborated by lithologic horizons, biostratigraphic datums, and physical property features (see “[Stratigraphic correlation](#)”). Our correlation is presented in Table T14 and is shown in Figures F24, F25, F26, and F28.

We correlate the normal to reversed polarity transition in Core 342-U1409A-2H at ~ 9 mbsf to the Bruhnes (C1n)/Matuyama (C1r.1r) boundary (0.781 Ma). The magnetostratigraphy observed in Sections 342-U1409A-3H-2 through 5H-2 is correlated to lower Chron C6Cr (~ 23.962 Ma) through upper Chron C13r (~ 33.7 Ma). We did not observe the distinctive Chron C9n–C9r magnetozonation in any hole at Site U1409 in this interval. In Hole U1409A, we also did not observe the Chron C12r–C13n transition; however, it is recorded in sediment in Hole U1409B, suggesting that this chron boundary is in the core gap between Cores 342-U1409A-4H and 5H. We correlate the well-resolved magnetozonation observed in Sections 342-U1409A-6H-5 to 13H-4 (~ 46 to ~ 111 mbsf) to lower Chron C19r (~ 42 Ma) continuously downhole to upper Chron C22r (~ 49.4 Ma). Paleomagnetism data from archive half sections and discrete samples suggest that a magnetostratigraphy can be developed in deeper intervals at Site U1409, but this magnetostratigraphy cannot be resolved in sufficient detail with shipboard data to correlate with confidence to the GPTS. Magnetozone correlations for Holes U1409B and U1409C are similar to Hole U1409A, with the exception that we did not observe the Oligocene magnetostratigraphy as clearly in Holes U1409B and U1409C as we did in Hole U1409A.

The correlations described above provide a shipboard chronostratigraphic framework for interpreting the Oligocene and middle Eocene sediment re-

cord at Site U1409. The most salient implications of this age model are as follows:

- Average linear sedimentation rates during the Oligocene at Site U1409 are very low (0.29 cm/k.y.) (Fig. F30). The condensed nature of this Oligocene interval is consistent with the abundant manganese nodules that are as large as 10 cm in diameter.
- We do not observe either the Chron C9n–C9r transition (27.439 Ma) or the Chron C9r–C10n.1n transition (27.859 Ma) in any hole at Site U1409. Notably, we observed a hiatus over the same time interval at Site U1406. Site U1409 at Southeast Newfoundland Ridge and Site U1406 at J-Anomaly Ridge are at similar midwater depths (~3500 and 3800 mbsl, respectively). Notably, deep-sea benthic foraminiferal $\delta^{18}\text{O}$ values increase distinctly during Chron C9 (Zachos et al., 2008). Therefore, we tentatively suggest that the regional Chron C9 hiatus observed at J-Anomaly Ridge and Southeast Newfoundland Ridge is linked to regional oceanographic changes spurred by changes in global ice volume.
- We tentatively correlate the downhole normal to reversed transition in Sections 342-U1409A-6H-5, 342-U1409B-6H-3 and 6H-4, and 342-U1409C-6H-5 and 6H-6 to the Chron C13n–C13r transition (33.705 Ma). If this correlation is robust, then the Eocene–Oligocene transition may be recorded in the sediment at Site U1409. Thorough shore-based paleomagnetism and chemostratigraphic studies are necessary to verify this shipboard correlation. We note that the magnetic record, distinctive in both downhole directional and magnetic intensity behavior during the transition, is remarkably similar to the paleomagnetism record correlated to this transition at Site U1404 (see Fig. F22 in the “Site U1404” chapter [Norris et al., 2014c]).
- Average linear sedimentation rates during the middle Eocene at Site U1409 are similar to those calculated for Sites U1407 and U1408. Sedimentation rates are highest during Chron C20r (1.31 cm/k.y. from ~43.4 to 45.7 Ma) and are ~52% and 65% lower before and after this interval, respectively (Fig. F30).

Magnetic susceptibility and anisotropy of magnetic susceptibility

Bulk magnetic susceptibility measured on 71 discrete samples is summarized in Table T15. Although discrete samples were collected from each core section from the entire depth of Hole U1409A, we chose to measure only odd-numbered samples. Downhole

variation in whole-round magnetic susceptibility (WRMS) and discrete sample magnetic susceptibility (DSMS) for Hole U1409A are shown in Figure F24. The WRMS data for Hole U1409A are shown in raw form; they have not been trimmed at section ends or filtered for obvious outliers, so noise in the data probably reflects edge effects or spurious measurements. We multiplied the WRMS data, which are in instrument units, by a factor of 0.577×10^{-5} to convert to approximate SI volume susceptibilities (see “Paleomagnetism” in the “Methods” chapter [Norris et al., 2014a]). WRMS and DSMS data agree very well after this conversion, and we attribute small absolute differences to the fact that the conversion factor applied to the WRMS data is not constant downhole because of changes in core diameter and density; only discrete samples provide calibrated susceptibility values in SI units. Both magnetic susceptibility data sets show the same first- and second-order cyclic trends, indicating that these trends are robust features of Site U1409 sediment.

AMS results for the discrete samples are also summarized in Table T15 and are shown in Figure F29. The eigenvalues associated with the maximum (τ_1), intermediate (τ_2), and minimum (τ_3) magnetic susceptibilities at Site U1409 show some downhole variations that correspond to changes in lithostratigraphy. We also observed a change in AMS values at the transition from APC to XCB coring technologies, with greater consistent divergence between principal eigenvalues indicative of more oblate fabrics in XCB cores. We do not observe consistently steeper inclinations of the minimum principal eigenvector (V_3) in this same interval however, suggesting that although there is a stronger oblate AMS in XCB-recovered intervals, this does not correspond to a strong fabric orientation.

Triaxial fabrics are greatest, and most variable, at the top of lithostratigraphic Subunit IVa, just below the contact with Unit III (~100–110 mbsf). Magnetic fabrics, reflected in the degree of anisotropy (P), lineation (τ_1/τ_2), and foliation (τ_2/τ_3) values, are the most developed of any observed at previous Expedition 342 sites. This interval corresponds to an increase in radiolarian abundance and a distinct lithostratigraphic transition from pink nannofossil ooze below to alternating layers of pink and white nannofossil oozes with varying amounts of foraminifers and radiolarians within the zone of high AMS (see “Lithostratigraphy”). The highest AMS values also correspond to an interval in which the sediment was noticeably softer than intervals above and below it. Although the degree of anisotropy and fabric parameters are high, the minimum principal eigenvector does not show a systematic trend, suggesting that



whatever produced the strong AMS was not simply compaction from overburden.

Age-depth model and mass accumulation rates

At Site U1409, we recovered a 200 m thick sequence of Pleistocene to lower Paleocene nannofossil ooze and nannofossil clay, with foraminifers and radiolarians. Thin Pleistocene and Oligocene intervals overlie a middle Eocene through lower Paleocene succession with significant hiatuses between the lower Pleistocene and upper Oligocene (22 m.y. duration) and lower Oligocene and middle Eocene (8.3 m.y. duration). A short hiatus or condensed interval is also identified at the Paleocene/Eocene boundary. The Oligocene is highly condensed and may contain substantial hiatuses. Sedimentation rates are 0.65–1.31 cm/k.y. through the middle Eocene, 0.81–1.44 cm/k.y. through the lower Eocene, and ~0.47–1.80 cm/k.y. through the Paleocene.

Biostratigraphic datums and magnetostratigraphic datums from Hole U1409A (Table T16) were compiled to construct an age-depth model for this site (Fig. F24). A selected set of datums (Table T17) was used to create an age-depth correlation and calculate linear sedimentation rates (LSRs). Total mass accumulation rate (MAR), carbonate MAR (CAR), and noncarbonate MAR (nCAR) were calculated at 0.2 m.y. intervals using a preliminary shipboard splice rather than the sampling splice described in this volume (Table T18; Fig. F31).

Age-depth model

The age-depth model is primarily tied to paleomagnetic datums in the upper 39 m of Hole U1409A, along with a single Pleistocene nannofossil datum. A nearly complete sequence of magnetochrons has been identified in the Oligocene. A lower Oligocene–upper Eocene unconformity is identified by nannofossil datums. Paleomagnetic datums provide the primary tie points in the underlying middle to upper lower Eocene interval. The remaining lower Eocene and Paleocene section is tied to radiolarian and nannofossil datums with the base of planktonic foraminifer, *Morozovella angulata*, providing the final tie point in the age model. All datums are in good agreement through the Eocene and Paleocene.

Linear sedimentation rates

This site has a short Pleistocene section, with a LSR of 0.32 cm/k.y. A condensed Oligocene section (LSR of < 0.5 cm/k.y.) is bounded by hiatuses. The Eocene has a relatively stable LSR that ranges from 0.65 to

1.44 cm/k.y. and averages ~0.9 cm/k.y. The Paleocene comprises a condensed upper interval (LSR of 0.21 cm/k.y.), an expanded middle interval (LSR of 1.8 cm/k.y.), and an average LSR at the base (0.47 cm/k.y.).

Mass accumulation rates

MARs at Site U1409 range from 0.1 to 0.9 g/cm²/k.y. in the Pleistocene and Oligocene to maximum values of ~2.5 g/cm²/k.y. in the middle Paleocene. In the Pleistocene sequence recovered at Site U1409, MAR is dominated by noncarbonate components. Oligocene MARs are also strongly modulated by noncarbonate components; indeed, carbonate contents are close to 0 wt% for much of the upper Oligocene. Carbonate and noncarbonated fractions are approximately equal throughout the middle Eocene, and carbonate becomes the predominant contributor to mass accumulation below the middle Eocene. A broad distinctive peak in MARs occurs in the middle Eocene; two shorter peaks, driven primarily by carbonate accumulation, occur in the early Eocene and a large and distinctive peak in MARs, also driven primarily by carbonate accumulation, occurs across the upper/middle Paleocene boundary.

Geochemistry

The geochemistry program during operations at Site U1409 included

- Analysis of interstitial gas compounds on headspace samples;
- Measurement of minor and trace element concentrations in interstitial water squeezed from whole-round samples from Hole U1409A;
- Inorganic carbon, total carbon, and total nitrogen determinations of solid sediment samples from multiple holes; and
- Characterization of organic matter by source-rock pyrolysis.

Headspace gas samples

Headspace gas samples for routine safety monitoring were collected typically at a frequency of one sample per core in Hole U1409A (Table T19), generally in the bottom half of each core (i.e., Sections 4, 5, or 6). Methane increases very slightly downhole, with values between 1.79 and 6.43 ppmv. Higher molecular weight hydrocarbons were not detected in measurable amounts.

Interstitial water samples

Eighteen interstitial water samples were squeezed from whole-round samples, which were typically



taken at a frequency of one per core in Hole U1409A (Table T20). Whole-round samples were collected immediately after the cores were sectioned on the catwalk. In some cases, disturbed cores or low recovery precluded whole-round sampling, as in the case with Cores 342-U1409A-15H and 16H, which were too short to collect a whole-round sample.

Results

Salinity, pH, alkalinity, ammonium, manganese, iron, and sulfate

The pH profile decreases uniformly throughout the hole from 7.6 at the seafloor to 6.9 at 200 mbsf (Fig. F32). Alkalinity decreases in lithostratigraphic Units I and II (0–35 mbsf) from 3.7 to 2.9 mM and then increases uniformly downhole to 4.1 mM. Ammonium ranges from ~10 to ~75 µM, with an average down-hole trend of ~20 µM in Unit I through Subunit IVa (0–124 mbsf) and an average trend of ~45 µM in Sub-units IVb and IVc. Manganese shows a characteristic, lithology-correlated profile of relatively high (>18 µM) values in Unit II, low values (<18 µM) in Unit III and Subunit IVa, and again higher values in Subunits IVb and IVc. Iron is below detection limit except for two samples with values of <5 µM. Sulfate increases from 28 to ~30 mM in Unit II and then decreases uniformly to ~23 mM at the bottom of the hole, except for Subunit IVa, where sulfate shows increased values. Overall, the sulfate concentrations at Site U1409 are high (average = ~27 mM), suggesting that the influence of organic matter respiration within the sediment column at Site U1409 is modest.

Calcium, magnesium, sodium, chloride, boron, and potassium

Calcium concentrations at Site U1409 uniformly increase downhole from lithostratigraphic Unit I through Subunit IVa (0–124 mbsf), where a step increase from 15 to 18 mM occurs. Below this depth, through Subunits IVb and IVc, calcium concentrations increase further to ~20 mM at the bottom of the hole. Magnesium mirrors the calcium profile, with slightly decreasing values in Unit I through Subunit IVa, where a step decrease from ~51 to ~44 mM occurs. Below this depth, magnesium concentrations decrease further to 40 mM at the base of the hole. Magnesium/calcium ratios show a gentle decline from 4.5 near the top of the core to ~3.0 at the Subunit IVa/IVb boundary and then decrease further to ~2.0 at the base of the hole.

Potassium concentrations decrease downhole throughout the hole. Throughout the sequence, sodium and chloride concentrations covary. Sodium concentrations range from 480 to 505 mM. Chloride

concentrations range from ~580 to ~620 mM, with an overall increasing downhole trend.

Interstitial water boron concentrations show a broad maximum of ~550 µM within Unit III at ~65 mbsf and significantly lower values of ~300–350 µM in Unit IV at depths greater than 130 mbsf.

Discussion

Interstitial water profiles display evidence of compartmentalization with pronounced abrupt down-hole shifts in magnesium, manganese, and potassium at ~125–130 mbsf, suggesting that the unrecovered sequence of cherts acts as an aquiclude. Overall, interstitial water profiles of potassium, calcium, and magnesium are consistent with those resulting from exchange with and alteration of basaltic basement at depth (Gieskes and Lawrence, 1981). Potassium and magnesium concentrations decrease and calcium concentrations increase with depth (Fig. F32). Inflections at ~180 mbsf correspond to an increase in alkalinity and indicate possible dissolution/reprecipitation of carbonate, which is high in the nannofossil chalk that comprises the basal lithostratigraphic Subunit IVc (see “[Lithostratigraphy](#)”).

The downhole patterns of alkalinity and manganese suggest two zones of organic matter degradation within the recovered sequence. The typical succession of electron acceptor use during early diagenesis is manganese followed by iron and then sulfate (cf. Berner, 1980). Elevated concentrations of manganese in the upper 30 m coupled with iron concentrations of 0 µm within the upper 50 m of the sediment column indicate oxic to suboxic diagenesis driven by microbial reduction of manganese oxides. The manganese maximum is coincident with an interval comprised of disseminated manganese nodules as well as dispersed sulfides. Further reduction of manganese oxides occurs below the aquiclude between ~130 and 140 mbsf. This portion of the sequence was likely a reservoir of relatively high organic carbon contents, and the interstitial fluid profiles reflect the diffusional signal following the degradation of this reservoir. The degradation of this reservoir of organic matter below the chert aquiclude resulted in sulfate reduction, as evidenced by the concomitant decrease in sulfate concentrations.

Laboratory experiments under controlled temperatures and pressures have shown that boron is leached from terrigenous sediment into fluids (e.g., James et al., 2003), and a study of Ocean Drilling Program Leg 186 interstitial water samples concluded that the removal of boron from clays and volcanic ash was responsible for boron enrichment in the interstitial water (Deyhle and Kopf, 2002). There-



fore, the broad downhole maximum in concentrations at Site U1409 at 59 mbsf presumably indicates increased supply from the terrigenous sediment component in lithostratigraphic Unit II (see “[Lithostratigraphy](#)”).

Sediment samples

Sediment plugs (5 cm³) for downhole analysis of sediment elemental geochemistry were taken from Cores 342-U1409A-1H through 24X at an average resolution of one sample per section, adjacent to the moisture and density samples (Table [T21](#)).

Additional sampling commenced at roughly 40 cm intervals in Cores 342-U1409B-18X and 342-U1409C-20X to resolve high-amplitude features in carbonate contents associated with lithologic changes associated with the PETM (see “[Biostratigraphy](#)” and “[Lithostratigraphy](#)”). Samples were also taken at ~20–40 cm spacing from Core 342-U1409C-6H over a series of decimeter-scale dark-light intervals in Sections 342-U1409C-6H-3 through 6H-5.

Results

Concentrations of inorganic carbon vary from 0.04 to 12.4 wt% in Holes U1409A–U1409C (Table [T21](#); Fig. [F33](#)). These concentrations are equivalent to 0–93 wt% CaCO₃, assuming that all of the carbonate is calcite.

Carbonate concentrations are between 5 and 50 wt% in lithostratigraphic Unit I and decrease to 0–20 wt% in Unit II, which is consistent with low-carbonate levels observed in other Oligocene age sequences recovered during Expedition 342. In the expanded middle Eocene sequence represented by Unit III, the alternating clay-rich bedding and white nannofossil ooze layers have fluctuating carbonate values of ~30 to ~80 wt%, with a few peaks of ~85 wt% carbonate. The clay and ooze layers are further differentiated by physical properties including color reflectance (L*), magnetic susceptibility, and NGR. Carbonate increases to 90 wt% in Unit IV, which corresponds to early Eocene age sediment. A further decrease to 20 wt% at ~154 mbsf is associated with a ~45 cm thick silicified interval representing at least a portion of the PETM. Placement is based on the occurrence of nannofossil excursion taxa (nannofossil Zone NP9b; see “[Biostratigraphy](#)”). The downhole carbonate decrease is associated with a decrease in sediment lightness (L*) and increase in magnetic susceptibility (Fig. [F34](#)). In general, NGR and L* show five major peaks at ~38, 47, 70, 100, and 155 mbsf, all of which correlate with the major variations in calcium carbonate content.

Total organic carbon (TOC) values are typically 0.1–0.3 wt% throughout the sediment column. TOC values, together with total nitrogen values, appear to decrease downhole from lithostratigraphic Unit III to IV. Organic matter is thermally immature and relatively well preserved with low T_{max} values (380°–420°C). Organic matter is a mixture of Type II (algal and microbial) and Type III (land plant/detrital) kerogen. (Fig. [F35](#)).

Discussion

As with other sites drilled to date on the Southeast Newfoundland Ridge (Sites U1407–U1409), the most prominent change is a step increase in carbonate (from 50 to 90 wt% CaCO₃; ~100 mbsf) in sediment during nannofossil Zone NP14 (around the early/middle Eocene boundary). This step correlates with shifts in several proxies (e.g., color reflectance, magnetic susceptibility, NGR, TOC, and total nitrogen values) and marks a transition from pelagic chalk sedimentation to clay deposition in the initial stages of sediment drift development.

Physical properties

We made physical properties measurements on whole-round sections, section halves, and discrete samples from section halves from Holes U1409A–U1409C. Gamma ray attenuation (GRA) bulk density, magnetic susceptibility, P-wave velocity, and NGR measurements were made on whole-round sections using the Whole-Round Multisensor Logger and NGR Logger. Thermal conductivity measurements were also performed on whole-round sections before they were split. Compressional wave velocity was measured on section halves at a frequency of two in each section (at ~50 and 100 cm) using the P-wave caliper (PWC). For moisture and density (MAD) analyses, one discrete sample was collected in each section (typically at ~35 cm from the top of a section). The Section Half Multisensor Logger was used to measure spectral reflectance and magnetic susceptibility on archive section halves.

Magnetic susceptibility

Overall, magnetic susceptibility ranges from 0 to 160 IU (Fig. [F36](#)). From the top of the sediment column at Site U1409 to ~18 mbsf (Lithostratigraphic Unit I; see “[Lithostratigraphy](#)”), magnetic susceptibility is characterized by large-amplitude variations. In the upper part of this lithostratigraphic unit, magnetic susceptibility averages ~45 IU, and from 10 to 18 mbsf, values increase from ~8 to 120 IU. Below Unit I, magnetic susceptibility is lower (generally <30 IU) and shows low-amplitude variability. In Unit II, mag-



netic susceptibility steadily decreases downhole from ~40 to <20 IU. Unit III is characterized by small but high-frequency variations, which correspond to interbedded light greenish gray nannofossil clay and carbonate-rich, white nannofossil ooze. We note several superimposed peaks that correlate among all three holes. The first of these peaks occurs at ~20 mbsf and is associated with a manganese- and sulfide-rich interval. At ~35 mbsf, particularly in Holes U1409A and U1409B, a small peak in magnetic susceptibility values correlates with the downhole transition to the greenish gray sediment. We observe three major peaks in Unit III at ~50, ~72, and ~90 mbsf. Each of these peaks correspond to oxide-rich intervals characterized by yellowish to reddish color. Finally, we note a major peak in magnetic susceptibility (~100 IU) at ~157 mbsf that corresponds to the PETM.

Density and porosity

Two methods were used to evaluate bulk density at Site U1409. The GRA method provided a bulk density estimate from whole-round sections. The MAD methods applied to 134 discrete samples provided a second, independent measure of bulk density, as well as dry density, grain density, water content, and porosity.

Overall, MAD bulk density values vary between 1.37 and 1.95 g/cm³. Changes in MAD bulk density are in general consistent with those in GRA bulk density (Fig. F36). MAD values are ~2.5% lower than GRA values in APC-cored intervals and somewhat higher than GRA values in XCB-cored intervals. In lithostratigraphic Unit I, bulk density increases from 1.4 to 1.75 g/cm³. At the top of Unit II at ~18 mbsf, bulk density decreases to 1.4 g/cm³. Bulk density increases downhole throughout the remainder of the sediment section and reaches ~1.9 g/cm³ at ~140 mbsf; this behavior is typical of sedimentary compaction. Bulk density is relatively constant from 150 mbsf to the bottom of Hole U1409A. We observe several downhole trends toward higher densities in individual cores from Holes U1409B and U1409C in these lower intervals; we attribute these trends to artifacts of XCB drilling.

At Site U1409, water content and porosity vary between 25 and 60 wt% and between 45 and 80 vol%, respectively. From the top of the hole to ~140 mbsf, both parameters gradually decrease downhole to 30 wt% water content and 50 vol% porosity. Porosity and water content shift to substantially lower values in the lower part of Unit I, between ~10 and 18 mbsf. The base of this 8 m thick interval correlates to a large stratigraphic hiatus (see “Age-depth model

and mass accumulation rates”). Below 140 mbsf, water content and porosity remain relatively constant and average 27 wt% and 50 vol%, respectively. A significant increase to 37 wt% and 61 vol% occurs at ~160 mbsf.

Grain density generally varies between 2.65 and 2.85 g/cm³ throughout Hole U1409A. These data are more variable in lithostratigraphic Units I and II than they are lower in the hole.

P-wave velocity

P-wave velocity was measured using the *P*-wave logger (PWL) on all whole-round sections and using the PWC on undisturbed section halves from Holes U1409A–U1409C. Whole-round and section half data are generally coherent, but the PWC values are ~20 m/s lower than PWL values in APC-cored intervals (Fig. F37). Overall, *P*-wave velocity gradually increases downhole from 1500 to 1800 m/s, similar to trends observed in bulk density and water content data; we attribute these trends to downhole compaction of the recovered sediment. A small stepwise decrease from 1570 to 1525 m/s occurs at the transition between lithostratigraphic Units I and II. *P*-wave velocity data remain relatively constant and average ~1560 m/s throughout Subunit IVa. We did not complete PWL measurements for almost all of Subunits IVb and IVc intervals (between ~125 and ~200 mbsf), but PWC measurements show higher variability than observed uphole. We attribute this greater variability to a change in coring method from APC to XCB at ~125 mbsf.

Natural gamma radiation

NGR values range between 3 and 35 cps at Site U1409, and two major trends are observed. First, NGR values average ~25 cps between 0 and 100 mbsf, and the profile is characterized by many superimposed peaks and troughs within this interval that can be correlated among all three holes. Second, at ~100 mbsf NGR values decrease abruptly to ~5 cps and remain low downhole to the bottom of the hole. NGR is anticorrelated with calcium carbonate content, with low NGR counts in the high-carbonate lithostratigraphic Unit IV and high NGR counts in the low-carbonate content Units I–III (see “Geochemistry”).

Color reflectance

The standard operating resolution of data acquisition was decreased from 2.5 to 5 cm for Holes U1409A and U1409C to speed up processing time during periods of very rapid core recovery. From the top of the sediment column to ~100 mbsf, color re-



flectance parameters a^* and b^* follow similar trends and features in all three holes (Fig. F38). In lithostratigraphic Unit I, values average ~1.9 for a^* and ~10 for b^* . At the contact between Units I and II, a^* increases from 1.9 to 4.4 and b^* increases from 10 to ~16. This change in color reflectance values reflects the sharp contact between the brown, red, and gray-banded Pleistocene sediment and the underlying yellowish brown Oligocene-age silty clay (see “[Lithostratigraphy](#)”). In the lower intervals of Unit II, a^* and b^* values decrease sharply (a^* from 4.4 to ~1 and b^* from 10 to 1.3). This decrease corresponds to a downhole transition in sediment color from light yellow to greenish gray (see “[Lithostratigraphy](#)”). Throughout Unit III, a^* and b^* remain relatively constant with average values of ~0.2 and ~0.3, respectively. The b^* record shows distinctive peaks at ~50, ~72, and ~90 mbsf in all three holes. These peaks correlate to peaks in the magnetic susceptibility record and probably signify Fe oxide-rich horizons (Fig. F36). The a^* record shows a pronounced downhole step increase (from ~0.6 to 4) at the contact between Units III and IV (~100 mbsf). Values for a^* and b^* both increase downhole throughout Subunit IVa. In Subunits IVb and IVc, a^* remains relatively constant but b^* continues to increase. Peaks in both parameters occur at 155 mbsf, which is consistent with peaks observed in nearly all the other physical properties; this is the PETM interval.

L^* generally follows pronounced lithostratigraphic changes and can be readily correlated among all three holes (Fig. F38). L^* averages 50 in Unit I and increases to 56 at the contact with the underlying Unit II. L^* decreases slightly from ~60 to 55 throughout Unit II and increases sharply from 55 to 65 at the boundary with Unit III (~35 mbsf). In Unit III, L^* values average ~64, but some superimposed cyclic variations occur at ~38, 47, and 70 mbsf. At the top of Unit IV, L^* increases abruptly to 84; this interval correlates with the transition from interbedded gray and white nannofossil clay and ooze to pinkish white carbonate-rich nannofossil ooze with foraminifers (see “[Lithostratigraphy](#)”). Throughout Unit IV, L^* decreases downhole from ~84 to 68. In Holes U1409A and U1409B at the Subunit IVb/IVc boundary (~155 mbsf), L^* values decrease from 70 to 57; this interval also correlates with the lithostratigraphic expression of the PETM. The major variations in L^* recorded at Site U1409 are consistent with the magnetic susceptibility and NGR data series (Fig. F37) and appear to correlate mainly with changes in calcium carbonate content (see “[Geochemistry](#)”).

Thermal conductivity

Fifty-one measurements were completed on whole-round sections from Holes U1409A–U1409C (Table

T22). Thermal conductivity values increase in magnitude downhole from 0.9 to 1.4 W/(m·K) near the top and bottom of the holes, respectively, and generally correlate among all three holes (Fig. F39). Thermal conductivity measurements show a good correlation ($R^2 = \sim 0.84$) with GRA bulk density (Fig. F40). Thermal conductivity data are more scattered in lithostratigraphic Unit I, probably because of higher water content and the presence of foraminifer sand in these intervals. Throughout Units II and III and Subunit IVa, thermal conductivity values increase gradually from ~1.1 to 1.2 W/(m·K) at ~115 mbsf. Across the Subunit IVa/IVb boundary (~135 mbsf), thermal conductivity increases abruptly to 1.45 W/(m·K). This increase correlates to the transition from ooze to chalk (see “[Lithostratigraphy](#)”). Thermal conductivity remains relatively constant at ~1.4 W/(m·K) in Subunits IVb and IVc.

Stratigraphic correlation

Sampling splice

We constructed a splice for Site U1409 that is stratigraphically continuous from ~0 to ~130 m core composite depth below seafloor (CCSF) and ~150 to 190 m CCSF (Fig. F41). From ~130 to 150 m CCSF, poor recovery associated with the change to XCB coring prevented the generation of a continuous splice. Hole U1409A spans the thickest sediment column recovered at this site, with a maximum depth for the bottom of Core 342-U1409A-26X of 200.1 mbsf (231.63 m CCSF). Holes U1409B and U1409C extend to 170.5 m mbsf (192.32 m CCSF) and 160.8 m mbsf (179.85 m CCSF), respectively. We based our correlation and splice construction on magnetic susceptibility and NGR measured on whole-round sections. Our correlation yields a growth rate of 16% for Hole U1409A, 14% for Hole U1409B, and 13% for U1409C (Fig. F42), which represents the average increase of the CCSF depth scale relative to each hole’s mbsf depth scale. The affine table (Table T23) summarizes the individual offsets for each core drilled.

Correlation during drilling operations

To aid real-time correlation at Site U1409, we assessed magnetic susceptibility and GRA bulk density data collected at 2.5 cm resolution on the Special Task Multisensor Logger before allowing cores to equilibrate to room temperature. A clear signal in magnetic susceptibility allowed reliable correlation during drilling operations downhole to ~120 m CCSF.

After partial strokes for Cores 342-U1409A-15H and 16H at ~143 m CCSF, with recovery of 1.5 and 0.9 m, respectively, drilling operations switched to XCB cor-



ing for Core 17X, which was a short (4.6 m) core. After 77% nominal recovery for Core 18X, Core 19X had <1% nominal recovery from a 9.6 m advance. Core 20X achieved >100% nominal recovery, whereas nominal recovery was <100% for Cores 21X through 24X, and the hole was ended after two consecutive advances of <2 m for Cores 25X and 26X.

Based on the poor recovery of Core 342-U1409A-19X and identification of the Paleocene/Eocene boundary associated with a chert layer in Core 20X, the strategy for Holes U1409B and U1409C was to core until just below the Paleocene/Eocene boundary. In Hole U1409B, we switched to XCB coring after a 0.2 m partial stroke for Core 342-U1409B-14H. The Paleocene/Eocene boundary interval was recovered in Core 18X. In Hole U1409C, we directed drilling operations to switch to XCB coring for Core 342-U1409C-15X (~143 m CCSF). Cores 15X through 19X were all short cores of ~6 m or less. Hole U1409C was terminated after recovering Core 21X, which had a 3.5 m advance and recovered nannofossil Subzones NP9a and NP9b, associated with the Paleocene/Eocene boundary, in the core catcher.

Correlation and splice construction

For stratigraphic correlation and splice construction, we used magnetic susceptibility and NGR data. These two data series showed clear, correlatable features throughout the sediment column (see “Physical properties”). Magnetic susceptibility proved to be the most useful data set for correlation from 0 to ~130 m CCSF, and NGR was most useful from ~130 to 180 m CCSF (Figs. F41, F43). We also considered line-scan core images of section halves for cores associated with the Paleocene/Eocene boundary interval from ~170 to 185 m CCSF. Our correlation is consistent with biostratigraphic and paleomagnetic results (see “Biostratigraphy” and “Paleomagnetism”).

We defined Core 342-U1409C-1H as the anchor in our splice, though a clear agreement exists between mudline cores from all three holes. Clearly correlatable, large-amplitude cycles in magnetic susceptibility are present in the upper ~25 m CCSF of the sediment column, corresponding to Pleistocene sediment (Fig. F44). Magnetic susceptibility decreases significantly below ~25 m CCSF, but clear cycles in physical properties are recognizable from ~25 to ~100 m CCSF, allowing the identification of mostly reliable tie points. The color change from pale brown to white sediment at ~115 m CCSF corresponds to a pronounced decrease in magnetic susceptibility, so the splice tie point at ~120 m CCSF is tentative. Below ~135 m CCSF, magnetic susceptibility values begin to increase, but the data are noisy because of the numerous chert layers in this interval,

which are responsible for magnetic susceptibility peaks that are not easily correlatable between holes. As a result, NGR was more useful for the identification of splice tie points below ~135 m CCSF (Fig. F43). Tie points are labeled as tentative in Table T24 if they occur in sections where physical properties do not show highly distinctive features.

Poor recovery following the transition from APC to XCB coring at the first hard layer (~140 m CCSF) impeded construction of a continuous splice from ~130 to 150 m CCSF. We were able to correlate individual cores from the three holes in this interval, but insufficient coverage across coring gaps prevented us from building a splice (Fig. F43).

The splice tie point between Cores 342-U1409B-17X and 342-U1409C-20X is reliable, but the splice tie point between Cores 342-U1409C-20X and 342-U1409B-18X is tentative because both magnetic susceptibility and NGR of Sections 342-U1409C-20X-5 and 20X-6 are different from the records for Core 342-U1409B-18X. We interpreted an overlap between Cores 342-U1409C-20X and 342-U1409B-18X because

- Biostratigraphic datums suggest that these two cores are equivalent in age;
- Analysis of line-scan core images demonstrates that the lithologies of the two cores are similar; and
- The Paleocene/Eocene boundary chert layer in Core 342-U1409B-18X correlates to the chert layer in the core catcher of Core 342-U1409C-21X, suggesting that it would be inappropriate to add a large offset to Core 342-U1409B-18X in order to eliminate any overlap between Core 342-U1409B-18X and Core 342-U1409C-20X.

The Site U1409 splice (Table T24) can be used as a sampling guide, but we suggest using caution when using the splice for sampling associated with the Paleocene/Eocene boundary interval in Cores 342-U1409C-20X through 342-U1409B-18X, given the uncertain splice tie point between Holes U1409C and U1409B.

References

- Berner, R.A., 1980. *Early Diagenesis: A Theoretical Approach*: Princeton, NJ (Princeton Univ. Press).
- Deyhle, A., and Kopf, A., 2002. Strong B enrichment and anomalous $\delta^{11}\text{B}$ in pore fluids from the Japan Trench forearc. *Mar. Geol.*, 183(1–4):1–15. doi:10.1016/S0025-3227(02)00186-X
- Gieskes, J.M., and Lawrence, J.R., 1981. Alteration of volcanic matter in deep-sea sediments: evidence from the chemical composition of interstitial waters from deep sea drilling cores. *Geochim. Cosmochim. Acta*,



- 45(10):1687–1703. doi:[10.1016/0016-7037\(81\)90004-1](https://doi.org/10.1016/0016-7037(81)90004-1)
- Gradstein, F.M., Ogg, J.G., Schmitz, M.D., and Ogg, G.M. (Eds.), 2012. *The Geological Time Scale 2012*: Amsterdam (Elsevier).
- James, R.H., Allen, D.E., and Seyfried, W.E., Jr., 2003. An experimental study of alteration of oceanic crust and terrigenous sediments at moderate temperatures (51 to 350°C): insights as to chemical processes in near-shore ridge-flank hydrothermal systems. *Geochim. Cosmochim. Acta*, 67(4):681–691. doi:[10.1016/S0016-7037\(02\)01113-4](https://doi.org/10.1016/S0016-7037(02)01113-4)
- Kirschvink, J.L., 1980. The least-squares line and plane and the analysis of palaeomagnetic data. *Geophys. J. R. Astron. Soc.*, 62(3):699–718. doi:[10.1111/j.1365-246X.1980.tb02601.x](https://doi.org/10.1111/j.1365-246X.1980.tb02601.x)
- Norris, R.D., Wilson, P.A., Blum, P., Fehr, A., Agnini, C., Bornemann, A., Boulila, S., Bown, P.R., Cournede, C., Friedrich, O., Ghosh, A.K., Hollis, C.J., Hull, P.M., Jo, K., Junium, C.K., Kaneko, M., Liebrand, D., Lippert, P.C., Liu, Z., Matsui, H., Moriya, K., Nishi, H., Opdyke, B.N., Penman, D., Romans, B., Scher, H.D., Sexton, P., Takagi, H., Turner, S.K., Whiteside, J.H., Yamaguchi, T., and Yamamoto, Y., 2014a. Methods. In Norris, R.D., Wilson, P.A., Blum, P., and the Expedition 342 Scientists, *Proc. IODP*, 342: College Station, TX (Integrated Ocean Drilling Program). doi:[10.2204/iodp.proc.342.102.2014](https://doi.org/10.2204/iodp.proc.342.102.2014)
- Norris, R.D., Wilson, P.A., Blum, P., Fehr, A., Agnini, C., Bornemann, A., Boulila, S., Bown, P.R., Cournede, C., Friedrich, O., Ghosh, A.K., Hollis, C.J., Hull, P.M., Jo, K., Junium, C.K., Kaneko, M., Liebrand, D., Lippert, P.C., Liu, Z., Matsui, H., Moriya, K., Nishi, H., Opdyke, B.N., Penman, D., Romans, B., Scher, H.D., Sexton, P., Takagi, H., Turner, S.K., Whiteside, J.H., Yamaguchi, T., and Yamamoto, Y., 2014b. Site U1403. In Norris, R.D., Wilson, P.A., Blum, P., and the Expedition 342 Scientists, *Proc. IODP*, 342: College Station, TX (Integrated Ocean Drilling Program). doi:[10.2204/iodp.proc.342.104.2014](https://doi.org/10.2204/iodp.proc.342.104.2014)
- Norris, R.D., Wilson, P.A., Blum, P., Fehr, A., Agnini, C., Bornemann, A., Boulila, S., Bown, P.R., Cournede, C., Friedrich, O., Ghosh, A.K., Hollis, C.J., Hull, P.M., Jo, K., Junium, C.K., Kaneko, M., Liebrand, D., Lippert, P.C., Liu, Z., Matsui, H., Moriya, K., Nishi, H., Opdyke, B.N., Penman, D., Romans, B., Scher, H.D., Sexton, P., Takagi, H., Turner, S.K., Whiteside, J.H., Yamaguchi, T., and Yamamoto, Y., 2014c. Site U1404. In Norris, R.D., Wilson, P.A., Blum, P., and the Expedition 342 Scientists, *Proc. IODP*, 342: College Station, TX (Integrated Ocean Drilling Program). doi:[10.2204/iodp.proc.342.105.2014](https://doi.org/10.2204/iodp.proc.342.105.2014)
- Norris, R.D., Wilson, P.A., Blum, P., Fehr, A., Agnini, C., Bornemann, A., Boulila, S., Bown, P.R., Cournede, C., Friedrich, O., Ghosh, A.K., Hollis, C.J., Hull, P.M., Jo, K., Junium, C.K., Kaneko, M., Liebrand, D., Lippert, P.C., Liu, Z., Matsui, H., Moriya, K., Nishi, H., Opdyke, B.N., Penman, D., Romans, B., Scher, H.D., Sexton, P., Takagi, H., Turner, S.K., Whiteside, J.H., Yamaguchi, T., and Yamamoto, Y., 2014d. Site U1405. In Norris, R.D., Wilson, P.A., Blum, P., and the Expedition 342 Scientists, *Proc. IODP*, 342: College Station, TX (Integrated Ocean Drilling Program). doi:[10.2204/iodp.proc.342.106.2014](https://doi.org/10.2204/iodp.proc.342.106.2014)
- Norris, R.D., Wilson, P.A., Blum, P., Fehr, A., Agnini, C., Bornemann, A., Boulila, S., Bown, P.R., Cournede, C., Friedrich, O., Ghosh, A.K., Hollis, C.J., Hull, P.M., Jo, K., Junium, C.K., Kaneko, M., Liebrand, D., Lippert, P.C., Liu, Z., Matsui, H., Moriya, K., Nishi, H., Opdyke, B.N., Penman, D., Romans, B., Scher, H.D., Sexton, P., Takagi, H., Turner, S.K., Whiteside, J.H., Yamaguchi, T., and Yamamoto, Y., 2014e. Site U1408. In Norris, R.D., Wilson, P.A., Blum, P., and the Expedition 342 Scientists, *Proc. IODP*, 342: College Station, TX (Integrated Ocean Drilling Program). doi:[10.2204/iodp.proc.342.109.2014](https://doi.org/10.2204/iodp.proc.342.109.2014)
- Pälike, H., Lyle, M.W., Nishi, H., Raffi, I., Ridgwell, A., Gamage, K., Klaus, A., Acton, G., Anderson, L., Backman, J., Baldauf, J., Beltran, C., Bohaty, S.M., Bown, P., Busch, W., Channell, J.E.T., Chun, C.O.J., Delaney, M., Dewangan, P., Dunkley Jones, T., Edgar, K.M., Evans, H., Fitch, P., Foster, G.L., Gussone, N., Hasegawa, H., Hathorne, E.C., Hayashi, H., Herrle, J.O., Holbourn, A., Hovan, S., Hyeong, K., Iijima, K., Ito, T., Kamikuri, S., Kimoto, K., Kuroda, J., Leon-Rodriguez, L., Malinverno, A., Moore, T.C., Jr., Murphy, B.H., Murphy, D.P., Nakamura, H., Ogane, K., Ohneiser, C., Richter, C., Robinson, R., Rohling, E.J., Romero, O., Sawada, K., Scher, H., Schneider, L., Sluijs, A., Takata, H., Tian, J., Tsujimoto, A., Wade, B.S., Westerhold, T., Wilkens, R., Williams, T., Wilson, P.A., Yamamoto, Y., Yamamoto, S., Yamazaki, T., and Zeebe, R.E., 2012. A Cenozoic record of the equatorial Pacific carbonate compensation depth. *Nature (London, U. K.)*, 488(7409):609–614. doi:[10.1038/nature11360](https://doi.org/10.1038/nature11360)
- Sanfilippo, A., and Blome, C.D., 2001. Biostratigraphic implications of mid-latitude Paleocene–Eocene radiolarian faunas from Hole 1051A, ODP Leg 171B, Blake Nose, western North Atlantic. In Kroon, D., Norris, R.D., and Klaus, A. (Eds.), *Western North Atlantic Palaeogene and Cretaceous Palaeoceanography*. Geol. Soc. Spec. Publ., 183(1):185–224. doi:[10.1144/GSL.SP.2001.183.01.10](https://doi.org/10.1144/GSL.SP.2001.183.01.10)
- Tucholke, B.E., and Vogt, P.R., 1979. Western North Atlantic: sedimentary evolution and aspects of tectonic history. In Tucholke, B.E., Vogt, P.R., et al., *Init. Repts. DSDP*, 43: Washington, DC (U.S. Govt. Printing Office), 791–825. doi:[10.2973/dsdp.proc.43.140.1979](https://doi.org/10.2973/dsdp.proc.43.140.1979)
- Zachos, J.C., Dickens, G.R., and Zeebe, R.E., 2008. An early Cenozoic perspective on greenhouse warming and carbon-cycle dynamics. *Nature (London, U. K.)*, 451(7176):279–283. doi:[10.1038/nature06588](https://doi.org/10.1038/nature06588)

Publication: 3 March 2014
MS 342-110



Figure F1. Bathymetric map of northwestern Southeast Newfoundland Ridge northeast of J-Anomaly Ridge. Data are based upon multibeam mapping by KNR179-1 site survey. Single-channel seismic reflection profiles are shown in Figures F2 and F3.

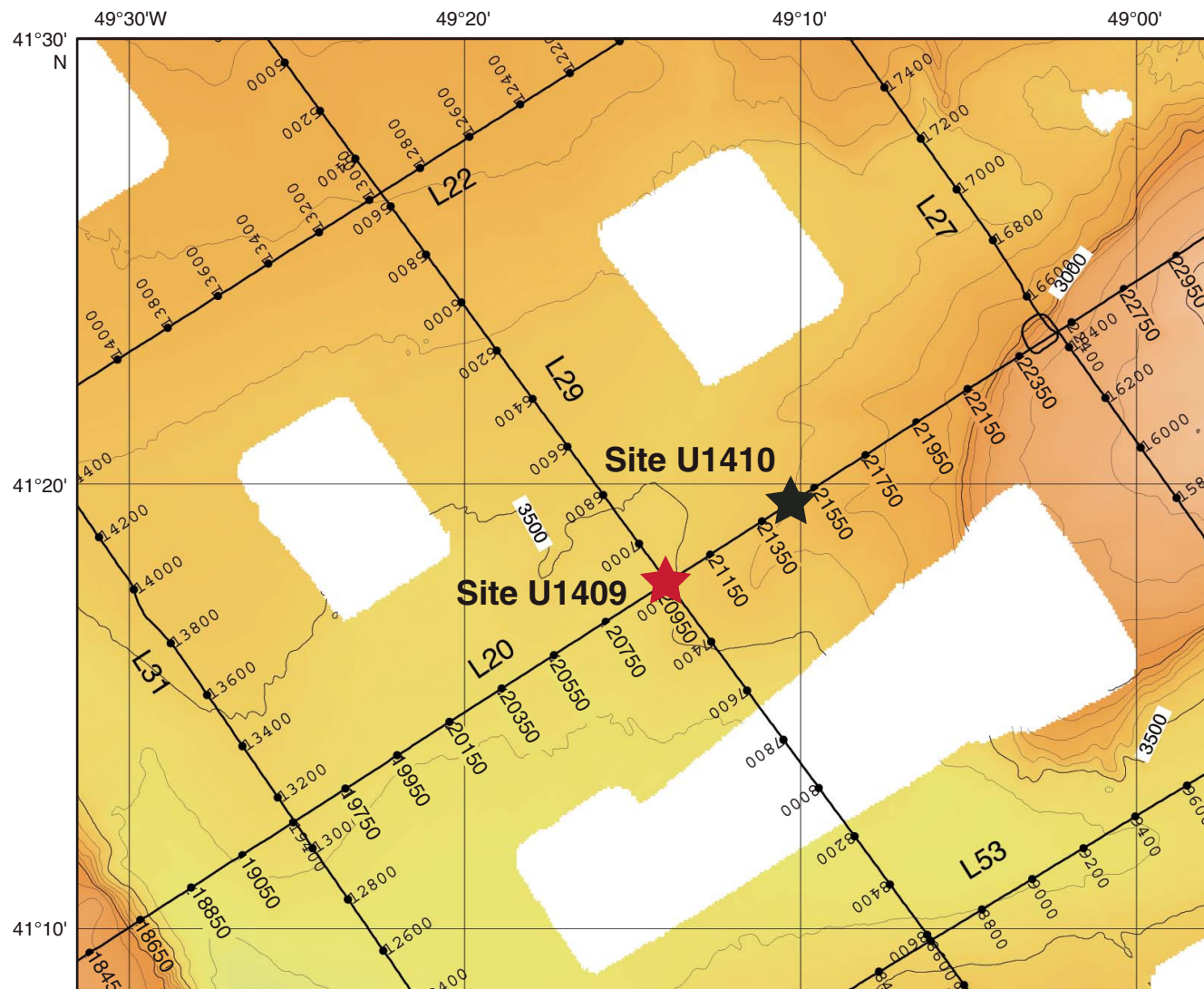


Figure F2. Single-channel seismic KNR179-1 Line 20. This is the southwest–northeast line crossing Site U1409 (at shotpoint [SP] 21000). White bars approximate depth of penetration at Site U1409 and nearby Site U1410.

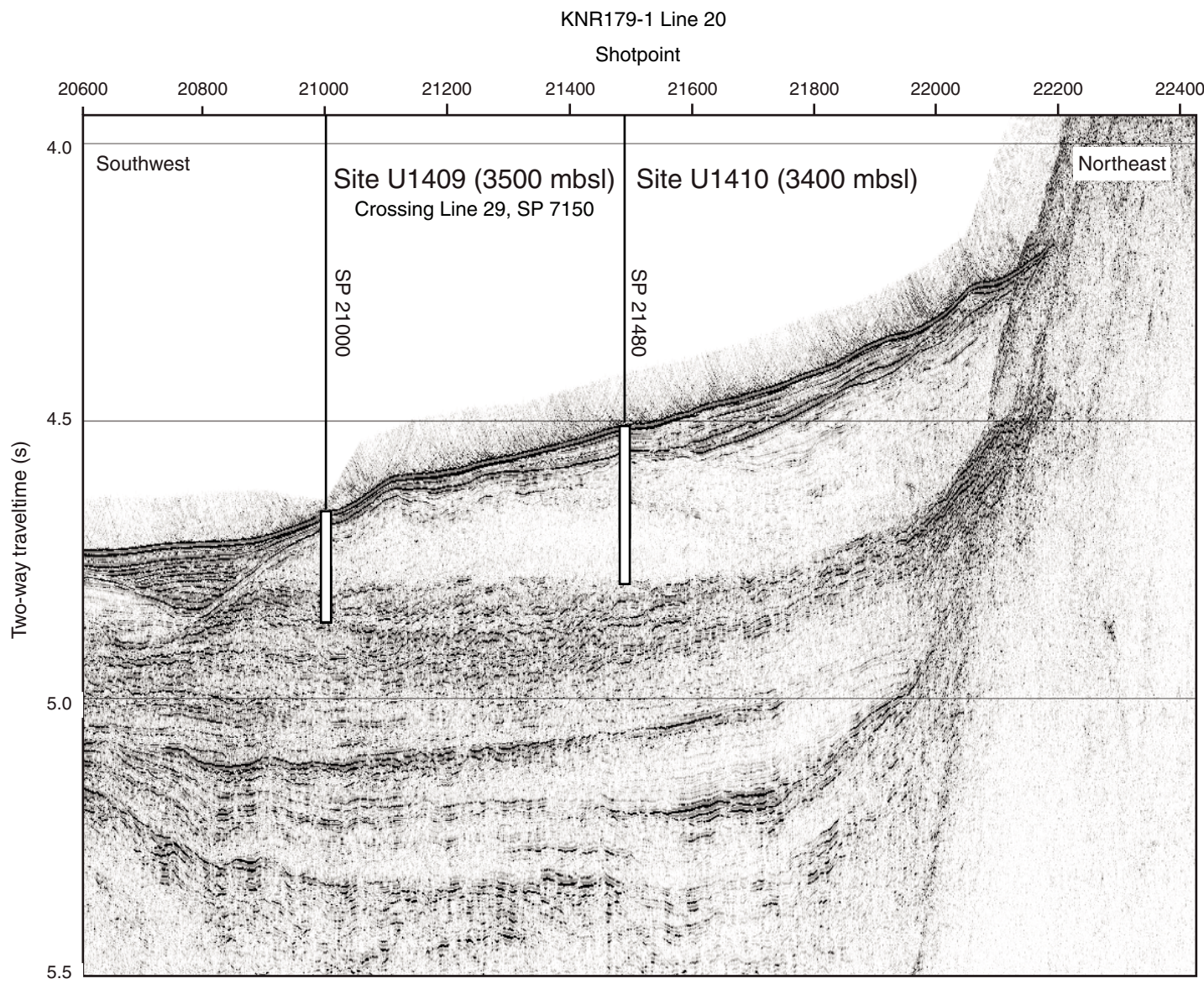


Figure F3. Single-channel seismic KNR179-1 Line 29. This is the northwest–southeast line crossing KNR179-1, Line 20 (at shotpoint [SP] 7150 on Line 29). White bar approximates depth of penetration at Site U1409.

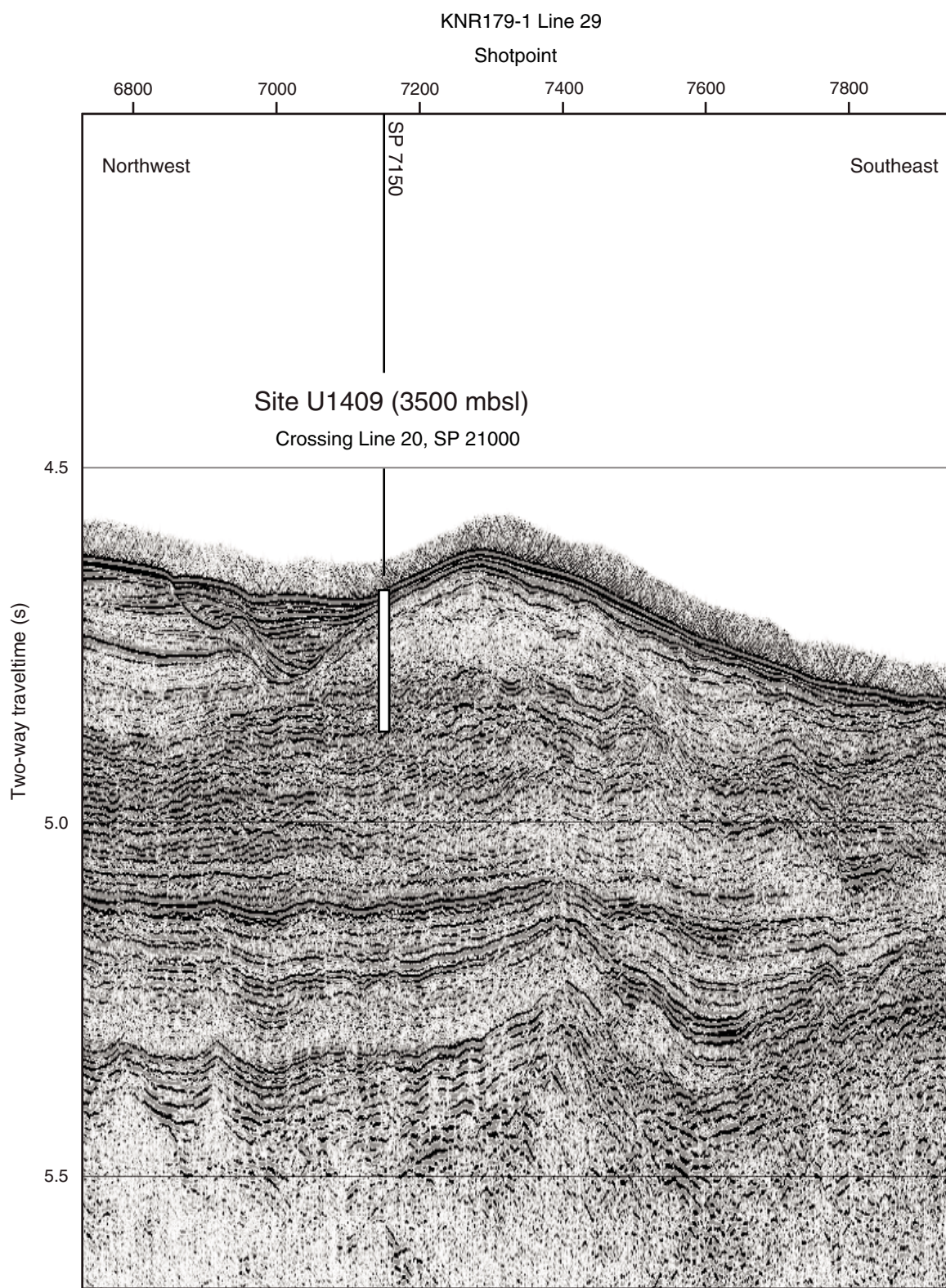


Figure F4. Lithostratigraphic summary, Site U1409. Typically the lighter colors in sediment reflect higher carbonate content. Note the green to pink/tan transition in the color data at the Unit III/IV boundary.

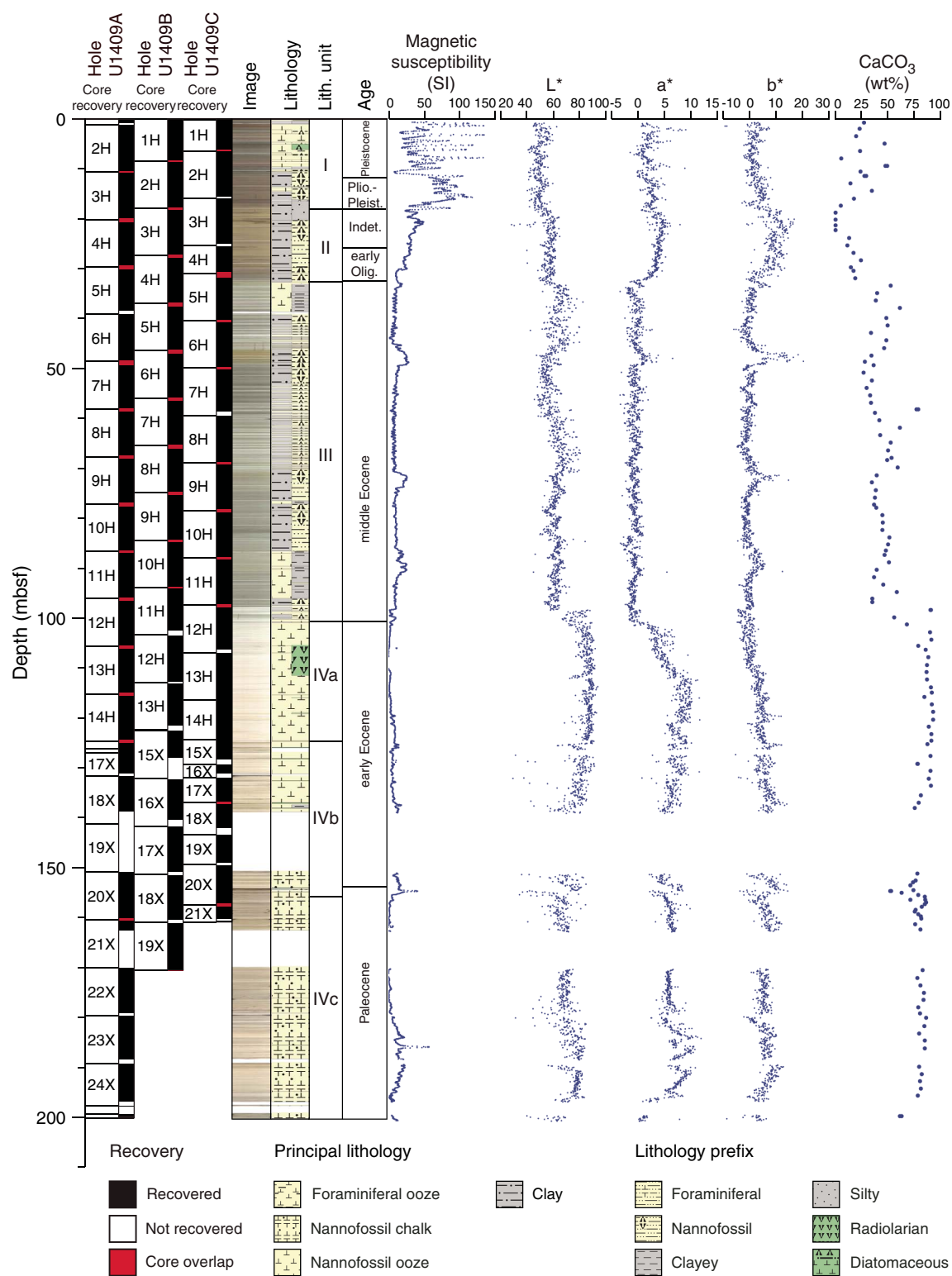


Figure F5. Core images of most common lithologies, Site U1409. A. Pleistocene muddy foraminiferal sand overlying silty clay, Unit I. B. Pleistocene reddish brown clay, Unit I. C. Silty clay with manganese nodule, Unit II. D. Middle Eocene green nannofossil clay and white nannofossil ooze, Unit III. E. Early Eocene nannofossil ooze, Subunit IVa. F. Early Eocene nannofossil chalk, Subunit IVb. G. Paleocene nannofossil chalk, Subunit IVc.

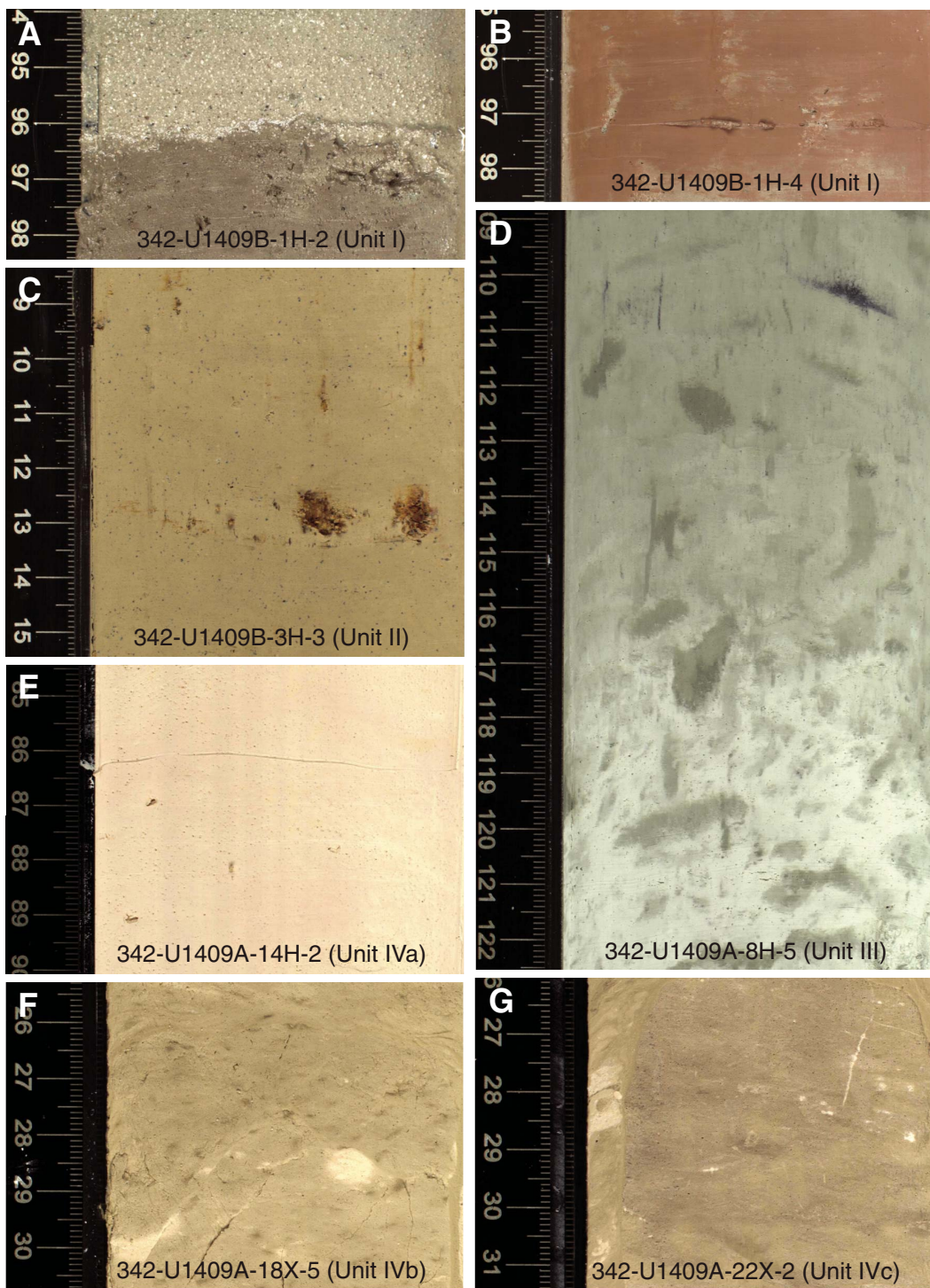


Figure F6. Photomicrographs of smear slides indicating the dominant lithologies of Units I-III, Site U1409. A. Diatomaceous nannofossil ooze with foraminifers, Unit I. B. Nannofossil clay, Unit II. C. Nannofossil ooze, Unit III. D. Nannofossil clay, Unit III.

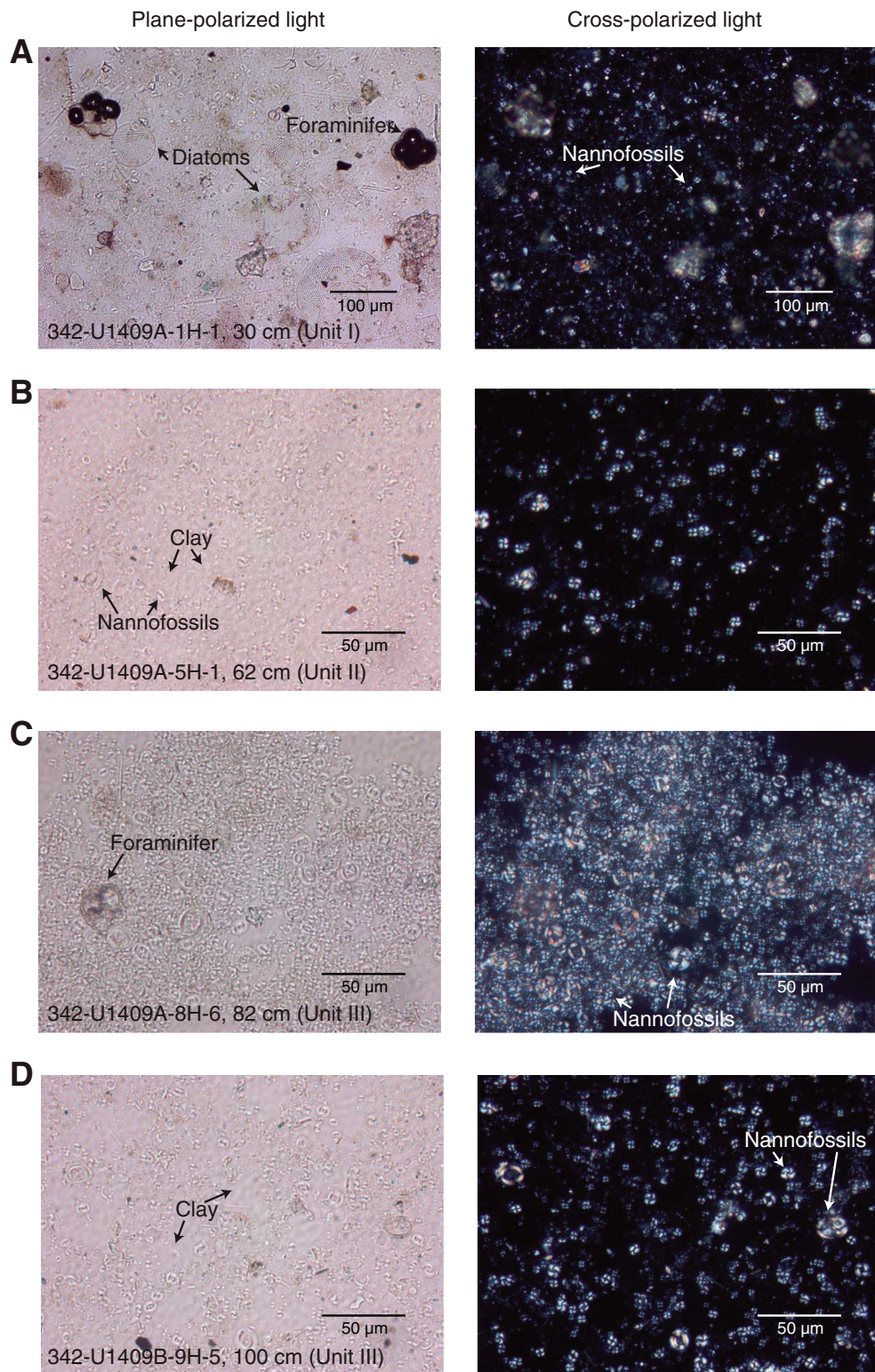


Figure F7. Photomicrographs of smear slides indicating the dominant lithologies of Unit IV, Site U1409. A. Nannofossil ooze with radiolarians, Subunit IVa. B. Nannofossil ooze with foraminifers, Subunit IVb. C. Nannofossil claystone, Subunit IVb. D. Nannofossil chalk with radiolarians, Subunit IVc.

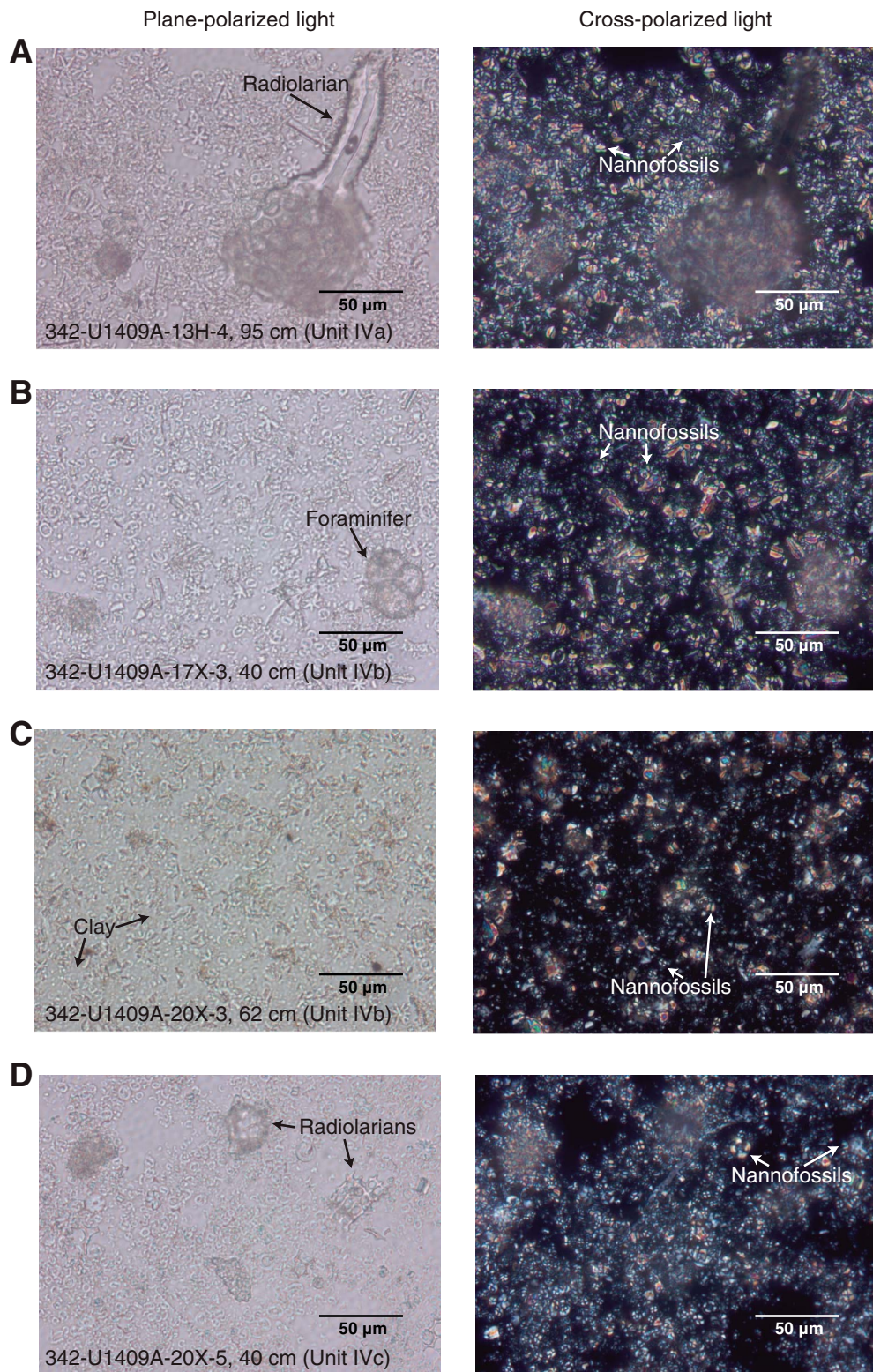


Figure F8. Plots of smear slide results of major biogenic and lithologic components and their relative abundance, Hole U1409A. VA = very abundant, A = abundant, C = common, F = few, P = present.

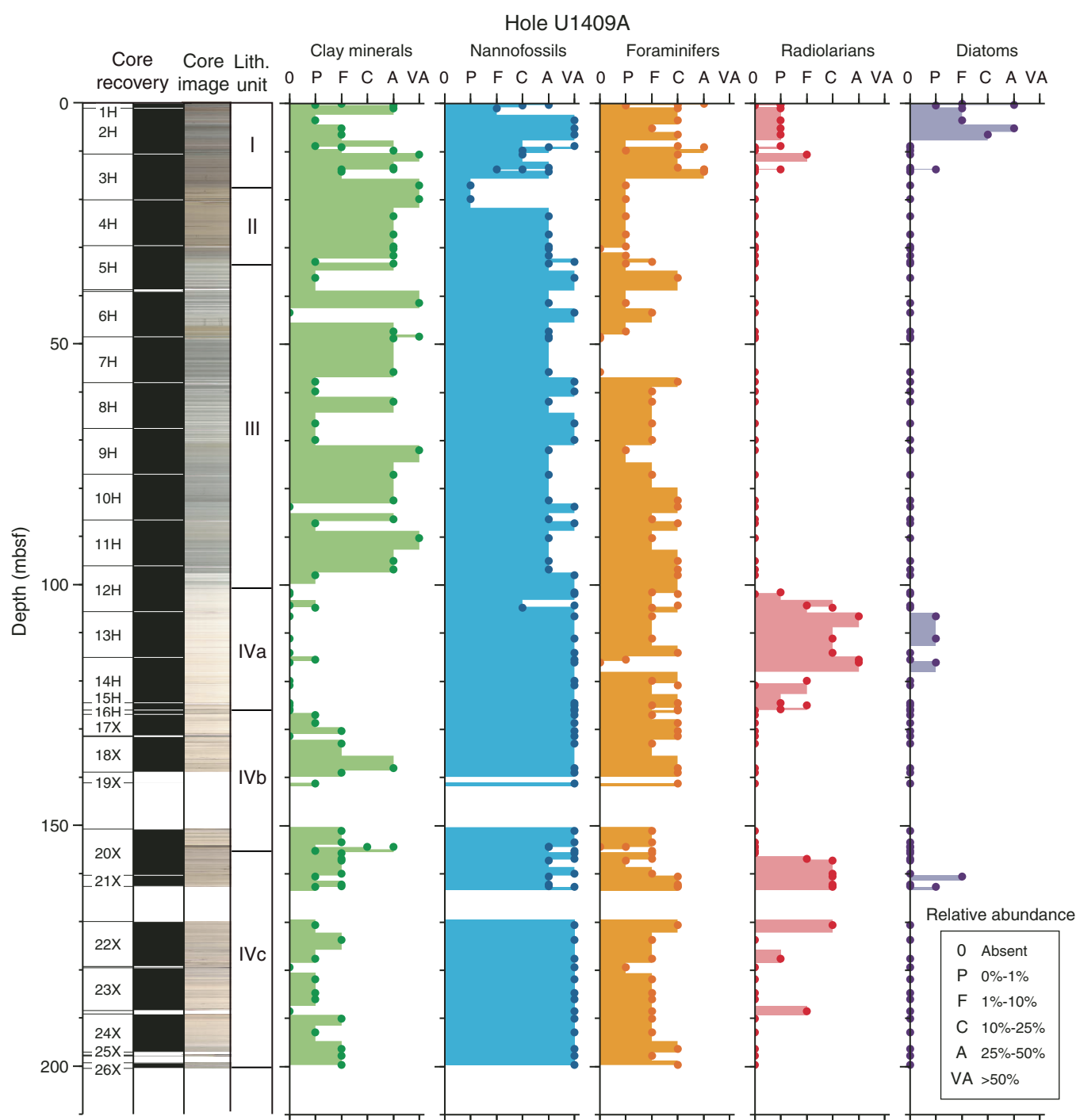


Figure F9. Plots of smear slide results of major biogenic and lithologic components and their relative abundance, Hole U1409B. VA = very abundant, A = abundant, C = common, F = few, P = present.

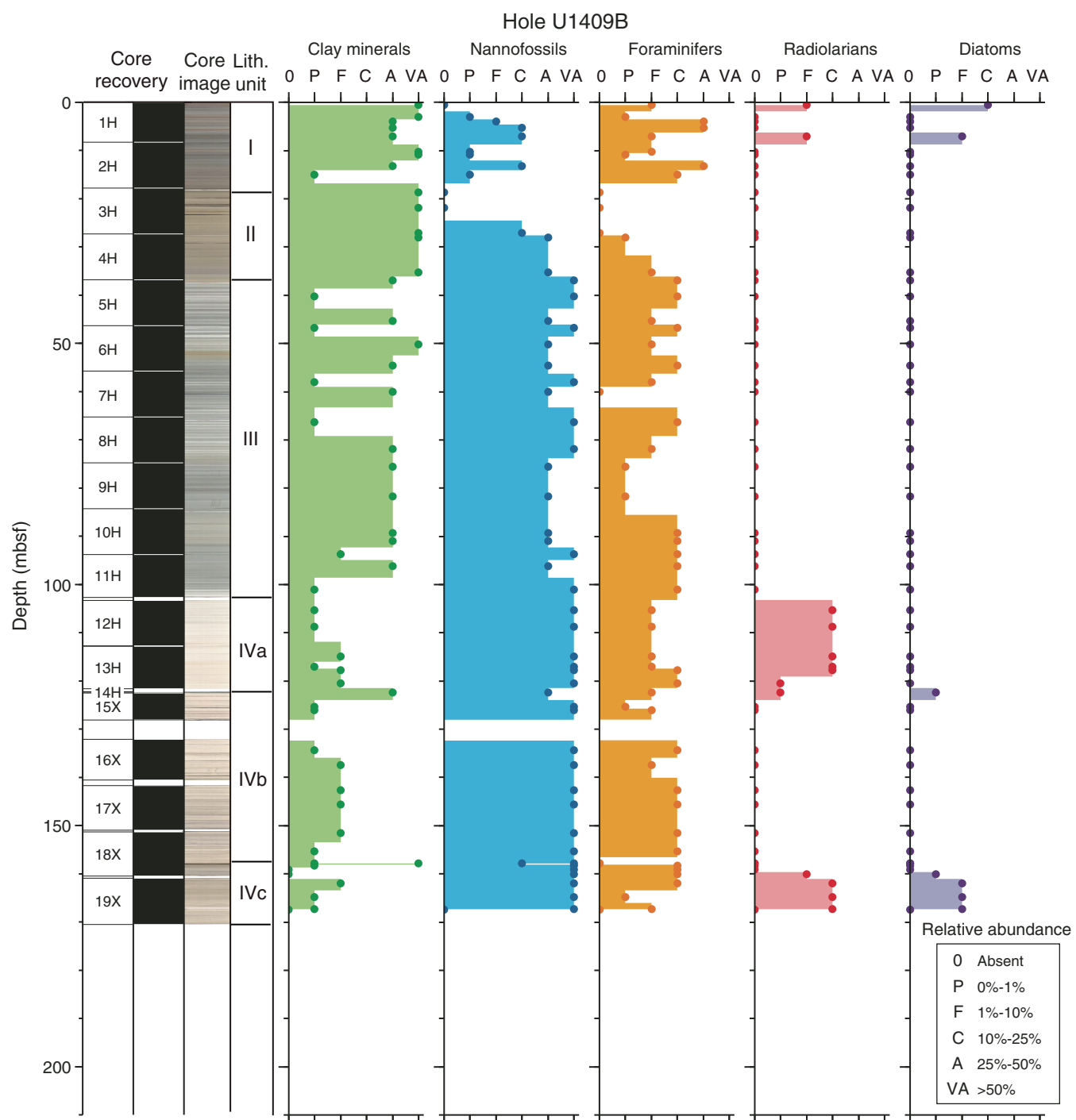


Figure F10. Plots of smear slide results of major biogenic and lithologic components and their relative abundance, Hole U1409C. VA = very abundant, A = abundant, C = common, F = few, P = present.

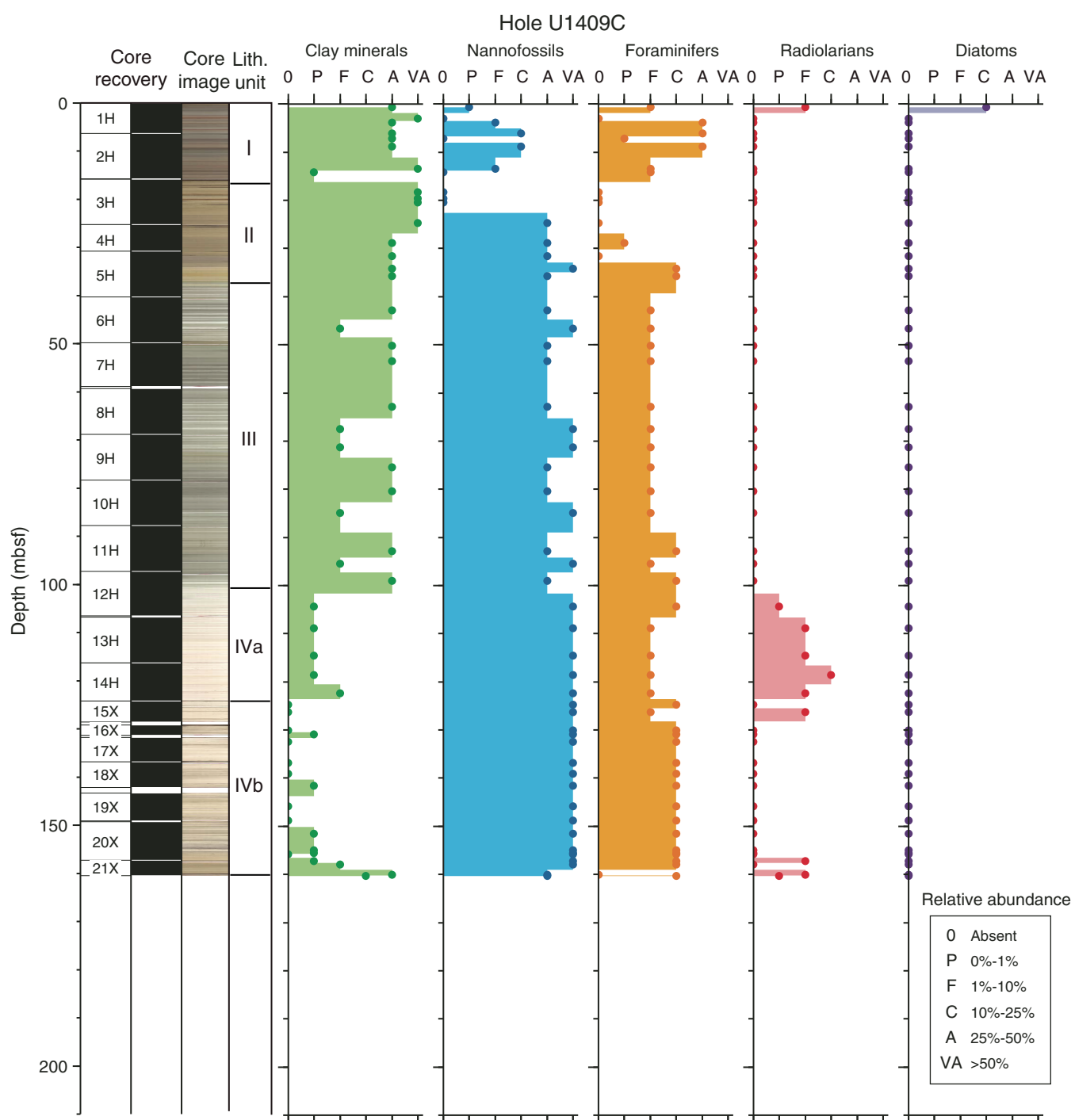


Figure F11. Core images of muddy sand intervals in Unit I, Hole U1409A. **A.** Three muddy sand intervals observed in Unit I in all holes. **B.** Close-up of the intercalated beds showing the grayer beds containing more foraminifers and the greener beds containing more silt. The lowermost two beds are normally graded. **C.** Lithology of grayer beds. **D.** Lithology of greener beds.

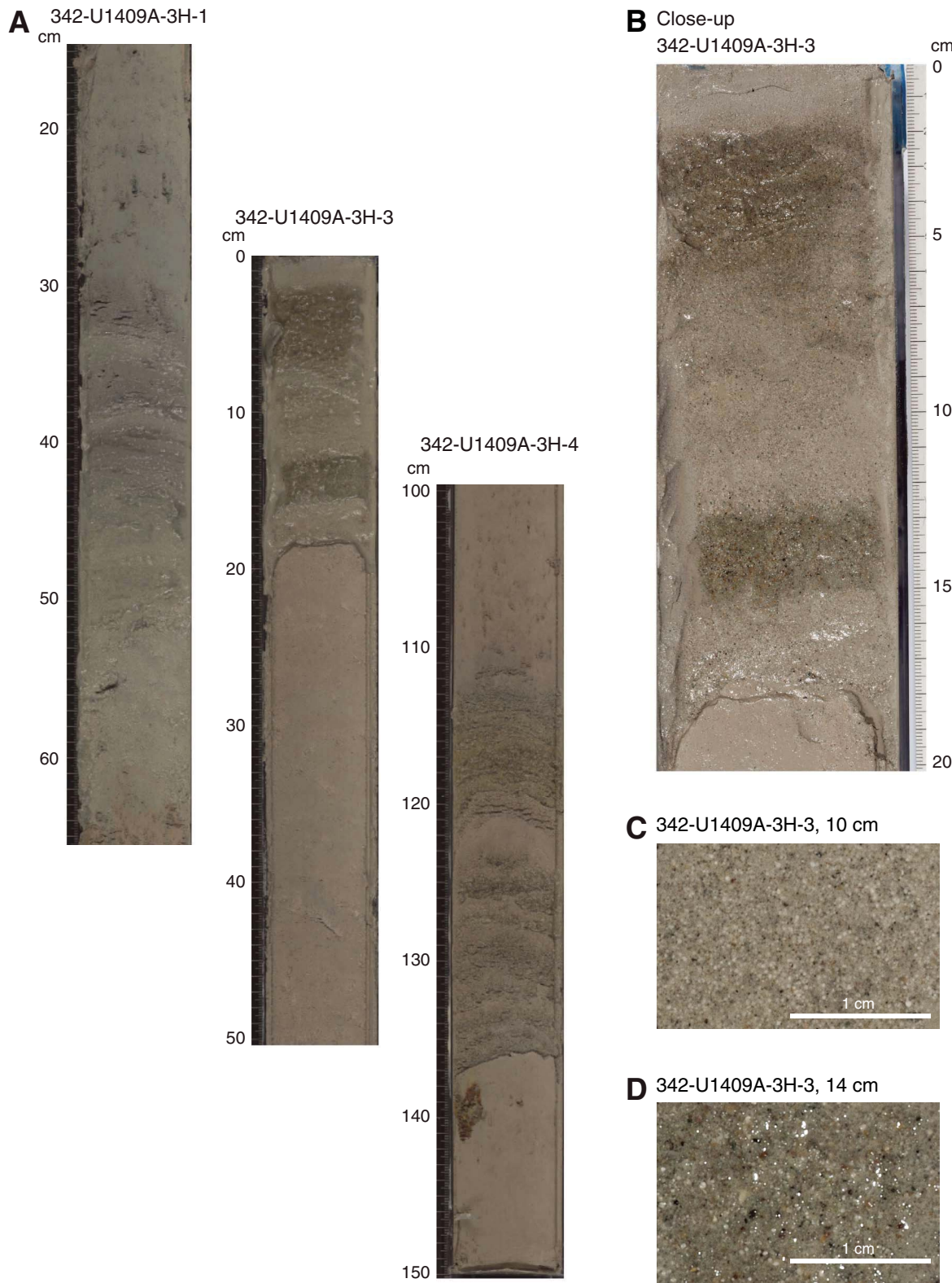


Figure F12. Core image and plot of carbonate content showing cyclicity in middle Eocene interbedded greenish gray nannofossil clay and white nannofossil ooze, Hole U1409C.

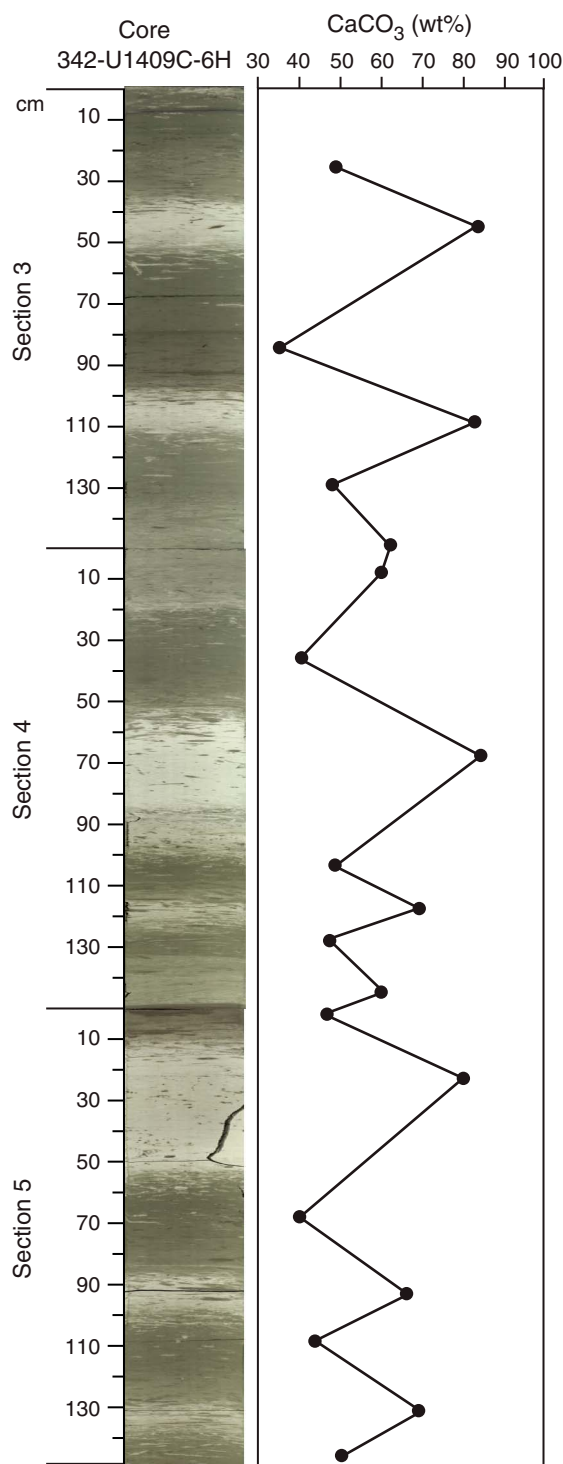


Figure F13. Core image and physical property plots showing middle Eocene cyclicity, Hole U1409A. All holes show well-expressed cyclicity over this interval (nannofossil Subzone NP15c; ~44 Ma).

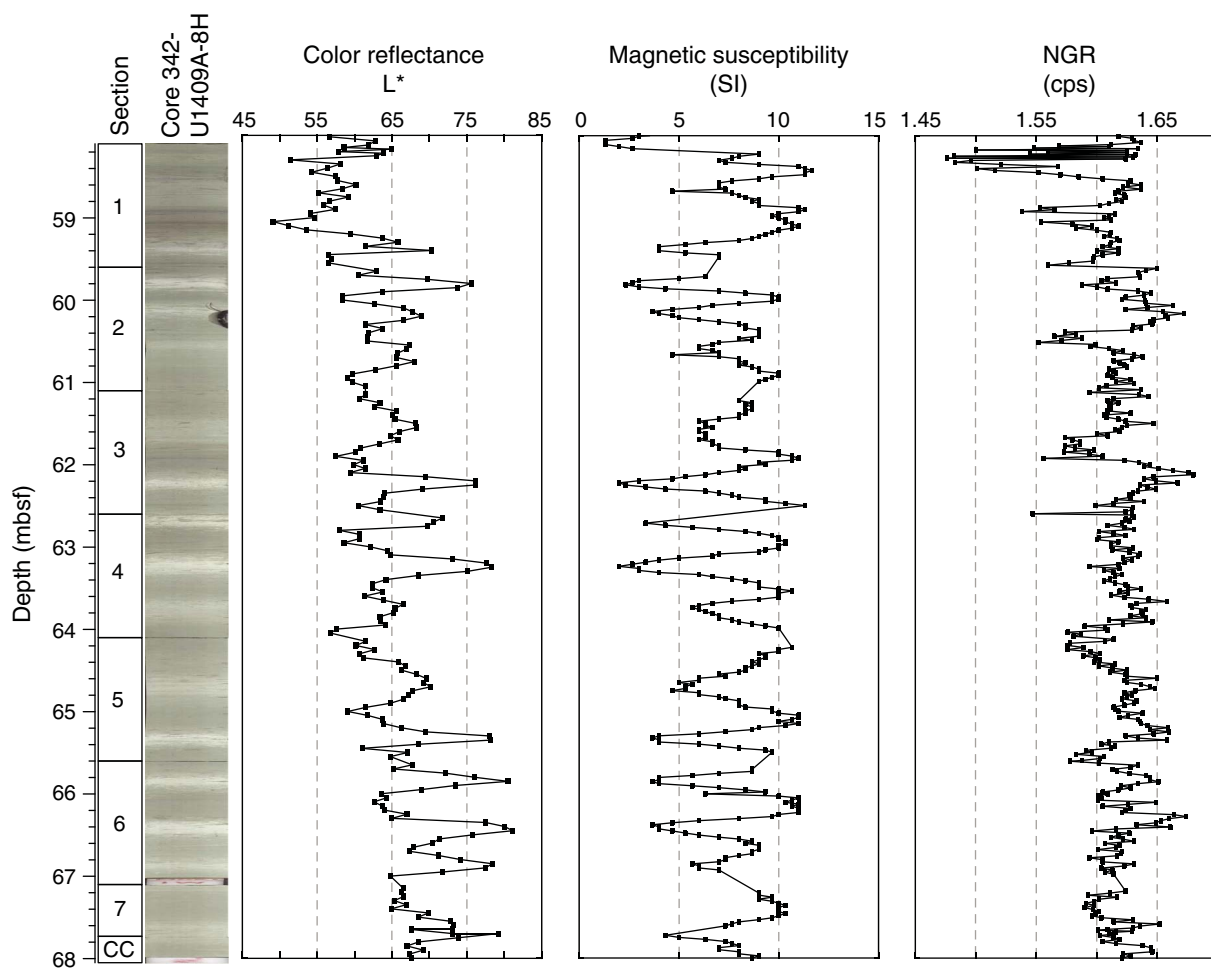


Figure F14. Core images showing examples of graded red oxide horizons in Unit III, Site U1409. Decimeter- to centimeter-scale graded red oxide horizons occur in two discrete intervals in Unit III. Note gradation from light reddish brown to dense brick-red over the length of an oxide horizon.

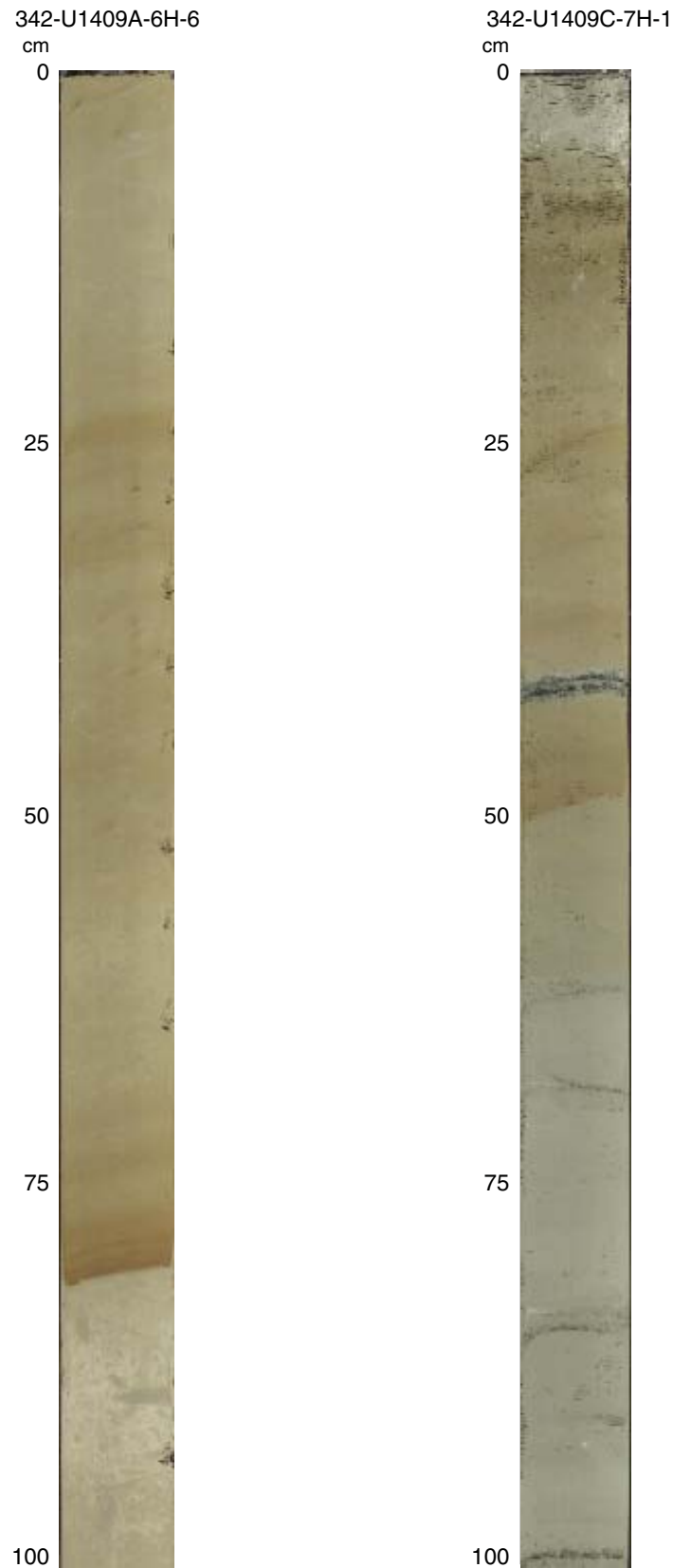


Figure F15. Core images and photomicrographs of siliceous sediment spanning the Paleocene/Eocene boundary, Hole U1409A. A. Smear slide photomicrograph showing examples of nannofossil excursion taxa (Sample 342-U1409A-20X-3, 56 cm). B. Photomicrograph of thin section showing recrystallized foraminifers and a calcified radiolarian (Sample 342-U1409A-20X-3, 69–70 cm). C. Planktonic foraminifer excursion taxa *Acarinina africana* recovered from the clayey nannofossil chalk below the siliceous unit.

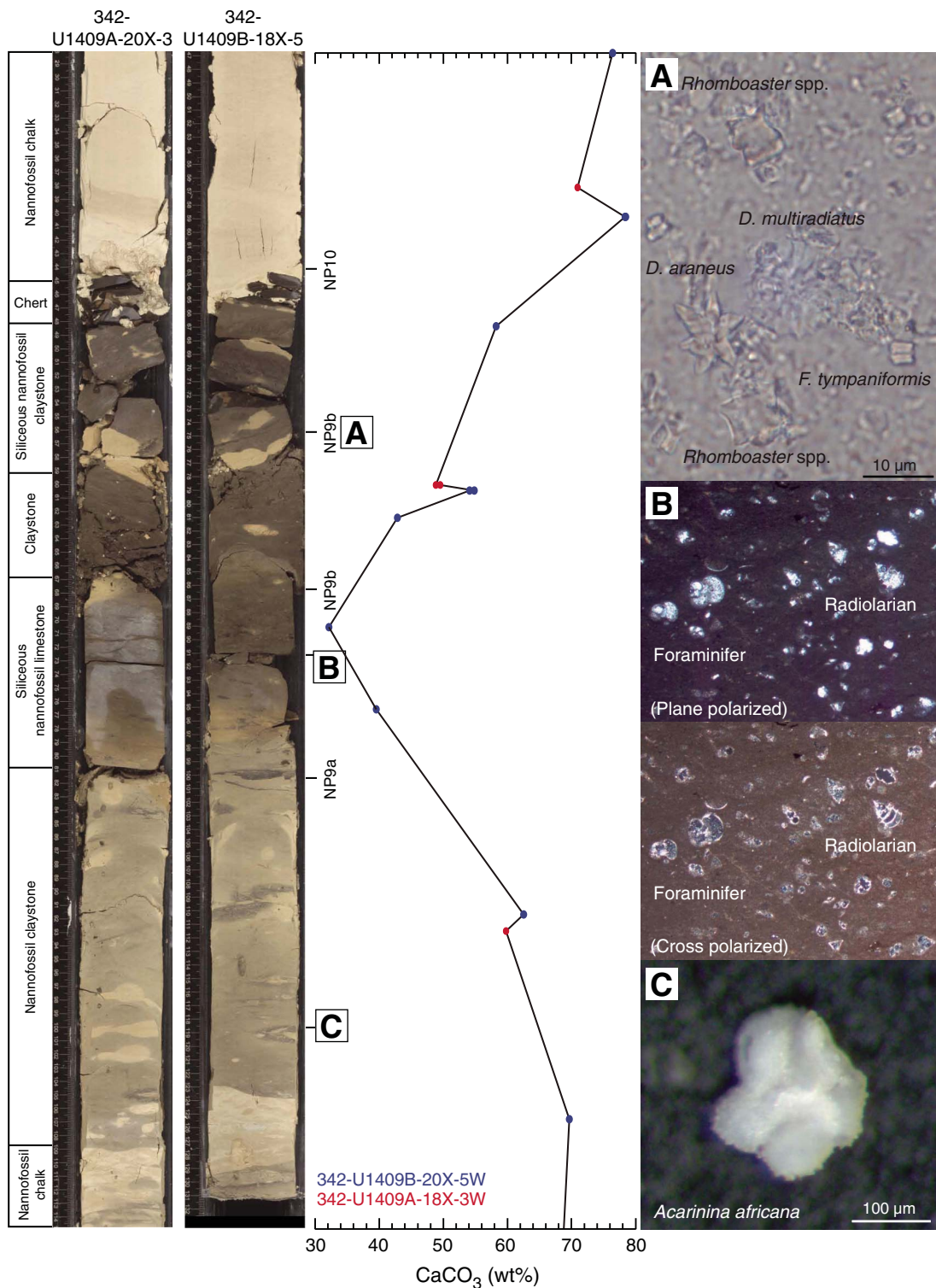


Figure F16. Core images of an example of long-period variation in the strength of cyclicity in greenish gray nannofossil clay to white nannofossil ooze, Hole U1409A.

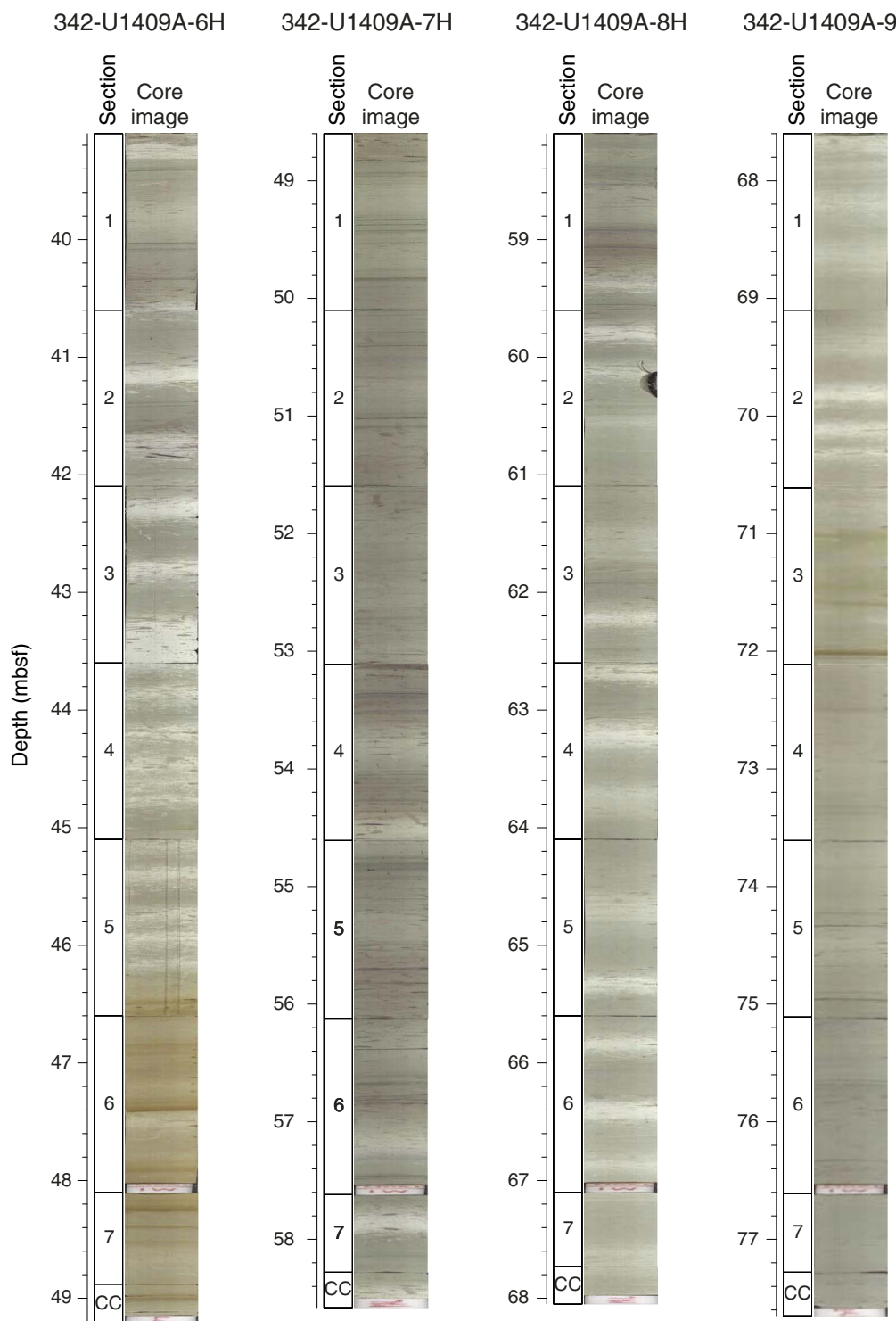


Figure F17. Core images of red-brown oxide horizons in Hole U1408A for comparison with Figure F14. These horizons were only observed in this section at Site U1408 but occur more frequently at Site U1409.

Section 342-U1408A-4H-5



Figure F18. Core images of slump deposits in middle Eocene nannofossil Subzone NP15b, Hole U1409A. Evidence of slumping includes clasts, discordant strata, and contorted bedding. White nannofossil ooze clasts are pervasively reworked and include nannofossils indicative of Zones NP12 and NP14 and Subzone NP15b.

Core 342-U1409A-10H

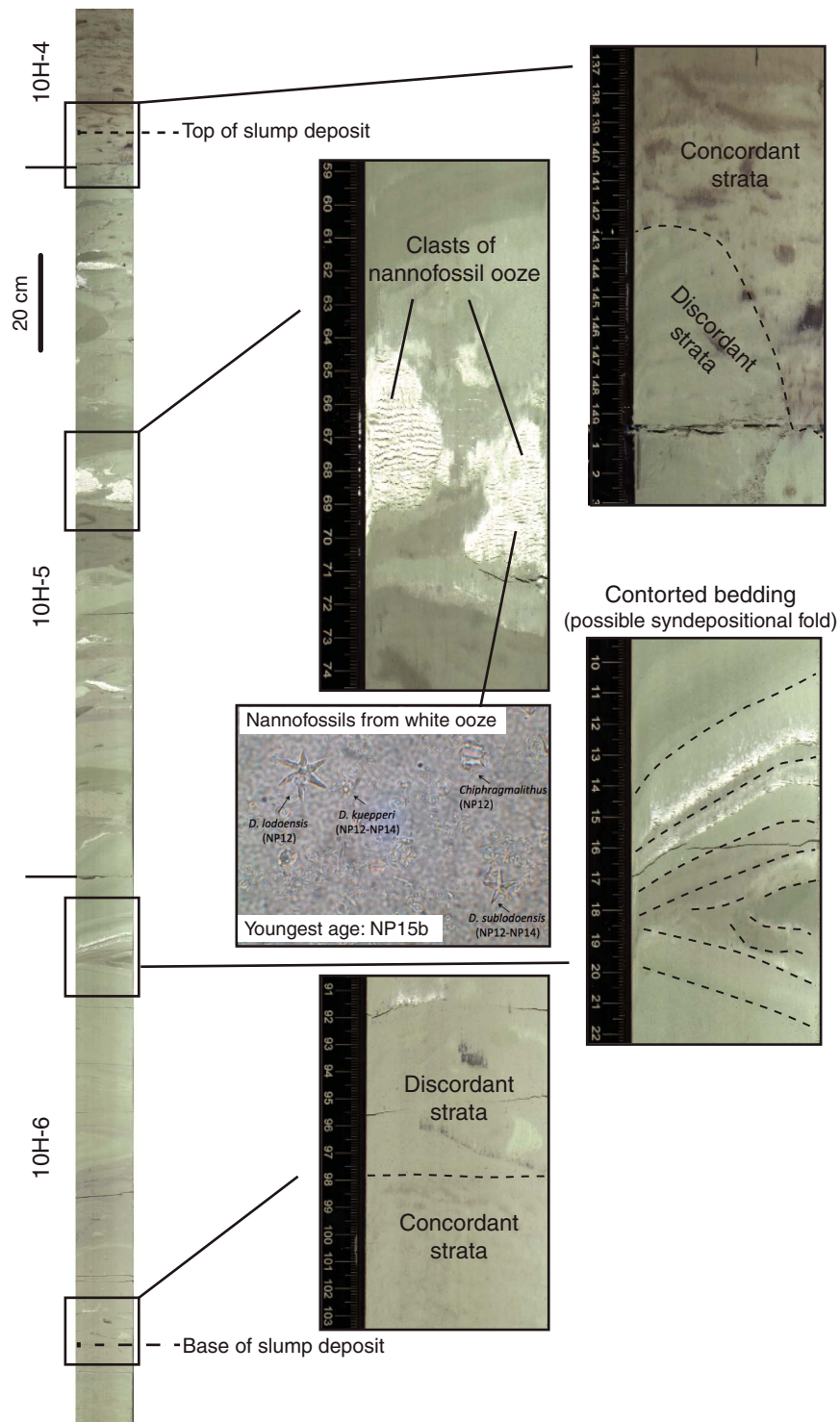


Figure F19. Core images of an example of the bright pink (2.5YR 8/4) montmorillonite blebs and nodules, Hole U1409A.

Section 342-U1409A-13H-1

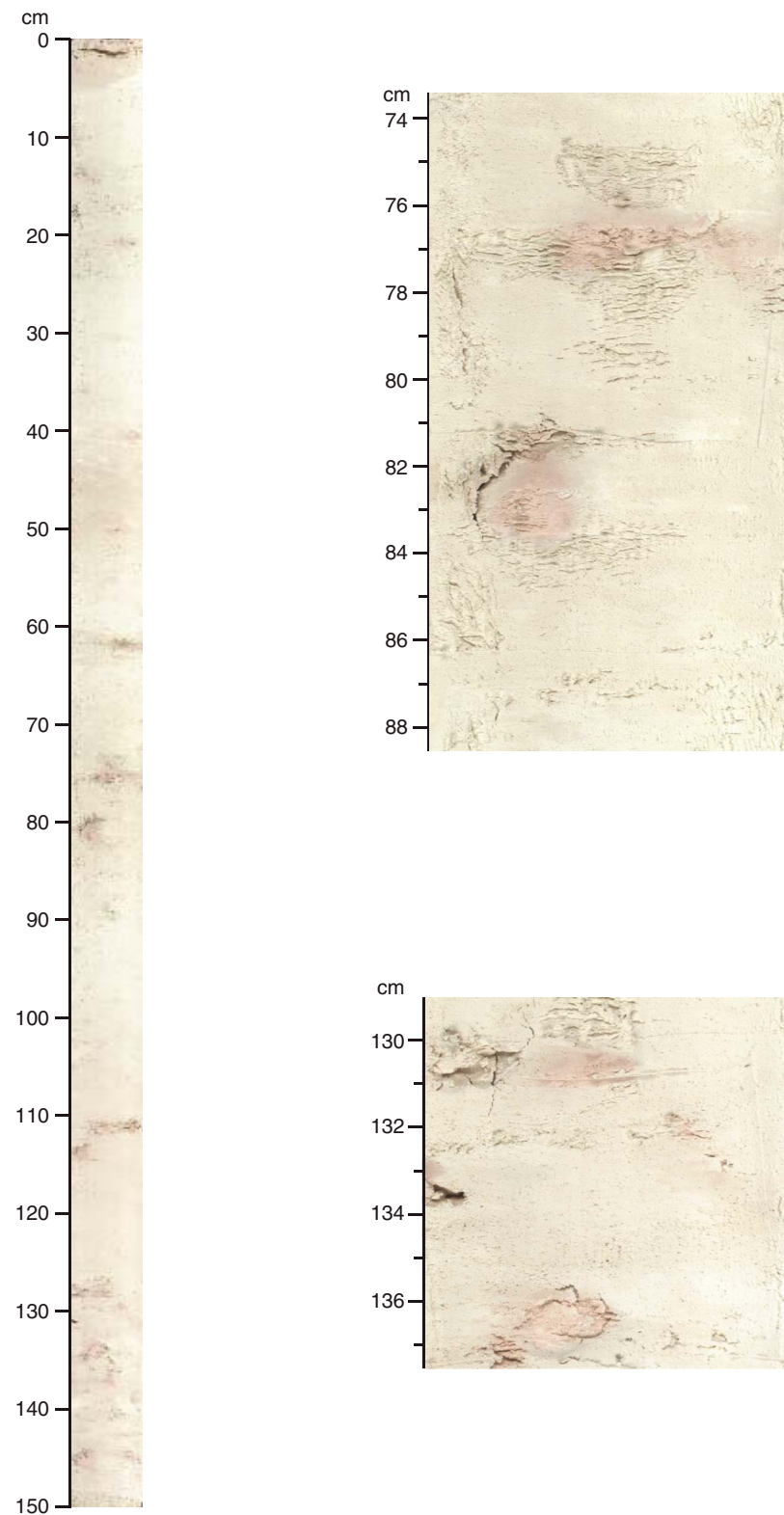


Figure F20. Core images, biostratigraphic datums, and X-ray diffractograms for the Paleocene/Eocene Thermal Maximum (PETM) interval, Hole U1409B. (A, C) Two samples from the dark PETM interval display incipient silicification, as indicated by a double peak caused by the presence of tridymite (20.5° and $21.6^\circ 2\theta$) and possibly also cristobalite ($21.9^\circ 2\theta$), whereas samples from the more carbonate-rich clayey level in the center of the (B) chert interval and from (D) above the PETM show a mineralogical background composition with mainly calcite, quartz, and clay minerals like illite.

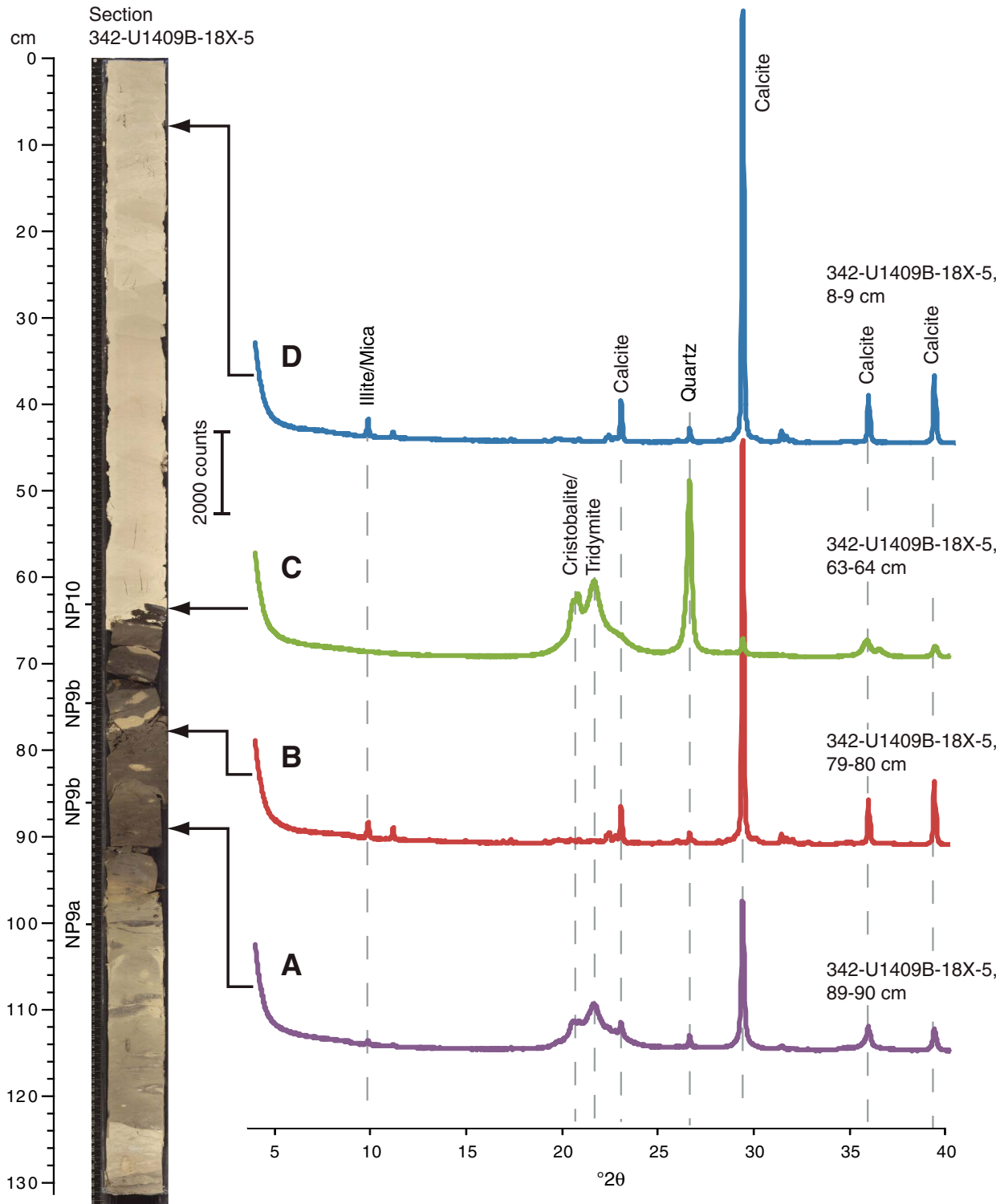


Figure F21. Integrated calcareous and siliceous microfossil biozonation, Site U1409.

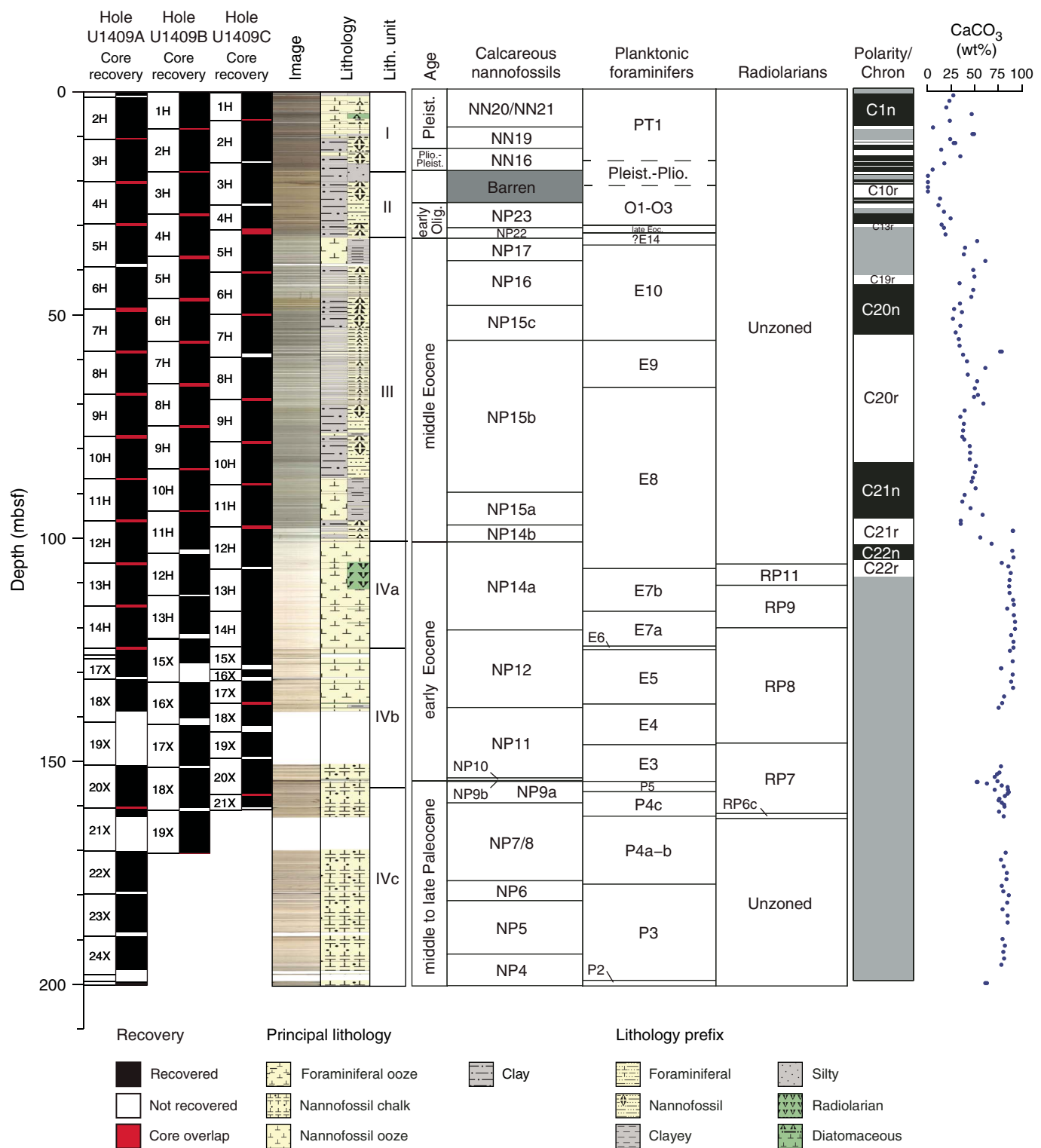


Figure F22. Group abundance and preservation of calcareous and siliceous microfossils, Site U1409. Solid and open symbols represent Holes U1409A and U1409B, respectively. Abundance: B = barren, P = present, R = rare, F = few, C = common, A = abundant, D = dominant. Preservation: P = poor, M = moderate, G = good, VG = very good.

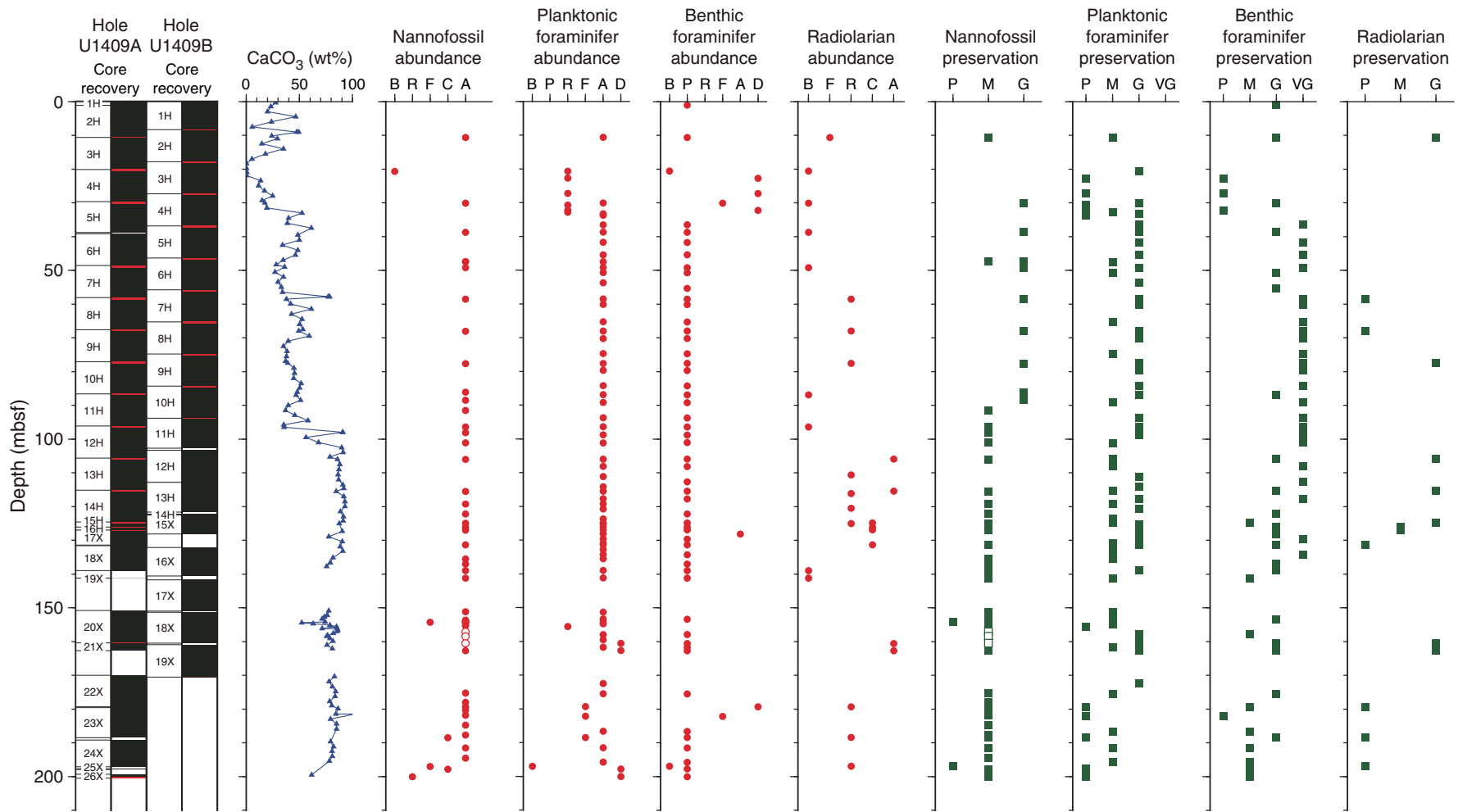


Figure F23. Infaunal- and epifaunal-dominated benthic foraminifer assemblages from the middle Eocene, Hole U1409A. Field of view is ~0.5 cm.

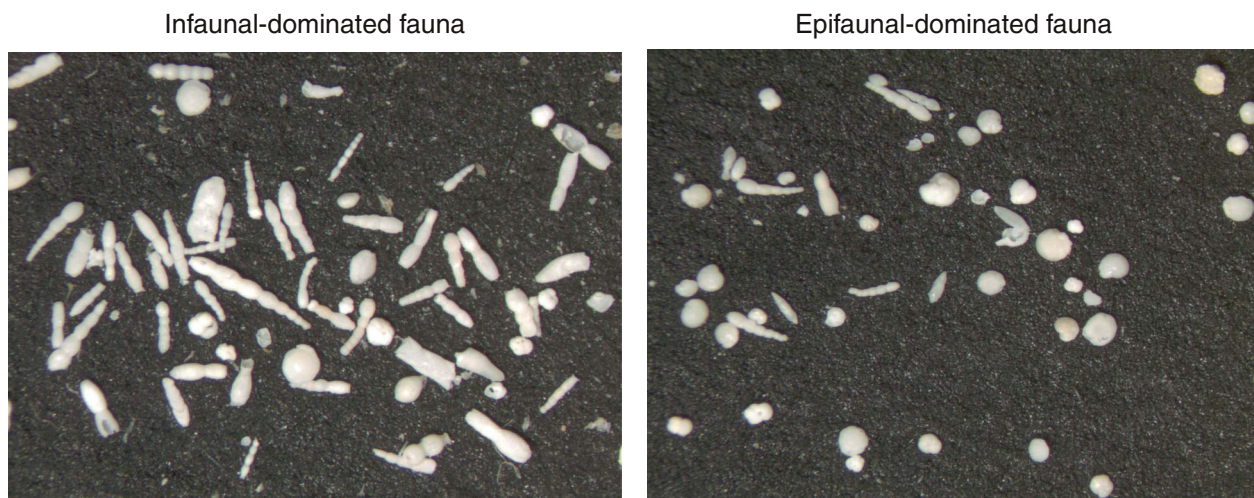


Figure F24. Plots of downhole variation of magnetic susceptibility and paleomagnetism data, Hole U1409A. Magnetization intensity, inclination, and declination are after 20 mT demagnetization. Only oriented advanced piston corer (APC) intervals show directions in geographic coordinates. Directions from all other intervals are shown in sample coordinates. For discrete sample data, if the samples were analyzed by principal component analysis (PCA; Kirschvink, 1980), then directions are shown according to PCA declination and inclination. Otherwise, directions following 20 mT demagnetization are shown. XCB = extended core barrel. Polarity: black = normal chron, white = reversed chron, gray = unidentified interval.

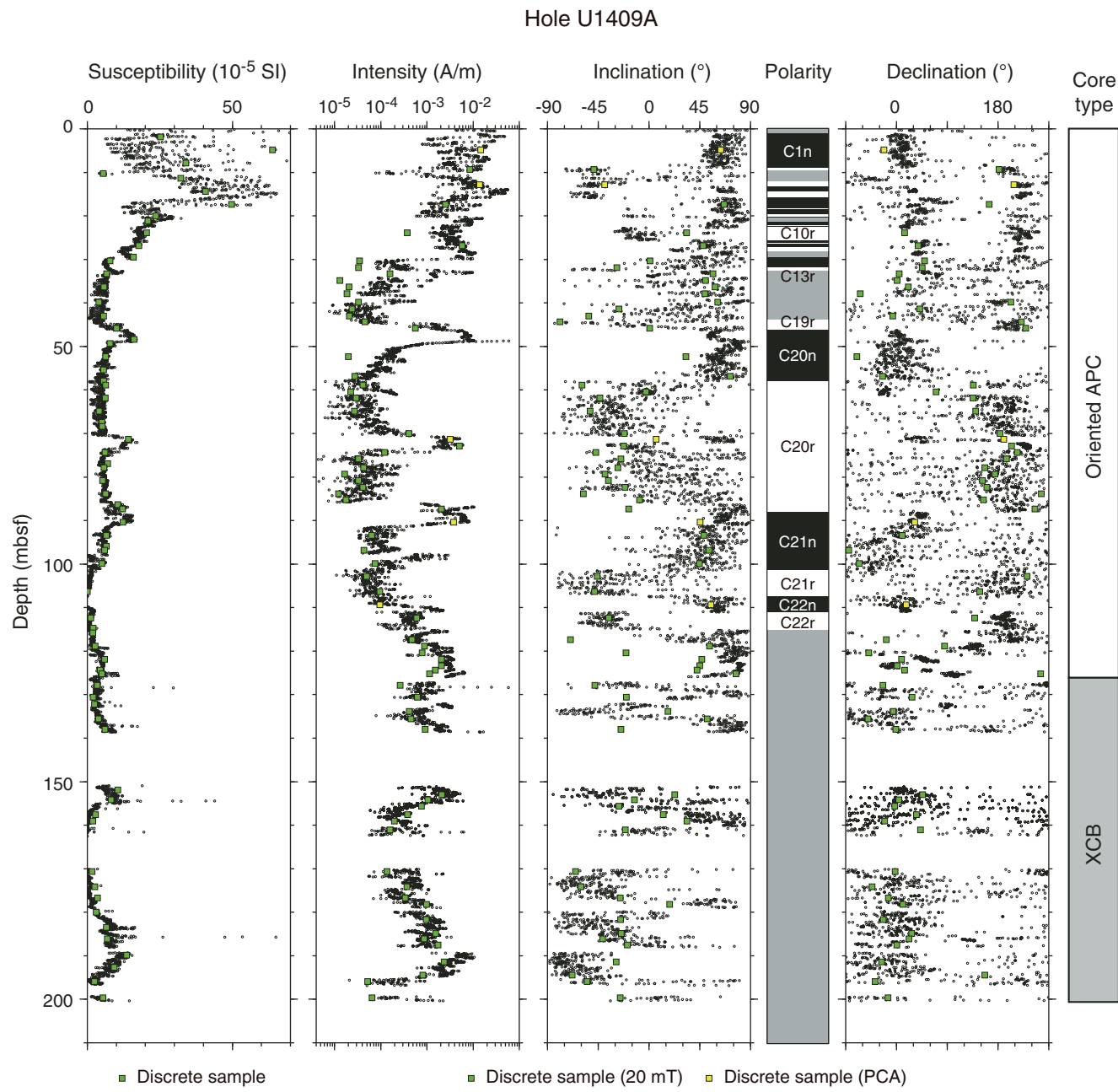


Figure F25. Plots of downhole variation of magnetic susceptibility and paleomagnetism data, Hole U1409B. Magnetization intensity, inclination, and declination are after 20 mT demagnetization. Directions are shown in geographic coordinates for oriented advanced piston corer (APC) intervals. Directions for extended core barrel (XCB) intervals are shown in sample coordinates. Polarity: black = normal chron, white = reversed chron, gray = unidentified interval.

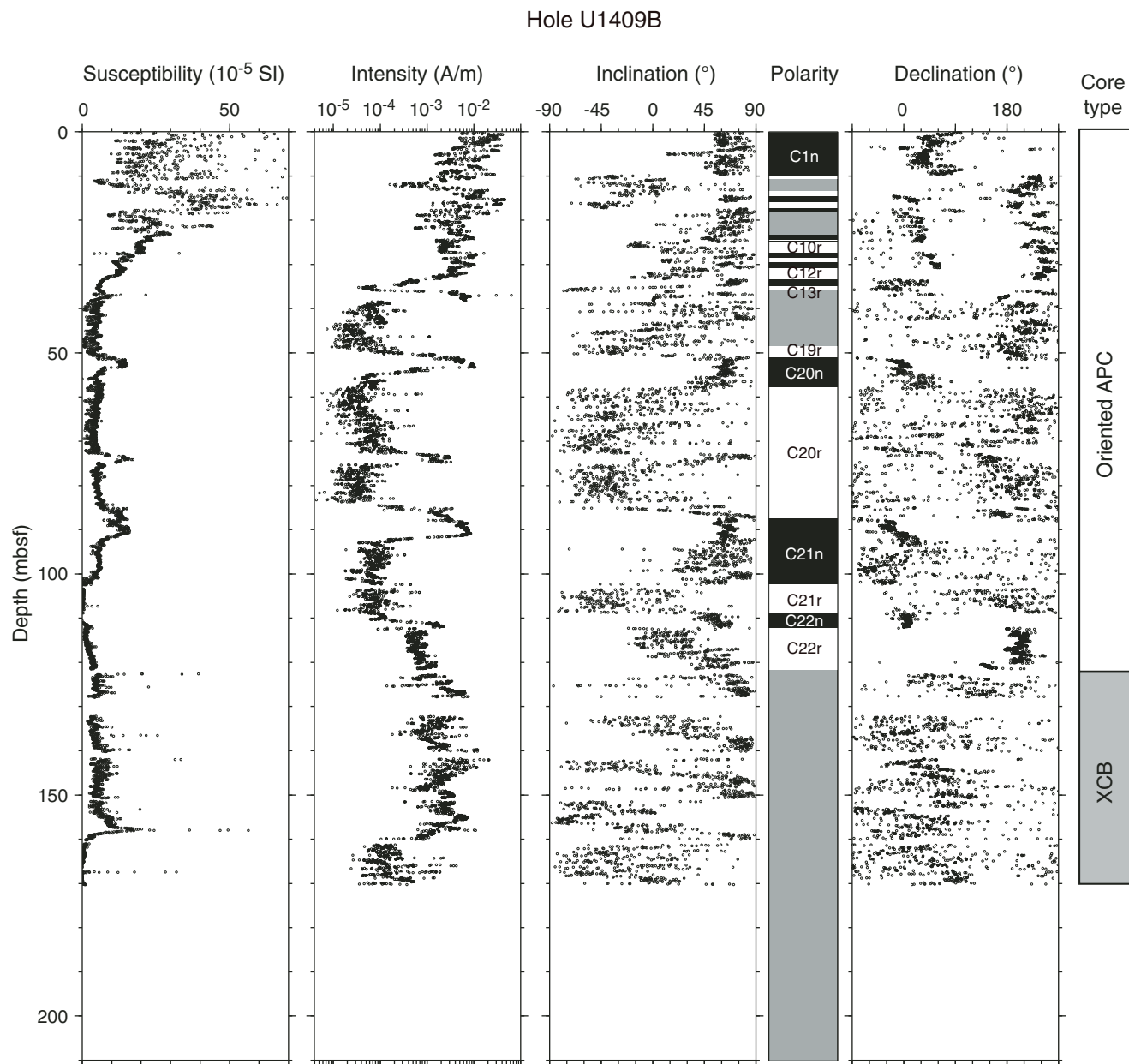


Figure F26. Plots of downhole variation of magnetic susceptibility and paleomagnetism data, Hole U1409C. Magnetization intensity, inclination, and declination are after 20 mT demagnetization. Directions are shown in sample coordinates. APC = advanced piston corer, XCB = extended core barrel. Polarity: black = normal chron, white = reversed chron, gray = unidentified interval.

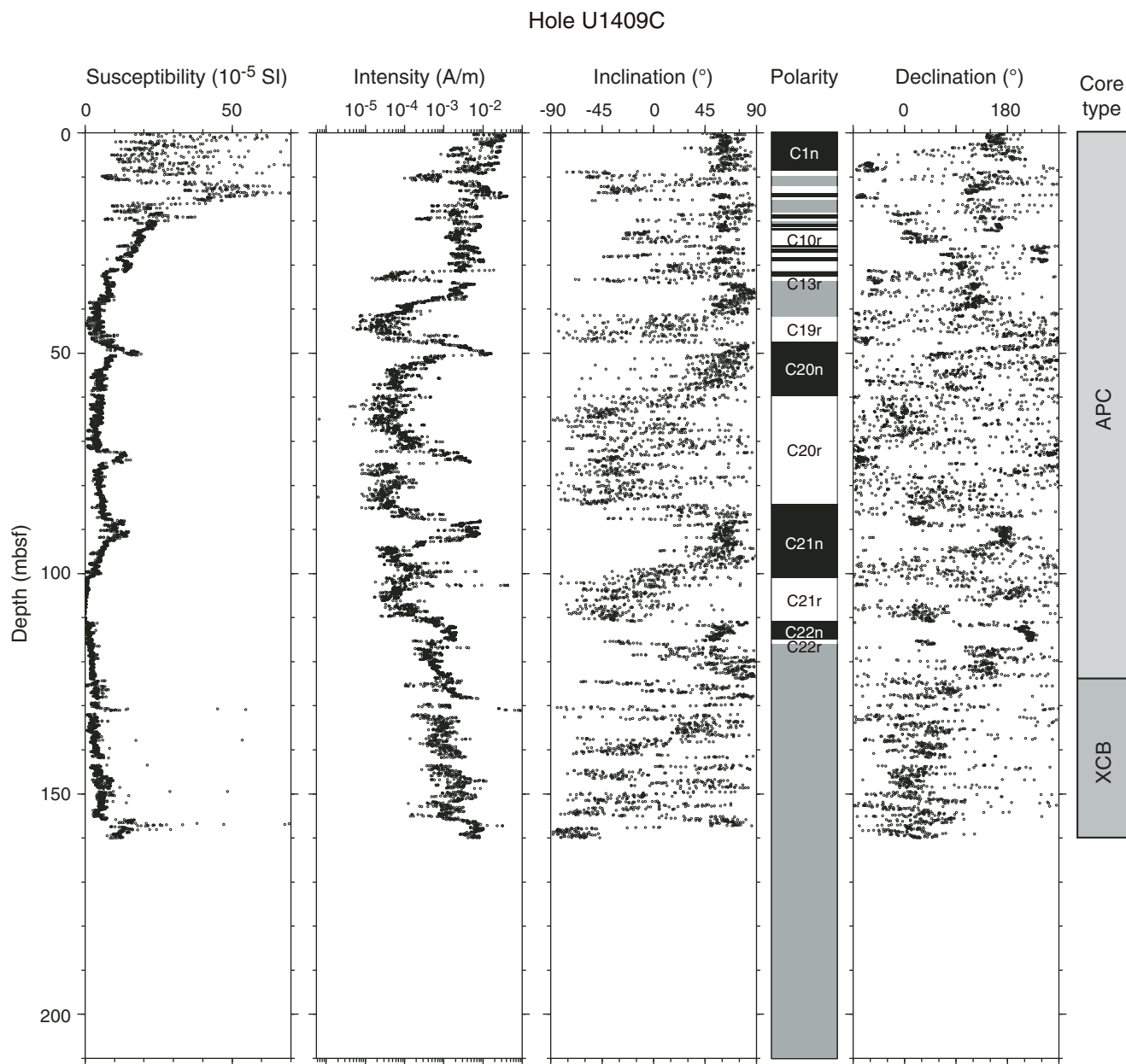


Figure F27. Plots of representative alternating field (AF) demagnetization results for discrete paleomagnetism samples, Site U1409. Upper plots show intensity variation with progressive demagnetization, and lower plots show vector endpoints of paleomagnetism directions on orthogonal vector diagrams (i.e., Zijderveld plots). Vector diagrams indicate reasonably resolved calculate the characteristic remanent magnetization (ChRM) directions for the (A) normal and (B) reversed chronos from the APC core intervals, whereas (C) some samples do not show stable component. Solid circles = horizontal projections, open circles = vertical projections, gray circles = data not used to calculate ChRM direction, black dashed line = ChRM direction. Inc = inclination, Dec = declination, MAD = maximum angle of deviation.

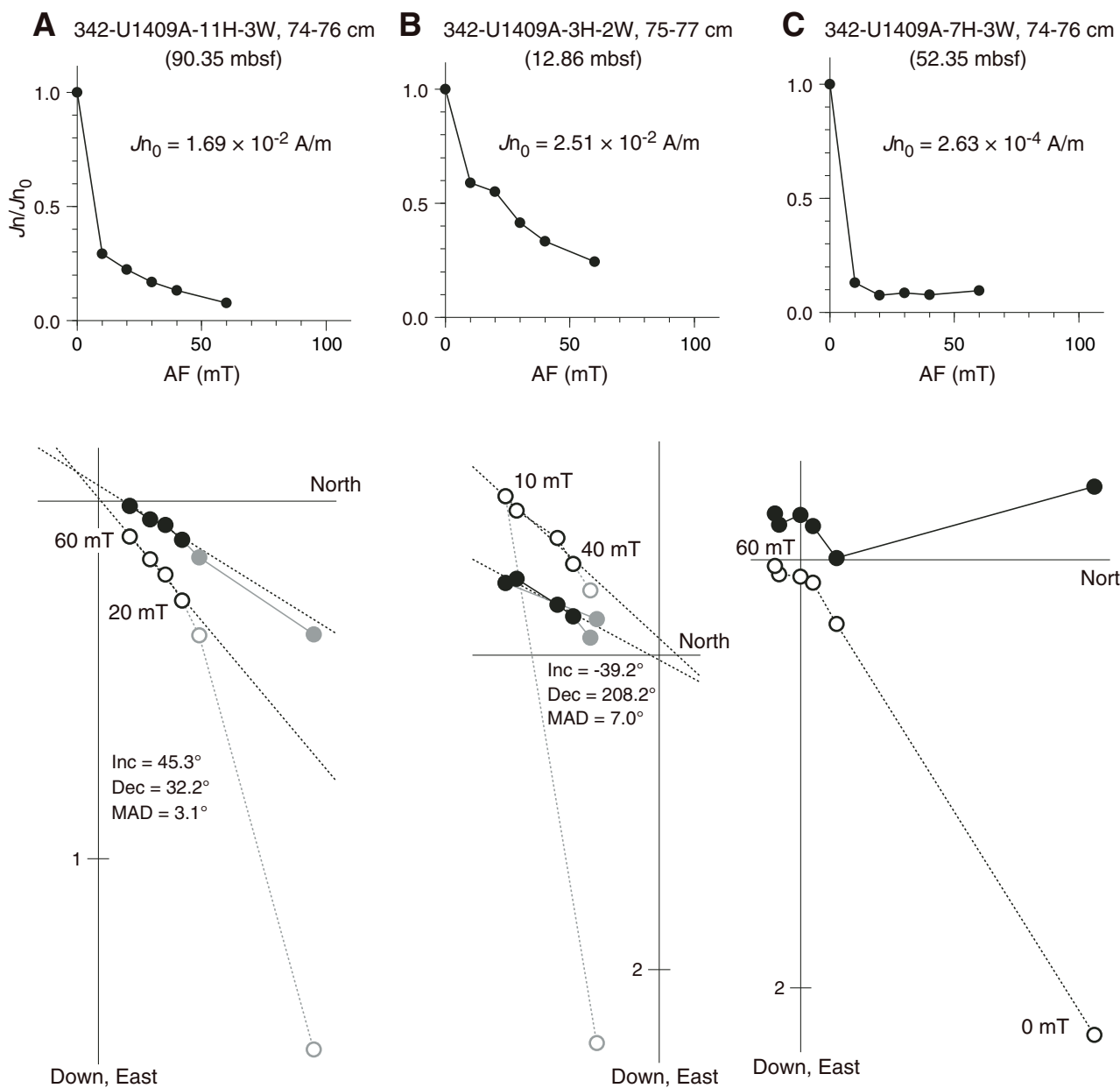


Figure F28. Illustration of magnetostratigraphy, Site U1409. Core recovery: black = recovered, white = not recovered, red = core overlap.

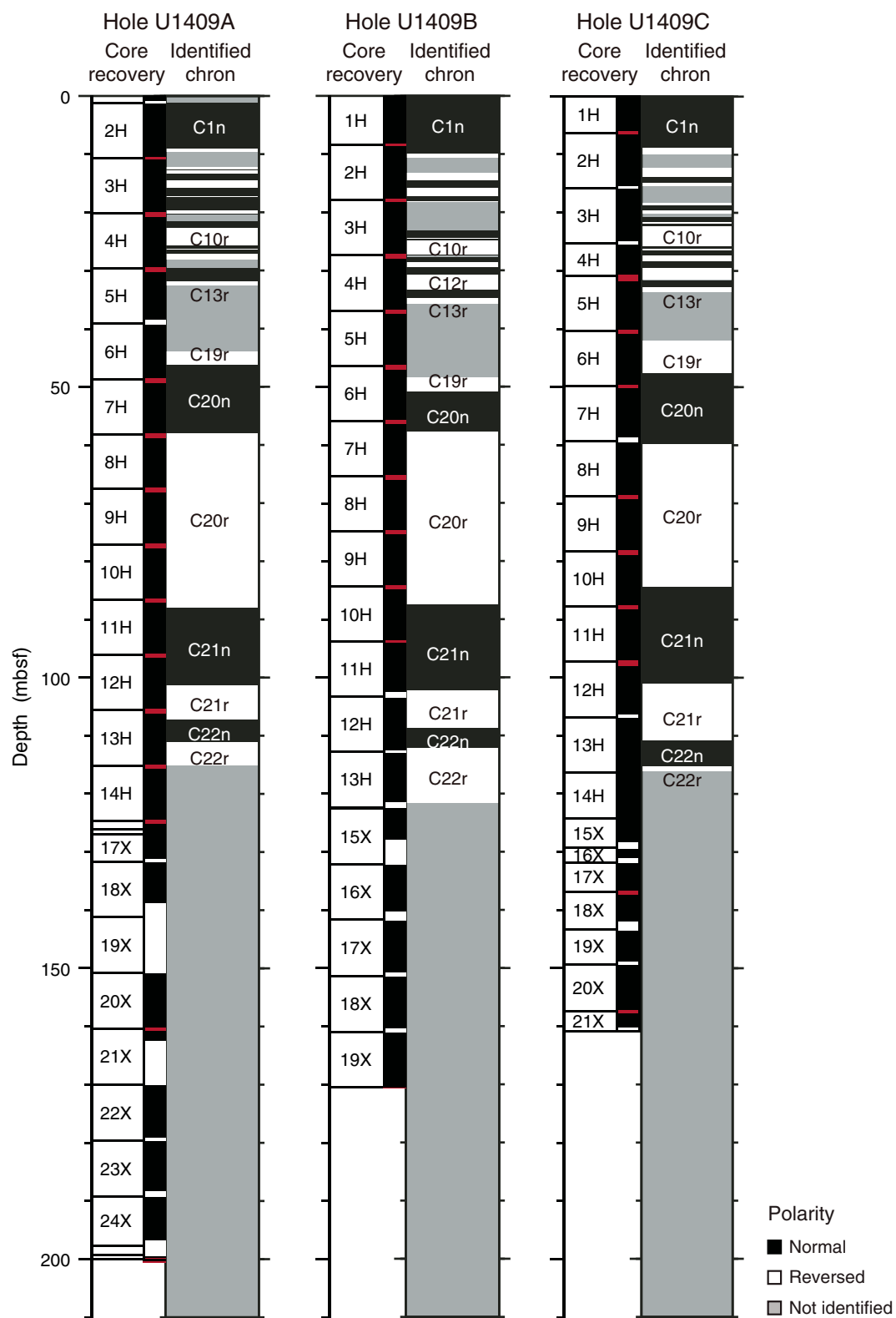




Figure F29. Plots of anisotropy of magnetic susceptibility vs. depth, Hole U1409A. Separation of eigenvalues is related to the shape and degree of the magnetic fabric (see “**Paleomagnetism**” in the “Methods” chapter [Norris et al., 2014a]). For example, if τ_1 and τ_2 are close or indistinguishable but distinct from τ_3 , then the bulk fabric is oblate. Lithostratigraphic units are described in “**Lithostratigraphy**.” Eigenvalues: τ_1 = maximum, τ_2 = intermediate, τ_3 = minimum. V_3 = minimum eigenvector, P = degree of anisotropy (τ_1/τ_3). APC = advanced piston corer, XCB = extended core barrel.

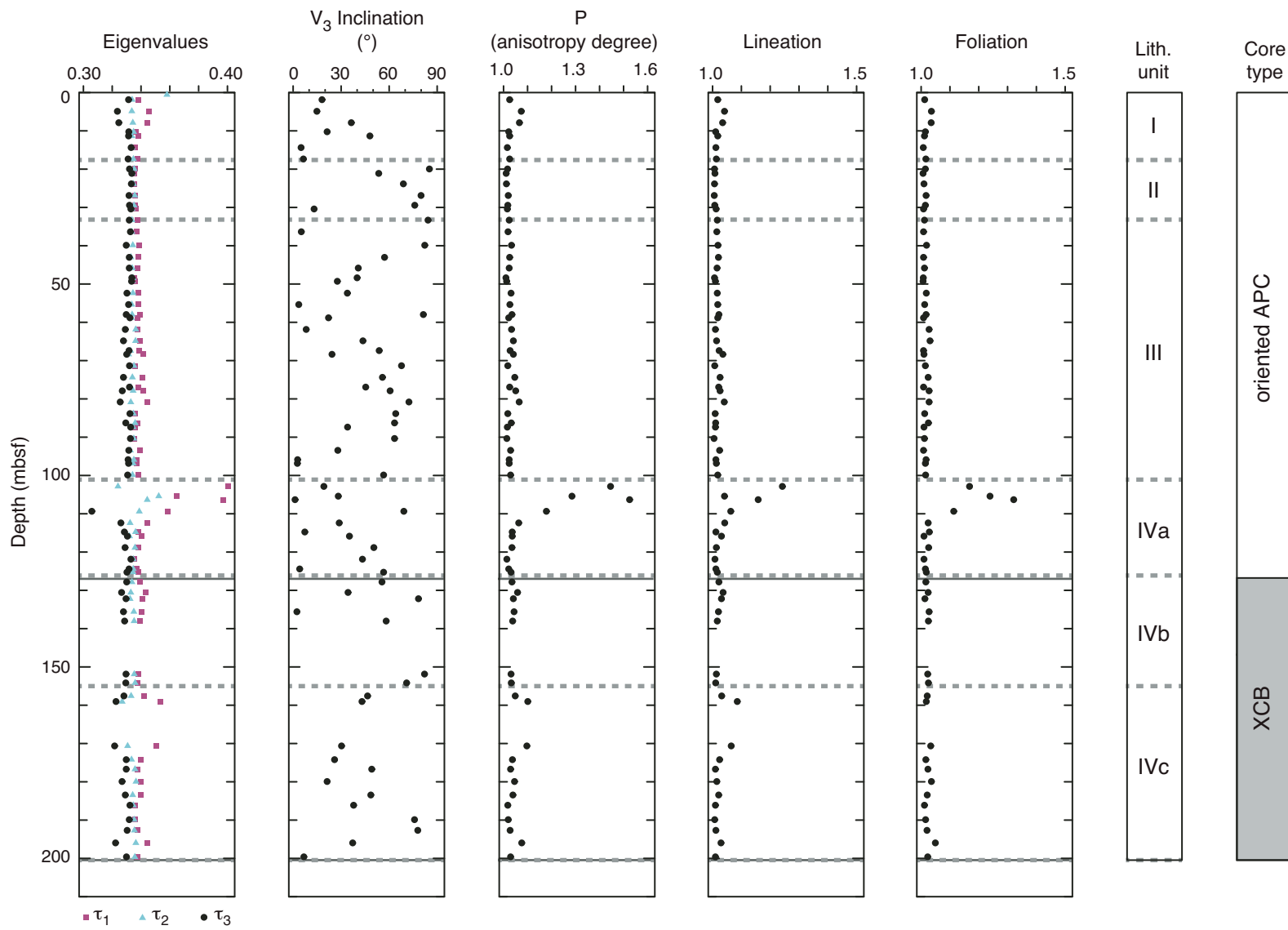


Figure F30. Age-depth model for Hole U1409A showing biostratigraphic and magnetostratigraphic datums. Also shown are estimated linear sedimentation rates for line segments based on the datums listed in Table T17.

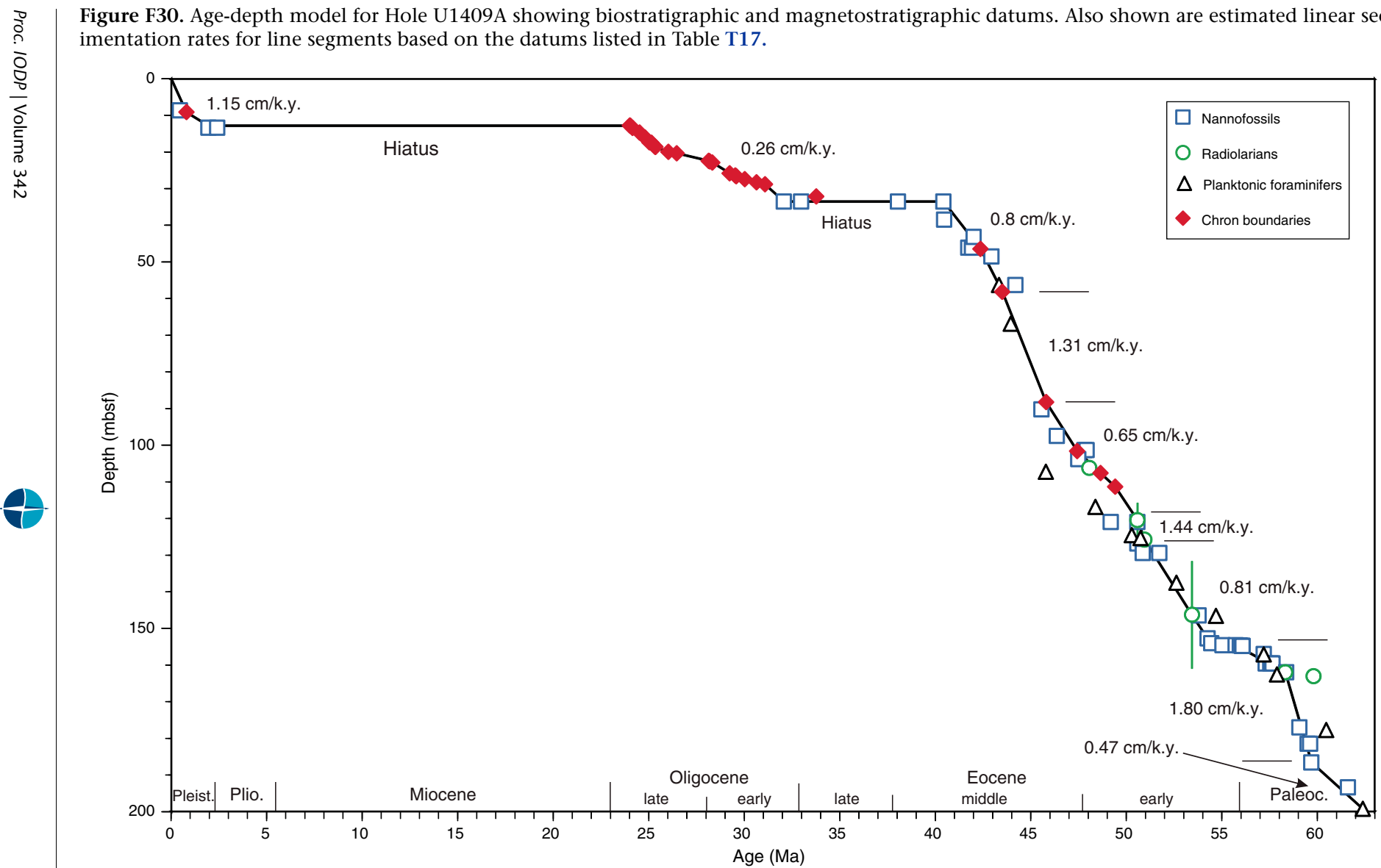


Figure F31. Linear sedimentation rate (LSR), dry bulk density (DBD), carbonate content, and mass accumulation rate (MAR) at a 200 k.y. time step, Hole U1409A. Solid black diamonds show the inflection points in estimated LSR, DBD, and carbonate content. Geologic ages are shown on the GTS2012 timescale (Gradstein et al., 2012). CAR = carbonate mass accumulation rate, nCAR = noncarbonate mass accumulation rate.

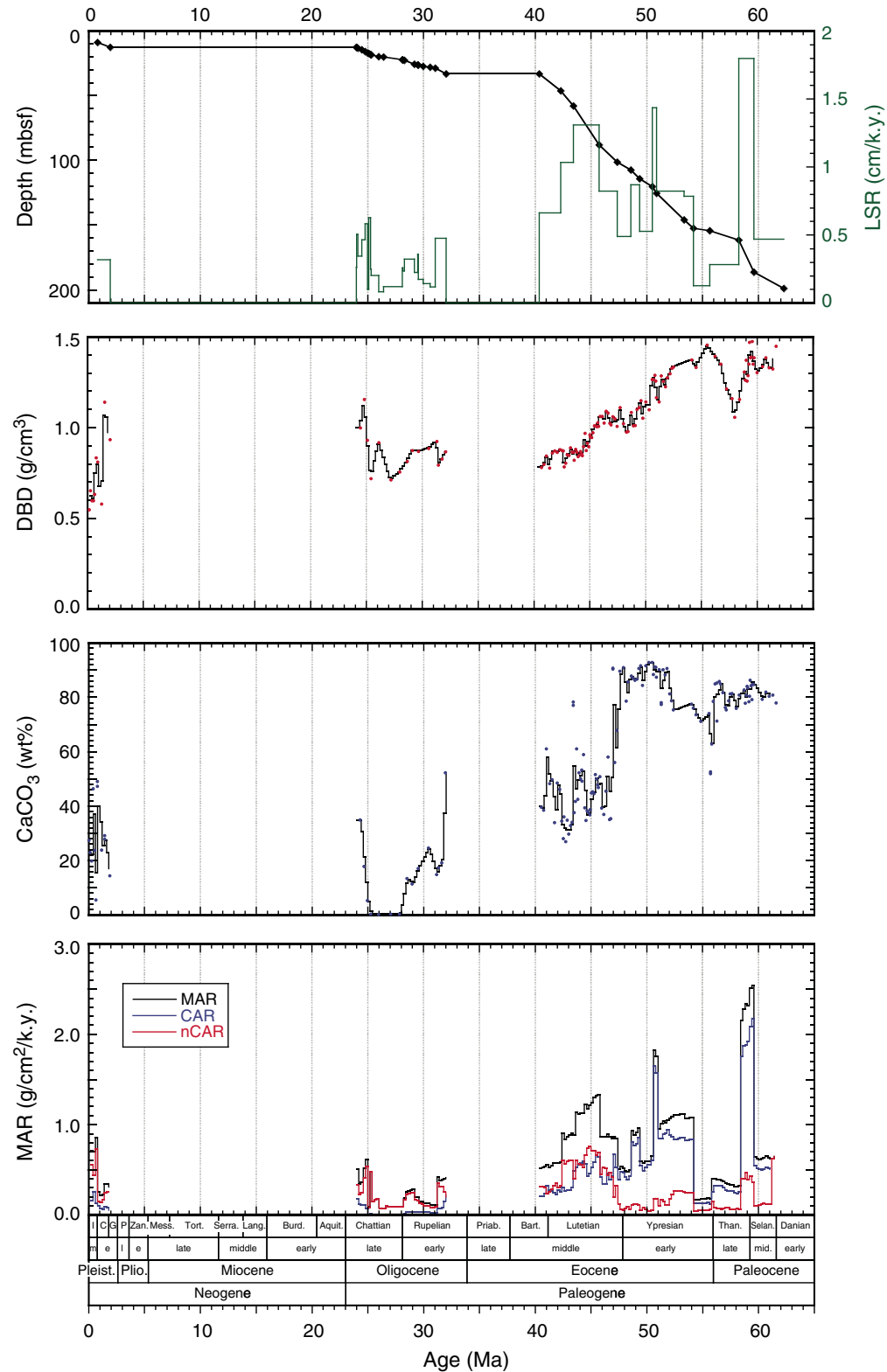


Figure F32. Plots of interstitial water constituent concentrations, Hole U1409A.

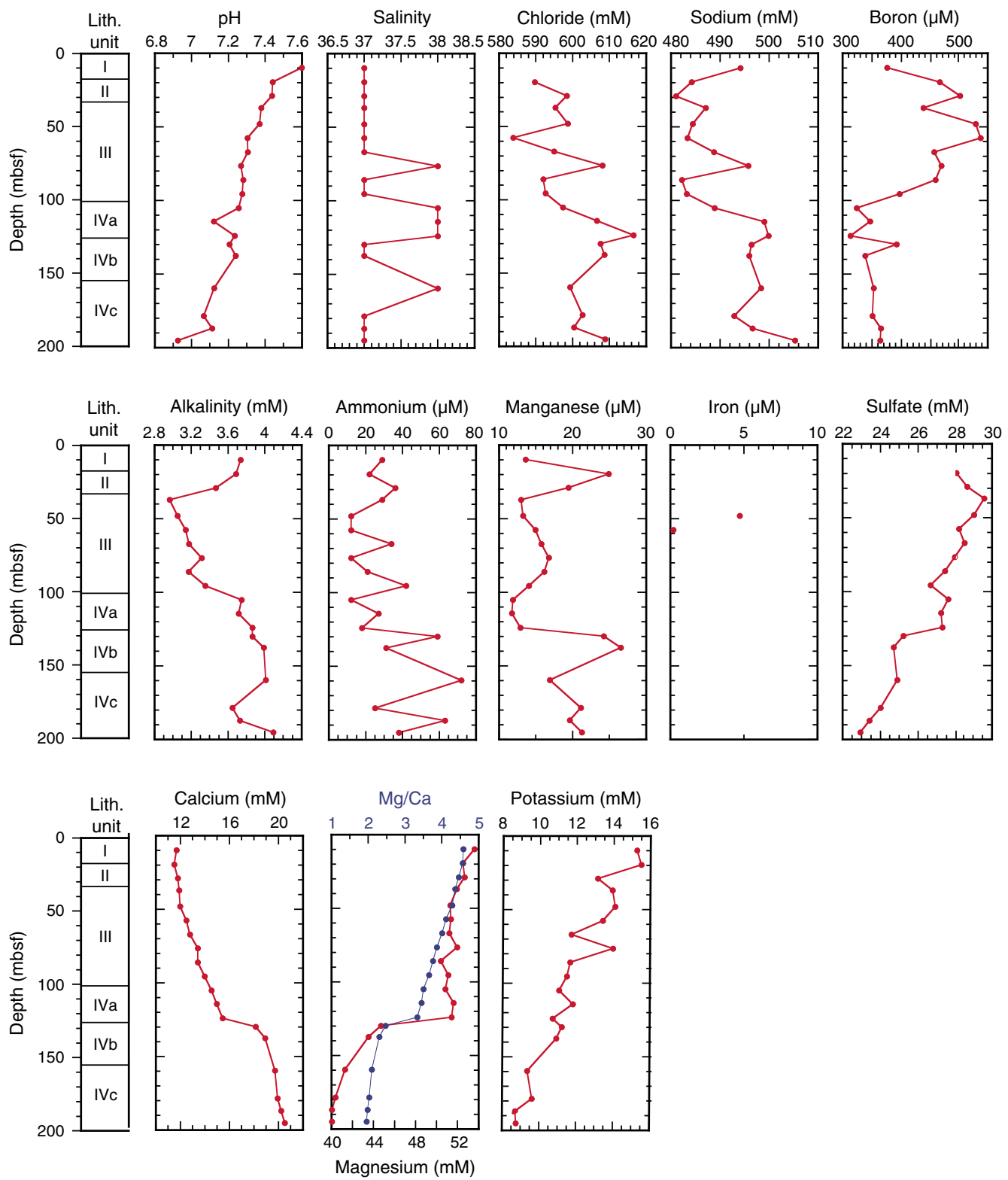




Figure F33. Plots of sedimentary carbonate, total organic carbon (TOC), and total nitrogen contents in Hole U1409A (red) and sedimentary carbonate content in Holes U1409B (blue) and U1409C (green). Core recovery: black = recovered, white = not recovered, red = core overlap.

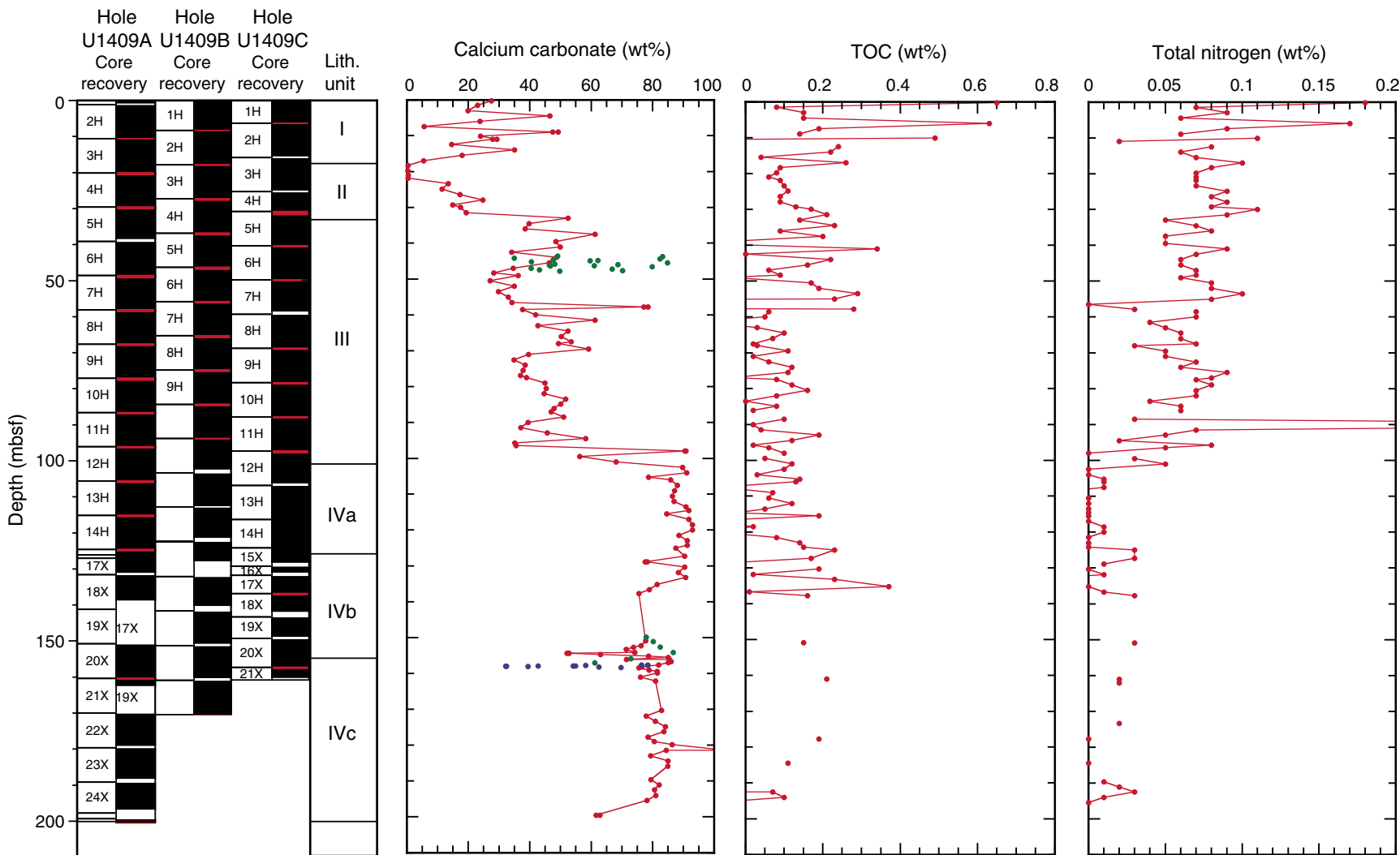


Figure F34. Core image of the Paleocene/Eocene boundary and plots of carbonate content, magnetic susceptibility, and sediment lightness (L^*), Hole U1409B.

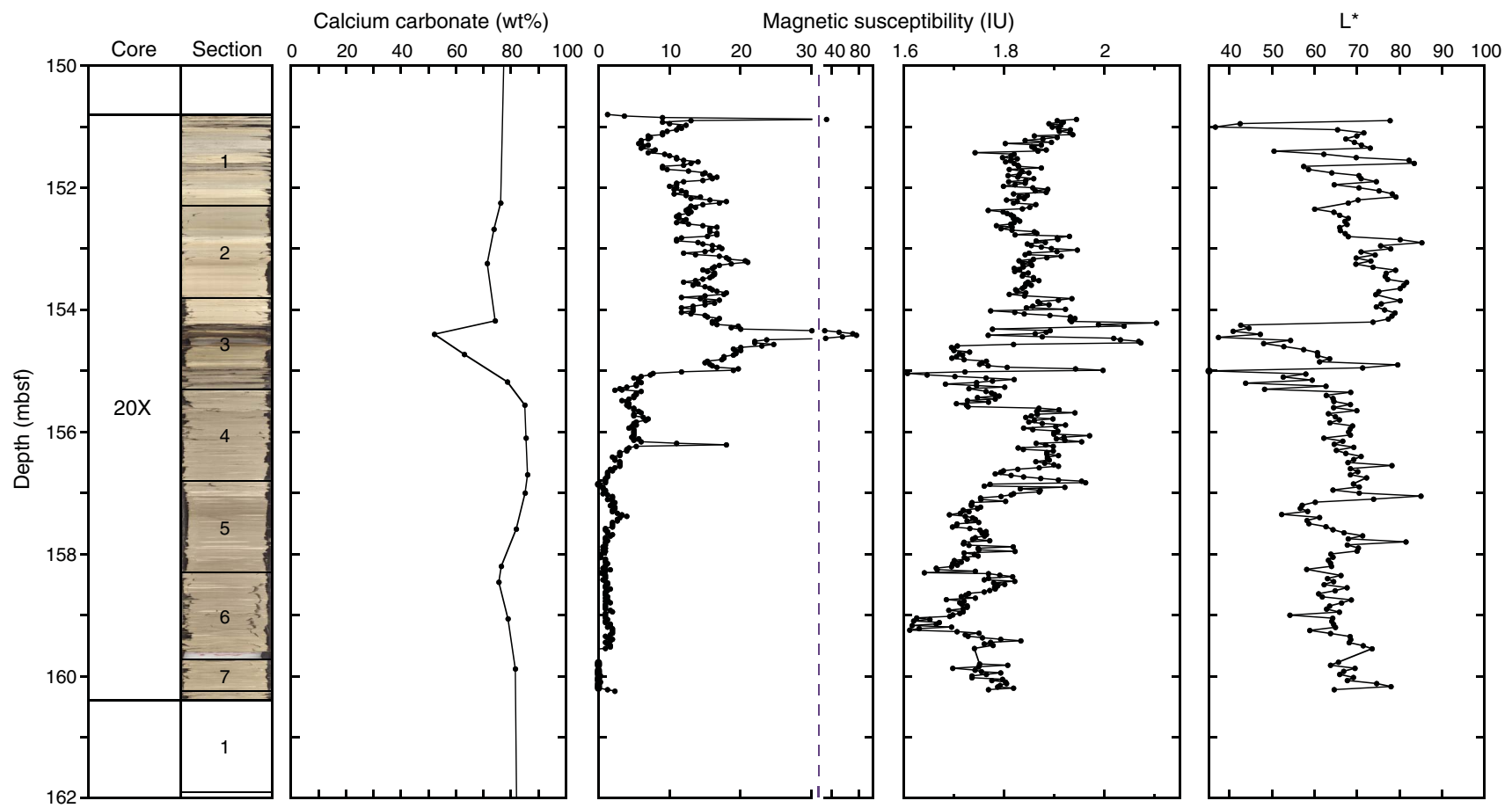


Figure F35. Plot of source rock pyrolysis hydrogen index and T_{\max} values for lithostratigraphic Unit III and Sub-units Iva–IVc. Fields for Types I (waxy), II (algal/microbial), and III (land plant/detrital) organic matter are shown. Compositions of sediment at Site U1409 are dominated by thermally immature algal/microbial and detrital organic matter.

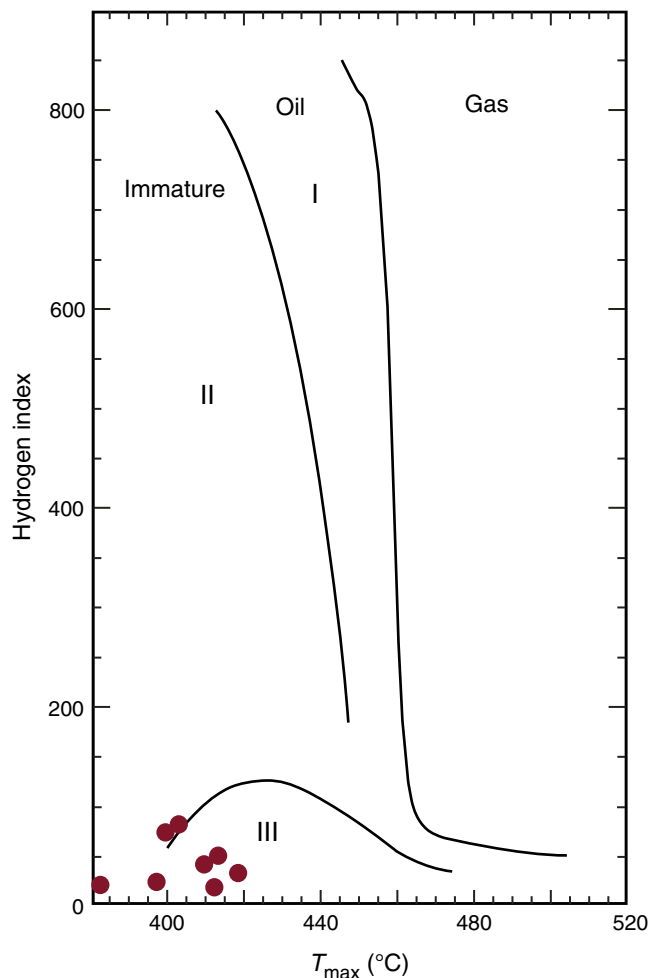


Figure F36. Plots of magnetic susceptibility (MS), bulk density (gray line = gamma ray attenuation density from Whole-Round Multisensor Logger, black circles = moisture and density analysis from discrete samples), porosity, water content, and grain density, Site U1409. Core recovery: black = recovered, white = not recovered, red = core overlap. Horizontal gray lines indicate lithostratigraphic unit boundaries (see “[Lithostratigraphy](#)”). APC = advanced piston corer, XCB = extended core barrel.

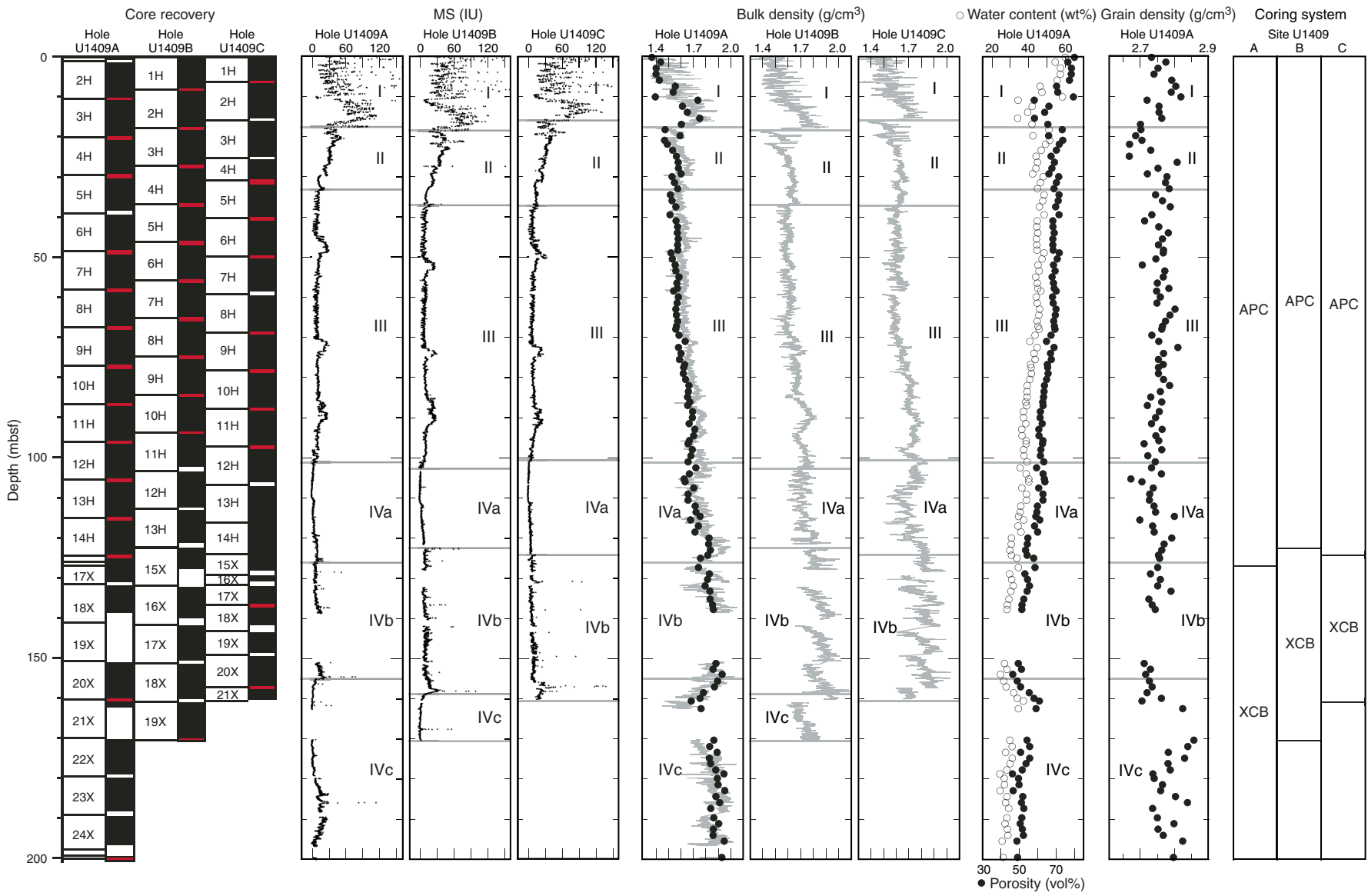


Figure F37. Plots of magnetic susceptibility (MS), *P*-wave velocity (gray line = *P*-wave logger data from whole-round sections, black circles = *P*-wave caliper probe data from working section halves), and natural gamma radiation (NGR), Site U1409. Core recovery: black = recovered, white = not recovered, red = core overlap. Horizontal gray lines indicate lithostratigraphic unit boundaries (see “[Lithostratigraphy](#)”). APC = advanced piston corer, XCB = extended core barrel.

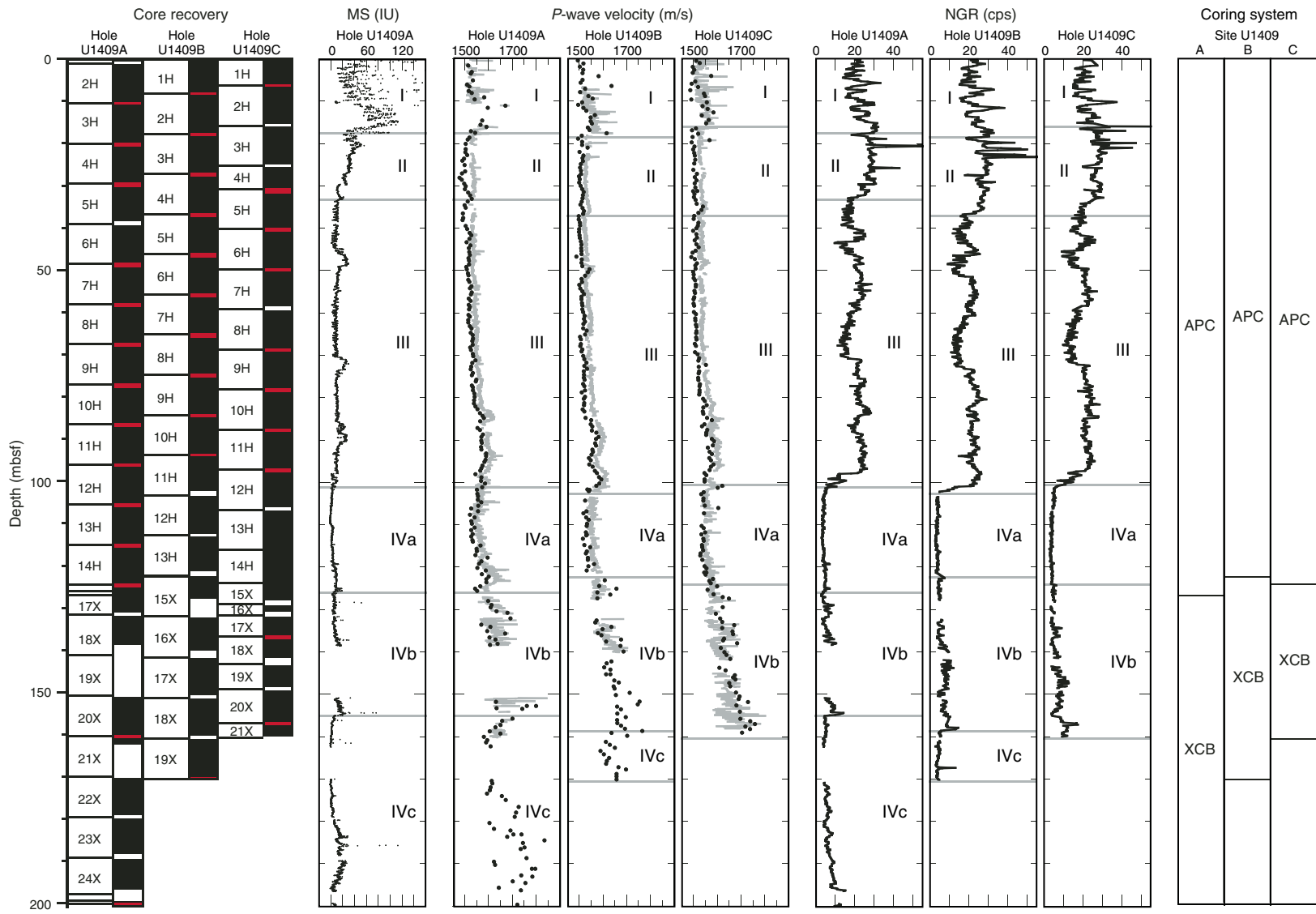


Figure F38. Plots of magnetic susceptibility (MS) and color reflectance (a^* , b^* , and L^*), Site U1409. Core recovery: black = recovered, white = not recovered, red = core overlap. Horizontal gray lines indicate lithostratigraphic unit boundaries (see “[Lithostratigraphy](#)”). APC = advanced piston corer, XCB = extended core barrel.

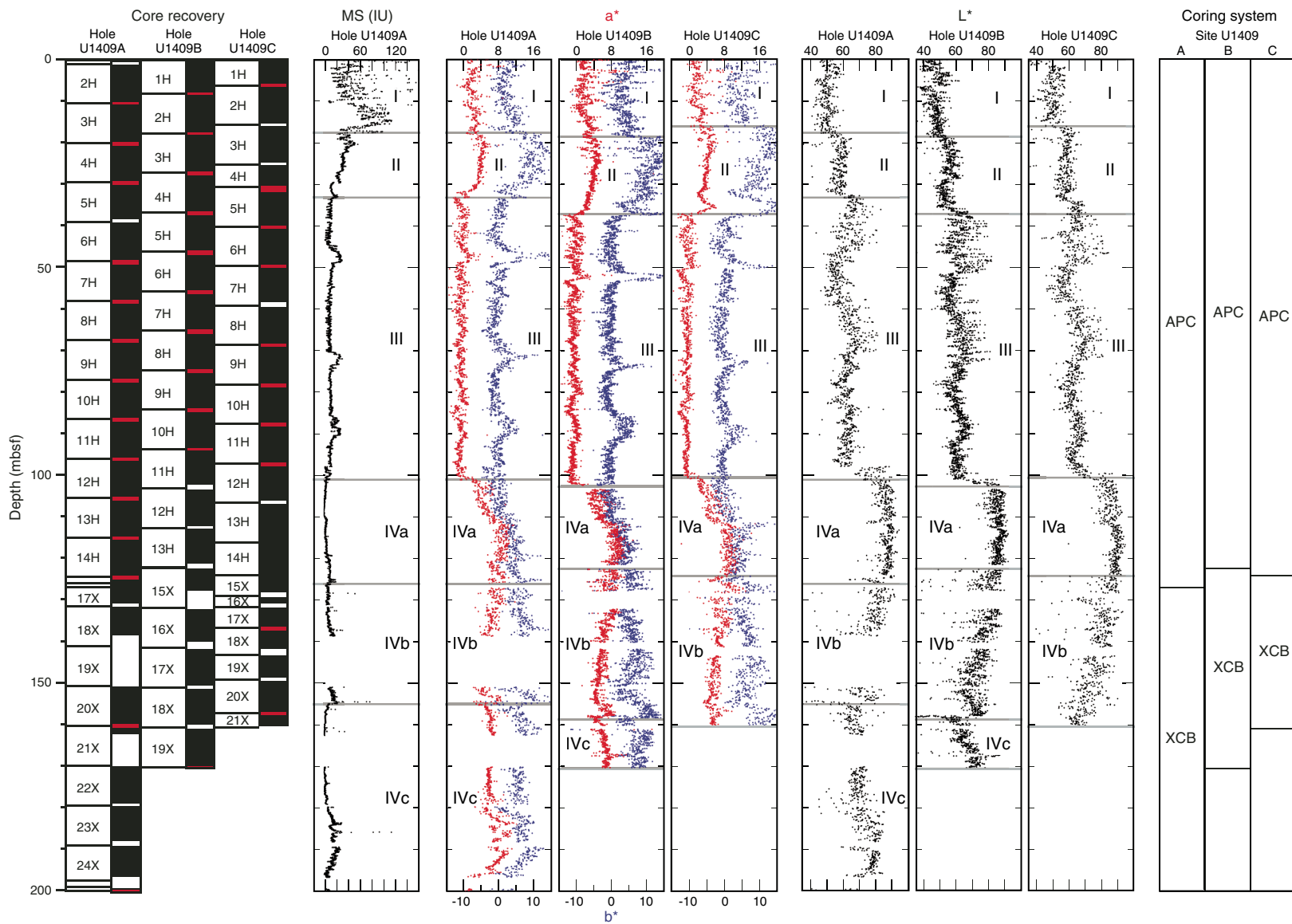


Figure F39. Plots of thermal conductivity measurements, Site U1409. Core recovery: black = recovered, white = not recovered, red = core overlap. Blue lines are the smooth-curve fits for these data sets. Horizontal gray lines indicate lithostratigraphic unit boundaries (see “[Lithostratigraphy](#)”).

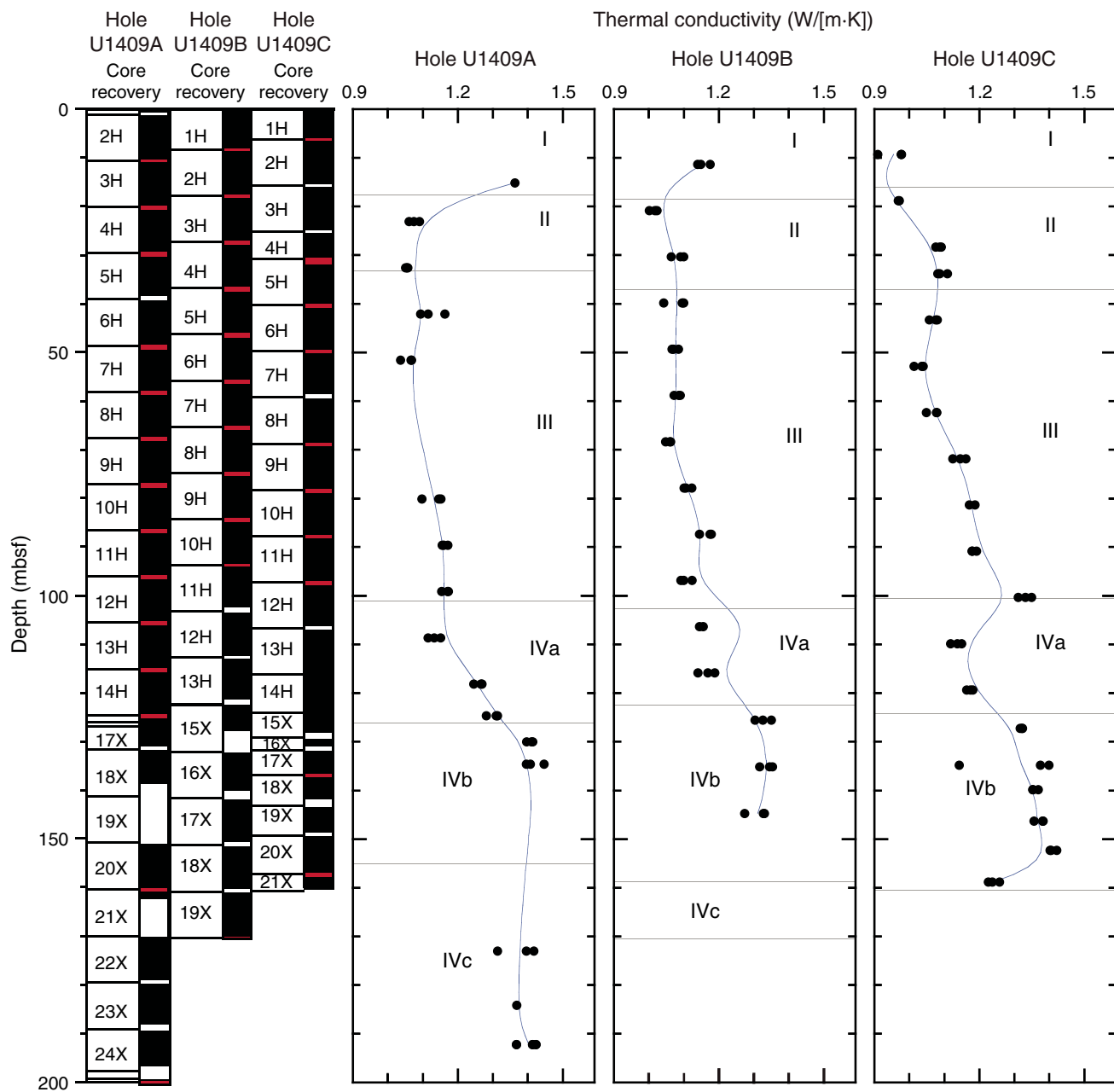


Figure F40. Plot of thermal conductivity vs. gamma ray attenuation (GRA) bulk density, Hole U1409A. Black line is the linear-curve fit for this data set, and R^2 is the correlation coefficient.

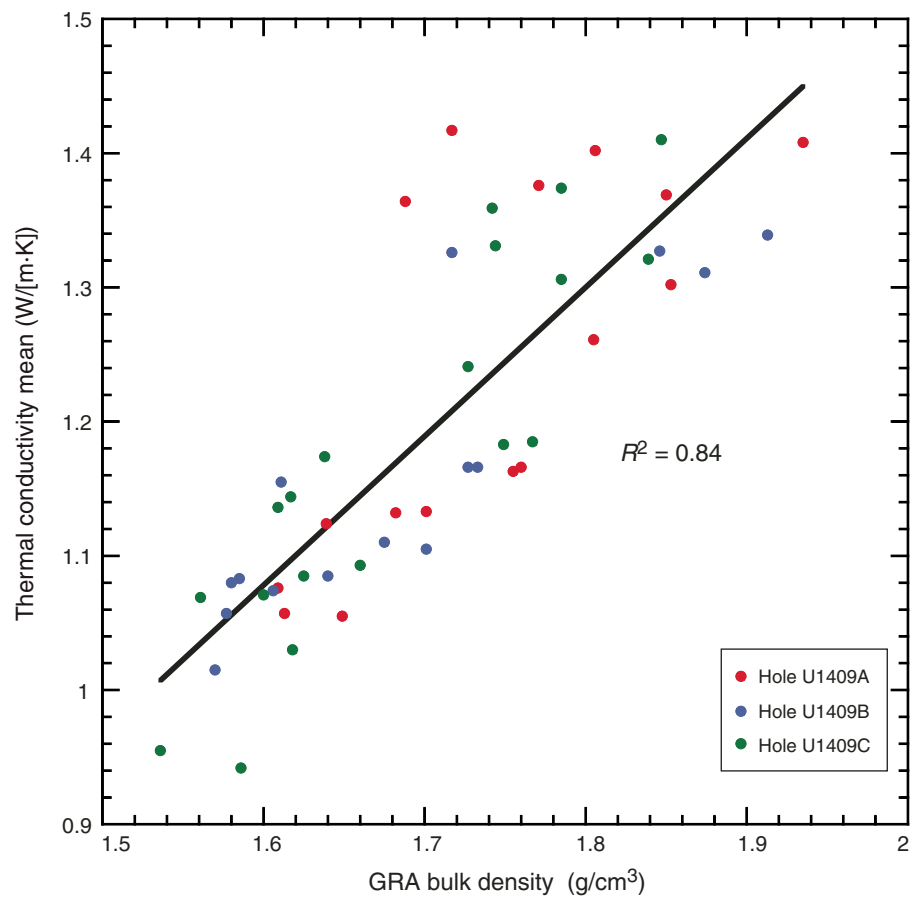


Figure F41. Plots of magnetic susceptibility data, Site U1409. Top panels show the spliced section for each interval of the splice. Bottom panels show all complete magnetic susceptibility data sets. Data from Holes U1409B and U1409C are offset by 10 and 20 IU, respectively, to aid visualization. Open circles indicate core tops. A. 0–50 m CCSF. (Continued on next four pages.)

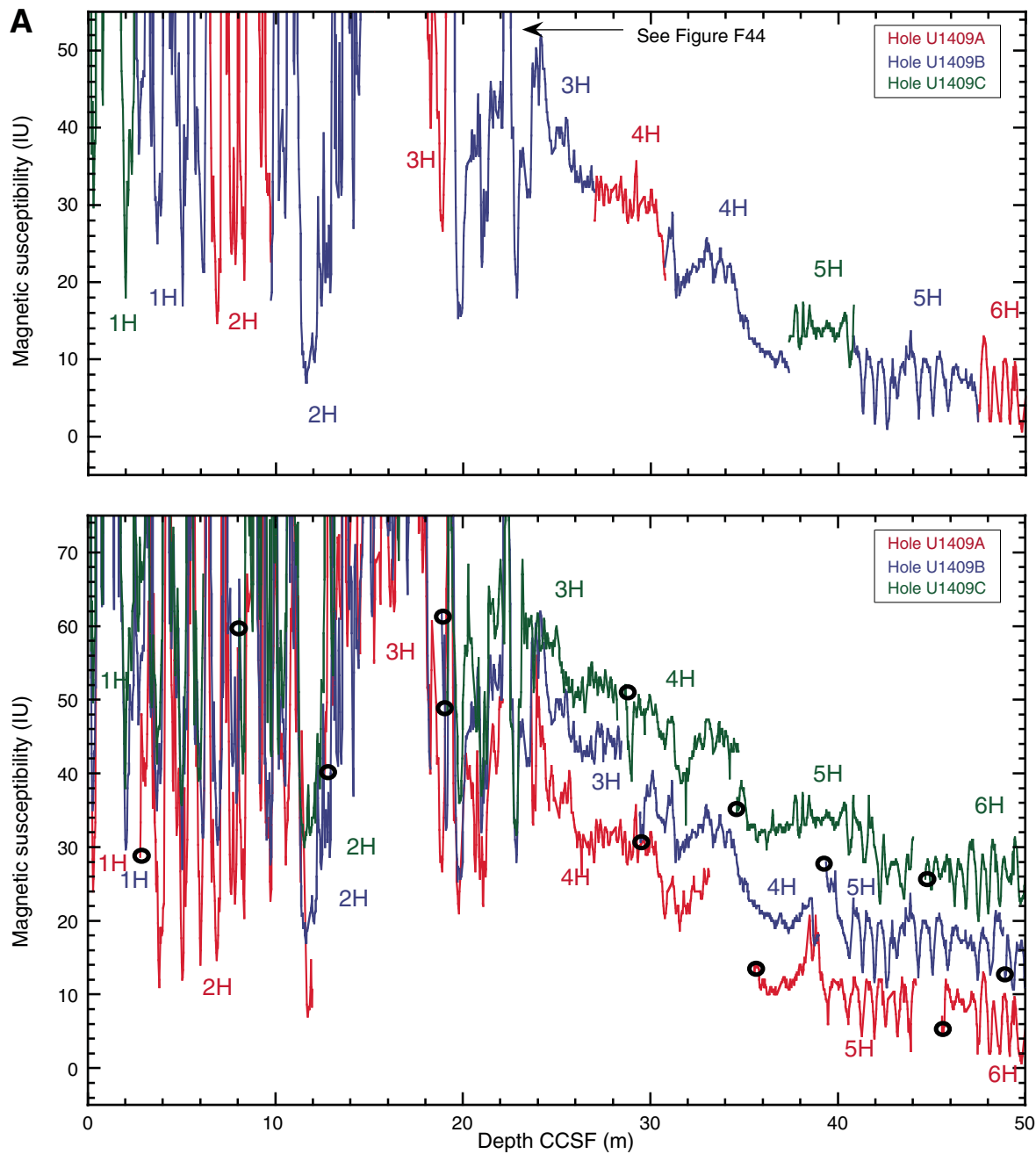


Figure F41 (continued). B. 50–100 m CCSF. (Continued on next page.)

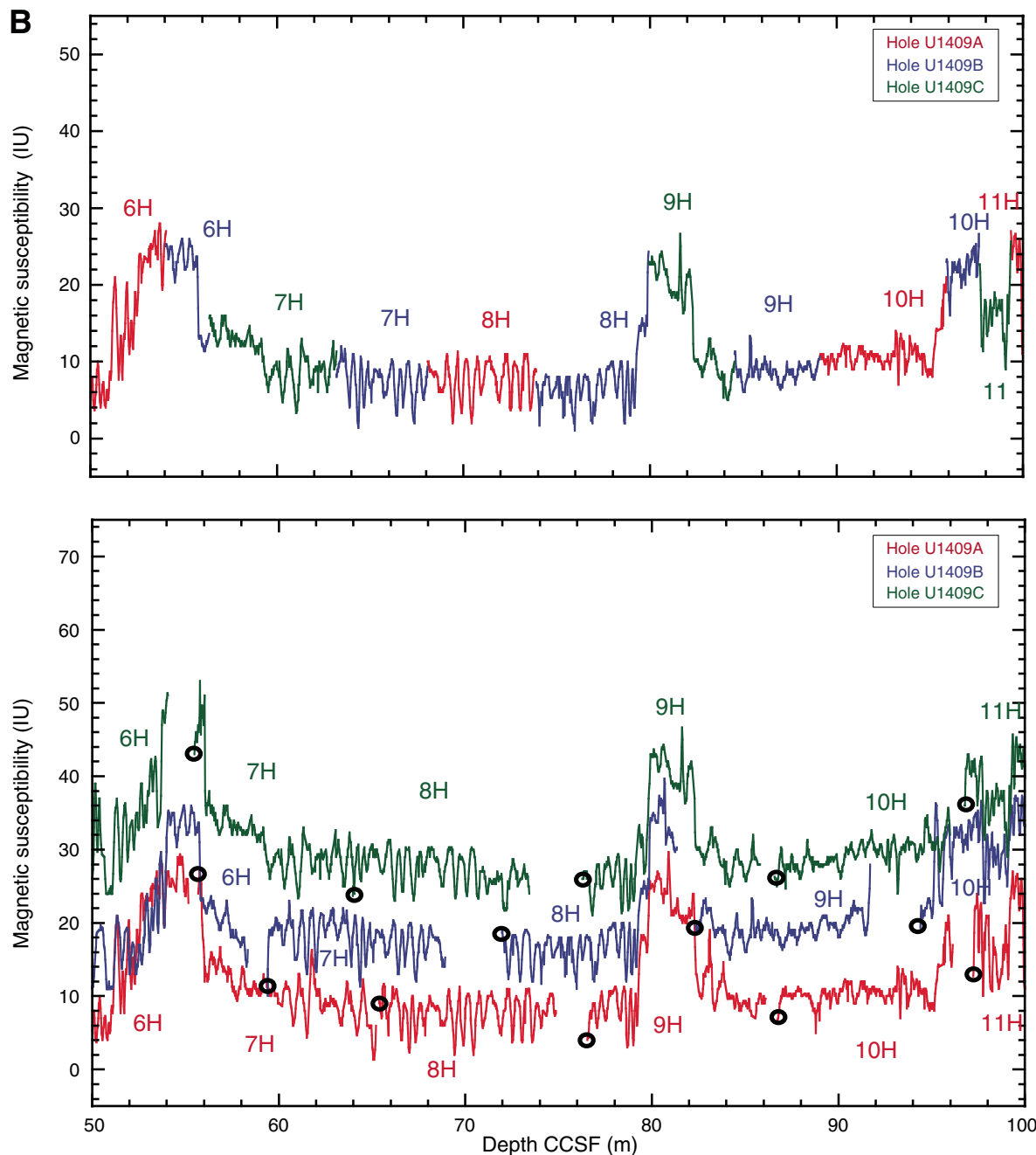


Figure F41 (continued). C. 100–150 m CCSF. (Continued on next page.)

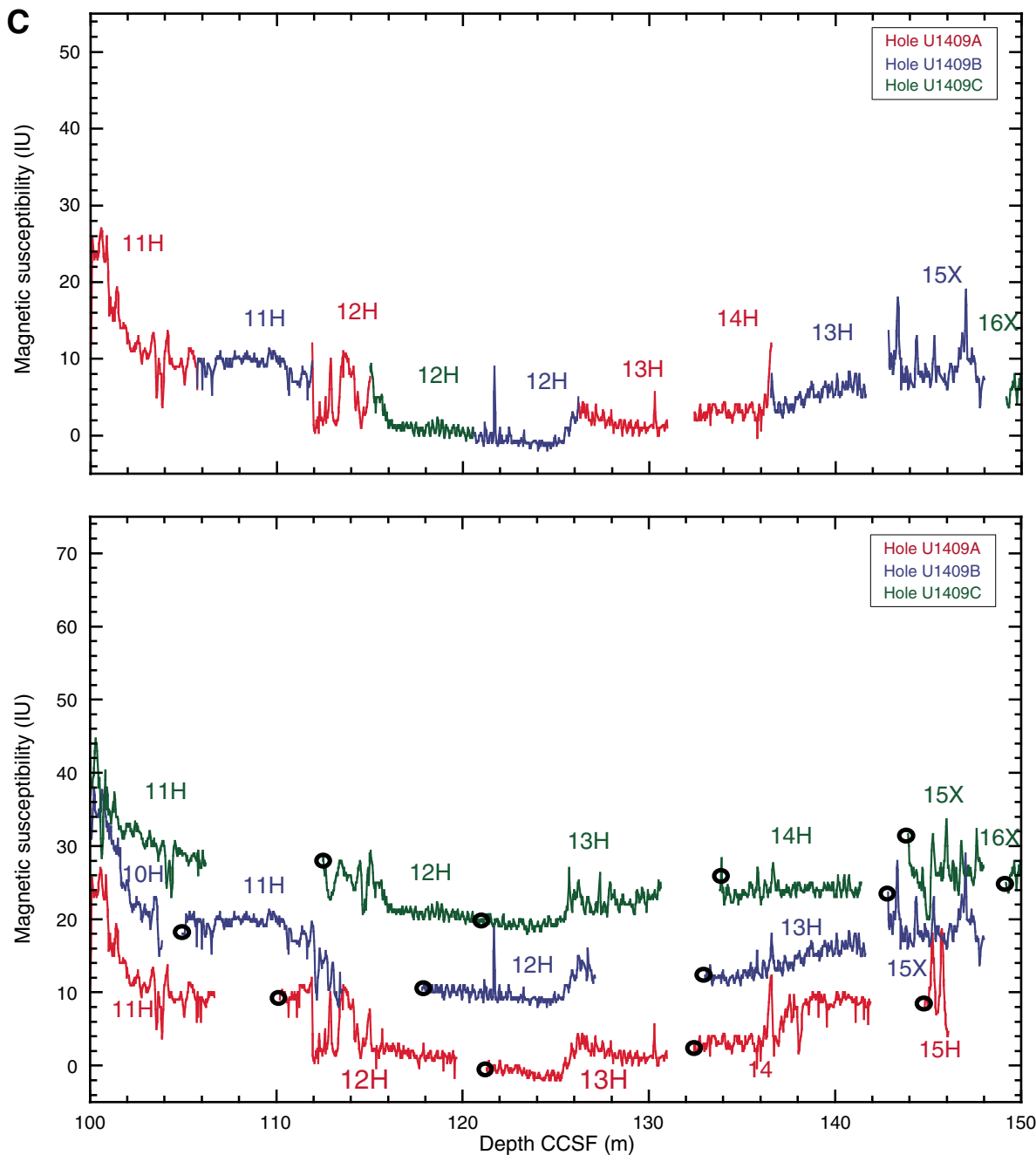


Figure F41 (continued). D. 150–200 m CCSF. (Continued on next page.)

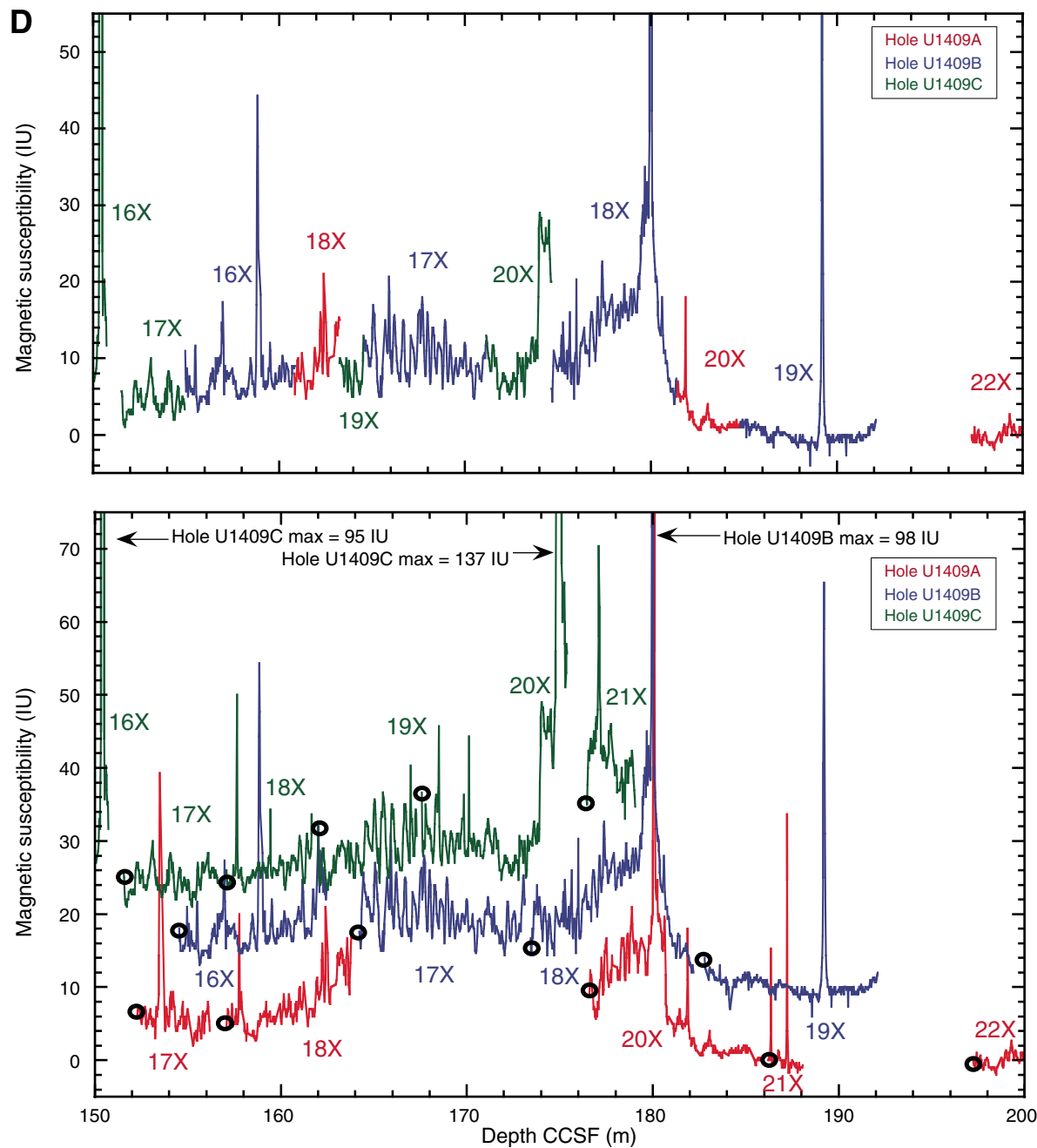


Figure F41 (continued). E. 200–250 m CCSF.

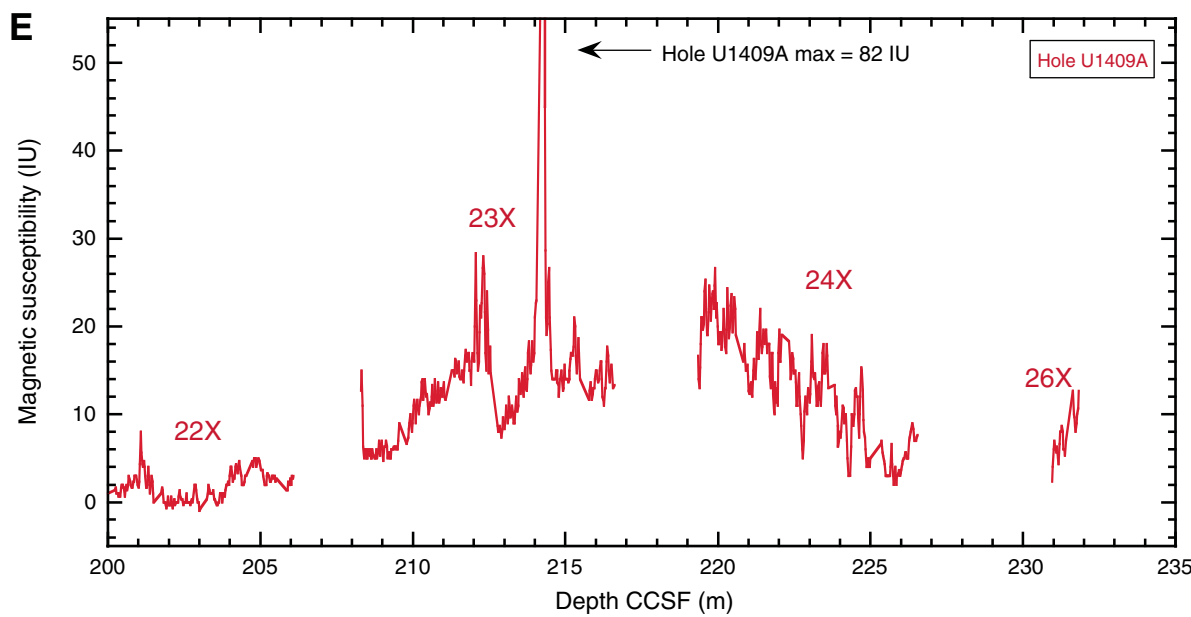


Figure F42. Plot of mbsf depth vs. CCSF depth, Site U1409. Growth factors are equal to the slopes of the regression lines.

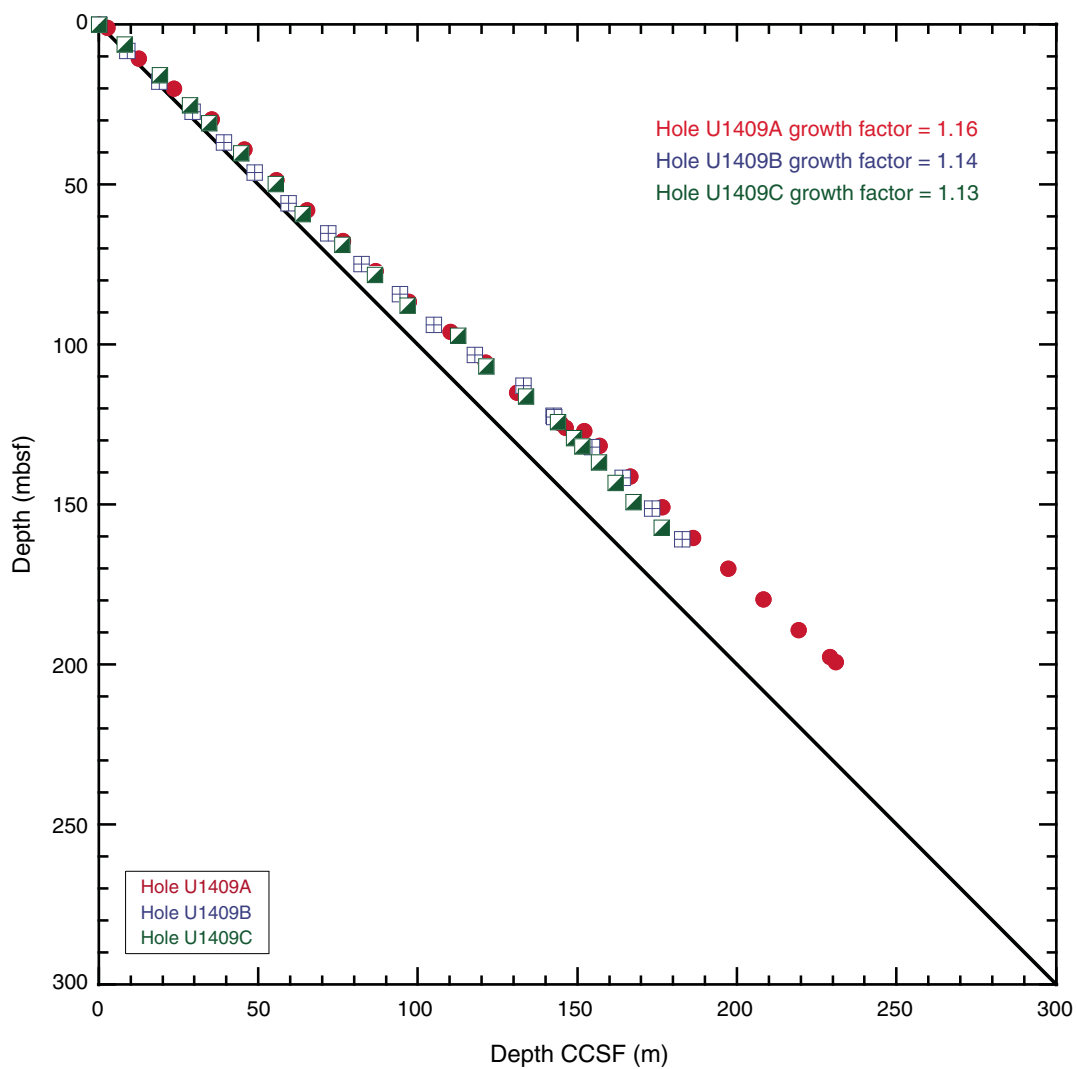


Figure F43. Plots of natural gamma radiation (NGR) data, Site U1409. Data from Holes U1409B and U1409C are offset by 10 and 20 cps, respectively, to aid visualization. Open circles indicate core tops.

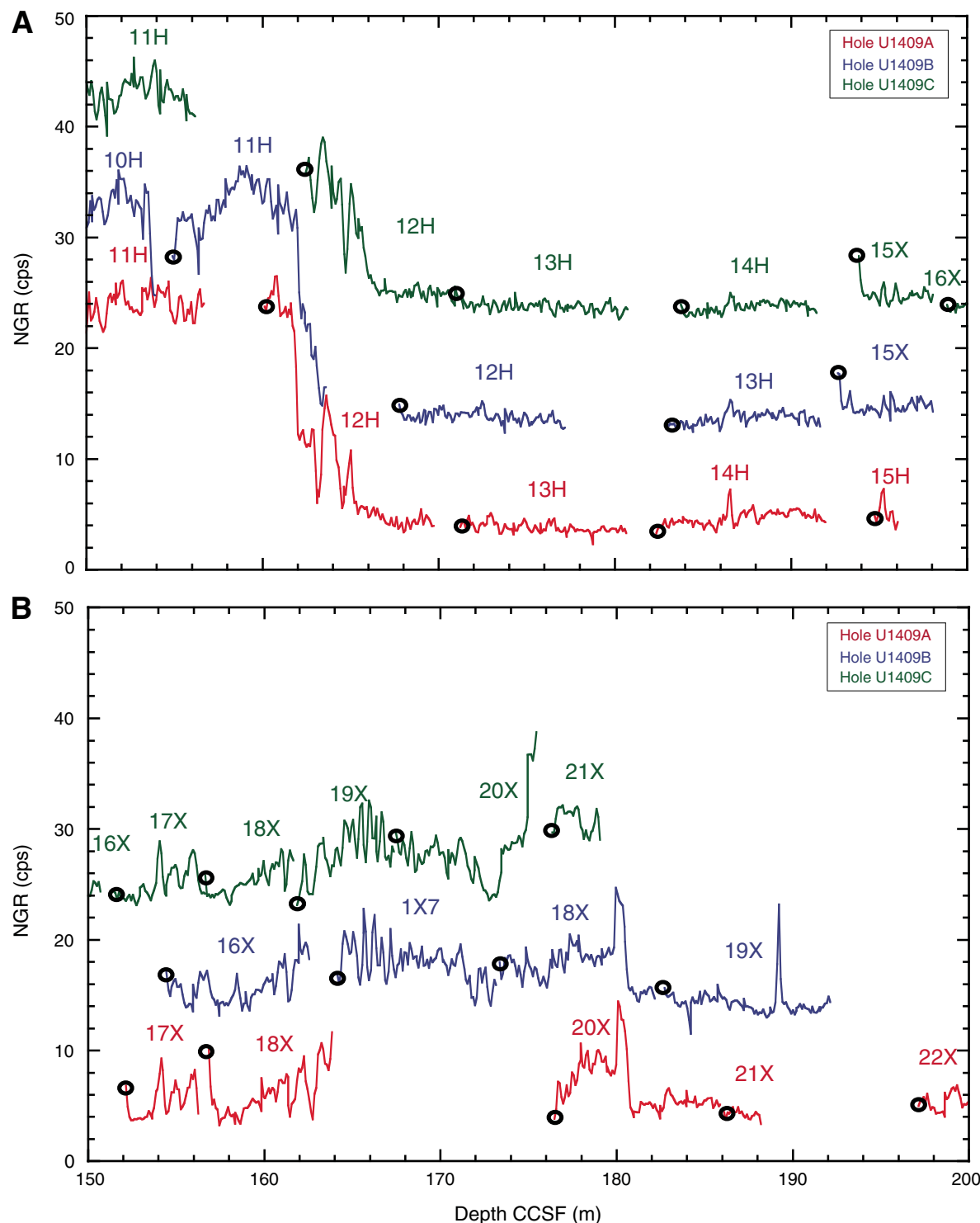


Figure F44. Plots of magnetic susceptibility data showing large-amplitude cycles in magnetic susceptibility, Site U1409. Top panel shows the splice section, and bottom panel shows all complete magnetic susceptibility data sets.

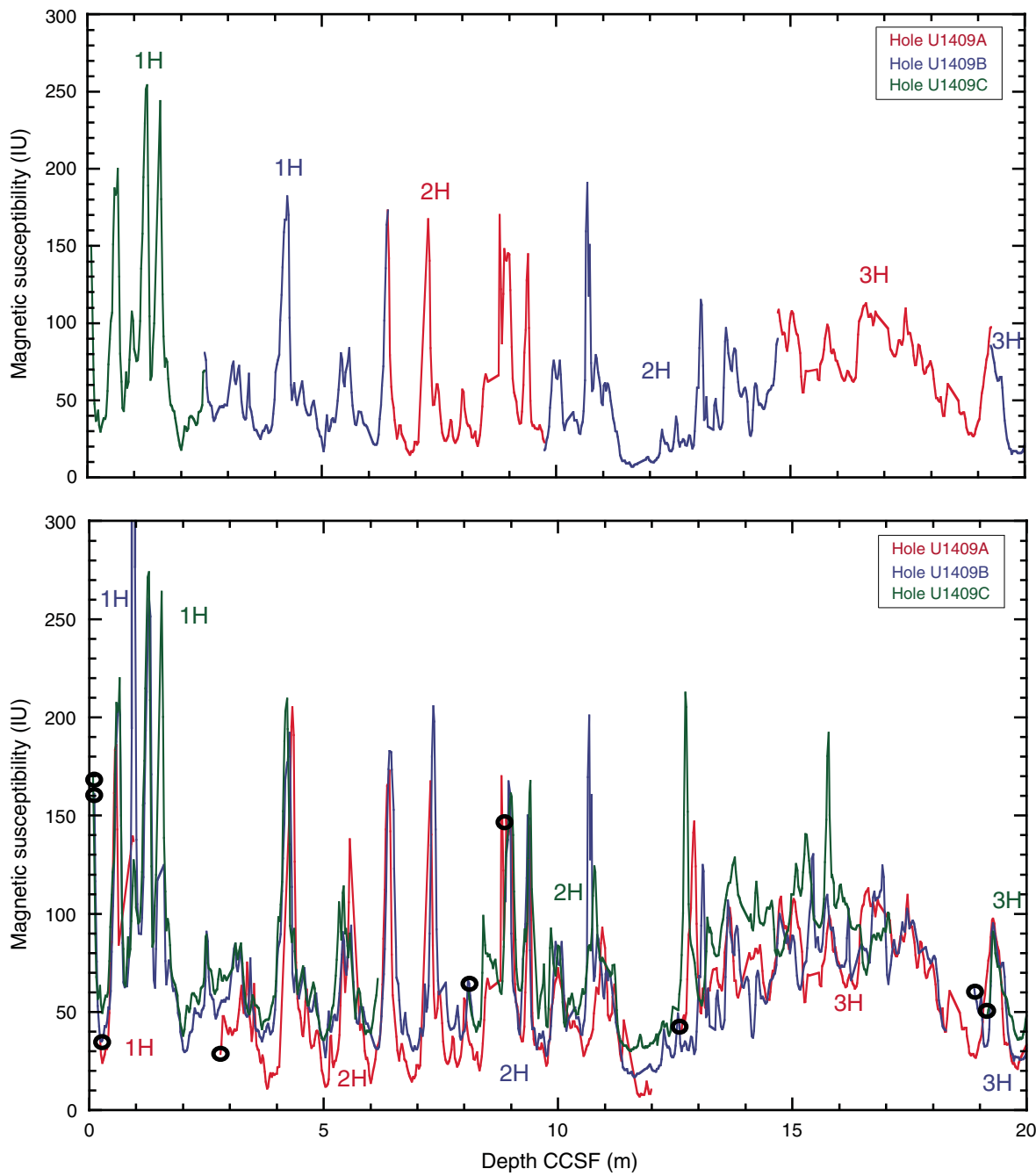


Table T1. Coring summary, Site U1409. (Continued on next page.)

Core	Date (2012)	Time UTC (h)	Depth DSF (m)				Depth CSF-A (m)			
			Top of cored interval	Bottom of cored interval	Interval cored (m)	Curated length (m)	Top of core	Bottom of core	Recovery (%)	Sections (N)
342-U1409A-										
1H	17 Jul	0055	0.0	1.1	1.1	1.07	0.00	1.07	97	2
2H	17 Jul	0205	1.1	10.6	9.5	9.57	1.10	10.67	101	8
3H	17 Jul	0255	10.6	20.1	9.5	10.04	10.60	20.64	106	8
4H	17 Jul	0350	20.1	29.6	9.5	10.03	20.10	30.13	106	8
5H	17 Jul	0440	29.6	39.1	9.5	9.14	29.60	38.74	96	7
6H	17 Jul	0530	39.1	48.6	9.5	10.12	39.10	49.22	107	8
7H	17 Jul	0620	48.6	58.1	9.5	9.98	48.60	58.58	105	8
8H	17 Jul	0710	58.1	67.6	9.5	9.95	58.10	68.05	105	8
9H	17 Jul	0800	67.6	77.1	9.5	10.05	67.60	77.65	106	8
10H	17 Jul	0855	77.1	86.6	9.5	9.86	77.10	86.96	104	8
11H	17 Jul	0945	86.6	96.1	9.5	9.85	86.60	96.45	104	8
12H	17 Jul	1040	96.1	105.6	9.5	9.91	96.10	106.01	104	8
13H	17 Jul	1130	105.6	115.1	9.5	9.91	105.60	115.51	104	8
14H	17 Jul	1225	115.1	124.6	9.5	9.86	115.10	124.96	104	8
15H	17 Jul	1330	124.6	126.1	1.5	1.53	124.60	126.13	102	2
16H	17 Jul	1435	126.1	127.0	0.9	0.93	126.10	127.03	103	2
17X	17 Jul	1605	127.0	131.6	4.6	4.37	127.00	131.37	95	4
18X	17 Jul	1730	131.6	141.2	9.6	7.41	131.60	139.01	77	6
19X	17 Jul	1835	141.2	150.8	9.6	0.03	141.20	141.23	0	1
20X	17 Jul	1945	150.8	160.4	9.6	9.81	150.80	160.61	102	8
21X	17 Jul	2040	160.4	170.0	9.6	2.33	160.40	162.73	24	3
22X	17 Jul	2145	170.0	179.6	9.6	9.37	170.00	179.37	98	8
23X	17 Jul	2305	179.6	189.2	9.6	8.91	179.60	188.51	93	7
24X	18 Jul	0115	189.2	197.7	8.5	7.89	189.20	197.09	93	6
25X	18 Jul	0340	197.7	199.3	1.6	0.24	197.70	197.94	15	1
26X	18 Jul	0615	199.3	200.1	0.8	1.17	199.30	200.47	146	2
Totals:			200.1	183.33				92	155	
342-U1409B-										
1H	18 Jul	1050	0.0	8.3	8.3	8.36	0.00	8.36	101	7
2H	18 Jul	1205	8.3	17.8	9.5	9.74	8.30	18.04	103	8
3H	18 Jul	1300	17.8	27.3	9.5	9.86	17.80	27.66	104	8
4H	18 Jul	1400	27.3	36.8	9.5	10.02	27.30	37.32	105	8
5H	18 Jul	1450	36.8	46.3	9.5	10.00	36.80	46.80	105	8
6H	18 Jul	1540	46.3	55.8	9.5	9.94	46.30	56.24	105	8
7H	18 Jul	1630	55.8	65.3	9.5	10.01	55.80	65.81	105	8
8H	18 Jul	1725	65.3	74.8	9.5	9.93	65.30	75.23	105	8
9H	18 Jul	1820	74.8	84.3	9.5	9.95	74.80	84.75	105	8
10H	18 Jul	1910	84.3	93.8	9.5	9.64	84.30	93.94	101	7
11H	18 Jul	2005	93.8	103.3	9.5	8.89	93.80	102.69	94	7
12H	18 Jul	2100	103.3	112.8	9.5	9.48	103.30	112.78	100	8
13H	18 Jul	2150	112.8	122.3	9.5	8.81	112.80	121.61	93	7
14H	18 Jul	2240	122.3	122.5	0.2	0.20	122.30	122.50	100	1
15X	19 Jul	0030	122.5	132.1	9.6	5.63	122.50	128.13	59	5
16X	19 Jul	0140	132.1	141.7	9.6	8.45	132.10	140.55	88	7
17X	19 Jul	0235	141.7	151.3	9.6	9.30	141.70	151.00	97	7
18X	19 Jul	0350	151.3	160.9	9.6	9.21	151.30	160.51	96	8
19X	19 Jul	0445	160.9	170.5	9.6	9.67	160.90	170.57	101	8
Totals:			170.5	167.09				98	136	
342-U1409C-										
1H	19 Jul	1050	0.0	6.3	6.3	6.38	0.00	6.38	101	6
2H	19 Jul	1400	6.3	15.8	9.5	9.43	6.30	15.73	99	8
3H	19 Jul	1705	15.8	25.3	9.5	9.45	15.80	25.25	99	8
4H	19 Jul	1855	25.3	30.8	5.5	6.40	25.30	31.70	116	6
5H	19 Jul	1955	30.8	40.3	9.5	9.83	30.80	40.63	103	8
6H	19 Jul	2040	40.3	49.8	9.5	9.73	40.30	50.03	102	8
7H	19 Jul	2130	49.8	59.3	9.5	9.03	49.80	58.83	95	7
8H	19 Jul	2215	59.3	68.8	9.5	9.77	59.30	69.07	103	8
9H	19 Jul	2305	68.8	78.3	9.5	9.94	68.80	78.74	105	8
10H	19 Jul	2350	78.3	87.8	9.5	9.79	78.30	88.09	103	8
11H	20 Jul	0040	87.8	97.3	9.5	9.99	87.80	97.79	105	8
12H	20 Jul	0125	97.3	106.8	9.5	9.22	97.30	106.52	97	8
13H	20 Jul	0205	106.8	116.3	9.5	9.53	106.80	116.33	100	8
14H	20 Jul	0255	116.3	124.2	7.9	7.93	116.30	124.23	100	7
15X	20 Jul	0420	124.2	129.2	5.0	4.35	124.20	128.55	87	4
16X	20 Jul	0555	129.2	131.8	2.6	2.09	129.20	131.29	80	3

Table T1 (continued).

Core	Date (2012)	Time UTC (h)	Depth DSF (m)				Depth CSF-A (m)			
			Top of cored interval	Bottom of cored interval	Interval cored (m)	Curated length (m)	Top of core	Bottom of core	Recovery (%)	Sections (N)
17X	20 Jul	0705	131.8	136.8	5.0	5.44	131.80	137.24	109	5
18X	20 Jul	0855	136.8	143.3	6.5	5.39	136.80	142.19	83	5
19X	20 Jul	1015	143.3	149.3	6.0	5.80	143.30	149.10	97	5
20X	20 Jul	1235	149.3	157.3	8.0	8.32	149.30	157.62	104	7
21X	20 Jul	1410	157.3	160.8	3.5	3.17	157.30	160.47	91	3
Totals:				160.8	160.98				99	138
Site U1409 totals:				531.4	511.40				96	429

DSF = drilling depth below seafloor, CSF-A = core depth below seafloor, method A. H = advanced piston core, X = extended core barrel core.

Table T2. Lithostratigraphic unit intervals, Site U1409.

Lith. unit	Core, section, interval (cm)		Depth (mbsf)	
	Top	Bottom	Top	Bottom
342-U1409A-				
I	1H-1, 0	3H-5, 101	0.00	17.61
II	3H-5, 101	5H-3, 59	17.61	33.19
III	5H-3, 59	12H-4, 49	33.19	101.09
IVa	12H-4, 49	15H-CC, 14	101.09	126.13**
IVb	16H-1, 0	20X-3, 122	126.10**	155.02
IVc	20X-3, 122	26X-CC, 49	155.02	200.47*
342-U1409B-				
I	1H-1, 0	3H-1, 72	0.00	18.52
II	3H-1, 72	4H-CC, 30	18.52	37.32
III	4H-CC, 30	11H-CC, 20	37.32	102.69
IVa	12H-1, 0	14H-CC, 20	103.30	122.50
IVb	15X-1, 0	18X-6, 31	122.50	158.73
IVc	18X-6, 31	19X-CC, 24	158.73	170.57*
342-U1409C-				
I	1H-1, 0	3H-1, 19	0.00	15.99
II	3H-1, 19	5H-5, 34	15.99	37.14
III	5H-5, 34	12H-3, 27	37.14	100.57
IVa	12H-3, 27	14H-CC, 21	100.57	124.23**
IVb	15X-1, 0	21X-CC, 40	124.20**	160.47*

* = end of hole, ** = unit or subunit boundary falls between cores and results in overlapping depths between Section 1 and the core catcher of the previous core.



Table T3. Calcareous nannofossil datums, Site U1409. (Continued on next page.)

Core, section, interval (cm)	Top	Bottom	Age	Zone/ Subzone	Marker species	Age (Ma)	Depth (mbsf)				
							Top	Bottom	Midpoint	±	
342-U1409A-	342-U1409A-										
				Pleistocene							
2H-4, 75	2H-CC			NN20	T <i>Pseudoemiliania lacunosa</i>	0.44	6.35	10.64	8.50	2.15	
2H-CC	3H-4, 75			NN19	T <i>Discoaster brouweri</i>	1.93	10.64	15.85	13.25	2.61	
2H-CC	3H-4, 75			Pliocene	NN17	T <i>Discoaster pentaradiatus</i>	2.39	10.64	15.85	13.25	2.61
5H-2, 75	5H-4, 75			Oligocene	NP23	T <i>Reticulofenestra umbilicus</i> (>14 µm)	32.02	31.85	34.85	33.35	1.50
5H-2, 75	5H-4, 75				NP22	T <i>Coccolithus formosus</i>	32.92	31.85	34.85	33.35	1.50
5H-2, 75	5H-4, 75			Eocene		T <i>Chiasmolithus grandis</i>	37.98	31.85	34.85	33.35	1.50
5H-2, 75	5H-4, 75					B <i>Dictyococcites bisectus</i> (>10 µm)*	40.36	31.85	34.85	33.35	1.50
						T <i>Sphenolithus furcatolithoides</i>					
5H-6, 75	5H-CC			NP17	T <i>Chiasmolithus solitus</i>	40.40	37.85	38.70	38.28	0.43	
6H-4, 84	6H-6, 80				B <i>Reticulofenestra reticulata</i>	41.66	44.44	47.40	45.92	1.48	
6H-4, 84	6H-6, 80				T <i>Nannotetraena</i> spp.	41.85	44.44	47.40	45.92	1.48	
6H-2, 100	6H-4, 84				B <i>Reticulofenestra umbilicus</i> (>14 µm)	41.94	41.60	44.44	43.02	1.42	
6H-6, 81	6H-CC				T <i>Nannotetraena fulgens</i>	42.87	47.41	49.18	48.30	0.89	
7H-4, 57	7H-CC			NP15c	T <i>Chiasmolithus gigas</i>	44.12	53.68	58.54	56.11	2.43	
8H-CC	9H-CC				B <i>Sphenolithus furcatolithoides</i>		68.01	77.61	72.81	4.80	
11H-2, 39	11H-4, 39			NP15b	B <i>Chiasmolithus gigas</i>	45.49	88.49	91.49	89.99	1.50	
11H-CC	12H-2, 50			NP15a	B <i>Nannotetraena fulgens</i>	46.29	96.40	98.10	97.25	0.85	
12H-4, 43	12H-4, 50				B <i>Nannotetraena cristata</i>	47.73	101.03	101.10	101.07	0.03	
12H-4, 43	12H-4, 50				B <i>Blackites inflatus</i>	47.84	101.03	101.10	101.07	0.03	
12H-4, 50	12H-CC				T <i>Discoaster lodoensis</i>	47.41	101.10	105.96	103.53	2.43	
14H-3, 110	14H-5, 110			NP14	B <i>Discoaster sublodoensis</i> (5 rayed)	49.11	119.21	122.20	120.71	1.49	
14H-3, 110	14H-5, 110			NP13	T <i>Tribrachiatus orthostylus</i>	50.50	119.21	122.20	120.71	1.49	
15H-CC	16H-CC				B <i>Dictyococcites/Reticulofenestra</i>	50.50	126.09	126.97	126.53	0.44	
16H-CC	17X-CC				T <i>Tow eius</i> spp. [‡]	50.78	126.97	131.33	129.15	2.18	
16H-CC	17X-CC				B <i>Coccolithus crassus</i> [‡]	51.64	126.97	131.33	129.15	2.18	
19X-CC	20X-1, 35			NP12	B <i>Discoaster lodoensis</i>	53.70	141.22	151.15	146.18	4.97	
19X-CC	20X-1, 35				B <i>Girgisia gammation</i>		141.22	151.15	146.18	4.97	
20X-1, 35	20X-2, 135			NP11	T <i>Tribrachiatus contortus</i>	54.17	151.15	153.65	152.40	1.25	
20X-2, 135	20X-2, 150				B <i>Tribrachiatus orthostylus</i>	54.37	153.65	153.80	153.73	0.08	
20X-3, 45	20X-3, 48				B <i>Tribrachiatus contortus</i>		154.25	154.28	154.27	0.02	
20X-3, 45	20X-3, 48				B <i>Discoaster diastypus</i>	54.95	154.25	154.28	154.27	0.02	
20X-3, 45	20X-3, 48				T <i>Fasciculithus</i> spp.	55.64	154.25	154.28	154.27	0.02	
20X-3, 48	20X-3, 56			NP10	B <i>Rhomboaster bramlettei</i>	55.86	154.25	154.36	154.31	0.06	
20X-3, 56	20X-3, 77			NP9b	B <i>Rhomboaster</i> spp.	55.96	154.36	154.57	154.47	0.10	
				Paleocene							
20X-3, 56	20X-3, 77				Fasciculithus diversity decline [†]	56.00	154.36	154.57	154.47	0.10	
20X-3, 56	20X-3, 77				T <i>Fasciculithus alani</i> [†]	56.00	154.36	154.57	154.47	0.10	
20X-3, 150	20X-5, 114				T <i>Ericsonia robusta</i> (>9 µm) [†]	57.10	155.30	157.95	156.62	1.32	
20X-5, 114	20X-CC			NP9a	B <i>Discoaster multiradiatus</i>	57.21	157.95	160.59	159.27	1.32	
20X-5, 114	20X-CC				Tc <i>Sphenolithus anarrhopus</i>		157.95	160.59	159.27	1.32	
20X-5, 114	20X-CC				B <i>Discoaster delicatus</i> [†]	57.45	157.95	160.59	159.27	1.32	
20X-5, 114	20X-CC				B <i>Ericsonia robusta</i> (>9 µm) [†]	57.54	157.95	160.59	159.27	1.32	
20X-5, 114	20X-CC				Tc <i>Discoaster backmani</i> [†]	57.57	157.95	160.59	159.27	1.32	
20X-CC	21X-CC				B <i>Discoaster backmani</i> [†]	58.28	160.59	162.73	161.66	1.07	
				NP8	B <i>Heliolithus riedellii</i>	58.70					



Table T3 (continued).

Core, section, interval (cm)			Age	Zone/ Subzone	Marker species	Age (Ma)	Depth (mbsf)			
Top	Bottom	Age					Top	Bottom	Midpoint	±
22X-4, 78	22X-6, 51		NP7	B <i>Discoaster mohleri</i>	58.97	175.28	178.01	176.65	1.36	
23X-1, 75	23X-2, 75			B <i>Sphenolithus anarrhopus</i> †	59.40	180.35	181.85	181.10	0.75	
23X-1, 75	23X-2, 75		NP6	B <i>Heliolithus kleinpellii</i>	59.54	180.35	181.85	181.10	0.75	
23X-4, 64	23X-6, 56			B <i>Heliolithus cantabricae</i>	59.60	184.74	187.66	186.20	1.46	
24X-2, 80	24X-4, 78		NP5	B <i>Fasciculithus tympaniformis</i>	61.51	191.50	194.53	193.02	1.52	
			NP4	B <i>Ellipsolithus macellus</i>	63.25					

* = from Fornaciari et al. (2010) recalibrated to GTS2012. † = from Agnini et al. (2007) recalibrated to GTS2012. ‡ = from Agnini et al. (2006) recalibrated to GTS2012. B = base, Bc = base common, T = top, Tc = top common.

Table T4. Nannofossil distribution, Site U1409. This table is available in an [oversized format](#).**Table T5.** Radiolarian datums, Site U1409.

Core, section			Age	Zone/ Subzone	Marker species	Age (Ma)	Depth (mbsf)			
Top	Bottom	Age					Top	Bottom	Midpoint	±
342-U1409A-	342-U1409A-									
				Eocene						
12H-CC		RP11	B <i>Dictyoprora mongolfieri</i>			47.98	105.96	105.96		
13H-CC	14H-CC	RP09	B <i>Theocorys plesioanaclasta</i>			50.50	115.46	124.91	120.19	4.72
14H-CC	15H-CC		T <i>Buryella tetradica</i>			50.87	124.91	126.09	125.50	0.59
17X-CC	20X-CC	RP08	B <i>Buryella clinata</i>			53.35	131.33	160.59	145.96	14.63
				Paleocene						
20X-CC	21X-CC	RP07	X <i>Bekoma campechensis</i> – <i>Bekoma bidartensis</i>			58.23	160.59	162.71	161.65	1.06
21X-CC		RP06c	T <i>Buryella pentadica</i>			59.71	162.71		162.71	

B= base, T = top, X = faunal crossover.



Table T6. Radiolarian species list for Sample 342-U1409A-1H-CC.

Spumellaria
<i>Actinomma leptodernum</i>
<i>Actinomma medianum</i>
<i>Dictyocoryne profunda</i>
<i>Heliodiscus asteriscus</i>
<i>Larcopyle buetschlii</i>
Orosphaerid fragments
<i>Spongocore puella</i>
<i>Spongopyle osculosa</i>
<i>Spongodiscus resurgens</i>
<i>Stylochlamydium</i> sp.
<i>Stylatractus</i> sp.
<i>Thecosphaera inermis</i>
<i>Tholospira cervicornis</i>
Nassellaria
<i>Peripyramis circumtexta</i>
<i>Botryostrobus aquilonaris</i>
<i>Cycladophora davisiana</i>
<i>Dictyophimus hirundo</i>
<i>Eucyrtidium acuminatum acuminatum</i>
<i>Eucyrtidium acuminatum octocolum</i>
<i>Lamprocyclas? hannai</i>
<i>Theocorythium trachelium</i>

**Table T7.** Radiolarian distribution, Site U1409. (Continued on next page.)

Core, section	Depth (mbsf)	Age	Zone/Subzone	Preservation	Abundance	<i>Amphicraspedum gracilis</i>	<i>Amphicraspedum ignorabilis</i>	<i>Amphicraspedum murayanum</i>	<i>Amphicraspedum prolatum</i>	<i>Amphipteris alamedensis</i>	<i>Amphisphaera coronata</i>	<i>Amphisphaera goruna</i>	<i>Amphisphaera macrospheara</i>	<i>Axopunum pierinae</i>	<i>Bekoma bidartensis</i>	<i>Bekoma campechensis</i>	<i>Bunella clinata</i>	<i>Bunella pentadica</i>	<i>Bunella tetradiaca</i>	<i>Calocyclas hispida</i>	<i>Calocyclas triporcha</i>	<i>Calocyclus ampulla</i>	<i>Calocyclus castum</i>	<i>Clathrocyclas australis</i>	<i>Clathrocyclas capiteanum</i>	<i>Clithracdas universa</i>	<i>Cyathocarpium ornatum</i>	<i>Dendrospyris galii</i>	<i>Dictyocephalus midouri</i>	<i>Dictyopora amphora</i>	<i>Dictyopora mongolfieri</i>	<i>Dictyopora urceolus</i>	<i>Diplocyclas bicorona bicorona</i>	<i>Dordacospyris platyacantha</i>	<i>Heliosylus</i> sp.	<i>Lampodium fabaeforme chaunothorax</i>	<i>Lampodium fabaeforme constrictum</i>	<i>Lampodium incohatum</i>	<i>Lampodium pennatum</i>	<i>Lithocyclis archaea</i>
342-U1409A-12H-CC	105.96	middle Eocene	RP11	G A F							F P	P				? R R		R	F	C P P							P													
13H-CC	115.46	early Eocene	RP9	G A F P P							F ? P				F P P	P R		R R	F	— F P						P R														
14H-CC	124.91	early Eocene	RP8	G C R P F P							F				F			? F																						
15H-CC	126.09	early Eocene	RP8	M C P P P							C				R R			? R																						
16H-CC	126.97	early Eocene	RP8	M C P P							C				R R			? R P																						
17X-CC	131.33	early Eocene	RP8	M C P P							F ?				P A																									
20X-CC	160.59	late Paleocene	RP7	G A R P							F R F R				C						P			P R									R							
21X-CC	162.71	late Paleocene	RP6c	G A							C F F				C P C				R	P			P P			P F														

Preservation: G = good, M = moderate. Abundance: A = abundant, C = common, F = few, R = rare, P = present. ? = undetermined. — = not present. See “Biostratigraphy” in the “Methods” chapter (Norris et al., 2014a) for preservation and abundance definitions.

Core, section	Depth (mbsf)	Age	Zone/Subzone	Preservation	Abundance	<i>Lithocyclas vespertilio</i>	<i>Lithocyclas vespertilio</i>	<i>Lithomesoplites mendoza</i>	<i>Lophocystis jachia</i>	<i>Lophocystis klydus</i>	<i>Lophocystis semipolita</i> gr.	<i>Lophocystis? bianuria</i>	<i>Lophocystis? pseudojacchia</i>	<i>Lychnocanoma amphitrite</i>	<i>Lychnocanoma auxilla</i>	<i>Lychnocanoma bellum</i>	<i>Lychnocanoma elongata</i>	<i>Lychnocanoma carinatum</i>	<i>Lychnocanoma tripodium</i>	<i>Midourium regulans</i>	<i>Monobrachium irregularis</i>	<i>Peripheraea decora</i>	<i>Peripheraea heliastericus</i>	<i>Peripheraea triplacanis triangula</i>	<i>Phormocystis striata exquisita</i>	<i>Phormocystis striata preexquisita</i>	<i>Phormocystis striata striata</i>	<i>Podocystis acelles</i>	<i>Podocystis aphorma</i>	<i>Podocystis diamesa</i>	<i>Podocystis dorus</i>	<i>Podocystis papalis</i>	<i>Podocystis sinuosa</i>	<i>Pterocodon? ampla</i>	<i>Pterocodon? poculum</i>	<i>Pterocodon? penellus</i>	<i>Pteropodomytilina ornata</i>	<i>Sabellularia circinata</i>	<i>Sabellularia tuberculata</i>	<i>Sabellularia tuberculata</i>	<i>Sabellularia tuberculata</i>	<i>Sabellularia tuberculata</i>
342-U1409A-12H-CC	105.96	middle Eocene	RP11	G A P R R P							F R R			F R			F R		R									P F P														
13H-CC	115.46	early Eocene	RP9	G A — R R F							— R R			? F F			R R		R R R R	F								P P F P P														
14H-CC	124.91	early Eocene	RP8	G C R P P R							P R P R			C			P R P		F R									R R P														
15H-CC	126.09	early Eocene	RP8	M C P P P							? R			P R			R P		F F									R F														
16H-CC	126.97	early Eocene	RP8	M C P P							R			R R			P R		F F								R F															
17X-CC	131.33	early Eocene	RP8	M C P P							R			R R			R R		F F								R P															
20X-CC	160.59	late Paleocene	RP7	G A R												F R R		F		P		R	P R			P P P																
21X-CC	162.71	late Paleocene	RP6c	G A												R R R		C P	R			R R																				

Table T7 (continued).

Table T8. Planktonic foraminifer datums, Site U1409.

Core, section, interval (cm)		Age	Zone/ Subzone	Marker event	Age (Ma)	Depth (mbsf)			
Top	Bottom					Top	Bottom	Mid-point	±
342-U1409A- 7H-4, 57–59	342-U1409A- 7H-CC	middle Eocene	E10/E9	T <i>Morozovella aragonensis</i>	43.26	53.68	58.50	56.09	2.41
8H-5, 119–121	8H-CC	middle Eocene	E9/E8	B <i>Globigerinatheka kugleri</i>	43.88	65.29	67.97	66.63	1.34
12H-CC	13H-2, 100–102	middle Eocene	E8/E7b	B <i>Guembelitroides nuttalli</i>	45.7	105.91	108.13	107.02	1.11
13H-CC	14H-2, 110–112	early Eocene	E7b/E7a	B <i>Turborotalia frontosa</i>	48.3	115.41	117.70	116.56	1.15
14H-6, 110–112	14H-CC	early Eocene	E7a/E6	B <i>Acarinina cuneicamerata</i>	50.2	123.70	124.86	124.28	0.58
14H-CC	15-1, 71–73	early Eocene	E6/E5	T <i>Morozovella subbotinae</i>	50.7	124.86	125.31	125.09	0.23
18X-3, 87–89	18X-CC	early Eocene	E5/E4	B <i>Morozovella aragonensis</i>	52.5	135.47	138.96	137.22	1.75
19X-CC	20X-1, 55–56	early Eocene	E4/E3	B <i>Morozovella formosa</i>	54.6	141.20	151.35	146.28	5.08
20X-4, 29–30	20X-5, 114–115	late Paleocene	PS/P4c	T <i>Globanomalina pseudomenardii</i>	57.1	155.59	157.94	156.77	1.18

T = top, B = base.

Table T9. Planktonic foraminifer distribution, Site U1409. This table is available in an [oversized format](#).

Table T10. Benthic foraminifer distribution, Site U1409. (Continued on next page.)

Preservation: VG = very good, G = good, M = moderate. Abundance: B = barren, P = present, F = few, D = dominant. — = not assigned. See “[Biostratigraphy](#)” in the “Methods” chapter (Norris et al., 2014a) for preservation and abundance definitions.

Table T10 (continued).

Core, section	Depth (mbsf)	Preservation	Abundance	<i>Gryrodinoides gibbosus</i>	<i>Gryrodinoides spp.</i>	<i>Karenellina cf. adenensis</i>	<i>Lagenaria</i> sp.	<i>Melania</i> sp.	<i>Neoflabellina</i> sp.	<i>Nodularia adusta</i>	<i>Nodularia thunbergii</i>	<i>Notularia floraealis</i>	<i>Oridorsids unbonatus</i>	<i>Ovalularia</i> sp.	<i>Pleurostomella acuta</i>	<i>Pleurostomella tenuis</i>	<i>Pulilliopsis</i> sp.	<i>Pulilliopsis tuberculata</i>	<i>Pulilliopsis tenuissima</i>	<i>Ranularia</i> sp.	<i>Spirorbicella</i> sp.	<i>Spirorbicella depresso-</i>	<i>Spirorbicella gregaria</i>	<i>Spirorbicella speciosa</i>	<i>Tritonia</i> sp.	<i>Volutella spissosa</i>	Others					
342-U1409A-																																
1H-CC	1.02	G	P																										D	A	P	
2H-CC	10.64	G	P	B																									F	P		
3H-CC	20.60																															
4H-CC	30.08	G	F																													
5H-CC	38.70	G	P																													
6H-CC	49.18	VG	P																													
7H-CC	58.54	VG	P																													
8H-CC	68.01	VG	P																													
9H-CC	77.61	VG	P																													
10H-CC	86.91	G	P																													
11H-CC	96.40	VG	P																													
12H-CC	105.96	G	P																													
13H-CC	115.46	G	P																													
14H-CC	124.91	M	P																													
15H-CC	126.09	G	P																													
16H-CC	126.97	G	P																													
17X-CC	131.33	G	P																													
18X-CC	138.99	G	P																													
19X-CC	141.22	M	P																													
20X-CC	160.59	G	P																													
21X-CC	162.71	G	P	D	P	P																										
22X-CC	179.35	M	P																													
23X-CC	188.45	G	B																													
24X-CC	197.03	M	P																													
25X-CC	197.78	M	P																													
26X-CC	200.03	M	P																													



Table T11. Benthic foraminifer abundance and preservation, Site U1409.

Core, section, interval (cm)	Depth (mbsf)	Preservation	Group abundance
342-U1409A-			
4H-2W, 110–112	22.71	P	D
4H-5W, 110–112	27.21	P	D
5H-2W, 110–112	32.21	P	D
5H-5W, 91–93	36.52	VG	P
6H-2W, 111–113	41.72	VG	P
6H-5W, 30–32	45.41	VG	P
7H-2W, 57–59	50.68	G	P
7H-5W, 69–71	55.31	G	P
8H-2W, 50–52	60.11	VG	P
8H-5W, 119–121	65.30	VG	P
9H-2W, 110–112	70.21	VG	P
9H-5W, 110–112	74.72	VG	P
10H-2W, 110–112	79.71	VG	P
10H-5W, 110–112	84.21	VG	P
11H-2W, 110–112	89.21	VG	P
11H-5W, 110–112	93.71	VG	P
12H-2W, 120–122	98.81	VG	P
12H-4W, 41–43	101.02	VG	P
13H-2W, 100–102	108.14	VG	P
13H-5W, 100–102	112.65	VG	P
14H-2W, 110–112	117.71	VG	P
14H-5W, 110–112	122.21	G	P
17X-1W, 114–116	128.15	G	A
17X-2W, 114–116	129.65	VG	P
18X-2W, 118–120	134.29	VG	P
18X-4W, 94–96	137.05	G	P
20X-2W, 110–112	153.41	G	P
20X-5W, 114–115	157.95	M	P
21X-1W, 133–134	161.74	G	P
22X-4W, 100–102	175.51	G	P
23X-2W, 107–108	182.18	P	F
23X-5W, 101–102	186.62	M	P
24X-2W, 84–85	191.55	M	P
24X-5W, 59–60	195.80	M	P

Preservation: VG = very good, G = good, M = moderate, P = poor. Abundance: D = dominant, A = abundant, F = few, P = present. See “[Biostratigraphy](#)” in the “Methods” chapter (Norris et al., 2014a) for preservation and abundance definitions.

Table T12. Core orientation data, Site U1409.

Hole U1409A		Hole U1409B	
Core	MTF (°)	Core	MTF (°)
342-U1409A-		342-U1409B-	
1H	317	1H	301
2H	74	2H	329
3H	183	3H	143
4H	23	4H	120
5H	341	5H	77
6H	330	6H	109
7H	203	7H	283
8H	67	8H	242
9H	152	9H	198
10H	117	10H	122
11H	300	11H	281
12H	256	12H	323
13H	84	13H	55
14H	354	14H	230
15H	168		
16H	317		

MTF = magnetic tool face orientation from geomagnetic north.

Table T13. Summary of AF demagnetization results for discrete samples, Hole U1409A. (Continued on next page.)

Core, section, interval (cm)	Depth (mbsf)	Declination 20 mT or PCA (°)	Inclination 20 mT or PCA (°)	PCA MAD (°)	PCA range (mT)	NRM 20 mT (A/m)	Measurement error (%)
342-U1409A-							
2H-3W, 75-77	4.86	-22.1	63.5	8.8	10-60	1.47E-02	3.5
2H-6W, 75-77	9.36	181.8	-48.9			8.52E-03	4.6
3H-2W, 75-77	12.86	208.2	-39.2	7.0	10-40	1.38E-02	2.9
3H-5W, 75-77	17.36	164.5	66.7			2.54E-03	3.6
4H-3W, 75-77	23.86	14.5	33.4			3.72E-04	14.9
4H-5W, 75-77	26.86	38.4	47.9			5.74E-03	3.6
5H-1W, 75-77	30.36	50.1	0.8			3.45E-05	3.3
5H-2W, 75-77	31.86	45.3	-28.6			3.28E-05	5.1
5H-3W, 70-72	33.31	4.6	56.6			1.60E-04	3.9
5H-4W, 75-77	34.86	1.4	50.0			1.29E-05	24.0
5H-5W, 75-77	36.36	20.7	58.6			2.07E-05	11.7
5H-6W, 75-77	37.86	-64.0	49.6			1.85E-05	18.0
6H-1W, 74-76	39.85	202.9	60.9			3.27E-05	15.9
6H-2W, 74-76	41.35	41.1	-26.6			2.39E-05	15.3
6H-3W, 88-90	42.99	-6.5	-53.3			2.10E-05	10.7
6H-4W, 72-74	44.33	221.2	-79.0			4.53E-05	6.4
6H-5W, 74-76	45.85	228.9	0.7			5.63E-04	7.1
7H-3W, 74-76	52.35	-70.1	32.8			1.98E-05	15.1
7H-6W, 74-76	56.87	-24.4	72.1			2.74E-05	15.7
8H-1W, 74-76	58.85	136.3	-59.5			4.12E-05	9.8
8H-2W, 80-82	60.41	70.4	-2.8			2.23E-05	21.5
8H-3W, 74-76	61.85	135.4	-43.5			2.95E-05	13.5
8H-5W, 74-76	64.85	140.3	-52.2			2.67E-05	21.7
9H-2W, 86-88	69.97	183.3	-21.8			4.06E-04	3.2
9H-3W, 74-76	71.36	190.0	6.4	5.7	20-60	3.22E-03	2.7
9H-4W, 74-76	72.86	204.3	-22.6			5.01E-03	3.4
9H-5W, 74-76	74.36	213.9	-47.2			1.21E-04	1.9
9H-6W, 74-76	75.86	195.0	-25.0			3.32E-05	8.7
10H-1W, 74-76	77.85	156.4	-27.7			4.22E-05	7.2
10H-2W, 74-76	79.35	174.7	-38.9			1.66E-05	20.1
10H-3W, 74-76	80.85	152.3	-36.2			3.32E-05	8.8
10H-4W, 74-76	82.35	160.3	-21.2			4.13E-05	6.4
10H-5W, 74-76	83.85	257.1	-58.2			1.21E-05	34.9
10H-6W, 64-66	85.25	154.3	-8.5			1.77E-05	15.2
11H-1W, 74-76	87.35	245.4	-17.9			2.04E-03	7.2
11H-3W, 74-76	90.35	32.2	45.3	3.1	20-60	3.79E-03	4.8
11H-5W, 83-85	93.44	10.2	48.5			6.41E-05	9.0
12H-1W, 74-76	96.85	-84.6	53.0			4.30E-05	10.3
12H-3W, 74-76	99.85	-65.7	44.6			7.49E-05	4.7
12H-5W, 74-76	102.85	231.8	-45.8			4.91E-05	12.8
13H-1W, 74-76	106.35	147.9	-48.4			9.51E-05	4.8
13H-3W, 74-76	109.39	17.2	54.8	9.8	10-60	9.53E-05	9.0
13H-5W, 74-76	112.39	138.5	-35.7			6.02E-04	2.7
14H-2W, 74-76	117.35	-18.2	-69.5			4.73E-04	6.9
14H-3W, 74-76	118.85	85.4	53.6			8.86E-04	3.9
14H-4W, 78-80	120.39	-49.2	-20.3			7.93E-04	7.9
14H-5W, 74-76	121.85	9.0	46.9			2.08E-03	3.5
14H-6W, 74-76	123.35	1.3	45.0			2.05E-03	3.9
14H-7W, 29-31	124.40	14.7	42.6			1.52E-03	3.2
15H-1W, 63-65	125.24	255.3	77.0			1.14E-03	3.4
17X-1W, 82-84	127.83	-24.0	-47.9			2.64E-04	10.0
17X-3W, 55-57	130.56	27.8	-20.0			6.17E-04	2.3
18X-2W, 73-75	133.84	-5.8	16.8			4.16E-04	6.5
18X-3W, 96-98	135.57	-50.4	51.5			4.49E-04	5.8
18X-5W, 40-42	138.01	-1.1	-25.0			9.17E-04	5.2
20X-2W, 70-72	153.01	46.4	22.9			2.09E-03	1.7
20X-3W, 35-37	154.16	4.3	-13.0			1.06E-03	5.2
20X-4W, 29-31	155.60	-2.8	-26.8			7.61E-04	5.9
20X-5W, 75-77	157.56	35.6	12.6			3.84E-04	2.1
20X-6W, 75-77	159.06	-21.3	33.5			1.97E-04	6.8
21X-1W, 63-65	161.04	42.6	-20.9			1.58E-04	1.5
22X-1W, 62-64	170.63	-2.1	-65.2			1.36E-04	8.2
22X-3W, 117-119	174.18	-43.4	-60.2			3.66E-04	7.9
22X-5W, 71-73	176.72	-14.6	-25.4			3.39E-04	6.6
22X-6W, 66-68	178.17	11.6	18.4			9.81E-04	3.6



Table T13 (continued).

Core, section, interval (cm)	Depth (mbsf)	Declination 20 mT or PCA (°)	Inclination 20 mT or PCA (°)	PCA MAD (°)	PCA range (mT)	NRM 20 mT (A/m)	Measurement error (%)
23X-2W, 59–61	181.70	-23.4	-25.3			9.63E-04	6.3
23X-4W, 73–75	184.84	27.3	-24.5			1.56E-03	2.7
23X-5W, 52–54	186.13	22.0	-41.2			8.76E-04	4.2
23X-6W, 38–40	187.49	0.8	-19.3			1.73E-03	4.4
24X-2W, 70–72	191.41	-26.2	-29.2			2.36E-03	6.2
24X-4W, 74–76	194.45	156.6	-68.1			8.10E-04	5.3
24X-5W, 75–77	195.96	-37.8	-54.8			5.20E-05	7.3
26X-1W, 32–34	199.63	-14.9	-25.6			6.49E-05	7.0

Declinations for Cores 2H to 15H in geographic coordinates. PCA = principal component analysis, MAD = maximum angle of deviation, NRM = natural remanent magnetism.

Table T14. Magnetostratigraphic tie points, Site U1409. (Continued on next two pages.)

Chron boundary	Age (Ma)	Hole U1409A				
		Top		Bottom		
		Core, section, interval (cm)	Depth (mbsf)	Core, section, interval (cm)	Depth (mbsf)	Mid-point (mbsf)
C1n (Brunhes)/C1r.1r (Matuyama)	0.781	342-U1409A-2H-6, 35.0	8.95	342-U1409A-2H-6, 37.5	8.98	8.97
C6Cr/C7n.1n	23.962	3H-2, 52.5	12.63	3H-2, 55.0	12.65	12.64
C7n.1n/C7n.1r	24.000	3H-2, 62.5	12.73	3H-2, 65.0	12.75	12.74
C7n.1r/C7n.2n	24.109	3H-2, 115.0	13.25	3H-2, 122.5	13.33	13.29
C7n.2n/C7r	24.474	3H-3, 92.5	14.53	3H-3, 97.5	14.58	14.56
C7r/C7An	24.761	3H-4, 72.5	15.83	3H-4, 85.0	15.95	15.89
C7An/C7Ar	24.984	3H-5, 57.5	17.18	3H-5, 60.0	17.20	17.19
C7Ar/C8n.1n	25.099	3H-5, 67.5	17.28	3H-5, 72.5	17.33	17.31
C8n.1n/C8n.1r	25.264	3H-6, 22.5	18.33	3H-6, 25.0	18.35	18.34
C8n.1r/C8n.2n	25.304	3H-6, 32.5	18.43	3H-6, 35.0	18.45	18.44
C8n.2n/C8r	25.987	3H-7, 20.0	19.80	3H-7, 25.0	19.85	19.83
C8r/C9n	26.420	3H-7, 55.0	20.15	3H-7, 62.5	20.23	20.19
C9n/C9r	27.439	NI	NI	NI	NI	NI
C9r/C10n.1n	27.859	NI	NI	NI	NI	NI
C10n.1n/C10n.1r	28.087	4H-2, 60.0	22.20	4H-2, 65.0	22.25	22.23
C10n.1r/C10n.2n	28.141	4H-2, 75.0	22.35	4H-2, 77.5	22.38	22.37
C10n.2n/C10r	28.278	4H-2, 105.0	22.65	4H-2, 112.5	22.73	22.69
C10r/C11n.1n	29.183	4H-4, 97.5	25.58	4H-4, 105.0	25.65	25.62
C11n.1n/C11n.1r	29.477	4H-5, 15.0	26.25	4H-5, 20.0	26.3	26.28
C11n.1r/C11n.2n	29.527	4H-5, 32.5	26.43	4H-5, 37.5	26.48	26.46
C11n.2n/C11r	29.970	4H-5, 97.5	27.08	4H-5, 127.5	27.38	27.23
C11r/C12n	30.591	4H-6, 50.0	28.10	4H-6, 55.0	28.15	28.13
C12n/C12r	31.034	4H-6, 130.0	28.10	4H-7, 10.0	29.20	28.65
C12r/C13n	33.157	NI	NI	NI	NI	NI
C13n/C13r	33.705	5H-2, 62.5	31.73	5H-2, 102.5	32.13	31.93
C19r/C20n	42.301	6H-5, 105.0	46.15	6H-5, 125.0	46.35	46.25
C20n/C20r	43.432	7H-7, 10.0	57.72	7H-7, 55.0	58.17	57.95
C20r/C21n	45.724	11H-1, 110.0	87.70	11H-2, 17.5	88.28	87.99
C21n/C21r	47.349	12H-3, 75.0	99.85	12H-5, 75.0	102.85	101.35
C21r/C22n	48.566	13H-1, 120.0	106.80	13H-2, 67.5	107.81	107.31
C22n/C22r	49.344	13H-4, 85.0	110.99	13H-4, 102.5	111.17	111.08

Ages from Gradstein et al. (2012). NI = not identified.



Table T14 (continued). (Continued on next page.)

Chron boundary	Age (Ma)	Hole U1409B				
		Top		Bottom		
		Core, section, interval (cm)	Depth (mbsf)	Core, section, interval (cm)	Depth (mbsf)	Mid-point (mbsf)
C1n(Brunhes)/C1r.1r (Matuyama)	0.781	2H-1, 140.0	9.70	2H-2, 22.5	10.03	9.87
C6Cr/C7n.1n	23.962	2H-5, 17.5	14.48	2H-5, 25.0	14.55	14.52
C7n.1n/C7n.1r	24.000	2H-5, 140.0	15.70	2H-6, 22.5	16.03	15.87
C7n.1r/C7n.2n	24.109	2H-6, 140.0	17.20	2H-7, 10.0	17.40	17.30
C7n.2n/C7r	24.474	3H-1, 25.0	18.05	3H-1, 32.5	18.13	18.09
C7r/C7An	24.761	NI	NI	NI	NI	NI
C7An/C7Ar	24.984	NI	NI	NI	NI	NI
C7Ar/C8n.1n	25.099	NI	NI	NI	NI	NI
C8n.1n/C8n.1r	25.264	NI	NI	NI	NI	NI
C8n.1r/C8n.2n	25.304	NI	NI	NI	NI	NI
C8n.2n/C8r	25.987	NI	NI	NI	NI	NI
C8r/C9n	26.420	NI	NI	NI	NI	NI
C9n/C9r	27.439	NI	NI	NI	NI	NI
C9r/C10n.1n	27.859	NI	NI	NI	NI	NI
C10n.1n/C10n.1r	28.087	3H-5, 60.0	24.40	3H-5, 72.5	24.53	24.47
C10n.1r/C10n.2n	28.141	3H-5, 85.0	24.65	3H-5, 90.0	24.70	24.68
C10n.2n/C10r	28.278	3H-5, 102.5	24.83	3H-5, 110.0	24.90	24.87
C10r/C11n.1n	29.183	3H-7, 52.5	27.33	3H-7, 62.5	27.43	27.38
C11n.1n/C11n.1r	29.477	NI	NI	NI	NI	NI
C11n.1r/C11n.2n	29.527	NI	NI	NI	NI	NI
C11n.2n/C11r	29.970	4H-1, 117.5	28.48	4H-1, 140.0	28.70	28.59
C11r/C12n	30.591	4H-2, 72.5	29.53	4H-2, 82.5	29.63	29.58
C12n/C12r	31.034	4H-3, 42.5	30.73	4H-3, 47.5	30.78	30.76
C12r/C13n	33.157	4H-4, 140.0	33.20	4H-5, 20.0	33.50	33.35
C13n/C13r	33.705	4H-5, 130.0	34.60	4H-6, 47.5	35.28	34.94
C19r/C20n	42.301	6H-3, 80.0	50.10	6H-4, 92.5	51.73	50.92
C20n/C20r	43.432	7H-1, 137.5	57.18	7H-2, 110.0	58.40	57.79
C20r/C21n	45.724	10H-2, 90.0	86.7	10H-3, 85.0	88.15	87.43
C21n/C21r	47.349	11H-6, 85.0	102.15	11H-6, 95.0	102.25	102.20
C21r/C22n	48.566	12H-4, 82.5	108.63	12H-4, 120.0	109.00	108.82
C22n/C22r	49.344	12H-6, 117.5	111.98	12H-7, 17.5	112.28	112.13



Table T14 (continued).

Chron boundary	Age (Ma)	Hole U1409C				
		Top		Bottom		
		Core, section, interval (cm)	Depth (mbsf)	Core, section, interval (cm)	Depth (mbsf)	Mid-point (mbsf)
C1n (Brunhes)/C1r.1r (Matuyama)	0.781	2H-2, 87.5	8.68	2H-2, 122.5	9.03	8.86
C6Cr/C7n.1n	23.962	2H-5, 135.0	13.65	2H-6, 10.0	13.90	13.78
C7n.1n/C7n.1r	24.000	2H-6, 100.0	14.80	2H-7, 12.5	15.05	14.93
C7n.1r/C7n.2n	24.109	NI	NI	NI	NI	NI
C7n.2n/C7r	24.474	NI	NI	NI	NI	NI
C7r/C7An	24.761	NI	NI	NI	NI	NI
C7An/C7Ar	24.984	NI	NI	NI	NI	NI
C7Ar/C8n.1n	25.099	NI	NI	NI	NI	NI
C8n.1n/C8n.1r	25.264	NI	NI	NI	NI	NI
C8n.1r/C8n.2n	25.304	3H-2, 140.0	18.70	3H-3, 10.0	18.90	18.80
C8n.2n/C8r	25.987	3H-3, 80.0	19.60	3H-3, 87.5	19.68	19.64
C8r/C9n	26.420	NI	NI	NI	NI	NI
C9n/C9r	27.439	NI	NI	NI	NI	NI
C9r/C10n.1n	27.859	NI	NI	NI	NI	NI
C10n.1n/C10n.1r	28.087	3H-4, 127.5	21.58	3H-4, 140.0	21.70	21.64
C10n.1r/C10n.2n	28.141	3H-5, 10.0	21.90	3H-5, 15.0	21.95	21.93
C10n.2n/C10r	28.278	3H-5, 42.5	22.23	3H-5, 57.5	22.38	22.31
C10r/C11n.1n	29.183	4H-1, 47.5	25.78	4H-1, 57.5	25.88	25.83
C11n.1n/C11n.1r	29.477	4H-1, 87.5	26.18	4H-1, 97.5	26.28	26.23
C11n.1r/C11n.2n	29.527	4H-1, 105.0	26.35	4H-1, 117.5	26.48	26.42
C11n.2n/C11r	29.970	4H-2, 42.5	27.23	4H-2, 75.0	27.55	27.39
C11r/C12n	30.591	4H-2, 140.0	28.20	4H-2, 17.5	28.48	28.34
C12n/C12r	31.034	4H-3, 95.0	29.25	4H-3, 130.0	29.60	29.43
C12r/C13n	33.157	NI	NI	NI	NI	NI
C13n/C13r	33.705	5H-2, 37.5	32.68	5H-2, 80.0	33.10	32.89
C19r/C20n	42.301	6H-5, 95.0	47.25	6H-6, 10.0	47.90	47.58
C20n/C20r	43.432	7H-6, 15.0	57.45	8H-3, 10.0	62.40	59.93
C20r/C21n	45.724	10H-4, 140.0	84.20	10H-5, 12.5	84.43	84.31
C21n/C21r	47.349	12H-3, 22.5	100.53	12H-3, 140.0	101.70	101.11
C21r/C22n	48.566	13H-3, 102.5	110.83	13H-3, 117.5	110.98	110.90
C22n/C22r	49.344	13H-6, 87.5	115.18	13H-6, 95.0	115.25	115.21



Table T15. Summary of anisotropy of magnetic susceptibility of discrete samples, Hole U1409A. (Continued on next page.)

Core, section, interval (cm)	Depth (mbfs)	τ_3	V_3 ($^{\circ}$)		V_2 ($^{\circ}$)		V_1 ($^{\circ}$)		Bulk susceptibility (SI)	Anisotropy (%)	P	L	F		
			Declination	Inclination	Declination	Inclination	Declination	Inclination							
342-U1409A-															
2H-1W, 75–77	1.86	0.3304	169.0	17.1	0.3328	318.4	70.3	0.3369	76.1	9.5	2.52E-04	0.7	1.020	1.012	1.007
2H-3W, 75–77	4.86	0.3227	36.7	13.9	0.3326	281.4	59.9	0.3447	133.7	26.1	6.38E-04	2.2	1.068	1.036	1.031
2H-5W, 75–77	7.86	0.3236	199.3	35.5	0.3333	90.8	24.0	0.3431	334.5	44.9	3.40E-04	2.0	1.060	1.030	1.030
2H-7W, 25–27	10.26	0.3305	41.2	20.3	0.3338	149.7	40.6	0.3356	291.3	42.5	5.47E-05	0.5	1.016	1.005	1.010
3H-1W, 75–77	11.36	0.3304	17.5	47.1	0.3327	174.0	40.5	0.3370	274.4	11.9	3.22E-04	0.7	1.020	1.013	1.007
3H-3W, 75–77	14.36	0.3321	80.8	4.1	0.3328	173.5	33.2	0.3351	344.6	56.5	4.08E-04	0.3	1.009	1.007	1.002
3H-5W, 75–77	17.36	0.3299	62.6	5.5	0.3337	159.5	51.3	0.3364	328.3	38.2	4.97E-04	0.7	1.020	1.008	1.012
3H-7W, 35–37	19.96	0.3311	95.1	84.2	0.3342	202.7	1.8	0.3346	292.8	5.5	2.35E-04	0.4	1.011	1.001	1.009
4H-1W, 101–103	21.12	0.3327	188.9	52.5	0.3330	80.3	13.7	0.3343	340.8	34.1	2.08E-04	0.2	1.005	1.004	1.001
4H-3W, 75–77	23.86	0.3322	318.7	67.9	0.3337	141.3	22.1	0.3341	50.9	0.9	2.04E-04	0.2	1.006	1.001	1.004
4H-5W, 75–77	26.86	0.3306	64.8	79.1	0.3346	283.0	8.6	0.3349	192.0	6.6	1.77E-04	0.4	1.013	1.001	1.012
4H-7W, 34–36	29.45	0.3311	131.4	75.1	0.3341	16.1	6.5	0.3348	284.5	13.4	1.59E-04	0.4	1.011	1.002	1.009
5H-1W, 75–77	30.36	0.3319	322.3	12.2	0.3328	206.8	63.5	0.3352	57.6	23.2	7.83E-05	0.3	1.010	1.007	1.003
5H-3W, 70–72	33.31	0.3308	224.2	83.3	0.3327	348.5	3.8	0.3365	78.9	5.5	6.59E-05	0.6	1.017	1.011	1.006
5H-5W, 75–77	36.36	0.3316	187.2	4.2	0.3326	291.3	73.4	0.3358	96.0	16.1	5.72E-05	0.4	1.013	1.010	1.003
6H-1W, 74–76	39.85	0.3288	159.7	81.3	0.3333	261.4	1.8	0.3379	351.6	8.5	3.95E-05	0.9	1.028	1.014	1.014
6H-3W, 88–90	42.99	0.3308	345.9	56.2	0.3320	173.0	33.6	0.3371	80.8	3.3	5.60E-05	0.6	1.019	1.015	1.004
6H-5W, 74–76	45.85	0.3308	29.0	39.9	0.3329	237.4	46.5	0.3363	131.5	14.5	1.00E-04	0.5	1.017	1.010	1.006
6H-7W, 29–31	48.40	0.3326	17.3	39.1	0.3334	267.6	22.5	0.3341	155.4	42.5	1.61E-04	0.2	1.005	1.002	1.002
7H-1W, 68–70	49.29	0.3324	77.2	26.8	0.3329	229.5	60.3	0.3346	341.1	11.9	7.81E-05	0.2	1.007	1.005	1.001
7H-3W, 74–76	52.35	0.3292	30.9	33.0	0.3334	236.4	54.3	0.3374	128.9	12.2	6.31E-05	0.8	1.025	1.012	1.013
7H-5W, 74–76	55.36	0.3303	287.9	2.5	0.3326	21.7	56.8	0.3371	196.2	33.1	5.54E-05	0.7	1.020	1.013	1.007
7H-7W, 34–76	57.97	0.3288	184.0	80.4	0.3328	351.8	9.4	0.3384	82.2	2.0	5.63E-05	1.0	1.029	1.017	1.012
8H-1W, 74–76	58.85	0.3312	121.0	21.1	0.3323	217.6	16.6	0.3365	342.7	62.7	6.33E-05	0.5	1.016	1.013	1.003
8H-3W, 74–76	61.85	0.3280	78.7	7.3	0.3353	338.6	53.6	0.3368	173.9	35.4	6.19E-05	0.9	1.027	1.004	1.022
8H-5W, 74–76	64.85	0.3268	283.0	42.6	0.3352	84.5	45.9	0.3381	184.3	9.4	4.12E-05	1.1	1.035	1.009	1.026
8H-7W, 29–31	67.40	0.3306	195.2	52.8	0.3317	74.6	21.1	0.3377	332.3	29.0	5.05E-05	0.7	1.022	1.018	1.003
9H-1W, 74–76	68.35	0.3290	108.5	23.4	0.3304	246.4	59.7	0.3406	10.4	18.1	5.18E-05	1.2	1.035	1.031	1.004
9H-3W, 74–76	71.36	0.3311	88.2	66.9	0.3341	288.5	21.8	0.3349	195.6	7.3	1.42E-04	0.4	1.011	1.002	1.009
9H-5W, 74–76	74.36	0.3269	132.6	54.9	0.3330	311.1	35.1	0.3401	41.6	0.7	6.07E-05	1.3	1.040	1.021	1.019
9H-7W, 32–34	76.94	0.3309	316.0	44.5	0.3319	207.3	18.1	0.3372	101.5	40.0	7.02E-05	0.6	1.019	1.016	1.003
10H-1W, 74–76	77.85	0.3260	74.2	59.7	0.3335	282.7	27.2	0.3404	186.2	12.4	5.66E-05	1.4	1.044	1.021	1.023
10H-3W, 74–76	80.85	0.3245	220.8	71.5	0.3319	347.5	11.3	0.3436	80.5	14.4	5.30E-05	1.9	1.059	1.035	1.023
10H-5W, 74–76	83.85	0.3313	152.2	63.2	0.3337	294.1	21.7	0.3350	30.2	15.0	6.30E-05	0.4	1.011	1.004	1.007
10H-7W, 29–31	86.31	0.3283	192.5	62.4	0.3349	72.3	14.8	0.3368	335.9	22.8	1.05E-04	0.9	1.026	1.006	1.020
11H-1W, 74–76	87.35	0.3318	145.9	33.2	0.3334	43.4	18.3	0.3349	289.4	50.8	1.21E-04	0.3	1.009	1.005	1.005
11H-3W, 74–76	90.35	0.3317	37.3	62.4	0.3340	291.0	8.3	0.3342	196.9	26.1	1.23E-04	0.2	1.007	1.000	1.007
11H-5W, 83–85	93.44	0.3305	37.4	27.0	0.3316	247.5	59.5	0.3380	134.2	13.1	6.48E-05	0.8	1.023	1.019	1.003
11H-7W, 29–31	95.90	0.3300	3.6	1.9	0.3340	272.3	35.0	0.3360	96.2	55.0	6.55E-05	0.6	1.018	1.006	1.012
12H-1W, 74–76	96.85	0.3303	234.7	1.7	0.3335	144.5	6.7	0.3361	338.6	83.1	5.94E-05	0.6	1.018	1.008	1.010
12H-3W, 74–76	99.85	0.3296	251.1	55.6	0.3331	9.4	18.0	0.3373	109.4	28.3	4.99E-05	0.8	1.023	1.013	1.010
12H-5W, 74–76	102.85	0.2776	87.4	18.3	0.3230	332.3	52.1	0.3995	189.2	31.9	-4.87E-07	12.2	1.439	1.237	1.163
12H-7W, 29–31	105.40	0.2847	6.2	27.3	0.3513	100.1	7.4	0.3640	204.0	61.6	-1.82E-06	7.9	1.278	1.036	1.234
13H-1W, 74–76	106.35	0.2607	216.1	0.3	0.3433	124.1	82.3	0.3959	306.2	7.7	4.51E-07	13.5	1.519	1.153	1.317
13H-3W, 74–76	109.39	0.3049	126.5	68.3	0.3378	259.2	15.1	0.3573	353.4	15.2	-3.70E-06	5.2	1.172	1.058	1.108
13H-5W, 74–76	112.39	0.3250	88.2	27.9	0.3314	184.1	11.0	0.3436	293.6	59.6	1.12E-05	1.9	1.057	1.037	1.020
13H-7W, 30–32	114.75	0.3275	113.9	6.3	0.3352	287.5	83.7	0.3373	23.8	0.7	1.94E-05	1.0	1.030	1.006	1.023
14H-1W, 74–76	115.85	0.3295	314.2	34.2	0.3310	63.4	25.8	0.3394	182.0	44.7	1.90E-05	1.0	1.030	1.025	1.005
14H-3W, 74–76	118.85	0.3279	357.3	49.5	0.3348	257.7	8.1	0.3373	161.0	39.3	2.69E-05	0.9	1.029	1.008	1.021

Table T15 (continued).

Core, section, interval (cm)	Depth (mbsf)	τ_3	V_3 ($^{\circ}$)		V_2 ($^{\circ}$)		V_1 ($^{\circ}$)		Bulk susceptibility (SI)	Anisotropy (%)	P	L	F		
			Declination	Inclination	Declination	Inclination	Declination	Inclination							
14H-5W, 74–76	121.85	0.3319	212.5	42.5	0.3336	73.0	39.7	0.3345	323.8	21.6	5.95E–05	0.3	1.008	1.003	1.005
14H-7W, 29–31	124.40	0.3306	213.0	3.2	0.3336	307.3	53.1	0.3358	120.7	36.7	4.42E–05	0.5	1.016	1.006	1.009
15H-1W, 63–65	125.24	0.3292	125.5	55.6	0.3334	5.7	18.8	0.3374	265.4	27.6	5.06E–05	0.8	1.025	1.012	1.013
17X-1W, 82–84	127.83	0.3290	287.2	54.6	0.3327	114.6	35.2	0.3383	22.1	3.5	3.37E–05	0.9	1.028	1.017	1.011
17X-3W, 55–57	130.56	0.3256	296.0	33.4	0.3319	150.0	51.6	0.3424	37.6	16.9	2.00E–05	1.7	1.052	1.032	1.019
18X-1W, 61–63	132.22	0.3286	85.6	77.4	0.3314	287.0	11.8	0.3400	196.1	4.5	2.42E–05	1.1	1.035	1.026	1.008
18X-3W, 96–98	135.57	0.3268	73.2	1.5	0.3340	168.5	74.0	0.3392	342.8	16.0	3.85E–05	1.2	1.038	1.015	1.022
18X-5W, 40–42	138.01	0.3276	228.7	57.2	0.3342	38.8	32.4	0.3381	131.7	4.5	6.11E–05	1.1	1.032	1.012	1.020
20X-1W, 107–109	151.88	0.3286	353.3	81.2	0.3343	128.0	6.2	0.3371	218.7	6.2	1.05E–04	0.8	1.026	1.008	1.017
20X-3W, 35–37	154.16	0.3283	121.7	69.9	0.3349	18.4	4.8	0.3368	286.7	19.5	8.22E–05	0.9	1.026	1.006	1.020
20X-5W, 75–77	157.56	0.3270	113.8	45.6	0.3321	252.8	36.5	0.3409	359.8	21.7	2.81E–05	1.4	1.043	1.027	1.016
21X-1W, 63–65	159.06	0.3217	250.1	42.1	0.3259	96.7	44.7	0.3523	352.8	13.7	1.85E–05	3.1	1.095	1.081	1.013
22X-1W, 62–64	170.63	0.3207	316.8	29.3	0.3297	59.6	21.6	0.3496	180.3	52.3	1.59E–05	2.9	1.090	1.060	1.028
22X-3W, 117–119	174.18	0.3288	263.7	24.9	0.3324	15.3	38.4	0.3388	149.6	41.4	2.60E–05	1.0	1.031	1.019	1.011
22X-5W, 71–73	176.72	0.3287	318.0	48.3	0.3348	93.3	32.3	0.3364	199.1	23.3	3.44E–05	0.8	1.024	1.005	1.019
23X-1W, 33–35	179.94	0.3257	314.5	20.3	0.3355	61.7	38.6	0.3387	203.2	44.5	3.02E–05	1.3	1.040	1.009	1.030
23X-3W, 83–85	183.44	0.3280	328.8	47.6	0.3332	61.2	2.1	0.3388	153.1	42.4	6.59E–05	1.1	1.033	1.017	1.016
23X-5W, 52–54	186.13	0.3314	238.9	36.8	0.3336	94.5	47.4	0.3350	343.3	18.4	6.85E–05	0.4	1.011	1.004	1.007
24X-1W, 67–69	189.88	0.3308	309.5	74.9	0.3342	100.4	13.3	0.3350	192.1	7.1	1.35E–04	0.4	1.013	1.003	1.010
24X-3W, 47–49	192.68	0.3293	144.4	76.9	0.3344	238.4	0.9	0.3364	328.6	13.0	9.20E–05	0.7	1.021	1.006	1.015
24X-5W, 75–77	195.96	0.3212	213.1	36.2	0.3354	323.0	25.0	0.3434	79.3	43.5	2.48E–05	2.2	1.069	1.024	1.044
26X-1W, 32–34	199.63	0.3289	97.0	5.8	0.3347	193.7	48.9	0.3365	2.0	40.5	5.33E–05	0.8	1.023	1.005	1.018

τ_1 , τ_2 , and τ_3 are eigenvalues, and V_3 , V_2 , and V_1 are eigenvectors associated with minimum, intermediate, and maximum susceptibility, respectively. Measurement field = 300 A/m, sample volume = 7 cm³. P = anisotropy degree, L = lineation, F = foliation.

Table T16. Biostratigraphic and magnetostratigraphic datums, Hole U1409A. (Continued on next page.)

Datum tie point	Datum	Datum type	Zone/Subzone	Age (Ma)	Depth (mbsf)		
					Top	Bottom	Mid-point
D02	T <i>Pseudoemilia lacunosa</i>	Calcareous nannofossil	NN20	0.44	6.35	10.64	8.50
	T <i>Discoaster brouweri</i>	Calcareous nannofossil	NN19	1.93	10.64	15.85	13.25
	T <i>Discoaster pentaradiatus</i>	Calcareous nannofossil	NN17	2.39	10.64	15.85	13.25
D23	T <i>Reticulofenestra umbilicus</i> (>14 µm)	Calcareous nannofossil	NP23	32.02	31.85	34.85	33.35
	T <i>Coccolithus formosus</i>	Calcareous nannofossil	NP22	32.92	31.85	34.85	33.35
	T <i>Chiasmolithus grandis</i>	Calcareous nannofossil		37.98	31.85	34.85	33.35
D24	B <i>Dictyococcites bisectus</i> (>10 µm)*	Calcareous nannofossil		40.36	31.85	34.85	33.35
	T <i>Chiasmolithus solitus</i>	Calcareous nannofossil	NP17	40.40	37.85	38.70	38.28
	B <i>Reticulofenestra reticulata</i>	Calcareous nannofossil		41.66	44.44	47.40	45.92
	T <i>Nannotetra</i> spp.	Calcareous nannofossil		41.85	44.44	47.40	45.92
	B <i>Reticulofenestra umbilicus</i> (>14 µm)	Calcareous nannofossil		41.94	41.60	44.44	43.02
	T <i>Nannotetra fulgens</i>	Calcareous nannofossil		42.87	47.41	49.18	48.30
	T <i>Chiasmolithus gigas</i>	Calcareous nannofossil	NP15c	44.12	53.68	58.54	56.11
	B <i>Sphenolithus furcatolithoides</i>	Calcareous nannofossil			68.01	77.61	72.81
	B <i>Chiasmolithus gigas</i>	Calcareous nannofossil	NP15b	45.49	88.49	91.49	89.99
	B <i>Nannotetra fulgens</i>	Calcareous nannofossil		46.29	96.40	98.10	97.25
	B <i>Nannotetra cristata</i>	Calcareous nannofossil		47.73	101.03	101.10	101.07
	B <i>Blackites inflatus</i>	Calcareous nannofossil		47.84	101.03	101.10	101.07
	T <i>Discoaster lodoensis</i>	Calcareous nannofossil		47.41	101.10	105.96	103.53
D34	B <i>Discoaster sublodoensis</i> (5 rayed)	Calcareous nannofossil	NP14	49.11	119.21	122.20	120.71
	T <i>Tribachiatius orthostylus</i>	Calcareous nannofossil		50.50	119.21	122.20	120.71
	B <i>Dictyococcites/Reticulofenestra</i>	Calcareous nannofossil		50.50	126.09	126.97	126.53
	T <i>Toweius</i> spp.	Calcareous nannofossil		50.78	126.97	131.33	129.15
	B <i>Coccolithus crassus</i>	Calcareous nannofossil		51.64	126.97	131.33	129.15
	B <i>Discoaster lodoensis</i>	Calcareous nannofossil	NP12	53.70	141.22	151.15	146.18
	B <i>Girgisia gammation</i>	Calcareous nannofossil			141.22	151.15	146.18
	T <i>Tribachiatius contortus</i>	Calcareous nannofossil	NP11	54.17	151.15	153.65	152.40
	B <i>Tribachiatius orthostylus</i>	Calcareous nannofossil		54.37	153.65	153.80	153.73
D35	B <i>Tribachiatius contortus</i>	Calcareous nannofossil			154.25	154.28	154.27
	B <i>Discoaster diastypus</i>	Calcareous nannofossil		54.95	154.25	154.28	154.27
	T <i>Fasciculithus</i> spp.	Calcareous nannofossil		55.64	154.25	154.28	154.27
	B <i>Rhomboaster bramlettei</i>	Calcareous nannofossil	NP10	55.86	154.25	154.36	154.31
	B <i>Rhomboaster</i> spp. CNET	Calcareous nannofossil		55.96	154.36	154.57	154.47
	<i>Fasciculithus</i> diversity decline†	Calcareous nannofossil		56.00	154.36	154.57	154.47
	T <i>Fasciculithus alani</i> †	Calcareous nannofossil		56.00	154.36	154.57	154.47
	T <i>Ericsonia robusta</i> (>9 µm)†	Calcareous nannofossil		57.10	155.30	157.95	156.62
	B <i>Discoaster multiradiatus</i>	Calcareous nannofossil	NP9a	57.21	157.95	160.59	159.27
	Tc <i>Sphenolithus anarrhopus</i>	Calcareous nannofossil			157.95	160.59	159.27
D37	B <i>Discoaster delicatus</i> †	Calcareous nannofossil		57.45	157.95	160.59	159.27
	B <i>Ericsonia robusta</i> (>9 µm)†	Calcareous nannofossil		57.54	157.95	160.59	159.27
	Tc <i>Discoaster backmani</i> †	Calcareous nannofossil		57.57	157.95	160.59	159.27
	B <i>Discoaster backmani</i> †	Calcareous nannofossil		58.28	160.59	162.73	161.66
	B <i>Heliolithus riedellii</i>	Calcareous nannofossil	NP8	58.70			
	B <i>Discoaster mohleri</i>	Calcareous nannofossil		58.97	175.28	178.01	176.65
	B <i>Sphenolithus anarrhopus</i> †	Calcareous nannofossil		59.40	180.35	181.85	181.10
	B <i>Heliolithus kleinpellii</i>	Calcareous nannofossil	NP6	59.54	180.35	181.85	181.10
	B <i>Heliolithus cantabriae</i>	Calcareous nannofossil		59.60	184.74	187.66	186.20
D31	B <i>Fasciculithus tympaniformis</i>	Calcareous nannofossil	NP5	61.51	191.50	194.53	193.02
	B <i>Ellipsolithus macellus</i>	Calcareous nannofossil		63.25			
	B <i>Dictyoprora mongolfieri</i>	Radiolarian	RP11	47.98		105.96	105.96
	B <i>Theocorys plesioanacista</i>	Radiolarian	RP9	50.50	115.46	124.91	120.19
	T <i>Buryella tetradica</i>	Radiolarian		50.87	124.91	126.09	125.50
	B <i>Buryella clinata</i>	Radiolarian	RP8	53.35	131.33	160.59	145.96
	X <i>Bekoma campechensis</i> - <i>B. bidartensis</i>	Radiolarian		58.23	160.59	162.71	161.65
	T <i>Buryella pentadica</i>	Radiolarian	RP6c	59.71	162.71		162.71
D32	T <i>Morozovella aragonensis</i>	Planktonic foraminifer	E10/E9	43.26	53.68	58.50	56.09
	B <i>Globigerinatheka kugleri</i>	Planktonic foraminifer	E9/E8	43.88	65.29	67.97	66.63
	B <i>Guembelitrioides nuttalli</i>	Planktonic foraminifer	E8/E7b	45.72	105.91	108.13	107.02
	B <i>Turborotalita frontosa</i>	Planktonic foraminifer	E7b/E7a	48.31	115.41	117.70	116.56
	B <i>Acarinina cuneicamerata</i>	Planktonic foraminifer	E7a/E6	50.20	123.70	124.86	124.28
	T <i>Morozovella subbotinae</i>	Planktonic foraminifer	E6/E5	50.67	124.86	125.31	125.09
	B <i>Morozovella aragonensis</i>	Planktonic foraminifer	E5/E4	52.54	135.47	138.96	137.22
	B <i>Morozovella formosa</i>	Planktonic foraminifer	E4/E3	54.61	141.20	151.35	146.28
	T <i>Globanomalina pseudomenardii</i>	Planktonic foraminifer	P5/P4c	57.10	155.59	157.94	156.77
	B <i>Acarinina soldadoensis</i>	Planktonic foraminifer	P4c/P4b	57.79	161.73	162.68	162.21
D33	B <i>Globanomalina pseudomenardii</i>	Planktonic foraminifer	P4/P3	60.37	175.5	179.32	177.41

Table T16 (continued).

Datum tie point	Datum	Datum type	Zone/ Subzone	Age (Ma)	Depth (mbsf)		
					Top	Bottom	Mid-point
D38	B <i>Morozovella angulata</i>	Planktonic foraminifer	P3/P2	62.29	197.75	200.00	198.88
D01	C1n (Brunhes)/C1r.1r (Matuyama)	Chron boundary		0.78			8.97
D03	C6Cr/C7n.1n	Chron boundary		23.96			12.64
D04	C7n.1n/C7n.1r	Chron boundary		24.00			12.74
D05	C7n.1r/C7n.2n	Chron boundary		24.11			13.29
D06	C7n.2n/C7r	Chron boundary		24.47			14.56
D07	C7r/C7An	Chron boundary		24.76			15.89
D08	C7An/C7Ar	Chron boundary		24.98			17.19
D09	C7Ar/C8n.1n	Chron boundary		25.10			17.31
D10	C8n.1n/C8n.1r	Chron boundary		25.26			18.34
D11	C8n.1r/C8n.2n	Chron boundary		25.30			18.44
D12	C8n.2n/C8r	Chron boundary		25.99			19.83
D13	C8r/C9n	Chron boundary		26.42			20.19
D14	C10n.1n/C10n.1r	Chron boundary		28.09			22.23
D15	C10n.1r/C10n.2n	Chron boundary		28.14			22.37
D16	C10n.2n/C10r	Chron boundary		28.28			22.69
D17	C10r/C11n.1n	Chron boundary		29.18			25.62
D18	C11n.1n/C11n.1r	Chron boundary		29.48			26.28
D19	C11n.1r/C11n.2n	Chron boundary		29.53			26.46
D20	C11n.2n/C11r	Chron boundary		29.97			27.23
D21	C11r/C12n	Chron boundary		30.59			28.13
D22	C12n/C12r	Chron boundary		31.03			28.65
	C13n/C13r	Chron boundary			33.71		31.93
D25	C19r/C20n	Chron boundary		42.30			46.25
D26	C20n/C20r	Chron boundary		43.43			57.95
D27	C20r/C21n	Chron boundary		45.72			87.99
D28	C21n/C21r	Chron boundary		47.35			101.35
D29	C21r/C22n	Chron boundary		48.57			107.31
D30	C22n/C22r	Chron boundary		49.34			111.08

* = from Fornaciari et al. (2010) recalibrated to GTS2012, † = from Agnini et al. (2007) recalibrated to GTS2012. B = base, T = top, Tc = Top common, X = faunal crossover.



Table T17. Datum tie points, Hole U1409A.

Datum tie point	Datum	Datum type	Zone	Age (Ma)	Mid-point depth (mbsf)	Distance (m)	Duration (Ma)	LSR (cm/k.y.)	Notes
D01	C1n (Brunhes)/C1r.1r (Matuyama)	Chron boundary		0.78	8.97				
D02	T <i>Discoaster brouweri</i>	Calcareous nannofossil	NN19	1.93	13.25	3.68	1.15	0.32	
D03	C6Cr/C7n.1n	Chron boundary		23.96	12.64	0.00	22.03	0.00	Hiatus
D04	C7n.1n/C7n.1r	Chron boundary		24.00	12.74	0.10	0.04	0.26	
D05	C7n.1r/C7n.2n	Chron boundary		24.11	13.29	0.55	0.11	0.50	
D06	C7n.2n/C7r	Chron boundary		24.47	14.56	1.27	0.36	0.35	
D07	C7r/C7An	Chron boundary		24.76	15.89	1.34	0.29	0.47	
D08	C7An/C7Ar	Chron boundary		24.98	17.19	1.30	0.22	0.58	
D09	C7Ar/C8n.1n	Chron boundary		25.10	17.31	0.12	0.11	0.10	
D10	C8n.1n/C8n.1r	Chron boundary		25.26	18.34	1.04	0.16	0.63	
D11	C8n.1r/C8n.2n	Chron boundary		25.30	18.44	0.10	0.04	0.25	
D12	C8n.2n/C8r	Chron boundary		25.99	19.83	1.39	0.68	0.20	
D13	C8r/C9n	Chron boundary		26.42	20.19	0.36	0.43	0.08	Average rate = 0.26 cm/k.y.
D14	C10n.1n/C10n.1r	Chron boundary		28.09	22.23	2.04	1.67	0.12	
D15	C10n.1r/C10n.2n	Chron boundary		28.14	22.37	0.14	0.05	0.26	
D16	C10n.2n/C10r	Chron boundary		28.28	22.69	0.32	0.14	0.24	
D17	C10r/C11n.1n	Chron boundary		29.18	25.62	2.93	0.91	0.32	
D18	C11n.1n/C11n.1r	Chron boundary		29.48	26.28	0.66	0.29	0.22	
D19	C11n.1r/C11n.2n	Chron boundary		29.53	26.46	0.18	0.05	0.36	
D20	C11n.2n/C11r	Chron boundary		29.97	27.23	0.77	0.44	0.17	
D21	C11r/C12n	Chron boundary		30.59	28.13	0.90	0.62	0.14	
D22	C12n/C12r	Chron boundary		31.03	28.65	0.52	0.44	0.12	
D23	T <i>Reticulofenestra umbilicus</i> (>14 µm)	Calcareous nannofossil	NP23	32.02	33.35	4.70	0.99	0.48	
D24	B <i>Dictyococcites bisectus</i> (>10 µm)	Calcareous nannofossil		40.36	33.35	0.00	8.34	0.00	Hiatus
D25	C19r/C20n	Chron boundary		42.30	46.25	12.90	1.94	0.66	Average rate = 0.80 cm/k.y.
D26	C20n/C20r	Chron boundary		43.43	57.95	11.70	1.13	1.03	
D27	C20r/C21n	Chron boundary		45.72	87.99	30.05	2.29	1.31	
D28	C21n/C21r	Chron boundary		47.35	101.35	13.36	1.62	0.82	
D29	C21r/C22n	Chron boundary		48.57	107.31	5.96	1.22	0.49	Average rate = 0.65 cm/k.y.
D30	C22n/C22r	Chron boundary		49.34	111.08	3.77	0.78	0.49	
D31	B <i>Thecocrys plesioanacasta</i>	Radiolarian	RP9	50.50	120.19	9.11	1.16	0.79	
D32	T <i>Buryella tetradica</i>	Radiolarian		50.87	125.50	5.31	0.37	1.44	
D33	B <i>Buryella clinata</i>	Radiolarian	RP8	53.35	145.96	20.46	2.48	0.82	Average rate = 0.82 cm/k.y.
D34	T <i>Tribrachiatius contortus</i>	Calcareous nannofossil	NP11	54.17	152.40	6.44	0.82	0.79	
D35	T <i>Fasciculithus</i> spp.	Calcareous nannofossil		55.64	154.27	1.86	1.47	0.13	Average rate = 0.23 cm/k.y.
D36	X <i>Bekoma campechensis</i> – <i>B. bidartensis</i>	Radiolarian	RP7	58.23	161.65	7.38	2.59	0.28	
D37	B <i>Heliolithus cantabriae</i>	Calcareous nannofossil		59.60	186.20	24.56	1.37	1.80	
D38	B <i>Morozovella angulata</i>	Planktonic foraminifer	P3/P2	62.29	198.88	12.68	2.69	0.47	

LSR = linear sedimentation rate. T = top, B = base, X = faunal crossover.



Table T18. Carbonate content accumulation rates, Site U1409. (Continued on next four pages.)

Age (Ma)	LSR (cm/k.y.)	Dry density (g/cm ³)	CaCO ₃ (wt%)	MAR (g/cm ² /k.y.)	CAR (g/cm ² /k.y.)	nCAR (g/cm ² /k.y.)
0.8	0.32	0.81	47.40	0.26	0.12	0.14
1.0	0.32	0.68	33.85	0.22	0.07	0.14
1.2	0.32	0.71	25.41	0.23	0.06	0.17
1.4	0.32	1.07	27.55	0.34	0.09	0.25
1.6	0.32	1.06	23.01	0.34	0.08	0.26
1.8	0.32	0.97	17.04	0.31	0.05	0.26
2.0	0.00	0.94	14.72	0.00	0.00	0.00
2.2	0.00	0.94	14.90	0.00	0.00	0.00
2.4	0.00	0.94	15.08	0.00	0.00	0.00
2.6	0.00	0.94	15.26	0.00	0.00	0.00
2.8	0.00	0.94	15.44	0.00	0.00	0.00
3.0	0.00	0.94	15.63	0.00	0.00	0.00
3.2	0.00	0.94	15.81	0.00	0.00	0.00
3.4	0.00	0.94	15.99	0.00	0.00	0.00
3.6	0.00	0.94	16.17	0.00	0.00	0.00
3.8	0.00	0.94	16.36	0.00	0.00	0.00
4.0	0.00	0.94	16.54	0.00	0.00	0.00
4.2	0.00	0.94	16.72	0.00	0.00	0.00
4.4	0.00	0.94	16.90	0.00	0.00	0.00
4.6	0.00	0.94	17.09	0.00	0.00	0.00
4.8	0.00	0.94	17.27	0.00	0.00	0.00
5.0	0.00	0.94	17.45	0.00	0.00	0.00
5.2	0.00	0.95	17.63	0.00	0.00	0.00
5.4	0.00	0.95	17.81	0.00	0.00	0.00
5.6	0.00	0.95	18.00	0.00	0.00	0.00
5.8	0.00	0.95	18.18	0.00	0.00	0.00
6.0	0.00	0.95	18.36	0.00	0.00	0.00
6.2	0.00	0.95	18.54	0.00	0.00	0.00
6.4	0.00	0.95	18.73	0.00	0.00	0.00
6.6	0.00	0.95	18.91	0.00	0.00	0.00
6.8	0.00	0.95	19.09	0.00	0.00	0.00
7.0	0.00	0.95	19.27	0.00	0.00	0.00
7.2	0.00	0.95	19.45	0.00	0.00	0.00
7.4	0.00	0.95	19.64	0.00	0.00	0.00
7.6	0.00	0.95	19.82	0.00	0.00	0.00
7.8	0.00	0.95	20.00	0.00	0.00	0.00
8.0	0.00	0.95	20.18	0.00	0.00	0.00
8.2	0.00	0.95	20.37	0.00	0.00	0.00
8.4	0.00	0.95	20.55	0.00	0.00	0.00
8.6	0.00	0.96	20.73	0.00	0.00	0.00
8.8	0.00	0.96	20.91	0.00	0.00	0.00
9.0	0.00	0.96	21.10	0.00	0.00	0.00
9.2	0.00	0.96	21.28	0.00	0.00	0.00
9.4	0.00	0.96	21.46	0.00	0.00	0.00
9.6	0.00	0.96	21.64	0.00	0.00	0.00
9.8	0.00	0.96	21.82	0.00	0.00	0.00
10.0	0.00	0.96	22.01	0.00	0.00	0.00
10.2	0.00	0.96	22.19	0.00	0.00	0.00
10.4	0.00	0.96	22.37	0.00	0.00	0.00
10.6	0.00	0.96	22.55	0.00	0.00	0.00
10.8	0.00	0.96	22.74	0.00	0.00	0.00
11.0	0.00	0.96	22.92	0.00	0.00	0.00
11.2	0.00	0.96	23.10	0.00	0.00	0.00
11.4	0.00	0.96	23.28	0.00	0.00	0.00
11.6	0.00	0.96	23.47	0.00	0.00	0.00
11.8	0.00	0.96	23.65	0.00	0.00	0.00
12.0	0.00	0.96	23.83	0.00	0.00	0.00
12.2	0.00	0.97	24.01	0.00	0.00	0.00
12.4	0.00	0.97	24.19	0.00	0.00	0.00
12.6	0.00	0.97	24.38	0.00	0.00	0.00
12.8	0.00	0.97	24.56	0.00	0.00	0.00
13.0	0.00	0.97	24.74	0.00	0.00	0.00
13.2	0.00	0.97	24.92	0.00	0.00	0.00
13.4	0.00	0.97	25.11	0.00	0.00	0.00
13.6	0.00	0.97	25.29	0.00	0.00	0.00
13.8	0.00	0.97	25.47	0.00	0.00	0.00
14.0	0.00	0.97	25.65	0.00	0.00	0.00
14.2	0.00	0.97	25.84	0.00	0.00	0.00
14.4	0.00	0.97	26.02	0.00	0.00	0.00



Table T18 (continued). (Continued on next page.)

Age (Ma)	LSR (cm/k.y.)	Dry density (g/cm ³)	CaCO ₃ (wt%)	MAR (g/cm ² /k.y.)	CAR (g/cm ² /k.y.)	nCAR (g/cm ² /k.y.)
14.6	0.00	0.97	26.20	0.00	0.00	0.00
14.8	0.00	0.97	26.38	0.00	0.00	0.00
15.0	0.00	0.97	26.56	0.00	0.00	0.00
15.2	0.00	0.97	26.75	0.00	0.00	0.00
15.4	0.00	0.97	26.93	0.00	0.00	0.00
15.6	0.00	0.98	27.11	0.00	0.00	0.00
15.8	0.00	0.98	27.29	0.00	0.00	0.00
16.0	0.00	0.98	27.48	0.00	0.00	0.00
16.2	0.00	0.98	27.66	0.00	0.00	0.00
16.4	0.00	0.98	27.84	0.00	0.00	0.00
16.6	0.00	0.98	28.02	0.00	0.00	0.00
16.8	0.00	0.98	28.20	0.00	0.00	0.00
17.0	0.00	0.98	28.39	0.00	0.00	0.00
17.2	0.00	0.98	28.57	0.00	0.00	0.00
17.4	0.00	0.98	28.75	0.00	0.00	0.00
17.6	0.00	0.98	28.93	0.00	0.00	0.00
17.8	0.00	0.98	29.12	0.00	0.00	0.00
18.0	0.00	0.98	29.30	0.00	0.00	0.00
18.2	0.00	0.98	29.48	0.00	0.00	0.00
18.4	0.00	0.98	29.66	0.00	0.00	0.00
18.6	0.00	0.98	29.85	0.00	0.00	0.00
18.8	0.00	0.98	30.03	0.00	0.00	0.00
19.0	0.00	0.98	30.21	0.00	0.00	0.00
19.2	0.00	0.99	30.39	0.00	0.00	0.00
19.4	0.00	0.99	30.57	0.00	0.00	0.00
19.6	0.00	0.99	30.76	0.00	0.00	0.00
19.8	0.00	0.99	30.94	0.00	0.00	0.00
20.0	0.00	0.99	31.12	0.00	0.00	0.00
20.2	0.00	0.99	31.30	0.00	0.00	0.00
20.4	0.00	0.99	31.49	0.00	0.00	0.00
20.6	0.00	0.99	31.67	0.00	0.00	0.00
20.8	0.00	0.99	31.85	0.00	0.00	0.00
21.0	0.00	0.99	32.03	0.00	0.00	0.00
21.2	0.00	0.99	32.22	0.00	0.00	0.00
21.4	0.00	0.99	32.40	0.00	0.00	0.00
21.6	0.00	0.99	32.58	0.00	0.00	0.00
21.8	0.00	0.99	32.76	0.00	0.00	0.00
22.0	0.00	0.99	32.94	0.00	0.00	0.00
22.2	0.00	0.99	33.13	0.00	0.00	0.00
22.4	0.00	0.99	33.31	0.00	0.00	0.00
22.6	0.00	1.00	33.49	0.00	0.00	0.00
22.8	0.00	1.00	33.67	0.00	0.00	0.00
23.0	0.00	1.00	33.86	0.00	0.00	0.00
23.2	0.00	1.00	34.04	0.00	0.00	0.00
23.4	0.00	1.00	34.22	0.00	0.00	0.00
23.6	0.00	1.00	34.40	0.00	0.00	0.00
23.8	0.00	1.00	34.58	0.00	0.00	0.00
24.0	0.50	1.00	34.77	0.50	0.18	0.33
24.2	0.35	1.00	34.95	0.35	0.12	0.23
24.4	0.35	1.04	30.74	0.36	0.11	0.25
24.6	0.47	1.12	21.40	0.52	0.11	0.41
24.8	0.58	1.05	12.19	0.61	0.07	0.54
25.0	0.10	0.90	4.76	0.09	0.00	0.09
25.2	0.63	0.77	1.40	0.48	0.01	0.47
25.4	0.20	0.76	0.36	0.15	0.00	0.15
25.6	0.20	0.82	0.35	0.17	0.00	0.16
25.8	0.20	0.87	0.33	0.18	0.00	0.18
26.0	0.08	0.91	0.32	0.08	0.00	0.08
26.2	0.08	0.88	0.34	0.07	0.00	0.07
26.4	0.08	0.84	0.37	0.07	0.00	0.07
26.6	0.12	0.80	0.40	0.10	0.00	0.10
26.8	0.12	0.76	0.42	0.09	0.00	0.09
27.0	0.12	0.73	0.44	0.09	0.00	0.09
27.2	0.12	0.72	0.43	0.09	0.00	0.09
27.4	0.12	0.73	0.41	0.09	0.00	0.09
27.6	0.12	0.75	0.39	0.09	0.00	0.09
27.8	0.12	0.76	0.67	0.09	0.00	0.09
28.0	0.12	0.77	3.85	0.09	0.00	0.09
28.2	0.24	0.79	7.73	0.19	0.01	0.17



Table T18 (continued). (Continued on next page.)

Age (Ma)	LSR (cm/k.y.)	Dry density (g/cm ³)	CaCO ₃ (wt%)	MAR (g/cm ² /k.y.)	CAR (g/cm ² /k.y.)	nCAR (g/cm ² /k.y.)
28.4	0.32	0.81	11.61	0.26	0.03	0.23
28.6	0.32	0.83	13.07	0.27	0.04	0.23
28.8	0.32	0.85	12.20	0.28	0.03	0.24
29.0	0.32	0.87	12.04	0.28	0.03	0.25
29.2	0.22	0.87	14.00	0.20	0.03	0.17
29.4	0.22	0.87	16.10	0.20	0.03	0.16
29.6	0.17	0.87	17.99	0.15	0.03	0.13
29.8	0.17	0.88	19.60	0.15	0.03	0.12
30.0	0.14	0.88	21.22	0.13	0.03	0.10
30.2	0.14	0.88	22.83	0.13	0.03	0.10
30.4	0.14	0.89	24.22	0.13	0.03	0.10
30.6	0.12	0.90	22.52	0.11	0.02	0.08
30.8	0.12	0.91	19.85	0.11	0.02	0.09
31.0	0.12	0.92	17.18	0.11	0.02	0.09
31.2	0.48	0.89	15.91	0.42	0.07	0.36
31.4	0.48	0.81	18.01	0.38	0.07	0.31
31.6	0.48	0.83	20.47	0.39	0.08	0.31
31.8	0.48	0.85	37.44	0.41	0.15	0.25
32.0	0.48	0.87	51.83	0.41	0.21	0.20
32.2	0.00	0.87	52.02	0.00	0.00	0.00
32.4	0.00	0.86	51.73	0.00	0.00	0.00
32.6	0.00	0.86	51.43	0.00	0.00	0.00
32.8	0.00	0.86	51.14	0.00	0.00	0.00
33.0	0.00	0.86	50.85	0.00	0.00	0.00
33.2	0.00	0.86	50.55	0.00	0.00	0.00
33.4	0.00	0.85	50.26	0.00	0.00	0.00
33.6	0.00	0.85	49.97	0.00	0.00	0.00
33.8	0.00	0.85	49.67	0.00	0.00	0.00
34.0	0.00	0.85	49.38	0.00	0.00	0.00
34.2	0.00	0.85	49.09	0.00	0.00	0.00
34.4	0.00	0.84	48.79	0.00	0.00	0.00
34.6	0.00	0.84	48.50	0.00	0.00	0.00
34.8	0.00	0.84	48.21	0.00	0.00	0.00
35.0	0.00	0.84	47.91	0.00	0.00	0.00
35.2	0.00	0.84	47.62	0.00	0.00	0.00
35.4	0.00	0.83	47.33	0.00	0.00	0.00
35.6	0.00	0.83	47.03	0.00	0.00	0.00
35.8	0.00	0.83	46.74	0.00	0.00	0.00
36.0	0.00	0.83	46.45	0.00	0.00	0.00
36.2	0.00	0.83	46.15	0.00	0.00	0.00
36.4	0.00	0.82	45.86	0.00	0.00	0.00
36.6	0.00	0.82	45.57	0.00	0.00	0.00
36.8	0.00	0.82	45.28	0.00	0.00	0.00
37.0	0.00	0.82	44.98	0.00	0.00	0.00
37.2	0.00	0.82	44.69	0.00	0.00	0.00
37.4	0.00	0.81	44.40	0.00	0.00	0.00
37.6	0.00	0.81	44.10	0.00	0.00	0.00
37.8	0.00	0.81	43.81	0.00	0.00	0.00
38.0	0.00	0.81	43.52	0.00	0.00	0.00
38.2	0.00	0.81	43.22	0.00	0.00	0.00
38.4	0.00	0.80	42.93	0.00	0.00	0.00
38.6	0.00	0.80	42.64	0.00	0.00	0.00
38.8	0.00	0.80	42.34	0.00	0.00	0.00
39.0	0.00	0.80	42.05	0.00	0.00	0.00
39.2	0.00	0.80	41.76	0.00	0.00	0.00
39.4	0.00	0.79	41.46	0.00	0.00	0.00
39.6	0.00	0.79	41.17	0.00	0.00	0.00
39.8	0.00	0.79	40.88	0.00	0.00	0.00
40.0	0.00	0.79	40.58	0.00	0.00	0.00
40.2	0.00	0.79	40.29	0.00	0.00	0.00
40.4	0.66	0.78	40.00	0.52	0.21	0.31
40.6	0.66	0.79	39.42	0.52	0.21	0.32
40.8	0.66	0.81	43.84	0.54	0.24	0.30
41.0	0.66	0.83	58.08	0.55	0.32	0.23
41.2	0.66	0.80	52.02	0.53	0.28	0.25
41.4	0.66	0.82	49.23	0.55	0.27	0.28
41.6	0.66	0.87	43.49	0.58	0.25	0.33
41.8	0.66	0.87	38.76	0.58	0.22	0.35
42.0	0.66	0.87	47.60	0.58	0.27	0.30



Table T18 (continued). (Continued on next page.)

Age (Ma)	LSR (cm/k.y.)	Dry density (g/cm ³)	CaCO ₃ (wt%)	MAR (g/cm ² /k.y.)	CAR (g/cm ² /k.y.)	nCAR (g/cm ² /k.y.)
42.2	0.66	0.88	44.49	0.58	0.26	0.32
42.4	1.03	0.88	33.36	0.91	0.30	0.60
42.6	1.03	0.81	32.12	0.83	0.27	0.57
42.8	1.03	0.83	31.57	0.86	0.27	0.59
43.0	1.03	0.86	31.27	0.89	0.28	0.61
43.2	1.03	0.88	33.41	0.91	0.30	0.61
43.4	1.03	0.86	54.86	0.88	0.49	0.40
43.6	1.31	0.87	46.60	1.14	0.53	0.61
43.8	1.31	0.85	49.61	1.12	0.55	0.56
44.0	1.31	0.86	51.23	1.13	0.58	0.55
44.2	1.31	0.86	52.97	1.13	0.60	0.53
44.4	1.31	0.93	45.79	1.22	0.56	0.66
44.6	1.31	0.90	36.85	1.18	0.43	0.74
44.8	1.31	0.92	37.63	1.21	0.46	0.76
45.0	1.31	0.95	42.57	1.25	0.53	0.72
45.2	1.31	0.99	45.26	1.30	0.59	0.71
45.4	1.31	1.01	50.18	1.32	0.66	0.66
45.6	1.31	1.02	48.11	1.34	0.64	0.69
45.8	0.82	1.06	48.36	0.87	0.42	0.45
46.0	0.82	1.06	39.58	0.87	0.34	0.52
46.2	0.82	1.05	40.00	0.86	0.35	0.52
46.4	0.82	1.09	50.83	0.89	0.45	0.44
46.6	0.82	1.05	45.52	0.86	0.39	0.47
46.8	0.82	1.03	51.02	0.85	0.43	0.41
47.0	0.82	1.06	77.32	0.87	0.67	0.20
47.2	0.82	1.03	61.60	0.85	0.52	0.33
47.4	0.49	1.05	75.61	0.51	0.39	0.12
47.6	0.49	1.10	88.66	0.54	0.48	0.06
47.8	0.49	1.05	90.68	0.51	0.47	0.05
48.0	0.49	1.00	85.71	0.49	0.42	0.07
48.2	0.49	0.98	81.78	0.48	0.39	0.09
48.4	0.49	1.02	86.63	0.50	0.43	0.07
48.6	0.87	1.07	87.75	0.93	0.81	0.11
48.8	0.87	1.02	87.01	0.89	0.77	0.12
49.0	0.87	1.05	86.66	0.91	0.79	0.12
49.2	0.87	1.11	89.00	0.96	0.86	0.11
49.4	0.53	1.13	91.08	0.60	0.55	0.05
49.6	0.53	1.08	86.33	0.57	0.49	0.08
49.8	0.53	1.11	89.40	0.59	0.53	0.06
50.0	0.53	1.13	92.22	0.60	0.55	0.05
50.2	0.53	1.12	92.90	0.59	0.55	0.04
50.4	0.53	1.23	92.84	0.65	0.60	0.05
50.6	1.44	1.27	90.05	1.83	1.65	0.18
50.8	1.44	1.22	89.69	1.76	1.58	0.18
51.0	0.82	1.15	89.37	0.95	0.85	0.10
51.2	0.82	1.23	83.29	1.01	0.84	0.17
51.4	0.82	1.27	86.09	1.05	0.90	0.15
51.6	0.82	1.24	89.04	1.02	0.91	0.11
51.8	0.82	1.27	89.50	1.05	0.94	0.11
52.0	0.82	1.30	83.37	1.07	0.89	0.18
52.2	0.82	1.32	79.03	1.09	0.86	0.23
52.4	0.82	1.34	75.79	1.10	0.84	0.27
52.6	0.82	1.34	75.85	1.11	0.84	0.27
52.8	0.82	1.35	76.12	1.11	0.85	0.27
53.0	0.82	1.35	76.38	1.11	0.85	0.26
53.2	0.82	1.36	76.65	1.12	0.86	0.26
53.4	0.79	1.36	76.92	1.07	0.82	0.25
53.6	0.79	1.37	77.19	1.07	0.83	0.24
53.8	0.79	1.37	77.46	1.08	0.83	0.24
54.0	0.79	1.37	77.37	1.08	0.83	0.24
54.2	0.13	1.35	75.71	0.17	0.13	0.04
54.4	0.13	1.34	73.83	0.17	0.13	0.04
54.6	0.13	1.36	72.64	0.17	0.13	0.05
54.8	0.13	1.39	71.65	0.18	0.13	0.05
55.0	0.13	1.41	72.01	0.18	0.13	0.05
55.2	0.13	1.44	72.78	0.18	0.13	0.05
55.4	0.13	1.45	73.55	0.18	0.14	0.05
55.6	0.13	1.44	66.61	0.18	0.12	0.06
55.8	0.28	1.42	62.91	0.40	0.25	0.15



Table T18 (continued).

Age (Ma)	LSR (cm/k.y.)	Dry density (g/cm ³)	CaCO ₃ (wt%)	MAR (g/cm ² /k.y.)	CAR (g/cm ² /k.y.)	nCAR (g/cm ² /k.y.)
56.0	0.28	1.40	80.03	0.40	0.32	0.08
56.2	0.28	1.39	81.43	0.40	0.32	0.07
56.4	0.28	1.37	82.61	0.39	0.32	0.07
56.6	0.28	1.35	84.93	0.38	0.33	0.06
56.8	0.28	1.30	81.81	0.37	0.30	0.07
57.0	0.28	1.25	77.24	0.36	0.27	0.08
57.2	0.28	1.21	76.94	0.34	0.26	0.08
57.4	0.28	1.18	80.26	0.34	0.27	0.07
57.6	0.28	1.16	81.24	0.33	0.27	0.06
57.8	0.28	1.09	78.96	0.31	0.24	0.07
58.0	0.28	1.09	76.87	0.31	0.24	0.07
58.2	0.28	1.14	79.76	0.33	0.26	0.07
58.4	1.80	1.20	81.57	2.16	1.76	0.40
58.6	1.80	1.27	82.40	2.29	1.88	0.40
58.8	1.80	1.31	80.25	2.35	1.89	0.46
59.0	1.80	1.30	82.99	2.33	1.93	0.40
59.2	1.80	1.40	83.17	2.52	2.10	0.42
59.4	1.80	1.42	85.68	2.55	2.18	0.36
59.6	0.47	1.37	84.66	0.64	0.54	0.10
59.8	0.47	1.32	83.30	0.62	0.52	0.10
60.0	0.47	1.32	81.83	0.62	0.51	0.11
60.2	0.47	1.33	80.36	0.63	0.50	0.12
60.4	0.47	1.35	80.07	0.64	0.51	0.13
60.6	0.47	1.38	81.66	0.65	0.53	0.12
60.8	0.47	1.36	81.28	0.64	0.52	0.12
61.0	0.47	1.33	80.70	0.63	0.51	0.12
61.2	0.47	1.33	80.92	0.62	0.51	0.12
61.4	0.47	1.38	79.68	0.65	0.52	0.13

LSR = linear sedimentation rate, MAR = mass accumulation rate, CAR = carbonate accumulation rate, nCAR = noncarbonate accumulation rate.

Table T19. Geochemistry of headspace gas samples, Hole U1409A.

Core, section, interval (cm)	Depth (mbsf)	Methane (ppmv)
342-U1409-A		
1H-1, 0–5	0.00	1.79
2H-7, 0–5	10.00	2.21
3H-7, 0–5	19.60	2.16
4H-7, 0–5	29.10	2.12
5H-6, 0–5	37.10	2.26
6H-7, 0–5	48.10	2.34
7H-7, 0–5	57.62	2.48
8H-7, 0–5	67.10	2.98
9H-7, 0–5	76.61	3.03
10H-7, 0–5	86.01	2.84
11H-7, 0–5	95.60	3.37
12H-7, 0–5	105.10	3.91
13H-7, 0–5	114.44	4.19
14H-7, 0–5	124.10	3.82
16H-1, 0–5	126.10	3.49
17X-3, 0–5	130.00	3.38
18X-5, 0–5	137.60	4.27
20X-7, 0–5	159.72	4.61
21X-2, 0–5	161.90	3.67
22X-7, 0–5	178.61	4.64
23X-6, 0–5	187.10	4.11
24X-5, 0–5	195.20	2.89
26X-1, 0–5	199.30	6.43



Table T20. Interstitial water constituents, Hole U1409A.

Core, section, interval (cm)	Depth (mbsf)	pH	Alkalinity (mM)	Ammonium (μM)	Salinity	Cl^- (mM)	Na^+ (mM)	SO_4^{2-} (mM)	HPO_4^{2-} (μM)	B (μM)	Mn^{2+} (μM)	Fe^{2+} (μM)	Ca^{2+} (mM)	Mg^{2+} (mM)	K^+ (mM)	Mg/Ca
342-U1409A-																
2H-6, 135–140	9.95	7.599	3.737	29	37	ND	494.204	ND	BDL	375.740	53.607	BDL	11.686	53.607	15.259	4.6
3H-6, 145–150	19.55	7.441	3.686	22	37	589.681	484.273	28.124	BDL	465.037	52.517	BDL	11.504	52.517	15.483	4.6
4H-6, 145–150	29.05	7.438	3.467	36	37	598.458	481.040	28.697	BDL	502.896	52.660	BDL	11.804	52.660	13.118	4.5
5H-5, 145–150	37.05	7.379	2.965	29	37	595.309	487.071	29.590	BDL	437.119	51.921	BDL	11.904	51.921	13.924	4.4
6H-6, 145–150	48.05	7.369	3.050	12	37	598.650	484.472	29.066	BDL	529.348	51.308	4.719	11.976	51.308	14.062	4.3
7H-6, 145–150	57.57	7.304	3.140	12	37	583.852	483.337	28.260	BDL	537.956	51.369	0.21	12.483	51.369	13.394	4.1
8H-6, 145–150	67.05	7.306	3.175	34	37	594.935	488.762	28.550	BDL	455.839	51.197	BDL	12.793	51.197	11.684	4.0
9H-6, 145–150	76.56	7.268	3.315	12	38	608.114	495.797	27.934	BDL	468.141	51.950	BDL	13.433	51.950	13.947	3.9
10H-6, 136–141	85.96	7.280	3.173	21	37	591.997	482.219	27.421	BDL	457.877	50.404	BDL	13.416	50.404	11.618	3.8
11H-6, 145–150	95.55	7.276	3.354	42	37	592.634	483.247	26.660	BDL	396.860	51.105	BDL	13.994	51.105	11.439	3.7
12H-6, 145–150	105.05	7.256	3.746	12	38	597.337	488.888	27.583	BDL	323.788	50.837	BDL	14.539	50.837	11.013	3.5
13H-6, 125–130	114.39	7.121	3.716	27	38	606.582	499.049	27.212	BDL	347.003	51.609	BDL	14.968	51.609	11.749	3.4
14H-6, 145–150	124.05	7.235	3.863	18	38	616.541	499.918	27.285	BDL	313.657	51.427	BDL	15.456	51.427	10.657	3.3
17X-2, 145–150	129.95	7.206	3.864	59	37	607.619	496.434	25.218	BDL	391.985	44.715	BDL	18.139	44.715	11.152	2.5
18X-4, 145–150	137.55	7.241	3.988	31	37	608.612	495.954	24.697	BDL	338.700	43.508	BDL	18.927	43.508	10.855	2.3
20X-6, 132–142	159.62	7.122	4.010	72	38	599.269	498.343	24.889	BDL	353.230	41.273	BDL	19.713	41.273	9.260	2.1
22X-6, 101–111	178.51	7.066	3.647	25	37	602.706	492.929	24.004	BDL	350.755	40.365	BDL	19.925	40.365	9.517	2.0
23X-5, 142–150	187.02	7.112	3.728	63	37	600.406	496.655	23.423	BDL	365.209	40.040	BDL	20.217	40.040	8.603	2.0
24X-4, 140–150	195.10	6.925	4.093	38	37	608.824	505.314	22.932	BDL	363.800	40.033	BDL	20.521	40.033	8.743	2.0

BDL = below detection limit ($\text{HPO}_4^{2-} = 0.2 \mu\text{M}$, $\text{Fe}^{2+} = 0.6 \mu\text{M}$), calculated as two times the standard deviation of multiple measures of a blank. ND = not detected.



Table T21. Sedimentary sample and bulk elemental geochemistry, Hole U1409A. (Continued on next two pages.)

Core, section, interval (cm)	Depth (mbsf)	CaCO ₃ (wt%)	IC (wt%)	TC (wt%)	TN (wt%)	TOC (wt%)
342-U1409A-						
1H-1, 26–27	0.26	27.56	3.30	3.95	0.18	0.65
2H-1, 38–39	1.48	23.062	2.765	2.85	0.07	0.08
2H-2, 38–39	2.98	19.974	2.395	2.54	0.09	0.15
2H-3, 38–39	4.48	46.568	5.583	5.73	0.06	0.15
2H-4, 38–39	5.98	23.831	2.857	3.49	0.17	0.63
2H-5, 38–39	7.48	5.635	0.676	0.87	0.09	0.19
2H-6, 38–39	8.98	47.468	5.691	5.83	0.06	0.14
2H-6, 38–39	8.98	49.268	5.907			
2H-7, 13–14	10.13	24.011	2.879	3.37	0.11	0.49
3H-1, 38–39	10.98	29.349	3.519	3.02	0.02	BDL
3H-1, 38–39	10.98	28.014	3.359			
3H-2, 38–39	12.48	14.606	1.751	1.99	0.08	0.24
3H-3, 38–39	13.98	35.048	4.202	4.42	0.06	0.22
3H-4, 38–39	15.48	17.991	2.157	2.20	0.07	0.04
3H-5, 38–39	16.98	5.435	0.652	0.91	0.10	0.26
3H-6, 21–22	18.31	0.375	0.045	0.13	0.08	0.09
3H-7, 18–19	19.78	0.314	0.038	0.12	0.07	0.08
4H-1, 85–86	20.95	0.452	0.054	0.11	0.07	0.06
4H-2, 30–31	21.90	0.365	0.044	0.13	0.07	0.09
4H-3, 30–31	23.40	13.509	1.62	1.72	0.07	0.10
4H-4, 30–31	24.90	11.501	1.379	1.49	0.09	0.11
4H-5, 30–31	26.40	17.278	2.072	2.16	0.08	0.09
4H-6, 30–31	27.90	24.726	2.965	3.05	0.09	0.09
4H-7, 17–18	29.27	14.987	1.797	1.93	0.08	0.13
5H-1, 38–39	29.98	17.511	2.099	2.27	0.11	0.17
5H-2, 38–39	31.48	19.333	2.318	2.53	0.09	0.21
5H-3, 38–39	32.98	52.396	6.282	6.42	0.05	0.14
5H-4, 38–39	34.48	39.807	4.773	5.00	0.07	0.23
5H-5, 38–39	35.98	38.586	4.626	4.72	0.08	0.09
5H-6, 38–39	37.48	61.228	7.341	7.54	0.05	0.20
6H-1, 38–39	39.48	48.484	5.813	5.69	0.05	BDL
6H-2, 38–39	40.98	49.924	5.986	6.33	0.09	0.34
6H-3, 38–39	42.48	34.119	4.091	4.09	0.07	0.00
6H-4, 38–39	43.98	48.683	5.837	6.06	0.06	0.22
6H-5, 38–39	45.48	46.362	5.559	5.72	0.06	0.16
6H-6, 38–39	46.98	34.626	4.151	4.21	0.07	0.06
6H-7, 18–19	48.28	28.242	3.386	3.48	0.07	0.09
7H-1, 38–39	48.98	36.242	4.345	4.32	0.06	BDL
7H-2, 38–39	50.48	27.106	3.25	3.42	0.08	0.17
7H-3, 38–39	51.98	34.983	4.194	4.38	0.08	0.19
7H-4, 38–39	53.49	29.844	3.578	3.87	0.10	0.29
7H-5, 38–39	54.99	32.977	3.954	4.18	0.08	0.23
7H-6, 38–39	56.50	34.205	4.101	0.10	0.00	BDL
7H-7, 19–20	57.81	77.182	9.254	9.53	0.03	0.28
7H-7, 19–20	57.81	78.481	9.41			
8H-1, 38–39	58.48	37.727	4.523	4.58	0.07	0.06
8H-2, 38–39	59.98	41.875	5.021	5.07	0.07	0.05
8H-3, 38–39	61.48	61.244	7.343	7.23	0.04	BDL
8H-4, 38–39	62.98	42.65	5.114	5.14	0.05	0.03
8H-5, 38–39	64.48	52.454	6.289	6.39	0.06	0.10
8H-6, 38–39	65.98	50.235	6.023	6.09	0.06	0.07
8H-7, 38–39	67.48	53.479	6.412	6.43	0.07	0.02
9H-1, 38–39	67.98	49.349	5.917	5.95	0.03	0.03
9H-2, 38–39	69.48	59.132	7.09	7.20	0.05	0.11
9H-3, 38–39	70.99	39.585	4.746	4.77	0.05	0.02
9H-4, 38–39	72.49	34.894	4.184	4.24	0.07	0.06
9H-5, 38–39	73.99	38.469	4.612	4.73	0.06	0.12
9H-6, 38–39	75.49	37.822	4.535	4.64	0.09	0.11
9H-7, 32–33	76.93	37.001	4.436	4.41	0.08	BDL
10H-1, 38–39	77.48	38.927	4.667	4.75	0.07	0.08
10H-2, 38–39	78.98	44.991	5.394	5.51	0.08	0.12
10H-3, 38–39	80.48	45.422	5.446	5.61	0.07	0.16
10H-4, 38–39	81.98	44.715	5.361	5.44	0.07	0.08
10H-5, 38–39	83.48	51.706	6.199	6.20	0.04	0.00
10H-6, 26–27	84.86	50.121	6.009	6.09	0.06	0.08
10H-7, 10–11	86.11	47.953	5.749	5.77	0.06	0.02

Table T21 (continued). (Continued on next page.)

Core, section, interval (cm)	Depth (mbsf)	CaCO ₃ (wt%)	IC (wt%)	TC (wt%)	TN (wt%)	TOC (wt%)
11H-1, 38–39	86.98	46.981	5.633			
11H-2, 38–39	88.48	51.022	6.117	6.22	0.03	0.10
11H-3, 38–39	89.98	39.488	4.734	4.75	0.45	0.02
11H-4, 38–39	91.48	37.067	4.444	4.48	0.07	0.04
11H-5, 31–32	92.91	45.727	5.482	5.67	0.05	0.19
11H-6, 38–39	94.48	58.235	6.982	7.10	0.02	0.12
11H-7, 14–15	95.74	35.143	4.213	4.23	0.08	0.02
12H-1, 38–39	96.48	35.513	4.258	4.32	0.05	0.06
12H-2, 38–39	97.98	90.902	10.899	11.00	0.00	0.10
12H-2, 38–39	97.98	90.506	10.851			
12H-3, 38–39	99.48	56.22	6.741	6.79	0.03	0.05
12H-4, 38–39	100.98	68.051	8.159	8.28	0.05	0.12
12H-5, 38–39	102.48	89.762	10.762	10.86	0.00	0.10
12H-6, 38–39	103.98	91.067	10.919	10.95	0.00	0.03
12H-7, 16–17	105.26	78.716	9.438	9.58	0.01	0.14
13H-1, 38–39	105.98	85.843	10.292	10.42	0.01	0.13
13H-2, 38–39	107.51	88.062	10.558	10.50	0.01	-0.06
13H-3, 38–39	109.02	87.14	10.448	10.52	-0.02	0.07
13H-4, 38–39	110.52	86.466	10.367	10.43	0.00	0.06
13H-5, 38–39	112.02	86.927	10.422	10.54	0.00	0.12
13H-6, 38–39	113.52	90.804	10.887	10.94	0.00	0.05
13H-7, 14–15	114.58	91.769	11.003	10.98	0.00	BDL
14H-1, 38–39	115.48	84.537	10.136	10.33	0.00	0.19
14H-2, 38–39	116.98	91.769	11.003	10.90	0.00	BDL
14H-3, 38–39	118.48	92.966	11.146	11.17	0.01	0.02
14H-4, 38–39	119.98	92.965	11.146	11.08	0.01	BDL
14H-5, 38–39	121.48	88.567	10.619	10.70	0.00	0.08
14H-6, 38–39	122.98	91.317	10.949	11.09	0.00	0.14
14H-7, 14–15	124.24	91.211	10.936	11.09	0.00	0.15
15H-1, 38–39	124.98	87.592	10.502	10.73	0.03	0.23
17X-1, 32–33	127.32	90.369	10.835	11.00	0.03	0.17
17X-2, 38–39	128.88	77.591	9.303	9.23	0.01	BDL
17X-2, 38–39	128.88	78.179	9.373			
17X-3, 31–32	130.31	90.362	10.834	11.02	0.00	0.19
18X-1, 25–26	131.85	88.399	10.599	10.62	0.01	0.02
18X-2, 12–13	133.22	90.765	10.882	11.11	-0.03	0.23
18X-3, 59–60	135.19	81.431	9.763	10.13	0.00	0.37
18X-4, 55–56	136.65	78.882	9.458	9.47	0.01	0.01
18X-5, 16–17	137.76	75.519	9.055	9.21	0.03	0.16
20X-1, 10–11	150.90	77.702	9.316	9.47	0.03	0.15
20X-1, 145–146	152.25	76.221	9.139			
20X-2, 38–39	152.68	73.783	8.846			
20X-2, 94–95	153.24	71.365	8.556			
20X-3, 38–39	154.18	74.216	8.898			
20X-3, 60–61	154.40	52.117	6.249			
20X-3, 60–61	154.40	52.814	6.332			
20X-3, 93–94	154.73	63.027	7.557			
20X-3, 138–139	155.18	78.624	9.427			
20X-4, 26–27	155.56	85.075	10.2			
20X-4, 80–81	156.10	71.431	8.564			
20X-4, 80–81	156.10	85.463	10.247			
20X-4, 140–141	156.70	86.003	10.311			
20X-5, 20–21	157.00	85.096	10.203			
20X-5, 79–80	157.59	81.928	9.823			
20X-5, 140–141	158.20	76.456	9.167			
20X-6, 16–17	158.46	75.549	9.058			
20X-6, 76–77	159.06	78.861	9.455			
20X-6, 115–116	159.45	81.464	9.767			
20X-7, 16–17	159.88	81.528	9.775			
21X-1, 63–64	161.03	76.051	9.118	9.33	0.02	0.21
21X-2, 20–21	162.10	80.965	9.707	BDL	0.02	BDL
22X-1, 32–33	170.32	82.873	9.936			
22X-2, 37–38	171.87	77.956	9.347			
22X-3, 34–35	173.34	80.892	9.699	BDL	0.02	BDL
22X-4, 32–33	174.82	84.179	10.093			
22X-5, 22–23	176.22	83.648	10.029			
22X-6, 24–25	177.74	78.518	9.414	9.60	0.00	0.19
22X-7, 33–34	178.94	80.531	9.655			
23X-1, 26–27	179.86	86.388	10.358			

Table T21 (continued).

Core, section, interval (cm)	Depth (mbsf)	CaCO ₃ (wt%)	IC (wt%)	TC (wt%)	TN (wt%)	TOC (wt%)
23X-2, 34–35	181.44	103.348	12.391			
23X-2, 34–35	181.44	84.433	10.123			
23X-3, 36–37	182.96	79.343	9.513			
23X-4, 32–33	184.42	84.948	10.185	10.30	0.00	0.11
23X-5, 30–31	185.90	84.927	10.182			
24X-1, 45–46	189.65	79.414	9.521	9.48	0.01	BDL
24X-2, 41–42	191.11	82.129	9.847	8.51	0.02	BDL
24X-3, 29–30	192.49	80.585	9.662	9.73	0.03	0.07
24X-4, 34–35	194.04	81.046	9.717	9.82	0.01	0.10
24X-5, 23–24	195.43	78.12	9.366	9.30	0.00	BDL
26X-1, 21–22	199.51	61.568	7.382			
26X-1, 21–22	199.51	62.82	7.532			
342-U1409B-						
18X-5, 47–48	157.58	76.403	9.16	ND	ND	ND
18X-5, 59–60	157.70	78.342	9.393	ND	ND	ND
18X-5, 59–60	157.70	78.487	9.41	ND	ND	ND
18X-5, 67–68	157.78	58.237	6.982	ND	ND	ND
18X-5, 79–80	157.90	54.097	6.486	ND	ND	ND
18X-5, 79–80	157.90	54.863	6.578	ND	ND	ND
18X-5, 81–82	157.92	42.806	5.132	ND	ND	ND
18X-5, 89–90	158.00	32.166	3.857	ND	ND	ND
18X-5, 89–90	158.00	32.437	3.889	ND	ND	ND
18X-5, 95–96	158.06	39.503	4.736	ND	ND	ND
18X-5, 110–111	158.21	62.518	7.496	ND	ND	ND
18X-5, 125–126	158.36	69.669	8.353	ND	ND	ND
342-U1409C-						
6H-3, 23–24	43.53	49.1	5.887	ND	ND	ND
6H-3, 43–44	43.73	83.217	9.977	ND	ND	ND
6H-3, 83–84	44.13	34.997	4.196	ND	ND	ND
6H-3, 107–108	44.37	82.382	9.877	ND	ND	ND
6H-3, 127–128	44.57	47.628	5.71	ND	ND	ND
6H-3, 148–149	44.78	62.213	7.459	ND	ND	ND
6H-4, 7–8	44.87	59.657	7.153	ND	ND	ND
6H-4, 35–36	45.15	40.554	4.862	ND	ND	ND
6H-4, 67–68	45.47	84.825	10.17	ND	ND	ND
6H-4, 103–104	45.83	48.131	5.771	ND	ND	ND
6H-4, 118–119	45.98	68.729	8.24	ND	ND	ND
6H-4, 128–129	46.08	46.387	5.562	ND	ND	ND
6H-4, 143–144	46.23	61.042	7.319	ND	ND	ND
6H-5, 2–3	46.32	46.702	5.599	ND	ND	ND
6H-5, 23–24	46.53	79.827	9.571	ND	ND	ND
6H-5, 68–69	46.98	40.439	4.849	ND	ND	ND
6H-5, 93–94	47.23	66.867	8.017	ND	ND	ND
6H-5, 109–110	47.39	43.197	5.179	ND	ND	ND
6H-5, 133–134	47.63	70.24	8.422	ND	ND	ND
6H-5, 147–148	47.77	49.754	5.965	ND	ND	ND
20X-1, 57–58	149.87	77.938	9.345	ND	ND	ND
20X-2, 33–34	151.13	80.166	9.612	ND	ND	ND
20X-3, 35–36	152.65	82.441	9.884	ND	ND	ND
20X-4, 36–37	154.16	86.666	10.391	ND	ND	ND
20X-5, 60–61	155.90	72.896	8.74	ND	ND	ND
20X-6, 24–25	157.04	61.138	7.33	ND	ND	ND

IC = inorganic carbon, TC = total carbon, TN = total nitrogen, TOC = total organic carbon. BDL = below detection limit. ND = not determined.



Table T22. Thermal conductivity results, Site U1409. (Continued on next two pages.)

Core, section, interval (cm)	Depth (mbsf)	Thermal conductivity (W/[m·K])			Heating power (W/m)
		Mean	Standard deviation	Observation	
342-U1409A-					
3H-4A, 75	15.11	1.364	—	1.364	2.015
4H-3A, 75	23.11	1.076	1.23E-02	1.061	2.016
4H-3A, 75	23.11			1.075*	2.016
4H-3A, 75	23.11			1.091	2.016
5H-3A, 75	32.61	1.055	2.40E-03	1.052*	2.017
5H-3A, 75	32.61			1.056	2.017
5H-3A, 75	32.61			1.058	2.017
6H-3A, 75	42.11	1.124	2.91E-02	1.094	2.017
6H-3A, 75	42.11			1.164	2.017
6H-3A, 75	42.11			1.116	2.017
7H-3A, 75	51.61	1.057	1.42E-02	1.037*	1.816
7H-3A, 75	51.61			1.068	1.816
7H-3A, 75	51.61			1.066	1.816
10H-3W, 75	80.11	1.132	2.41E-02	1.098*	1.613
10H-3W, 75	80.11			1.152*	1.613
10H-3W, 75	80.11			1.146	1.613
11H-3A, 75	89.61	1.163	6.70E-03	1.156	1.613
11H-3A, 75	89.61			1.172*	1.613
11H-3A, 75	89.61			1.160	1.613
12H-3A, 75	99.11	1.166	8.40E-03	1.154	1.613
12H-3A, 75	99.11			1.173*	1.613
12H-3A, 75	99.11			1.171	1.613
13H-3A, 75	108.65	1.133	1.49E-02	1.115	1.613
13H-3A, 75	108.65			1.133*	1.613
13H-3A, 75	108.65			1.151	1.613
14H-3A, 75	118.11	1.261	1.07E-02	1.246	1.612
14H-3A, 75	118.11			1.267	1.612
14H-3A, 75	118.11			1.27*	1.612
15H-1A, 75	124.61	1.302	1.42E-02	1.282	1.612
15H-1A, 75	124.61			1.31*	1.612
15H-1A, 75	124.61			1.314*	1.612
17X-3A, 60	130.01	1.408	7.50E-03	1.411*	1.612
17X-3A, 60	130.01			1.415*	1.612
17X-3A, 60	130.01			1.397	1.612
18X-3A, 75	134.61	1.417	2.15E-02	1.447*	1.612
18X-3A, 75	134.61			1.408*	1.612
18X-3A, 75	134.61			1.397*	1.612
22X-3A, 50	173.01	1.376	4.45E-02	1.315	1.612
22X-3A, 50	173.01			1.418*	1.612
22X-3A, 50	173.01			1.396*	1.612
23X-4A, 75	184.11	1.369	—	1.369*	1.612
24X-3A, 75	192.21	1.402	2.44E-02	1.368*	1.612
24X-3A, 75	192.21			1.424*	1.612
24X-3A, 75	192.21			1.414*	1.612
24X-3A, 75	192.21			1.368*	1.612
24X-3A, 75	192.21			1.424*	1.612
24X-3A, 75	192.21			1.414*	1.612
342-U1409B-					
2H-3A, 75	11.31	1.155	1.51E-02	1.140	1.612
2H-3A, 75	11.31			1.176*	1.612
2H-3A, 75	11.31			1.149	1.612
3H-3A, 75	20.81	1.015	9.60E-03	1.002	1.612
3H-3A, 75	20.81			1.018*	1.612
3H-3A, 75	20.81			1.024	1.612
4H-3A, 75	30.31	1.085	1.51E-02	1.065	1.612
4H-3A, 75	30.31			1.091*	1.612
4H-3A, 75	30.31			1.100	1.612
5H-3A, 75	39.81	1.08	2.60E-02	1.043*	1.612
5H-3A, 75	39.81			1.100	1.612
5H-3A, 75	39.81			1.096*	1.612
6H-3A, 75	49.31	1.074	7.50E-03	1.067	1.612
6H-3A, 75	49.31			1.071*	1.612
6H-3A, 75	49.31			1.085	1.612
7H-3A, 75	58.81	1.083	7.20E-03	1.073	1.612
7H-3A, 75	58.81			1.086*	1.612
7H-3A, 75	58.81			1.090	1.612



Table T22 (continued). (Continued on next page.)

Core, section, interval (cm)	Depth (mbsf)	Thermal conductivity (W/[m·K])			Heating power (W/m)
		Mean	Standard deviation	Observation	
8H-3W, 75	68.31	1.057	6.60E-03	1.048	1.612
8H-3W, 75	68.31			1.063	1.612
8H-3W, 75	68.31			1.060	1.612
9H-3A, 75	77.81	1.11	9.40E-03	1.106	1.612
9H-3A, 75	77.81			1.123*	1.612
9H-3A, 75	77.81			1.101*	1.612
10H-3A, 75	87.31	1.166	1.52E-02	1.145*	1.612
10H-3A, 75	87.31			1.179*	1.612
10H-3A, 75	87.31			1.175	1.612
11H-3W, 75	96.81	1.105	1.36E-02	1.100	1.612
11H-3W, 75	96.81			1.124*	1.612
11H-3W, 75	96.81			1.092*	1.612
12H-3W, 75	106.31	1.326	2.48E-01	1.676	1.612
12H-3W, 75	106.31			1.145*	1.612
12H-3W, 75	106.31			1.156*	1.612
13H-3W, 75	115.81	1.166	1.97E-02	1.169	1.612
13H-3W, 75	115.81			1.141*	1.612
13H-3W, 75	115.81			1.189*	1.612
15X-3W, 75	125.51	1.327	1.92E-02	1.304	1.612
15X-3W, 75	125.51			1.326*	1.612
15X-3W, 75	125.51			1.351*	1.612
16X-3W, 75	135.11	1.339	1.57E-02	1.317	1.612
16X-3W, 75	135.11			1.354*	1.612
16X-3W, 75	135.11			1.345	1.612
17X-3W, 75	144.71	1.311	2.63E-02	1.274	1.612
17X-3W, 75	144.71			1.331*	1.612
17X-3W, 75	144.71			1.328*	1.612
342-U1409C-					
2H-3A, 75	9.31	0.955	3.20E-02	0.91*	1.612
2H-3A, 75	9.31			0.978	1.612
2H-3A, 75	9.31			0.978	1.612
3H-3A, 75	18.81	0.942	4.03E-02	0.885*	1.612
3H-3A, 75	18.81			0.969	1.612
3H-3A, 75	18.81			0.972	1.612
4H-3A, 75	28.31	1.085	6.60E-03	1.076	1.612
4H-3A, 75	28.31			1.087*	1.612
4H-3A, 75	28.31			1.092*	1.612
5H-3A, 75	33.81	1.093	1.21E-02	1.082	1.612
5H-3A, 75	33.81			1.11*	1.612
5H-3A, 75	33.81			1.087*	1.612
6H-3A, 75	43.31	1.071	9.90E-03	1.057	1.612
6H-3A, 75	43.31			1.080	1.612
6H-3A, 75	43.31			1.076	1.612
7H-3W, 75	52.81	1.030	1.15E-02	1.014	1.612
7H-3W, 75	52.81			1.040	1.612
7H-3W, 75	52.81			1.036	1.612
8H-3W, 75	62.31	1.069	1.38E-02	1.049	1.612
8H-3W, 75	62.31			1.078*	1.612
8H-3W, 75	62.31			1.078	1.612
9H-3W, 75	71.81	1.144	1.53E-02	1.125	1.612
9H-3W, 75	71.81			1.146*	1.612
9H-3W, 75	71.81			1.162	1.612
10H-3W, 75	81.31	1.183	7.50E-03	1.188	1.612
10H-3W, 75	81.31			1.188*	1.612
10H-3W, 75	81.31			1.172*	1.612
11H-3W, 75	90.81	1.185	5.90E-03	1.181	1.612
11H-3W, 75	90.81			1.193*	1.612
11H-3W, 75	90.81			1.18*	1.612
12H-3W, 75	100.31	1.331	1.55E-02	1.312*	1.612
12H-3W, 75	100.31			1.35*	1.612
12H-3W, 75	100.31			1.332*	1.612
13H-3W, 75	109.81	1.136	1.28E-02	1.119	1.612
13H-3W, 75	109.81			1.15*	1.612
13H-3W, 75	109.81			1.138*	1.612
14H-3W, 75	119.31	1.174	7.20E-03	1.164	1.612
14H-3W, 75	119.31			1.175*	1.612
14H-3W, 75	119.31			1.182	1.612



Table T22 (continued).

Core, section, interval (cm)	Depth (mbsf)	Thermal conductivity (W/[m·K])			Heating power (W/m)
		Mean	Standard deviation	Observation	
15X-3W, 60	127.21	1.321	2.70E-03	1.317	1.612
15X-3W, 60	127.21			1.324*	1.612
15X-3W, 60	127.21			1.322*	1.612
17X-3A, 80	134.81	1.306	1.15E-01	1.144	1.612
17X-3A, 80	134.81			1.399*	1.612
17X-3A, 80	134.81			1.375*	1.612
18X-3A, 75	139.81	1.359	7.30E-03	1.354*	1.612
18X-3A, 75	139.81			1.369*	1.612
18X-3A, 75	139.81			1.353*	1.612
19X-3A, 75	146.31	1.374	1.18E-02	1.357*	1.612
19X-3A, 75	146.31			1.383*	1.612
19X-3A, 75	146.31			1.381*	1.612
20X-3A, 75	152.31	1.410	8.30E-03	1.406*	1.612
20X-3A, 75	152.31			1.403*	1.612
20X-3A, 75	152.31			1.422*	1.612
21X-2A, 70	158.81	1.241	1.30E-02	1.226	1.612
21X-2A, 70	158.81			1.238*	1.612
21X-2A, 70	158.81			1.258*	1.612

* = result obtained directly from the TK04 processing software. Other results were generated by the IODP uploader using raw data because they were rejected by the TK04 software. Thermal conductivity mean and standard deviation calculated from thermal conductivity observations. — = uncalculable data.



Table T23. Core top and composite depth, Site U1409. (Continued on next page.)

Core	Depth			Cumulative offset (m)	Comment
	(mbsf)	(m CCSF)	Offset (m)		
342-U1409A-					
1H	0.00	0.10	0.10	0.10	
2H	1.10	2.67	1.47	1.57	
3H	10.60	12.46	0.29	1.86	
4H	20.10	23.53	1.57	3.43	
5H	29.60	35.38	2.35	5.78	
6H	39.10	45.45	0.57	6.35	
7H	48.60	55.61	0.66	7.01	
8H	58.10	65.30	0.19	7.20	
9H	67.60	76.47	1.67	8.87	
10H	77.10	86.64	0.67	9.54	
11H	86.60	97.16	1.02	10.56	
12H	96.10	110.11	3.45	14.01	
13H	105.60	121.22	1.61	15.62	
14H	115.10	132.35	1.63	17.25	Offset to remove overlap
15H	124.60	144.75	2.90	20.15	
16H	126.10	146.25	0.00	20.15	
17X	127.00	152.15	5.00	25.15	Large offset to align with Hole U1409C
18X	131.60	156.85	0.10	25.25	
19X	141.20	166.55	0.10	25.35	No recovery
20X	150.80	176.47	0.32	25.67	
21X	160.40	186.09	0.02	25.69	
22X	170.00	197.13	1.44	27.13	Offset = 15% of drilling advance
23X	179.60	208.17	1.44	28.57	Offset = 15% of drilling advance
24X	189.20	219.21	1.44	30.01	Offset = 15% of drilling advance
25X	197.70	228.99	1.28	31.29	Offset = 15% of drilling advance
26X	199.30	230.83	0.24	31.53	Offset = 15% of drilling advance
342-U1409B-					
1H	0.00	0.03	0.03	0.03	
2H	8.30	8.80	0.47	0.50	
3H	17.80	18.80	0.50	1.00	
4H	27.30	29.34	1.04	2.04	
5H	36.80	39.21	0.37	2.41	
6H	46.30	48.82	0.11	2.52	
7H	55.80	59.32	1.00	3.52	
8H	65.30	71.86	3.04	6.56	
9H	74.80	82.16	0.80	7.36	Tentative
10H	84.30	94.32	2.66	10.02	
11H	93.80	104.89	1.07	11.09	
12H	103.30	117.76	3.37	14.46	
13H	112.80	132.95	5.69	20.15	
14H	122.30	142.45	0.00	20.15	No recovery
15X	122.50	142.65	0.00	20.15	No offset because core is appended
16X	132.10	154.45	2.20	22.35	
17X	141.70	164.15	0.10	22.45	
18X	151.30	173.35	-0.40	22.05	
19X	160.90	182.72	-0.23	21.82	
342-U1409C-					
1H	0.00	0.00	0.00	0.00	
2H	6.30	8.01	1.71	1.71	
3H	15.80	19.08	1.57	3.28	
4H	25.30	28.56	-0.02	3.26	
5H	30.80	34.54	0.48	3.74	
6H	40.30	44.59	0.55	4.29	
7H	49.80	55.40	1.31	5.60	
8H	59.30	63.89	-1.01	4.59	
9H	68.80	76.21	2.82	7.41	
10H	78.30	86.51	0.80	8.21	
11H	87.80	96.68	0.67	8.88	
12H	97.30	112.43	6.25	15.13	
13H	106.80	121.32	-0.61	14.52	
14H	116.30	133.75	2.93	17.45	
15X	124.20	143.85	2.20	19.65	No offset because core is appended
16X	129.20	148.85	0.00	19.65	No offset because core is appended
17X	131.80	151.45	0.00	19.65	No offset because core is appended
18X	136.80	156.65	0.20	19.85	



Table T23 (continued).

Core	Depth		Offset (m)	Cumulative offset (m)	Comment
	(mbsf)	(m CCSF)			
19X	143.30	161.85	-1.30	18.55	
20X	149.30	167.45	-0.40	18.15	
21X	157.30	176.35	0.90	19.05	

Table T24. Splice tie points, Site U1409.

Hole, core, section, interval (cm)	Depth		Hole, core, section, interval (cm)	Depth		Comment
	(mbsf)	(m CCSF)		(mbsf)	(m CCSF)	
342-			342-			
U1409C-1H-2, 100	2.50	2.50	Tie to	U1409C-1H-1, 0	0.00	0.00
U1409B-1H-5, 38	6.38	6.41	Tie to	U1409B-1H-2, 97	2.47	2.50
U1409A-2H-5, 108	8.18	9.75	Tie to	U1409A-2H-3, 74	4.84	6.41
U1409B-2H-4, 143	14.23	14.73	Tie to	U1409B-2H-1, 95	9.25	9.75
U1409A-3H-5, 82	17.42	19.28	Tie to	U1409A-3H-2, 77	12.87	14.73
U1409B-3H-6, 69	25.99	26.99	Tie to	U1409B-3H-1, 48	18.28	19.28
U1409A-4H-5, 124	27.34	30.77	Tie to	U1409A-4H-3, 46	23.56	26.99
U1409B-4H-6, 54	35.34	37.38	Tie to	U1409B-4H-1, 143	28.73	30.77
U1409C-5H-5, 29	37.09	40.83	Tie to	U1409C-5H-2, 134	33.64	37.38
U1409B-5H-6, 75	45.05	47.46	Tie to	U1409B-5H-2, 12	38.42	40.83
U1409A-6H-6, 110	47.70	54.05	Tie to	U1409A-6H-2, 51	41.11	47.46
U1409B-6H-6, 6	53.86	56.38	Tie to	U1409B-6H-4, 73	51.53	54.05
U1409C-7H-6, 29	57.59	63.19	Tie to	U1409C-7H-1, 98	50.78	56.38
U1409B-7H-6, 127	64.57	68.09	Tie to	U1409B-7H-3, 87	59.67	63.19
U1409A-8H-6, 111	66.71	73.91	Tie to	U1409A-8H-2, 129	60.89	68.09
U1409B-8H-6, 57	73.37	79.93	Tie to	U1409B-8H-2, 55	67.35	73.91
U1409C-9H-6, 79	77.12	84.53	Tie to	U1409C-9H-3, 72	72.52	79.93
U1409B-9H-5, 96	81.76	89.12	Tie to	U1409B-9H-2, 87	77.17	84.53
U1409A-10H-7, 34	86.35	95.89	Tie to	U1409A-10H-2, 98	79.58	89.12
U1409B-10H-3, 33	87.63	97.65	Tie to	U1409B-10H-2, 7	85.87	95.89
U1409C-11H-2, 117	90.47	99.35	Tie to	U1409C-11H-1, 97	88.77	97.65
U1409A-11H-6, 107	95.17	105.73	Tie to	U1409A-11H-2, 69	88.79	99.35
U1409B-11H-5, 101	100.81	111.90	Tie to	U1409B-11H-1, 84	94.64	105.73
U1409A-12H-4, 41	101.01	115.02	Tie to	U1409A-12H-2, 29	97.89	111.90
U1409C-12H-6, 60	105.40	120.53	Tie to	U1409C-12H-2, 109	99.89	115.02
U1409B-12H-6, 94	111.74	126.20	Tie to	U1409B-12H-2, 127	106.07	120.53
U1409A-13H-CC, 45	115.51	131.13	Append to	U1409A-13H-4, 44	110.58	126.20
U1409A-14H-3, 120	119.30	136.55	Tie to	U1409A-14H-1, 0	115.10	132.35
U1409B-13H-CC, 7	121.61	141.76	Append to	U1409B-13H-3, 60	116.40	136.55
U1409B-15X-CC, 15	128.13	148.28	Append to	U1409B-15X-1, 0	122.50	142.65
U1409C-16X-CC, 10	131.24	150.89	Append to	U1409C-16X-1, 32	129.52	149.17
U1409C-17X-3, 50	135.30	154.95	Tie to	U1409C-17X-1, 0	131.80	151.45
U1409B-16X-5, 40	138.50	160.85	Tie to	U1409B-16X-1, 50	132.60	154.95
U1409A-18X-5, 40	138.00	163.25	Tie to	U1409A-18X-3, 100	135.60	160.85
U1409C-19X-2, 120	146.00	164.55	Tie to	U1409C-19X-1, 140	144.70	163.25
U1409B-17X-5, 100	148.70	171.15	Tie to	U1409B-17X-1, 40	142.10	164.55
U1409C-20X-5, 120	156.50	174.65	Tie to	U1409C-20X-3, 70	153.00	171.15
U1409B-18X-6, 90	159.32	181.37	Tie to	U1409B-18X-1, 130	152.60	174.65
U1409A-20X-6, 85	159.15	184.82	Tie to	U1409A-20X-4, 40	155.70	181.37
U1409B-19X-CC, 24	170.57	192.39	Append to	U1409B-19X-2, 60	163.00	184.82
U1409A-22X-CC, 29	179.37	206.50	Append to	U1409A-22X-1, 0	170.00	197.13
U1409A-23X-CC, 38	188.51	217.08	Append to	U1409A-23X-1, 0	179.60	208.17
U1409A-24X-CC, 45	197.09	227.10	Append to	U1409A-24X-1, 0	189.20	219.21
U1409A-26X-CC, 49	200.47	232.00	Append to	U1409A-26X-1, 0	199.30	230.83

